Thermophysical Properties and Microstructural Changes of Composite Materials at Elevated Temperature

Thomas William Goodrich

Thesis submitted to the faculty of the Virginia Polytechnic Institute and State University in partial fulfillment of the requirements for the degree of

Master of Science
In
Mechanical Engineering

Brian Y. Lattimer
Scott W. Case
Michael W. Ellis

November 19, 2009
Blacksburg, VA

Keywords: Composites, microstructure, decomposition, porosity, permeability

Thermophysical Properties and Microstructural Changes of Composite Materials at Elevated Temperature

Thomas William Goodrich

ABSTRACT

Experimental methods were developed and used to quantify the behavior of composite materials during heating to support development of heat and mass transfer pyrolysis models. Methods were developed to measure specific heat capacity, kinetic parameters, microstructure changes, porosity, and permeability. Specific heat and gravimetric data for kinetic parameters were measured with a simultaneous differential scanning calorimeter (DSC) / thermogravimetric analyzer (TGA). Experimental techniques were developed for quantitative specific heat measurement based on ASTM standards with modifications for accurate measurements of decomposing materials. An environmental scanning electron microscope (ESEM) was used in conjunction with a heating platform to record real-time video of microstructural changes of materials during decomposition and cooling following decomposition. A gas infusion technique was devised to measure porosity, in which nitrogen was infused into the pores of permeable material samples and used to determine the open-pore porosity of the material. Permeability was measured using a standard pressure differential gas flow technique with improvements over past sealing techniques and modifications to allow for potential high temperature use.

Experimental techniques were used to measure the properties of composite construction materials commonly used in naval applications: E-glass vinyl ester laminates and end-grain balsa wood core. The simultaneous DSC/TGA was used to measure the apparent specific heat required to heat the decomposing sample. ESEM experiments captured microstructural changes during decomposition for both E-glass vinyl ester laminate and balsa wood samples. Permeability and porosity changes during decomposition appeared to depend on microstructural changes in addition to mass fraction.

Dedication

For Erin, who has brought more joy to my life than I knew possible.

Acknowledgements

First and foremost, I would like to acknowledge Dr. Brian Lattimer. Dr. Lattimer has served as both an academic advisor and mentor to me over the past 22 months. I originally elected graduate school over a full-time job after completing my undergraduate work at Virginia Tech simply because I was far from ready to leave Blacksburg, and had no idea what I wanted to do next. Now, on the verge of completing a master's degree, all of that has changed under Dr. Lattimer's guidance. I believe that I have come into my own as a researcher and as an engineer. I know that I could not have chosen a better advisor.

I would also like to acknowledge my other committee members, Dr. Scott Case and Dr. Michael Ellis. As a research partner to Dr. Lattimer, Dr. Case has been involved in my research activities from the start, in addition to having taught two of my graduate courses. Graduate school most certainly would not have been the same without him! While I have had somewhat less interaction with Dr. Ellis, he has been both kind and helpful every time that I have had the opportunity to speak with him. I very much appreciate his serving on my committee.

The help of Steve McCartney of the Nanoscale Characterization and Fabrication Laboratory at Virginia Tech is greatly appreciated. The many hours of instrument training and sample preparation guidance that Mr. McCartney provided were invaluable to my research.

The Office of Naval Research provided funding for this study under contract number N00014-08-1-0528. The support of the ONR is greatly appreciated.

Table of Contents

List of Figures vi
List of Tables viii
List of Abbreviations ix
Chapter 1 – Introduction 1
Background 1
Literature Review 3
Research Objectives 6
Chapter 2 – Experimental Methods 7
Introduction 7
Thermal Analysis 7
Microstructure 11
Porosity 13
Permeability 16
Intermediate Scale Thermogravimetric Analyzer 20
Computerized Tomography X-ray Analysis 23
Materials Studied 23
Chapter 3 – Thermal Analysis 26
DSC Sensitivity Studies 26
E-glass Vinyl Ester Composite 31
Balsa Wood 33
Chapter 4 – Microstructure, Porosity, and Permeability of Balsa Wood 38
Microstructure 38
Parallel to the Grain 38
Grain Cross-section 40
Grain Cross-Section Analysis 43
Water Transport Vessel Analysis 45
Porosity & Permeability 47
CT Scans 50
Chapter 5 – Microstructure, Porosity, and Permeability of E-glass/Vinyl-ester 52
Microstructure 52
Derakane 411-350 Vinyl-Ester Resin 52
E-glass/Vinyl-Ester Composite 54
Porosity & Permeability 57
CT Scans 62
Chapter 6 – Summary & Conclusions 64
Summary 64
Conclusions 65
General 65
E-glass/Vinyl Ester 65
Balsa Wood 66
Chapter 7 – Recommendations 67
References 69
Appendices 72
Appendix A: Relevant Calculations 72
Porosity Error 72

Appendix B: Porosity & Permeability Test Data 73
E-Glass/Vinyl Ester 73
Balsa Wood 99
Appendix C: ISTGA Curves and ESEM Images of Intermediate-scale Samples 116
E-glass/Vinyl Ester 116
Balsa Wood 125
Appendix D: Technical Drawings 130
Porosity Test Section 130
Permeability Test Section 132
Intermediate Scale TGA 134
Appendix E: Additional Specific Heat Data 148
Aluminum 5083-H116 148
MACOR™ 149
NAD-11 150

List of Figures

Figure 1. One-dimensional pyrolysis model layout....2
Figure 2. Netzsch STA 449 F1 Jupiter external view and sample holder....8
Figure 3. DSC signals broken apart....9
Figure 4. ESEM and internal heating platform....12
Figure 5. Virgin balsa wood cut across the grain with a saw (a) and with a razor blade (b)....12
Figure 6. Porosity test apparatus....14
Figure 7. Typical porosity mass flow rate and total mass flow plots....15
Figure 8. E-glass/VE and balsa samples for porosity and permeability....15
Figure 9. Sample permeability data set – virgin balsa wood....17
Figure 10. Permeability Test Section....18
Figure 11. Sealed E-glass/VE sample....18
Figure 12. E-glass/VE thermogravimetric plot (limited range)....20
Figure 13. Images of the intermediate-scale TGA....21
Figure 14. Comparison of TGA and ISTGA....23
Figure 15. Baltek SB.100 panel....24
Figure 16. Specific heat curve for E-glass/VE based on initial mass, generated by Netzsch.....27
Figure 17. Comparison of solid and powdered E-glass/VE samples....27
Figure 18. Core drill, STA sample, sample pushed into platinum cup....28
Figure 19. Comparison of STA sample cup types....28
Figure 20. Comparison of sapphire DSC signals....30
Figure 21. Specific heat for E-glass/vinyl-ester with TGA result (20°C/min)....31
Figure 22. E-glass/vinyl-ester TGA results....32
Figure 23. E-glass/vinyl-ester results in terms of normalized mass fraction....32
Figure 24. TGA data for fibers, resin, and composite....33
Figure 25. Specific heat and TGA data for balsa wood (20°C/min)....34
Figure 26. Balsa wood TGA results....35
Figure 27. Balsa wood results in terms of normalized mass fraction....36
Figure 28. Balsa wood dehydration results....37
Figure 29. Balsa wood dehydration results in terms of normalized mass fraction....37
Figure 30. Balsa wood TGA curve from 50-550°C at 20°C/min, including dehydration....38
Figure 31. Micrographs of balsa parallel to the grain during heating....39
Figure 32. Micrographs of balsa parallel to the grain (a) before and (b) after cooling.....40
Figure 33. Micrographs of balsa grain cross section during heating at 20°C/min.....41
Figure 34. Micrographs of balsa grain before and after cooling....42
Figure 35. Grain cross-section I mages used in the surface analysis....43
Figure 36. Grain diameter and void fraction of grain cross-section at several temperatures....44
Figure 37. Average grain diameter, grain count, void fraction, and analysis area as functions of temperature.....45
Figure 38. Balsa wood water transport channels....46
Figure 39. Close of up a water transport channel....46
Figure 40. Inter-cell water transport vessels....47
Figure 41. Porosity of balsa wood vs. mass fraction....48
Figure 42. Permeability test data for balsa wood....49
Figure 43. Balsa wood permeability plots....50
Figure 44. Virgin balsa wood sample external view....50

Figure 45. Virgin balsa wood cutaway view (grain vertical) 51
Figure 46. Virgin balsa wood cross-sectional view showing water transport vessels....51
Figure 47. Micrographs of Derakane 411-350 vinyl-ester resin 53
Figure 48. E-glass/vinyl ester before heating 54
Figure 49. Micrographs of E-glass/VE during heating....55
Figure 50. Large view of E-glass/VE at 548°C 56
Figure 51. E-glass/VE sample at high and low temperature after cooling 57
Figure 52. Selected E-glass/VE permeability sample data sets....59
Figure 53. E-glass/VE porosity 60
Figure 54. E-glass/VE permeability data and fit 60
Figure 55. E-glass/VE permeability vs. porosity....61
Figure 56. E-glass/VE samples fully decomposed in (a) nitrogen and (b) air....62
Figure 57. Cracked intermediate-scale sample, F = 0.39 62
Figure 58. Internal cross-sectional views of virgin (top) and decomposed (bottom) E-glass/VE.63
Figure 59. Internal layer views of virgin (left) and decomposed (right) E-glass/VE....63
Figure 60. Specific heat of aluminum 5083-H116 on two scales....148
Figure 61. Specific heat of MACOR^{TM} 149
Figure 62. Specific heat of NAD-11....150

List of Tables

Table 1. Measurement errors for porosity 16
Table 2. Measurement errors for permeability 19
Table 4. Thermally induced changes in wood from Schaffer [34] 25
Table 5. Sapphire test matrix 29
Table 6. Balsa wood water transport vessel data 47
Table 7. Porosity results for balsa wood 48
Table 8. Permeability results for balsa wood 49
Table 9. Porosity results for E-glass/VE 58
Table 10. Permeability results for E-glass/VE 59

List of Abbreviations

TGA – Thermogravimetric Analysis

DSC – Differential Scanning Calorimeter/Calorimetry

CT – Computerized Tomography

VARTM – Vacuum Assisted Resin Transfer Molding

FRP – Fiber Reinforced Plastic

ESEM – Environmental Scanning Electron Microscope

Chapter 1 – Introduction

Background

Interest in using composite materials for naval applications is increasing due to the extremely low weight and high corrosion resistance of such materials when compared to traditional materials of construction such as steel. As a result of these properties, composites are being considered for construction of entire load-bearing structure. However, composites are combustible materials that will degrade and burn when exposed to a sufficiently strong heat source. In addition, their structural properties decrease significantly as the material temperature increases above the glass transition temperature (~120°C for the vinyl ester composites being considered for naval applications). As a result, a major design challenge for the use of composite materials is fire performance.

Improving the fire performance of composite structures is key to enabling their further use in naval applications. Fire performance includes evaluating a material's fire resistance, flammability, and smoke and toxic gas generation. Fire resistance is a measure of heat transmission from the fire-exposed side to the unexposed side of the material as well as the structural integrity. Heat transmission is ability of material to insulate the heat released by the heat source, thereby preventing fire spread through the material by conduction. Structural integrity is the material's ability to maintain strength as it is heated. The composite materials examined in this thesis begin to lose their structural properties as low as 120°C, and degrade at temperatures as low as 200°C, just fractions of the temperatures at which steel begins to lose strength. Flammability is a measure of how easily the material can be ignited and how rapidly flames spread along its surface. Strongly linked to flammability and material composition, smoke and toxic gas generation is an additional concern caused by the material during burning.

The fire performance of composite naval structures may be predicted either through large-scale testing or computational modeling. The more traditional method is to conduct large scale testing. While large-scale tests will always provide the most representative data that can be obtained for a given structure, they are expensive and time consuming. The high cost in terms of both money and time involved in running such tests renders doing parametric studies for design optimization highly impractical, if not impossible. In order to reduce the number of tests required, computational models can used to conduct parametric studies and design optimizations while saving expensive large-scale tests for validation at the end of the design cycle. Conducting modeling before testing saves both time and money, and allows for more design options to be explored. The focus of this research is development of experimental methods and test data in support of computational models.

All aspects of fire performance require prediction of temperature and fuel production from the degrading composite. Predictions are created with a heat and mass transfer model called a pyrolysis model. Figure 1 shows the layout of a typical one-dimensional pyrolysis model, in which one side of a panel is heated with a given boundary condition (constant heat flux, temperature ramp, etc). At any given time in these simulations, the composite may be comprised of char (fully decomposed material), the pyrolysis region where virgin material is converted into gas and char, and virgin composite that may be heated but has not yet lost mass. Gas produced from the pyrolysis process flows to the surface where it may ignite and burn. Ignoring char oxidation processes, the mass loss rate of the material is equal to the gas mass flow rate from the

pyrolysis region. The mass flow rate of fuel (pyrolysis products) is directly related to the heat produced by burning the material as well as the toxic gases and smoke produced from the material. Temperature profiles from the model can be used to predict the heat transmission, which is useful in predicting fire spread to the unexposed side of the material. In addition, the temperature profiles can be used to determine structural properties through the thickness of the material as it is degrading.

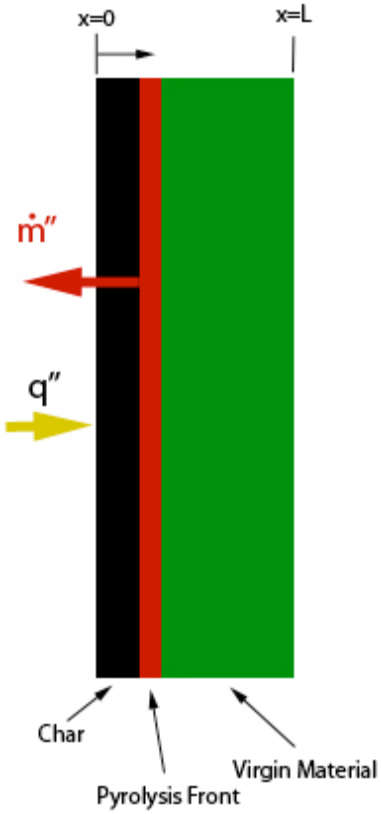

Figure 1. One-dimensional pyrolysis model layout

Pyrolysis models require a multitude of input properties for both the solid and gaseous states. Specific heat capacity, kinetic parameters, and thermal conductivity are required for the solid and pyrolysis stages of degradation. Several decomposition gas properties are also required. Most important is the specific heat of the gas, which represents the last piece of the temperature profile puzzle. Gas viscosity along with material porosity and permeability are required if the model includes predicting the details of gas flow through the charred material. Porosity and permeability describe the ease with which gases evolved during decomposition can make their way to the surface. Understanding these gas flow characteristics of the material is also important to obtaining the correct temperature distribution.

In this research, three major categories of material properties were studied to support pyrolysis model development. First, specific heat capacity data for all stages of the solid were generated and the gravimetric response was measured to support determining the kinetic decomposition parameters. Second, composite samples were heated, and video of the microstructural changes that took place was recorded in real-time in order to allow for new

modeling avenues based on microstructural changes to be explored. Lastly, open-pore porosity and permeability were evaluated on intermediate-scale specimens in order to facilitate modeling of pressure distributions through decomposing structures.

Literature Review

There are a number of studies in the literature with the objective of measuring high-temperature properties. Much of the literature content currently available is focused on materials that do not decompose with few studies on material property measurement on decomposing samples. The focus of this study is on decomposing materials. The literature was reviewed for relevant studies that explored measurement of specific heat capacity, kinetic parameters, microstructure at elevated temperatures, and changes in porosity and permeability after decomposition. This review highlights where studies on non-decomposing materials could be extended to support measurements on decomposing materials.

Specific heat capacity and mass loss of the material at elevated temperatures are routinely performed using a differential scanning calorimetry (DSC) and thermogravimetric analysis (TGA), respectively. There are ASTM standards in place that prescribe methods for conducting DSC experiments to obtain quantitative specific heat capacity (ASTM E-1269 [1]) as well as running TGA with the intent of obtaining kinetic parameters (ASTM E-1641 [2]). While these standards provide most of the information required to conduct testing, several things are left open in order to allow the standards to be widely applied. The details left unspecified or fairly open are primarily pertaining to sample geometry and type (solid, powder, shape), instrument specifics such as sample crucible material, and the details of the heating regimen. In addition to the specifics left open in the ASTM standards, there is very little in the literature where researchers used an instrument that simultaneously does both DSC and TGA on the same sample, which has the distinct advantage of ensuring that all conditions regarding the instrument and measurement are identical between the two types of data.

One major issue in DSC/TGA experiments is sample preparation. He et al. [3] studied the pyrolysis of wheat straw, cotton stalks, peanut shells, and pine wood. Samples were powdered, which is recommended for TGA by ASTM E-1641 [2] due to the very high surface-to-volume ratio in the sample. Powdered samples yield fairly poor DSC results due to the slow heat transfer within the sample. A significant amount of work [4,5,6,7] has been published on preparing samples from aluminum panels. Punching is the most common method, with sawing and spark cutting also in use, along with other methods. Stoliarov and Walters [8] cut samples into chunks of varying size and mass that covered only a portion of the sample pan surface, which goes directly against the recommendation in ASTM E-1269 [1] that the sample cover as much of the pan as possible. In essence, there are many approaches to sample preparation for DSC and TGA, but no clear answer on what the right method is, particularly when working with a simultaneous instrument.

Another important issue is sample cup material and the use of lids. ASTM E-1641 [2] simply states that the crucible should be constructed of a material that will not react with the sample. Beyond that, neither standard has anything to say on crucible materials. The crucible material was most likely left open-ended in order to maximize the applicability of the standard to different machines and materials. Platinum sample crucibles with pierced platinum lids were used to minimize the effect of emissivity on results as studied by Wolfinger [9], which was one

of a very few studies available on the ideal sample crucible material. Stanislav and Walters [8] used aluminum pans with aluminum lids to study the heats of gasification of a range of polymer samples using DSC.

One of the foremost issues when doing experiments in both DSC and TGA is using data from two different instruments. Henderson et al. [10] addressed the obvious problem of applying ASTM E-1269 [1], which stipulates that sample mass should not change more than 0.3%, to degrading materials. Henderson's work required both DSC data to obtain energetics for the sample, as well as a TGA curve to define the mass as a function of temperature. Henderson et al. broke up the apparent specific heat that the DSC instrument measured into two components: heat of decomposition and specific heat. Due to the unavailability of a simultaneous DSC/TGA at the time the work was done (1982), DSC and TGA results from similar specimens obtained at the same heating rate were used. This research goes one step further and utilizes a simultaneous DSC/TGA to remove any differences resulting from running two instruments and two samples to obtain the required data for energetics and kinetics.

The greatest difference between previous studies and this research in terms of DSC and TGA methods is the use of an instrument that combines both techniques into one package. Integrating the two types of measurements removes all of the issues associated with combining DSC and TGA measurements on the same material from two different instruments. These issues include obvious things like differences in the construction of the two instruments and the fact that two unique samples have to be tested, as well as more subtle issues such as repeatability between samples and variation in ambient conditions between tests.

Advanced pyrolysis models require information on the microscopic structure of the material in order to provide more accurate simulation results. Current understanding of the microscopic response of composite materials exposed to high temperature heating is primarily based on images of the material taken following heating. There is currently nothing available in the literature where specimens are heated in real-time during the microscopic evaluation, which has held back modelling efforts and prevented macroscopic properties from being discussed in the context of microstructural changes. Mouritz and Mathys [11] conducted a post-fire scanning electron microscope (SEM) examination of a graphite-reinforced polymer sample that had been degraded in the cone calorimeter while in an oxidizing (atmospheric air) environment and found delamination cracking inside of the composite. Chang [12] has found that polymer-matrix composite samples exposed to one-sided radiant heating can develop very steep temperature gradients due to their low thermal conductivity. Chang suggests that this high temperature gradient results in delamination cracking. Shanmuganathan et al. [13] used a transmission electron microscope (TEM) and an SEM to study the microstructure of nylon-6 nanocomposite materials with clay flame retardant additives before and after completely burning samples in the cone calorimeter. The results were used to examine the effects of differing levels and types of clay additives on the morphological changes in the material. Hanu et al. [14] conducted similar experiments on the SEM with polymer-ceramic composites which had been fired to 600°C, 800°C, and 1100°C in a tube furnace with an air atmosphere, again with the objective of learning more about the microstructure and fire resistance of the subject material. Boscoletto et al. [15] used the SEM and TEM to study the morphological changes in high-impact polystyrene blends after running the UL 94 fire test on them. Morphological changes are also used in support of developing other new materials with reduced flammability [16,17]. All of these studies were

performed on samples before and after heating, leaving all of the changes taking place in the microstructure during heating and cooling unknown.

Pyrolysis gas flow through the material microstructure is governed by the porosity and permeability of the material. Understanding the gas flow in a material is an important part of understanding the mass loss during decomposition, as gasified mass must flow out of the material.

A large variety of methods currently exist for measuring porosity. Methods exist for both permeable and non-permeable materials. Darvennes et al. [18] used ultrasonic C-scans in the pulse-echo mode to determine the porosity of thin graphite-epoxy composite laminates. Porosities on the range of 0.0003-0.067 were measured on virgin samples. Prokop [19] used X-ray computed tomography to measure the porosity of aluminum castings with porosities ranging from 0.005-0.02 with accuracy around 10%. Birt and Smith [20] conducted a review of non-destructive evaluation (NDE) techniques for measuring the porosity of fiber-reinforced polymer composites, in hopes of finding a method for measuring the porosity of composites during manufacture that was independent of the pore morphologic structure and the fiber/matrix material system used. Their study focused on ultrasonic methods, and they also made mention of thermographs [21] and microwaves [22]. They were unable to find a satisfactory technique for in-service NDE technique for porosity. Dehl [23] conducted a study on the use of mercury porosimetry for evaluating the porosity of PTFE-carbon composite implant materials, with particular concern for damaging the sample with the pressure (up to 1 atm) applied to these materials during testing due to the softness of the materials of interest. Leclare et al. [24] and much earlier Beranek [25] used comparison of air volumes determined by the ideal gas law to determine the solid (nonporous) volume in a sample, and then used simple calculations to back out the porosity. Methods involving actual gas infusion similar to those used by Leclare et al. [24] and Beranek [25] are most relevant to degrading composites. This type of test most closely simulates the conditions seen during fire, in which gases evolved in the pyrolysis region must diffuse through the pore structure to travel out of the material.

Methods for measuring permeability are less varied than those for porosity, and typically involve measuring some type of flow rate along with a pressure drop or time interval. Darcy [26] developed a law to govern permeability of sand beds to water that has been widely applied to porous materials. Morse et al. [27] pioneered a technique for determining the permeability of porous materials by drawing a known flow rate of atmospheric air through a sample from atmosphere and measuring the pressure on one side with a manometer. Hino et al. [28] conducted similar experiments on SiC/SiC composites using helium and somewhat more sophisticated instrumentation than Morse et al. [27]. Samples were sealed using a layer of epoxy resin. Wiecek [29] used this same technique to examine polymer composites, and made use of a test section that screwed together to seal on both sides of the sample. Wiecek [29] used vacuum grease and epoxy to seal samples, which had been degraded to predetermined temperatures to examine the permeability as a function of temperature. Golenstanian [30] calculated permeabilities of woven and straight fiber mats by taking measurements from video recordings of resin flow during resin infusion. Golenstanian [30] measured permeabilities at different porosity levels after calculating porosity based on the number of plies, the ply weight, the fiber density, and thickness of the laminated perform. A technique similar to that of Wiecek [29] was used in this research.

Research Objectives

This research builds on existing studies to expand the current understanding of the high temperature response of composite materials using new or improved methods. Specific methods used were DSC/TGA, real-time heated microscopy of heated specimens, and permeability and porosity by gas flow. These methods were used to quantify properties of composite laminate and balsa wood during decomposition. In addition, data gained from real-time heated microscopy was linked to changes in macroscopic properties, giving new insight on the decomposition of composite materials.

The ASTM standardizes DSC and TGA methods; however, there are several things that are not clearly specified in the standards including sample preparation and sample cup materials. This research develops experimental methods and sample preparation techniques optimized for degrading composite materials in a simultaneous DSC/TGA.

There is a fair amount of information in the literature on microstrucural changes in a variety of composite materials after heating, but nothing is currently available that shows the changes that take place in real-time. All of the literature currently available is limited to microscopy before and after heating. On this end, ESEM experiments were conducted to provide this level of insight into the morphological changes that take place in the materials during heating, as well as to determine whether or not further microstructural changes take place during cooling. These microstructural changes can then be linked to the changes that the macroscopic properties undergo as the material degrades, providing new insight into the decomposition of composites.

A variety of methods exist for measuring the porosity of both permeable and non-permeable composites. The gas infusion method is considered most similar of all the methods to what takes place in a degrading composite; therefore, it was selected for use in this research. There are also a variety of methods for testing permeability, however very little has been done on testing permeability of composite materials at different levels of decomposition. In this research, samples were degraded to a given mass fraction and then tested for both porosity and permeability.

Chapter 2 – Experimental Methods

Introduction

A series of experiments were performed on multiple size scales to develop a better understanding of the high temperature behavior of composite construction materials and obtain data for computer model input. The experiments encompassed both thermal and physical properties, as well as microscopic morphological structure and behavior during decomposition. Experiments included differential scanning calorimetry (DSC) to obtain specific heat and thermogravimetric analysis (TGA) to obtain kinetic data. Heated microstructural studies were conducted in the environmental scanning electron microscope (ESEM) to understand the morphological changes in the materials of interest during decomposition. Porosity and permeability tests were conducted at multiple levels of decomposition to obtain data on the gas flow properties of degrading composite materials.

Thermal Analysis

Two types of thermal analysis were conducted in this research. The first type was differential scanning calorimetry (DSC), which was used to obtain specific heat for the materials of interest by the ASTM E-1269 standard for the ratio method. While the standard was followed exactly, some things are not specified by the standard, primarily regarding sample preparation, the mass of the sapphire standard, and details specific to the DSC in use, such as sample pan material. The second type of thermal analysis was thermogravimetric analysis (TGA), which was used to obtain data on the mass loss during heating from the materials that were studied. Most of the techniques developed for obtaining correct specific heat measurements by DSC were also applied to TGA experiments, and not solely due to the fact that the instrument used was a simultaneous DSC/TGA. These techniques allowed for optimal temperature sensitivity during TGA experiments, which in turn yielded the best possible data for calculating the Arrhenius kinetic parameters used to describe decomposition of materials.

Thermal analysis experiments were conducted using a Netzsch STA 449 F1 Jupiter Simultaneous Thermogravimetric Analyzer/Differential Scanning Calorimeter (TGA/DSC). The instrument is capable of controlled heating and cooling at up to 50°C/min with isothermal segments at any point, and will reach temperatures up to 1500°C. Inside of the instrument's vertical tube furnace, there is a platinum sample platform with integrated type S thermocouples. Sample cups of various materials are placed on the sample platform in two positions (sample and reference). It is equipped with two 0-300 mL gas purge inlets, one in the furnace itself, and another below the furnace inside of the balance chamber. A vacuum pump is also attached to aid in setting up a consistent atmosphere for the full duration of an experimental run. The STA and its sample platform are shown in Figure 2. Note that there is no lid on the sample crucible to show where the sample is located. Lids with single 0.25 mm diameter holes were used for all experiments.

The instrument operates using a common furnace, in which sample and reference crucibles are exposed to the same heating conditions (commonly known as heat-flux compensated DSC). The furnace temperature is controlled (ramped at a set rate), and the temperature of the sample and reference crucible is recorded. A temperature difference between

the sample and reference crucible results from the energy required to heat the sample (heat flow). This temperature difference is then recorded as the DSC signal in units of volts. The DSC signal can be converted to units of watts by loading a calibration file prior to conducting the heating ramp.

The instrument allows the user to control the temperature from either the sample thermocouple, or from a furnace thermocouple. As recommended by the manufacturer, furnace temperature control was used in all experiments, as it gives better temperature accuracy and prevents temperature control problems from occurring as a result of reactions (melting, decomposition, etc) in the sample. When using furnace temperature control, the instrument will ramp until the furnace thermocouple reaches the selected temperature. This final temperature will always be higher than the sample temperature, which lags due to heat loss from the furnace and placement of the thermocouple within the furnace. The magnitude of the temperature lag depends on the exact temperature, but can range from 10-50°C. The heating rate of the sample is the same as that of the furnace, and all plots are done using sample temperature.

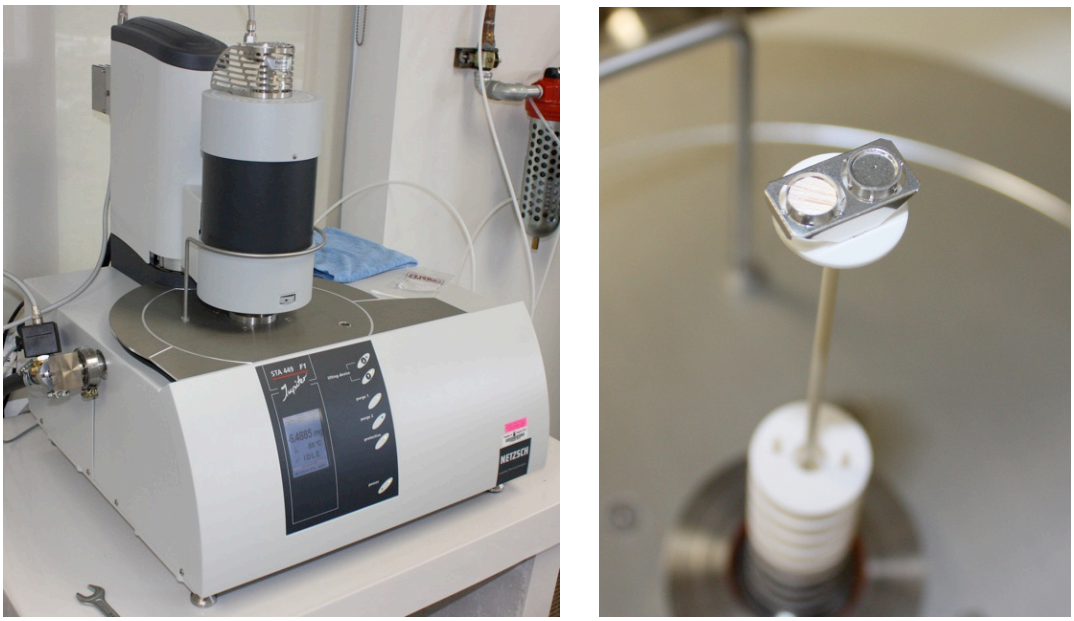

Figure 2. Netzsch STA 449 F1 Jupiter external view and sample holder

Obtaining a quantitative DSC heat flow measurement is a two-step process. First, a baseline measurement is conducted with everything (sample cups, gas flow rates, etc) in place except for the sample itself. Next, the sample is placed in the instrument and a sample measurement conducted. The signal resulting from the baseline measurement is then subtracted from that of the sample, resulting in a signal that shows a DSC signal for the sample only. Running a baseline and then running the instrument again on that baseline without loading a sample would result in a DSC signal that stayed at zero throughout the measurement. Figure 3 shows a breakdown of the DSC signal through a measurement plotted over time. The DSC Result is the combined sample and baseline measurements. Plots are shown for both time and temperature scaling. The time-scaled plot is useful for observing the effect of the baseline without a temperature ramp present. Note that the DSC Result in the time-scaled plot lies at zero before the temperature ramp begins. Prior to each run of the instrument, the sample chamber was

taken to 92-95% vacuum, and then refilled with pure nitrogen (inert). The flow of nitrogen then maintained at a rate of 50 mL/min for the duration of the experiment in order to prevent oxidation from taking place.

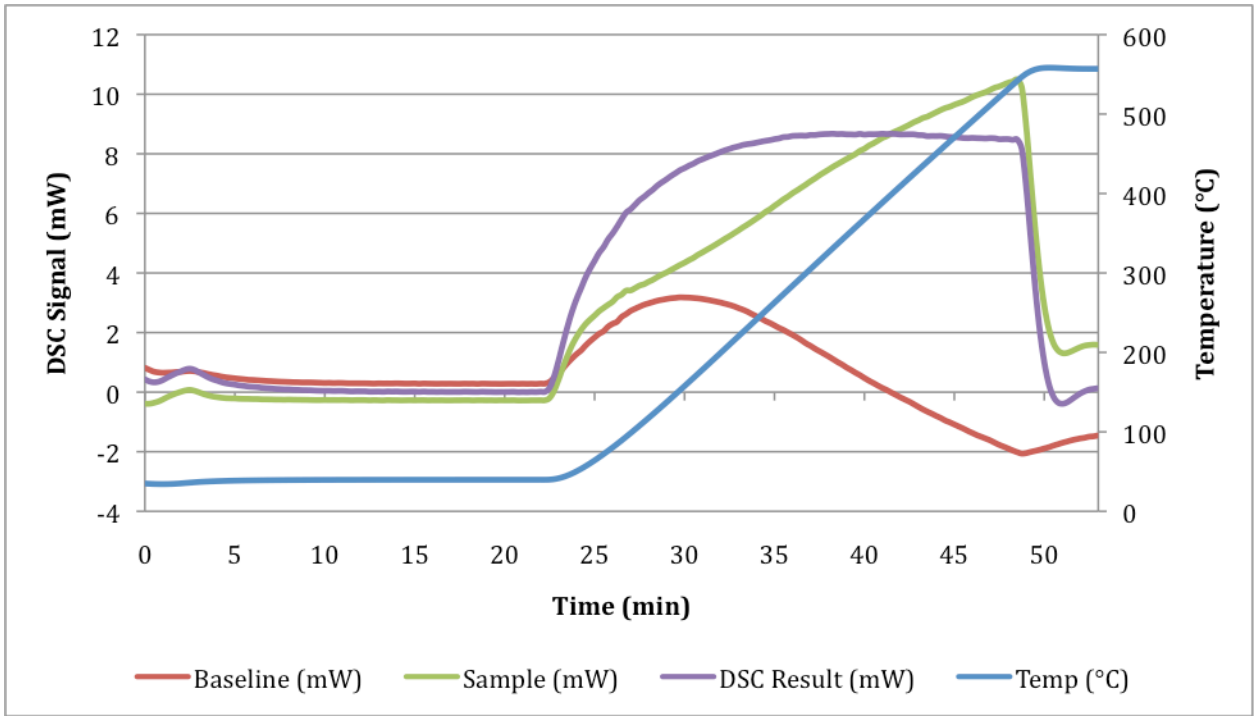

(a) Time-scaled

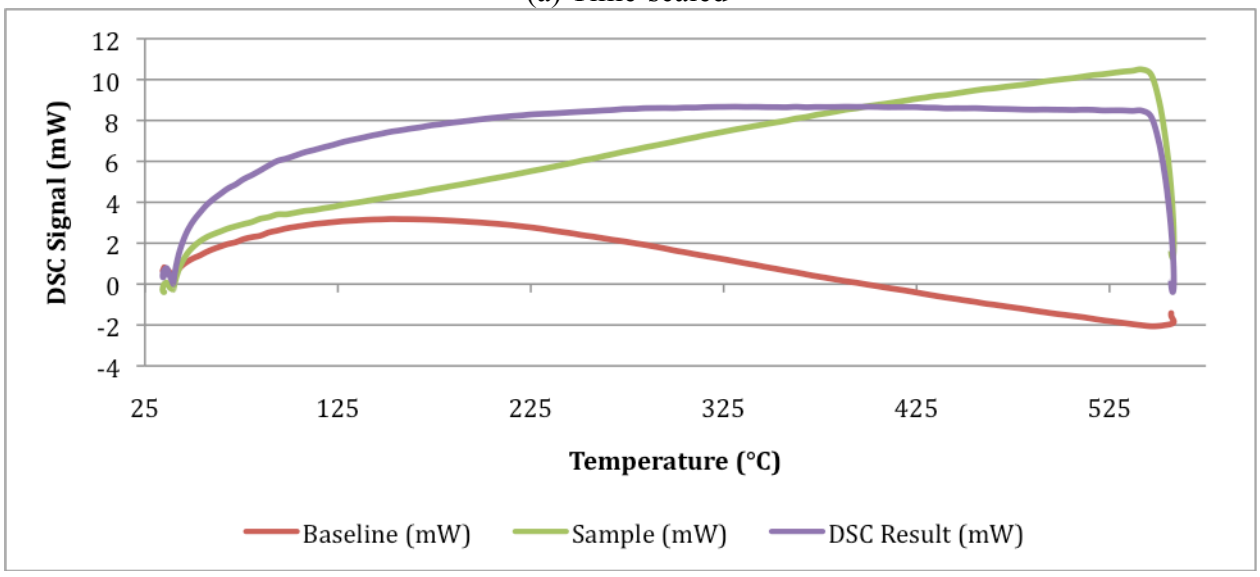

(b) Temperature-scaled

Figure 3. DSC signals broken apart

The ASTM standard (E-1269) for obtaining specific heat by the differential scanning calorimeter ratio method stipulates that heat flow curves be generated for a pure aluminum oxide (sapphire) standard and for a given sample. Assuming that the same crucibles are used for both experiments, the specific heat of the sample is determined as follows. The sample is assumed to

have lumped heat capacity, which is a good assumption for the very small samples used for DSC, and the basic specific heat equation is then applied,

$$\dot{Q} = m \bullet C_p \bullet \frac{dT}{dt} \Rightarrow C_p = \frac{\dot{Q}}{m \bullet \frac{dT}{dt}} \qquad \text{Equation 1}$$

where $\dot{Q}$ is the heat flow to the sample, m is the mass of the sample, C_p is the specific heat of the sample, and $\frac{dT}{dt}$ is the temperature rise of the sample with time. In the context of DSC, $\dot{Q}$ can be thought of as the DSC signal, and $\frac{dT}{dt}$ is assumed to be the same as the heating rate of the furnace. In order to increase the accuracy of the measurement, the equation is modified with a calibration factor, E, as shown in Equation 2.

$$C_p = \frac{E \bullet \dot{Q}}{m \bullet \frac{dT}{dt}} \qquad \text{Equation 2}$$

Determining E is a simple process, in which a DSC curve is generated for sample of known specific heat (a standard), and the data is then used to calculate E as shown in Equation 3.

$$C_{p,st} = \frac{E \bullet \dot{Q}_{st}}{m_{st} \bullet \frac{dT}{dt}} \Rightarrow E = \left(\frac{\frac{dT}{dt}}{\dot{Q}_{st}} \right) \left(m_{st} \bullet C_{p,st} \right) \qquad \text{Equation 3}$$

The calibration factor is then applied to the desired material's DSC curve, and specific heat of the sample is obtained with Equation 4.

$$C_{p,s} = \frac{E \bullet \dot{Q}_s}{m_s \bullet \frac{dT}{dt}} \qquad \text{Equation 4}$$

The sample mass, m_s, was taken from TGA data, and hence is a curve rather than a fixed value. The standard specifies that the mass of the sample should not change by more than 0.3% during the sample DSC run; however, the samples that were examined decompose as they are heated. As a result, the measured specific heat results were interpreted as an apparent specific heat, which includes both the sensible and latent portions of the energy required to heat the sample.

While the specific heat standard was followed exactly, some things were not specified by the standard in order to allow for it to be optimized to specific applications. Missing specifications include sample type and geometry (powder, solid), sample cup material, and sapphire standard geometry. In order to optimize DSC results, samples were prepared into solid

discs with masses on the range of 27-55 mg and placed in platinum cups with matching platinum lids. The best method that was found for preparing samples was to use a core drill and to then sand or file the sample to the desired thickness. Care was taken not to compress samples during preparation in order to preserve the microstructure of samples. The sapphire standards were selected and samples filed such that the average mass of the sample during the thermal experiment would match that of the sapphire, when possible. The details of why these choices were made are in the DSC Sensitivity Studies section of Chapter 3.

In some cases, where the initial and/or final masses of samples of a given material were substantially different, the TGA data was reformulated in terms of a normalized mass fraction, F. This fraction removes differences in initial and final mass, setting the initial mass to F = 1, and the final mass to F = 0. Equation 5 defines the normalized mass fraction.

$$F = \frac{m - m_f}{m_i - m_f} \qquad \text{Equation 5}$$

Microstructure

Experiments to examine the microstructure of decomposing materials were conducted on an environmental scanning electron microscope (ESEM). The ESEM differentiates itself from a traditional scanning electron microscope (SEM) in that it has the capability to run a very low-pressure (50-400 Pa) water vapor atmosphere. In an SEM, the sample is scanned in strong vacuum with a high-energy electron beam that is meant to conduct through the sample and ground into the sample platform. Typically, non-conductive samples are sputter coated to allow the electrons to disperse from the surface of the sample. Without this coating, the sample would simply appear to become highlighted, and no image could be taken. The low-pressure water vapor atmosphere of the ESEM replaces this carbon coating, allowing the electrons to disperse back out into the atmosphere and thus not requiring any coating on the samples.

The water vapor atmosphere in itself presents a challenge, as the pressure must be adjusted to optimize the image. If too much pressure is present, then the image will appear fuzzy, as the electron beam from the microscope will become partially or fully blocked by the conductive water molecules that form the atmosphere. On the opposite end of the spectrum, with the pressure too low, the electrons from the beam will collect on the sample surface in a phenomenon known as charging, and will make the surface appear very bright. In extreme cases, the image can become unusable due to charging.

The specific ESEM used was a Quanta 600 FEG, manufactured by FEI. The instrument is equipped with a heated sample holder consisting of a heated cylindrical ceramic chamber 7.5 mm in diameter and about 5 mm deep. During heated experiments, a stainless steel heat shield with a 1 mm hole covered the top opening of the heating chamber. The heat shield was put in place in order to enhance temperature uniformity over the sample. Images of the sample were taken through the 1 mm diameter opening in the heat shield. The heated sample holder is capable of achieving 1000°C at heating rates up to 100°C/min. Figure 4 shows the ESEM and its heating platform with the heat shield removed.

Figure 4. ESEM and internal heating platform

After loading the sample and closing the instrument, several vacuum cycles were completed to remove all oxygen from the sample chamber. The chamber was then given a low-pressure (50-400 Pascal) fill of water vapor. Once the vacuum cycles were completed and the electron detector centered over the desired portion of the sample, a series of images were taken at various magnification levels and positions. If conducting a heated experiment, the sample was then heated to the final temperature at 20°C/min while recording video. After images were taken at the final temperature, the sample was then cooled back to room temperature at 20°C/min (for as long as possible, as the maximum cooling rate is proportional to temperature) while continually recording video.

All microstructure balsa samples came from the same Baltek SB.100 panel as the TGA samples, and were again cut so as to avoid any glue lines between panel sub-sections. Samples were cut to rectangular prisms, roughly 2.5 x 2.5 x 5 mm, and then the desired surface was cut with a microscopy-grade razor blade manufactured by Scalpel-Klingen, which was the only method found that did not tear the material such that it obstructed the view of the wood grain. As supplied from Baltek, the panels have a sawed surface, which smears the grain together and obstructs the internal structure. Figure 5 shows two views of the balsa wood grain cross-section. The first shows the material as supplied, and the second shows it after being cut with the razor blade.

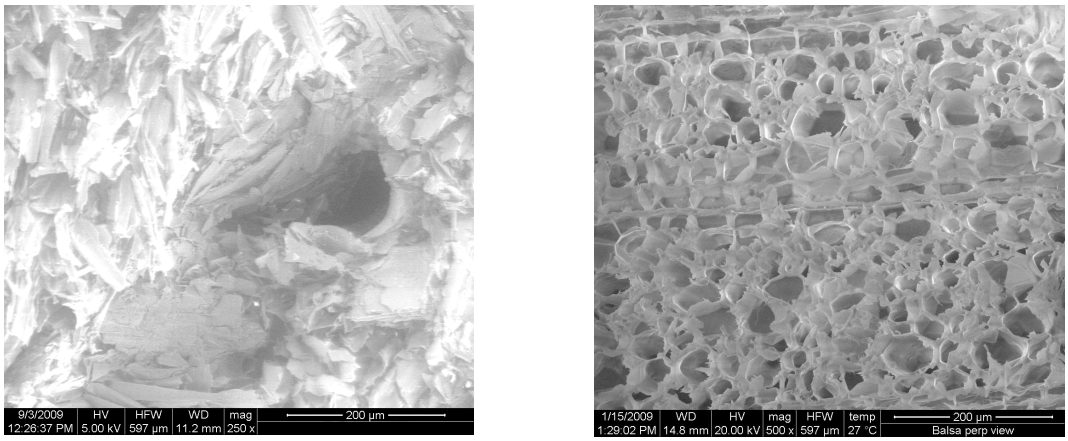

a. Saw cut b. Razor blade cut

Figure 5. Virgin balsa wood cut across the grain with a saw (a) and with a razor blade (b)

Preparation of E-glass/VE samples for microstructural analysis was accomplished by cutting small chunks of material from a larger panel, and then sanding and filing the desired surface. Samples were smaller in size than the weave pattern in the composite samples. Care was taken to capture views of fibers in multiple directions such that resin-rich regions between fiber bundles could be captured.

Porosity

Porosity, or the amount of empty space within a given material, is of interest when modeling burning and decomposing materials because it defines the amount of empty space inside of a given sample that is available for gas formation in the initial state, and describes the volume of material that has been lost as decomposition progresses. In the context of degrading permeable composites, focus is given to the open-pore porosity, or the amount of empty space inside of the material that is accessible to gases from the outside. Focus is placed on open-pore porosity because it is more closely tied to the volume of the flow paths through which pyrolysis gases may flow to the surface of the material being heated. Pores that are inaccessible to gases are of lesser interest because they do not allow gases to escape to the surface of the sample.

Several methods for measuring the open-pore porosity of virgin and decomposed material samples were considered. A single-chamber gas adsorption technique was selected due to the ease of constructing such a device and the speed with which experiments could be conducted. In this technique, a sealed chamber with a repeatable internal volume is used in conjunction with a vacuum pump and a gas mass flow controller to take volume measurements using the ideal gas law on the inside of the chamber.

The first step is to run a baseline measurement by sealing the chamber with nothing inside of it, evacuate it, and then fill it from vacuum to some pressure through the gas mass flow controller. The volume of gas in the chamber at elevated pressure is then calculated using the ideal gas law as written in Equation 6,

$$V_{gas} = \frac{m\dfrac{R}{M}T}{P_2 - P_{vac}} \qquad \text{Equation 6}$$

where m is the integral of the mass flow rate from the mass flow controller, R is the universal gas constant, M is the molar mass of the gas being used, T is the gas temperature in the chamber, P_{vac} is the vacuum pressure, and P_2 is the final pressure.

After running the baseline, the chamber is depressurized, the sample loaded, and the steps above repeated to obtain the gas volume with the sample present. The porosity is then calculated with Equation 7,

$$\phi = \frac{V_{empty}}{V_{total}} = \frac{V_{total} - \left(V_{empty} - V_{sample}\right)}{V_{total}} \qquad \text{Equation 7}$$

where V_{total} is the bulk volume of the sample as measured with calipers, and V_{empty} and V_{sample} are the baseline and sample gas volume measurement runs. All experiments (baselines and sample runs) were done twice and averaged in order to ensure reliable results. Volumes obtained were typically repeatable within 1%.

The open-pore porosity test apparatus is shown in Figure 6. The sample chamber volume was minimized in order to increase the accuracy of results by decreasing the amount of gas required to fill the chamber, thus decreasing the error resulting from measuring the gas flow. In addition, the time required to fill the chamber was minimized, reducing the time required to run experimnts. The chamber was sealed using a plug type design, consisting of a circumferential o-ring to create a consistent seal, and two ¼-20 bolts to hold the chamber shut. Two o-ring grooves were machined into the male portion of the test section in the event that more than one o-ring would be required to obtain a good seal, but only one o-ring was ever used. With this setup, the sample loading time was about 30 seconds. Complete technical drawings are available in Appendix D.

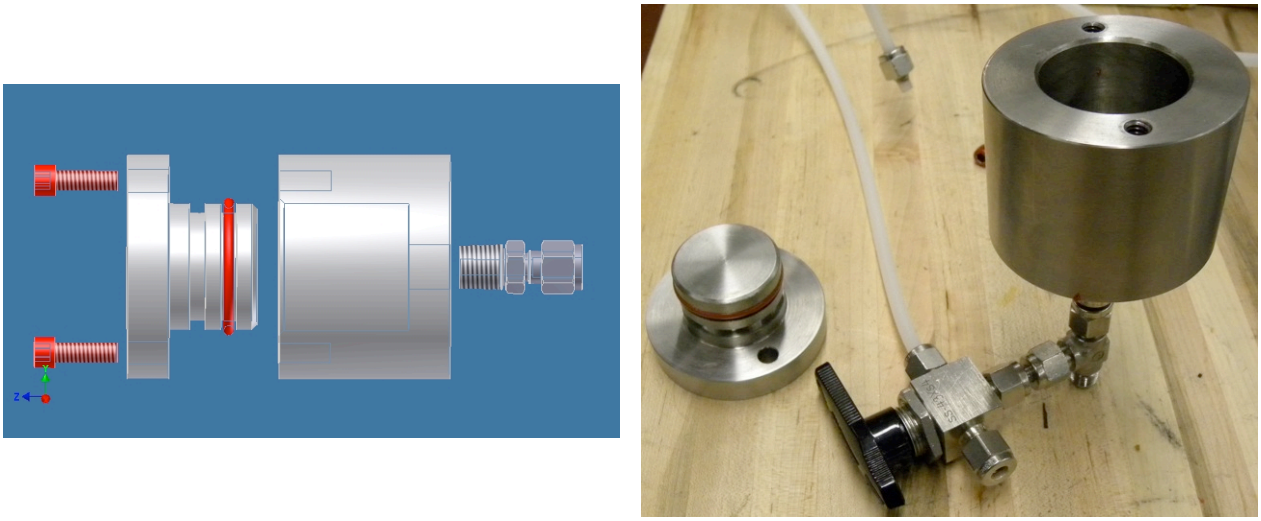

Figure 6. Porosity test apparatus

An Alicat MC-500SCCM-D mass flow controller with a 0-300 SCCM calibration and 100:1 turndown was used to set and obtain gas mass data as well as the pressure in the chamber. Typically, an upstream pressure regulator would be set to 275 kPa, and the mass flow controller would be run at 200 SCCM until the pressure in the chamber was high enough such that the gas flow would taper to less than 5 SCCM. Allowing the mass flow rate to drop so low made it easy to stop the mass flow controller at the same pressure each time, and allowing the same final pressure to be used in each experiment. Data was acquired using a National Instruments data acquisition system and a personal computer. Typically, a final pressure of 373 kPa was used. Figure 7 shows typical data for the mass flow rate and total mass flow during a baseline and sample test on the final porosity test section. Nitrogen was used as the test gas in all porosity experiments.

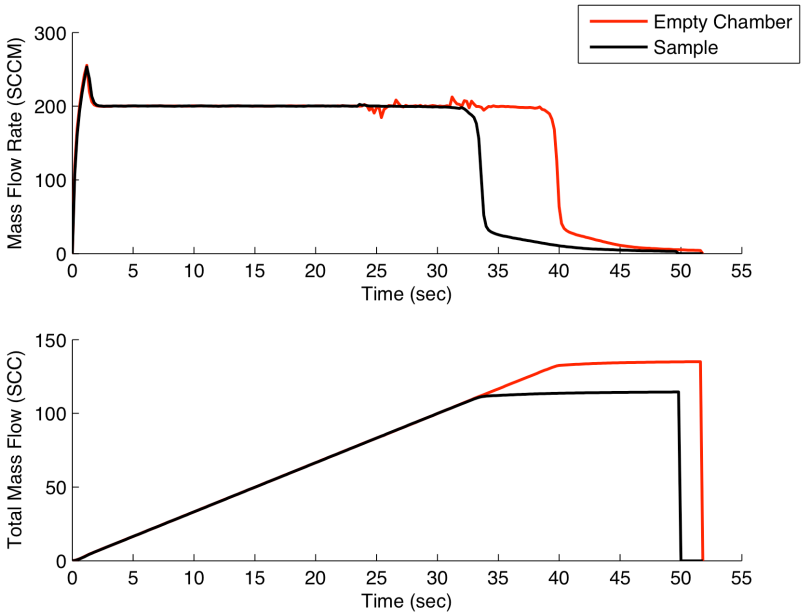

Figure 7. Typical porosity mass flow rate and total mass flow plots

Before doing any porosity tests on samples, two standards were tested to verify the function of the chamber. The volume of a steel slug 35.69 mm in diameter and 11.14 mm thick was measured, and the resulting volume obtained from the gas volume measurement was within 7% of the actual volume, as determined by measuring the sample with calipers and doing the appropriate calculation to obtain volume. A 35 mm diameter and 2.5 mm thick 100-grade disc of sintered 316L stainless steel as manufactured by the Mott Corporation was also tested, and a porosity of 0.56 was obtained, very close to the advertised value of 0.573.

Material samples for porosity were cut from panels using a core drill. The core drill produced samples with a 35.5 mm diameter, which allowed them to be used for both porosity and permeability. Figure 8 shows E-glass/vinyl-ester and balsa wood samples that were prepared for porosity and permeability testing.

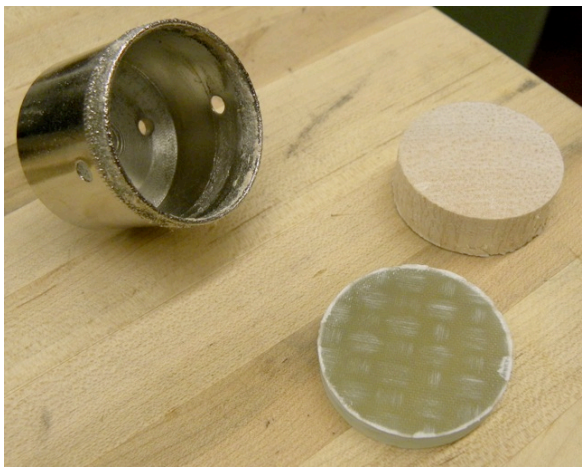

Figure 8. E-glass/VE and balsa samples for porosity and permeability

Quantifying the error in porosity experiments is important due to the large number of measurements (temperature, pressure, mass flow rate, and several dimensions) that are required to determine the value of porosity. The errors associated with each measurement are shown in Table 1.

Table 1. Measurement errors for porosity

Measurement	Error
Temperature	±1.5°C
Pressure	±5500 Pa
Mass Flow Rate	±(0.8% of reading + 0.6 SCCM)
Dimensions	±0.0025 mm

Equation 8 demonstrates the standard method for finding the error, E, in a calculated quantity, A, based on the parameters m_1 through m_n. This method was used to calculate the total error in porosity; the details are available in Appendix A.

$$E(A) = \sqrt{\left(\frac{\partial A}{\partial m_1} E_{m_1}\right)^2 + \left(\frac{\partial A}{\partial m_2} E_{m_2}\right)^2 + \ldots + \left(\frac{\partial A}{\partial m_n} E_{m_n}\right)^2} \qquad \text{Equation 8}$$

Permeability

Permeability is defined by the ease with which gas may flow through a given material in a given direction. Permeability is important in the context of degrading materials because it defines the ease with which gases evolved during decomposition can escape from the material, as well as being a primary factor in determining the internal pressures of the material during decomposition. Permeability is very strongly linked to porosity, in that when gas flows through a given specimen, it is essentially utilizing a series of linked pores to create flow channels. Tortuosity may also be a factor, however was not evaluated in this research.

In order to measure permeability, a one-dimensional gas flow must be established through a sample of uniform and known thickness while the pressure drop across the sample and the flow through it are measured. These parameters are then used to calculate the permeability by Darcy's law [26], which is given by Equation 9.

$$\gamma = \frac{\mu U t}{\Delta P} \qquad \text{Equation 9}$$

In Equation 9, μ is the dynamic viscosity of the fluid flowing through the sample, U is the velocity of the fluid through the sample, t is the thickness of the sample, and ΔP is the pressure drop through the sample. The relationship between pressure and flow rate for a given sample is linear, provided that the Reynolds number is within a certain range. Based on a review conducted by Zeng et al. [31], Darcy's law is valid for flows where the Reynolds number is less than 1. Equation 10 gives the Reynolds number for flow through porous materials. Figure 9 shows a

sample data set that demonstrates the linear relationship that exists between differential pressure and flow rate through a permeable material.

$$\mathrm{Re} = \frac{\rho U}{\mu} \gamma^{\frac{1}{2}} \qquad \text{Equation 10}$$

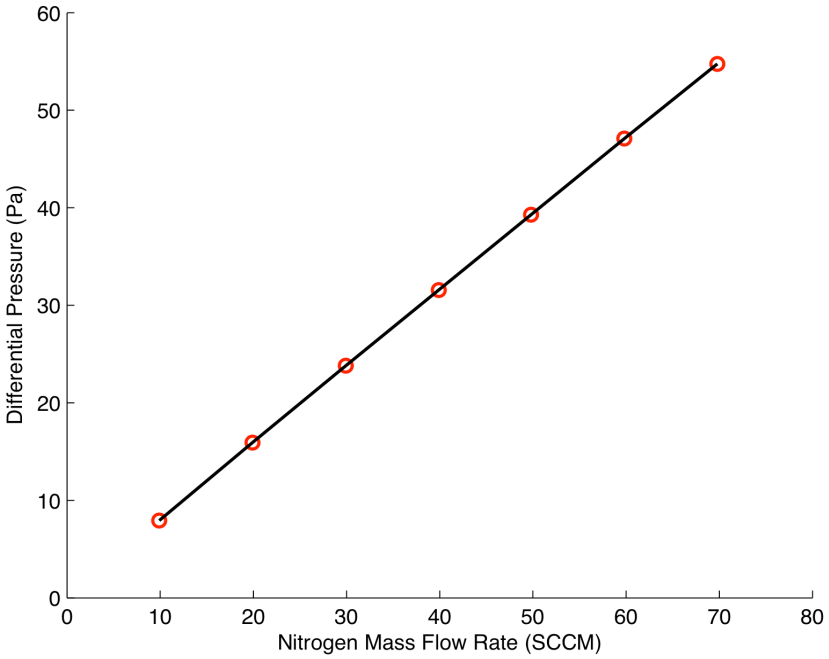

Figure 9. Sample permeability data set – virgin balsa wood

The permeability test section is shown in Figure 10. The permeability test section developed in this research was based on an instrument used for experiments on similar materials that was constructed by Wiecek [29]. The permeability test section consisted of a cylinder with female threads, geometry for the sample to seat onto, and a male end that pressed the sample into the female end, creating a seal. Three 1/8" NPT taps were installed on each side: one set for flow in/out, one set for differential pressure, and a third set to be used in the future for purge flow or thermocouple probes in elevated temperature experiments. The test section was designed to accommodate samples from 3 to 25 mm thick, with diameters ranging from 31 to 38 mm. The male end has a 25.4 mm (1") inside diameter over a 92 mm length in order to ensure even gas distribution over the face of the sample. Complete drawings are available in Appendix D.

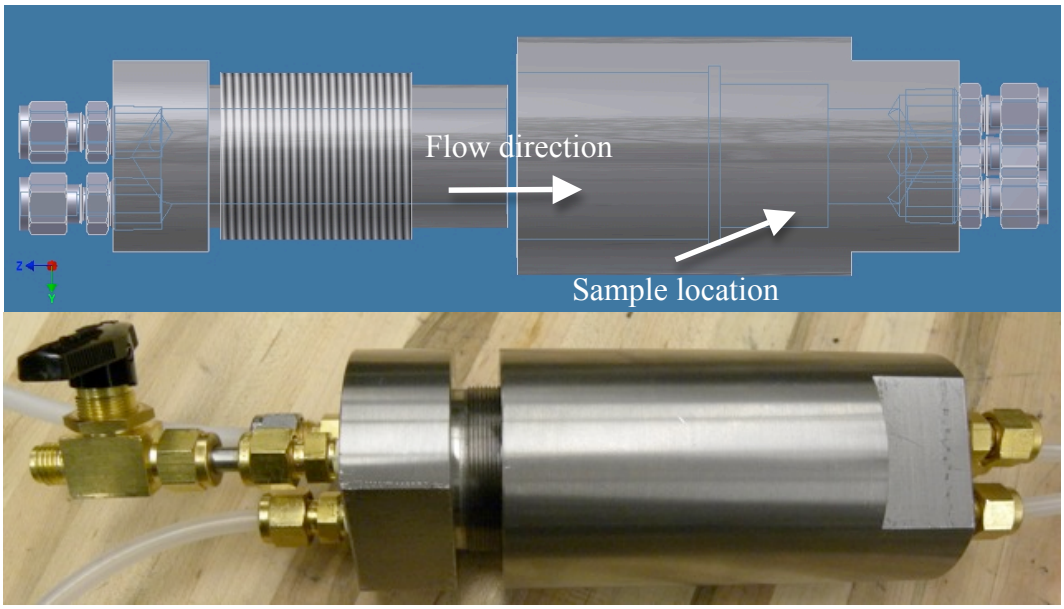

Figure 10. Permeability Test Section

One of the challenges to measuring permeability is in sealing the sample. In order to measure the permeability through the thickness, a steady, one-dimensional flow must be established through the sample. In order to do this, the sample must be sealed everywhere except for the front and back faces where flow is intended to enter and exit. The test section is designed to apply pressure to the face of the sample over the diameter range 25-38 mm in order to provide sealing and bracing, as well as setting the appropriate surface area for flow to enter and exit the sample. Applying washer-shaped silicone gaskets, with 1.6 mm thickness, 31 mm inside diameters, and 38 mm outside diameters, sealed the faces of samples. These gaskets were adhered to the samples with silicone RTV 106 silicone sealant manufactured by Momentive Performance Materials with a temperature rating of 260°F. Silicone sealant was also applied around the circumference of the sample to prevent any radial flow from taking place, thus forcing the flow to pass through the sample and stopping any potential for leaks. The samples used for permeability were the same as those used for porosity, and were cut as discussed in the previous section. Figure 11 shows a sealed E-glass/vinyl ester sample potted in silicone and loaded into the female end of the test section.

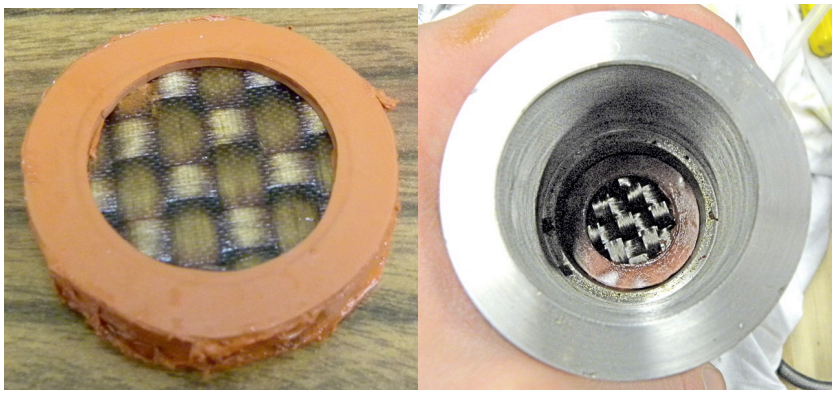
Figure 11. Sealed E-glass/VE sample

The Alicat mass flow controller that was used to conduct porosity tests was also utilized in the permeability tests. In this experiment, the mass flow rate was used to provide a known flow rate through the sample. A similar Alicat mass flow meter, model number M-500SCCM-D with a 0-300 SCCM calibration and 100:1 turndown was used downstream of the specimen in order to monitor for any leakage in the system. Flow rates between the controller and meter were typically within 0.5% at steady state flow. Nitrogen was used as the test gas for all experiments. A differential pressure transducer was connected to each side of the test section in order to measure differential pressure through the sample. A set of three differential pressure transducers was used for pressure measurements, a Setra model 204D with a 345 kPa range, and two Setra model 264 transducers with 2500 Pa and ±62 Pa ranges. The 2500 Pa transducer was never used for any samples, as all samples tested were either too impermeable or too permeable to use this transducer.

One issue presented when working with permeability is in where a true zero value lies. Permeability of materials can vary over a huge range of numbers (10E-16 to 10E-10 m^2 in this research). At the zero point, there will be very low flow and high differential pressure. The Alicat MFC has 100:1 turndown; so 3 SCCM is used as the minimum flow. The 345 kPa pressure transducer was the highest available, and so its full-scale reading is used as the differential pressure. These values yield a permeability "zero" value of 6.7E-18 m^2.

Two procedures were used in permeability tests, based on whether or not the sample appeared permeable. When samples appeared to be impermeable, the differential pressure was ramped to 345 kPa in steps to monitor for leakage or other failure in the sample sealing. When samples appeared to be permeable, the flow rate was ramped from a low mass flow rate (typically 10 SCCM). At each flow rate, the pressure was recorded, and then the flow rate raised until either the mass flow controller or pressure transducer was at the limit of its range. Only one pressure transducer was used for each sample. Using a second could have allowed for recording additional data points, but this was not done to avoid introducing errors from using different instrumentation on the same sample.

Table 2 shows the measurement errors associated with permeability provided by the manufacturers of the devices used. Note that the pressure error depends on which of the two transducers was used. Using Equation 8 and Equation 9, Equation 11 was formulated. It gives the error for permeability, where U and E_U are the mass flow rate and the associated error, reformulated into velocity.

Table 2. Measurement errors for permeability

Measurement	Error
Pressure	±0.38 kPa (345 kPa) ±0.62 Pa (62 Pa)
Mass Flow Rate	±(0.8% of reading + 0.6 SCCM)
Dimensions	±0.001 in

$$E_\gamma = \sqrt{\left(\frac{\mu t}{\Delta P} E_U\right)^2 + \left(\frac{\mu U}{\Delta P} E_t\right)^2 + \left(\frac{\mu U t}{\Delta P^2} E_{\Delta P}\right)^2} \qquad \text{Equation 11}$$

Intermediate Scale Thermogravimetric Analyzer

An instrument was also developed to decompose samples to evaluate the effect of sample decomposition on porosity and permeability. Wiecek [29] degraded samples to predetermined temperatures in a furnace while purging with nitrogen. While this is a useful and easy method, it only allows the mass fraction of the sample to be determined after cooling. In addition, this can make it difficult to obtain fine steps in the mass fraction with the types of materials that were used, which fully degrade over relatively small temperature ranges. The smallest temperature step that Wiecek [29] used was 50°C. Given that 50°C can make the difference between an almost virgin E-glass/VE sample (Figure 12), and a fully decomposed sample, finer control of the progress variable (mass fraction) was required.

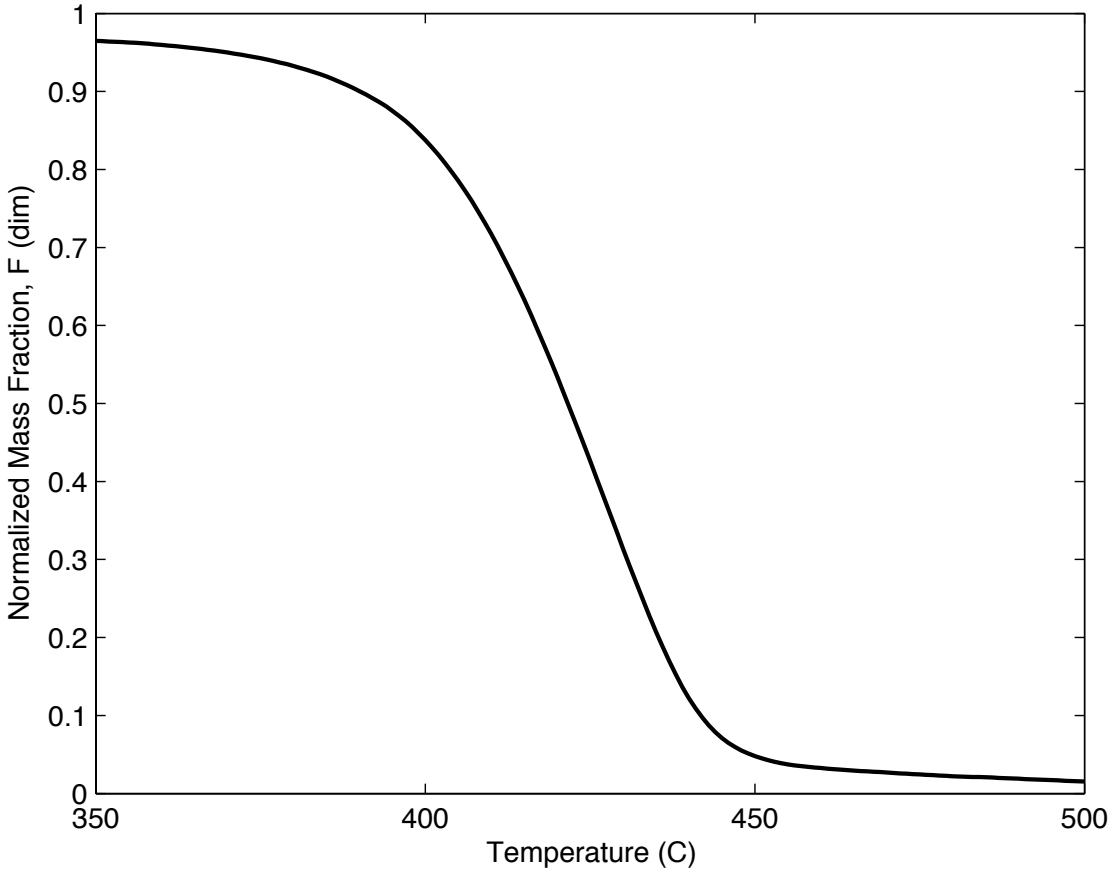

Figure 12. E-glass/VE thermogravimetric plot (limited range)

In order to obtain finer control of the decomposition progress, the concept of the thermogravimetric analyzer was scaled up to create an intermediate-scale TGA (ISTGA). The instrument provides very high sample mass resolution and total atmosphere control over the sample. The ISTGA is shown in Figure 13. The instrument has a mass range of 90 grams with 0.1-milligram resolution. With the ceramic sample cups that were used (also shown in Figure 13), samples up to 42 mm in diameter and up to 25 mm thick can be loaded.

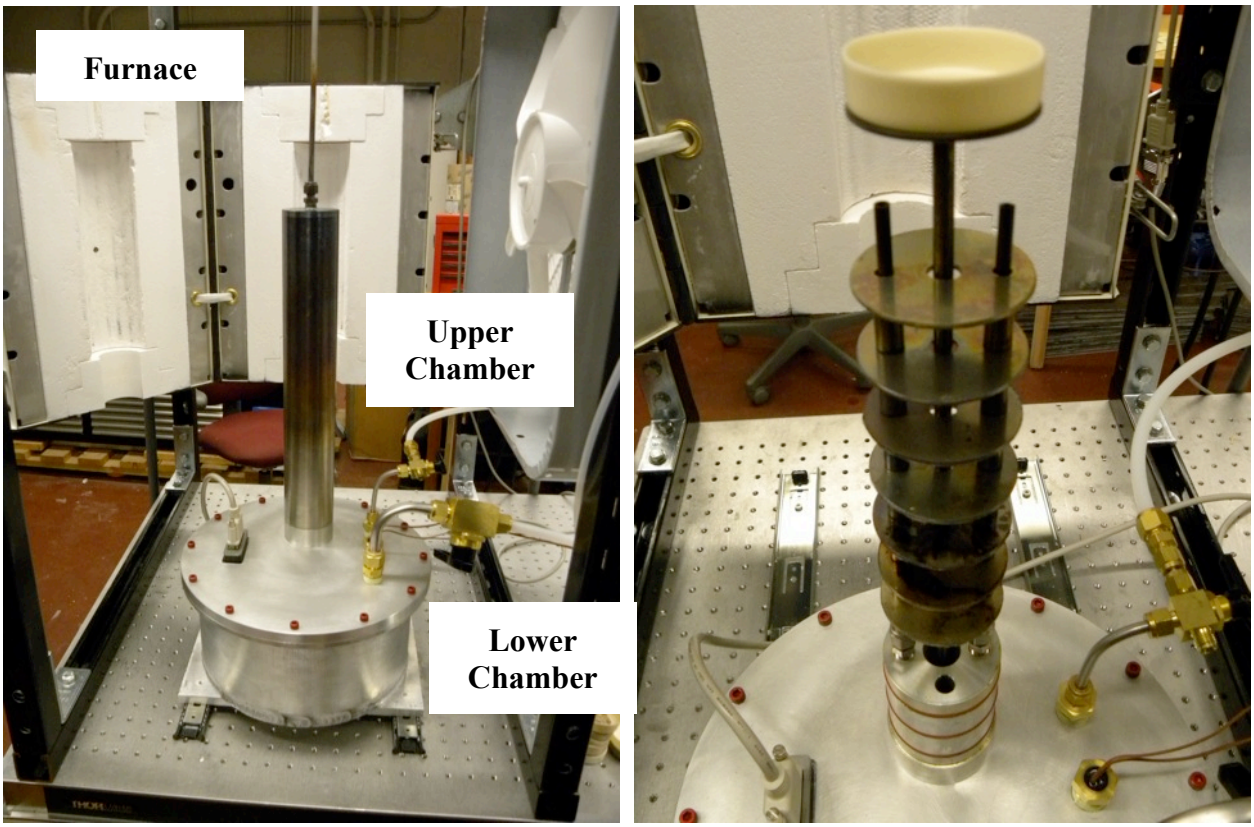

Figure 13. Images of the intermediate-scale TGA

The ISTGA consists of two chambers oriented one above the other with a series of o-rings forming a sealed joint between the two. The lower chamber was constructed of aluminum, and contains the balance and a gas inlet manifold. The Alicat mass flow controller and air-powered vacuum pump used for porosity and permeability tests were also used with the ISTGA to establish and maintain a given atmosphere (inert or oxidizing) throughout experiments. The mass flow controller and vacuum pump were connected via the gas inlet manifold. The balance, placed at the base of the lower chamber along with a secondary thermocouple for temperature monitoring, was a Sartorius WZA-224, which has a range of 220 grams with 0.1-milligram accuracy, and provided excellent stability as well as very good response time to mass loss due to sample decomposition. Hermetic seals were used to transfer wiring out of the casing for the balance as well as the two internal thermocouples.

The stainless steel upper chamber contains a seven-layer nickel heat shield and the sample holder. The two chambers were joined using o-rings. The o-rings provided an additional barrier against heat transfer from the heated upper section to the room-temperature lower section, as well as sealing against the external atmosphere. A type K thermocouple with a 6.35 mm stainless steel sheath was attached directly to the balance, and was used as the sample support. A titanium platform sat at the top of the thermocouple, providing support for a ceramic sample cup. The heat shield was put in place below the sample in order to ensure no direct radiation could be transferred from the sample holder to the balance, which has a maximum recommended operating temperature of 25°C. Despite being just fifteen inches from the sample, a type K thermocouple located in the balance chamber never read above 23°C, even when running 600°C

isothermal segments for up to one hour and then cooling. The upper portion of the instrument was designed to fit inside of a vertically oriented furnace.

A Thermcraft split-shell tube furnace mounted in the vertical orientation was used to heat the upper chamber of the TGA. The furnace had a 305 mm heated length with a primary diameter of 76 mm, and was equipped with a 63.5 mm vestibule block at the bottom to provide a tight fit around the 63.5 mm upper section of the ISTGA. The upper end of the furnace was equipped with a solid vestibule block that was cut to fit around the 6.35 mm exhaust tube from the instrument. A Watlow PM-series PID controller that is capable of running temperature profiles with multiple ramp/soak steps was used to control the furnace. A thermocouple located just inside of the heated region of the furnace was used for control, because the thermocouple that was located in the sample platform was determined to have too much lag relative to the furnace heating elements to be used for furnace control. The thermocouple lag was made evident by the temperature performance of the instrument, which would oscillate about the desired heating rate and never achieve a steady temperature ramp when controlled using this thermocouple.

Sample preparation techniques were scaled up from the smaller TGA, and a diamond-tipped core drill that produced 35.5 mm diameter samples was used. Prior to beginning all experiments that were done in an inert atmosphere, the instrument was evacuated to 90% vacuum and then refilled twice with pure nitrogen (inert), leaving a 99.8% inert atmosphere in the instrument before the experiment was begun. During experiments requiring an inert atmosphere, the flow of nitrogen was maintained at 300 SCCM through the Alicat mass flow controller. In the case of experiments that were done in air, the flow of air was maintained at 300 SCCM throughout the instrument, and no vacuum cycles were undertaken. A ramp rate of 10°C/min was used for all experiments, as this was the highest heating rate that could be used without having any effect on the balance reading. Higher heating rates resulted in interference with the balance, most likely due to the thermal expansion and flex induced in the instrument, furnace, and furnace support frame from rapid temperature change. When samples began to approach the desired mass fraction, the controller was turned off, the furnace opened and the ISTGA moved out on slides, and a large fan was turned on to rapidly cool the instrument. In addition, the flow of nitrogen was increased to provide direct cooling to the sample. In order to prevent unintentional oxidation of the sample, the instrument was not opened until the sample was cooled below 100°C.

While the ISTGA gives very good resolution on mass (0.0001 g on a 90 g range), it does yield results that differ slightly from traditional TGA. The differences are attributed to the three order-of-magnitude difference in sample mass between the two instruments. A curve comparing a data set generated in the STA to one from the ISTGA is shown in Figure 14. The larger sample scale results in a shift to the right equivalent to a change in the heating rate of 35°C, and also affects the slope of the line. The results most likely vary between the two instruments due to thermal gradients that develop across the larger samples in the ISTGA, and also due to the greater amount of material that gases evolved during decomposition must travel through to exit the sample. Lattimer et. al. [38] observed similar changes in the reaction kinetics when comparing samples degraded in the TGA to samples degraded in the cone calorimeter. While the curve shapes produced by the ISTGA should not be used to obtain kinetic parameters, the

instrument performs very well at the task it was built for – degrading samples to desired mass fractions.

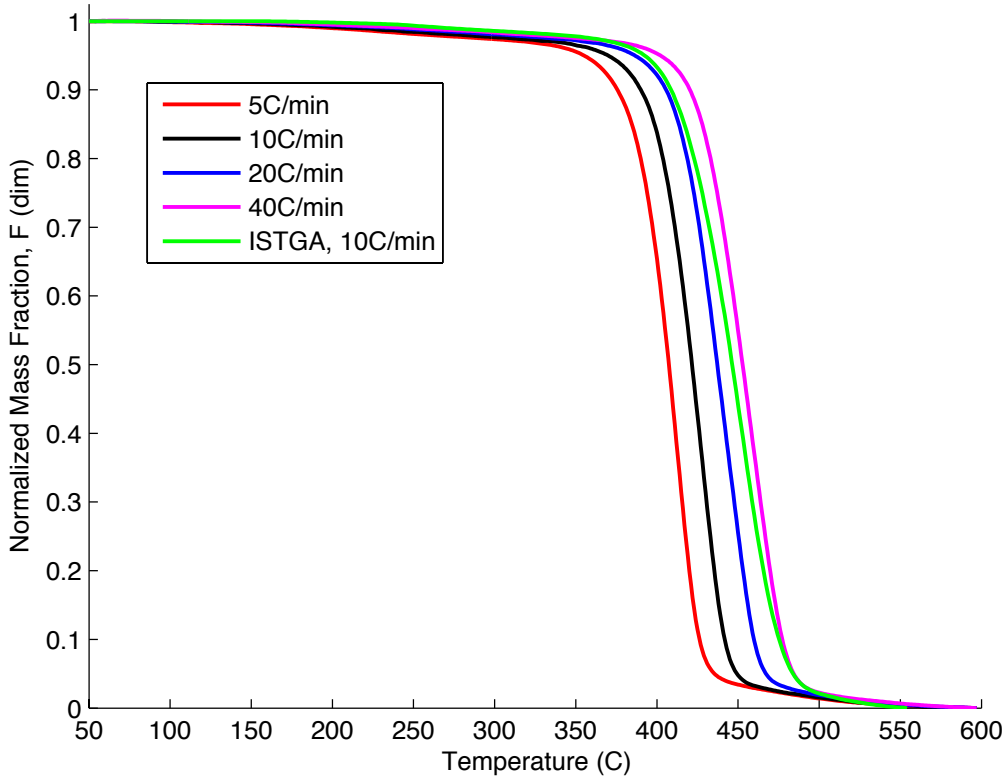

Figure 14. Comparison of TGA and ISTGA

Computerized Tomography X-ray Analysis

Samples were sent to the Carl Zeiss Corporation for X-ray CT scans. The instrument technicians at Zeiss used a Zeiss Metrotom 1500 to create three-dimensional computer models of the sample, which were then examined using VGL, produced by Volume Graphics. The software allows the model of the sample to be rotated into any orientation and sliced in any direction, allowing for any desired view to be obtained.

Materials Studied

The composite construction materials evaluated in this research were an E-glass/vinyl ester laminate, and balsa wood core material. These are two common materials used in sandwich panel construction, in which composite face sheets are formed on each side of a lightweight core. The details of these materials are provided below.

The composite laminate material evaluated in this study was E-glass/vinyl ester laminate. Laminates contained Vetrotex 324B fibers in a 55/45 woven roving with a 0.19" nominal width and 24 oz/yd^2 density. The resin was Derakane 411-350 vinyl-ester resin. The laminates were manufactured using the vacuum-assisted resin transfer molding (VARTM) process. In this

process, layers of woven roving glass were placed under a vacuum bag and the resin is drawn in via a vacuum pump. A package consisting of 1.5% methyl ethyl ketone peroxide (MEKP), 0.06% acetylacetone, and 0.2% CONAP® as percentages of the total resin mass was used to cure the resin. Panels used in this study had a 6 mm nominal thickness, and were not post-cured after manufacture. E-glass/VE samples were cut from larger panels, primarily using a hacksaw, and then the surface of interest was sanded with 600-grit sandpaper to obtain a smooth viewing surface for microstructural experiments, or the material was cored using the core drills.

The balsa that was used for these experiments was cut from a Baltek SB.100 (147 kg/m^3 nominal density) structural core panel 12.7 mm in thickness and 1.2 m by 0.6 m in length and width. The panel is formed by gluing small sub-sections (anywhere from 25 mm x 25 mm to 100 mm x 75 mm) together with the grain oriented such that it runs through the thickness of the panel. A Baltek panel is shown in Figure 15. The density of samples was observed to vary by as much as a factor of five within a given sub-section of the panel. Since balsa wood is biological in origin, it exhibits extremely variable properties, particularly density, which varies anywhere from 40-380 kg/m^3. In order to check the nominal density of the panel, a set of 20 samples ranging in size from 6-29 cm^2 were cut from the panel and the density was calculated using a Sartorius GD503 balance with 0.1 mg accuracy. The average density of these samples was 141 kg/m^3. TGA samples were first cut with a utility knife, reduced in size with 150-grit sandpaper, and then finished into discs with a fine mill bastard file. Care was taken to avoid glue lines in the panel when cutting samples. The finished discs were 6.25 mm in diameter, and varied in thickness in the range of 1.5-1.9 mm.

Figure 15. Baltek SB.100 panel

The biological nature and multiple components of balsa wood (lignin, cellulose, hemicellulose) lead to very complex thermal behavior. Table 3 shows the thermally induced

changes in Douglass Fir, compiled by Schaffer [34]. While no detailed DSC examination was conducted on balsa wood, it is safe to say that it will behave with equal complexity.

Table 3. Thermally induced changes in wood from Schaffer [34]

Temperature (°C)	Phenomenon
55	Natural lignin structure is altered Hemicellulose begins to soften
70	Transverse shrinkage of wood starts
110	Lignin slowly begins to lose weight
120	Hemicellulose content begins to decrease Lignin begin to soften
140	Bound water is freed
160	Lignin is melted and starts to harden
180	Hemicelluloses begin rapid weight loss after losing 4% lignin in torous flows
200	Wood begins to lose weight rapidly
210	Lignin hardens Cellulose softens and depolymerizes
225	Cellulose crystallinity decreases and recovers
280	Lignin reaches 10% weight loss Cellulose begins to lose weight
300	Hardboard softens irrecoverably
320	Hemicelluloses have completed degradation
370	Cellulose has lost 83% of initial weight
400	Wood is completely carbonized

Chapter 3 – Thermal Analysis

Thermal analysis experiments were performed on several materials using the STA to quantify the gravimetric response and specific heat capacity at elevated temperatures. These are, arguably, the most important parameters in characterizing the decomposition with a computer model, giving data on the mass losses and energy transfers associated with material degradation. In addition to experiments to obtain material properties, a series of sensitivity studies were conducted to determine optimal DSC test methods in order to obtain the best possible results from DSC and TGA tests.

Extensive thermogravimetric tests at multiple heating rates were conducted on E-glass/vinyl-ester and balsa wood specimens. Gravimetric data at multiple heating rates is required to develop decomposition kinetic parameters. The specific heat capacity was determined as a function of temperature for E-glass/vinyl-ester and balsa wood, as well as for three validation materials that are presented in Appendix E.

DSC Sensitivity Studies

As discussed in Chapter 2, several items are either not specified at all in the ASTM standard for specific heat by the sapphire ratio method (ASTM E-1269), or are left with only some guidance. These items that are not fully specified include sample type and geometry (powder, solid), sample cup type, and sapphire standard geometry and mass. As such, sensitivity studies were conducted to find the best approach to each item for the materials of interest.

The standard states that sample contact with the sample crucible should be maximized, which is done to maximize temperature sensitivity to the sample. Many attempts were made determining the specific heat of E-glass/vinyl ester by grinding it into a powder either with a drill or a file, and then running the sample. The results of these experiments were then compared to a specific heat curve for a solid piece of the same material provided by the manufacturer of the instrument, Netzsch, shown in Figure 16. It is worth noting that the initial mass of the sample was used to calculate the specific heat shown in this curve, rather than the mass curve from TGA. Different results were obtained by this method sample preparation method. This was attributed to poor contact between the surface of the powdered specimens and the sample crucible.

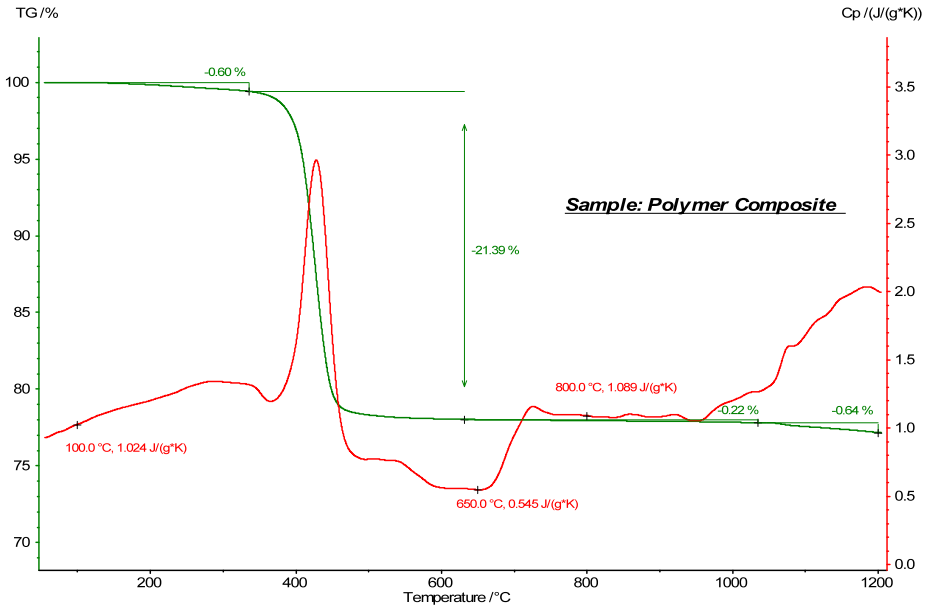

Figure 16. Specific heat curve for E-glass/VE based on initial mass, generated by Netzsch.

Tests with solid samples were performed, which gave results very similar to those shown in Figure 16. Figure 17 shows a comparison between solid and powdered E-glass/VE samples, note the higher mass-normalized signal strength that was obtained with the solid specimen, and the fact that the powdered sample gives a negative DSC signal after degrading, despite approximately 70% of the initial mass remaining at this stage. Both samples were run in platinum cups with matching lids. Techniques for forming solid samples were further developed, first with the use of a simple file and sandpaper, and then with a core drill that produced samples at 6.33 mm outer diameter, a perfect fit for the 6.35 mm inside diameter platinum sample cups. Figure 18 shows the core drill, a cored sample, and the sample having been pushed into a platinum sample cup with an aluminum rod. The core drill was the most effective means of making samples, and this technique was used to make the samples used in this research.

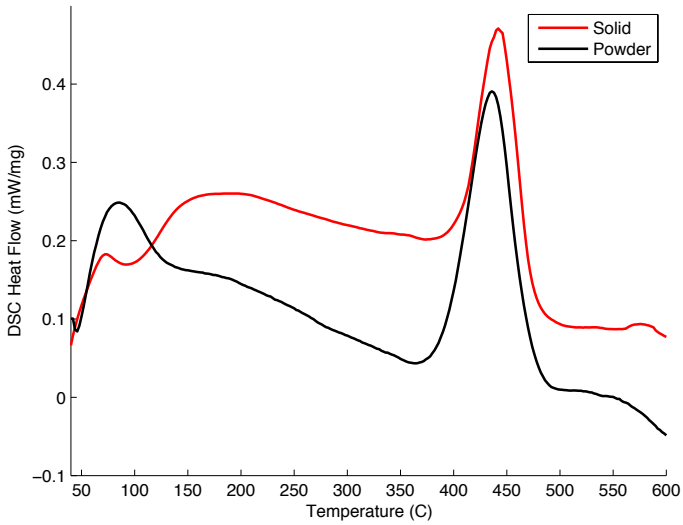

Figure 17. Comparison of solid and powdered E-glass/VE samples

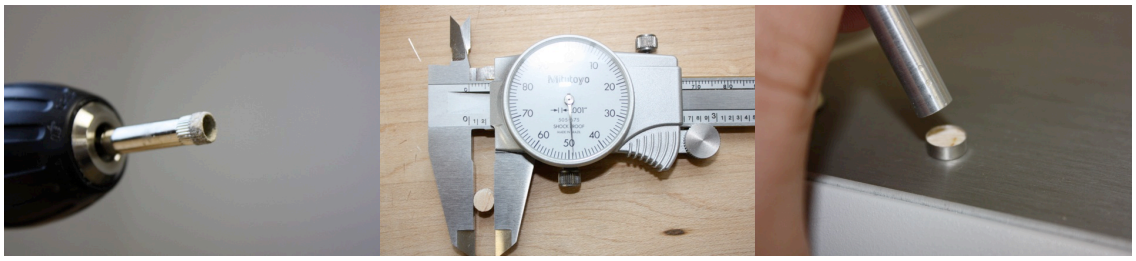

Figure 18. Core drill, STA sample, sample pushed into platinum cup

The ASTM E-1269 standard also does not stipulate is crucible and lid material or type. The STA was purchased with both alumina and platinum sample cups, and initially the alumina cups were used exclusively due to their substantially lower price and greater durability. However, through all types of samples (powdered and solid), alumina crucibles failed to produce results similar to those shown in Figure 16. Platinum cups provided much better sensitivity to thermal reactions due to the significantly thinner walls of the platinum cups, and also because of the relatively high thermal conductivity of 72 W/mK (four times that of alumina). When experiments were conducted in alumina cups, similar curve shapes to those in Figure 16 were obtained, but they would appear smoothed out in places. A comparison of DSC heat flow signals between platinum and alumina cups is shown in Figure 19. Note the much higher normalized signal yielded by platinum. Relatively inexpensive aluminum cups gave results similar to platinum in terms of to thermal changes in the sample and signal magnitude, most likely due to the very high thermal conductivity of aluminum, but were limited in use due to the low melting point of that material. Lids pierced with 0.5 mm diameter holes that matched the material of the crucible were used in all experiments to enhance the temperature uniformity of the sample, as the limited number of experiments that were done without lids gave worse reaction sensitivity (curve detail and signal magnitude) relative to those done with lids.

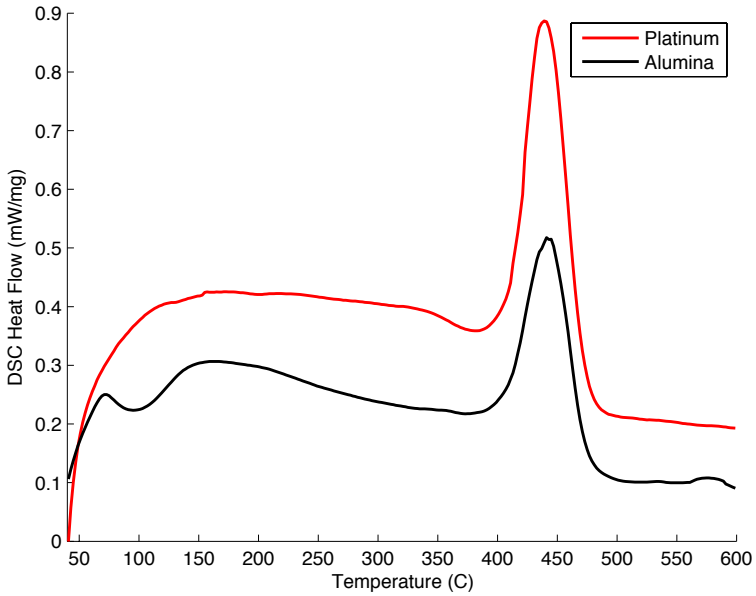

Figure 19. Comparison of STA sample cup types

The mass of the sapphire standard is specified to be somewhere in the range of 10-100 mg, which presents the issue of whether or not variations in sapphire mass make a difference in the final measurement. A series of DSC tests were conducted in platinum sample cups to determine the differences in the specific heat result, if any, resulting from geometric and mass variations in the sapphire standard. The STA was provided with eight unique pieces of sapphire for use as standards in determining the specific heat. Diameters of 0.25, 0.50, 0.75, and 1.00 mm were supplied at diameters of 5.2 and 6.0 mm, all of which except for the largest fall in the range of 10-100 mg. Table 4 shows the pieces of sapphire that were selected for testing. A mass range from ~21-63.4 mg was tested because all samples that were run for specific heat or kinetics results had an initial mass in this range. Two thicknesses at each diameter were used to show the differences resulting from each property.

Table 4. Sapphire test matrix

Diameter (mm)	Thickness (mm)	Mass (mg)
5.2	0.25	21.0
5.2	0.75	63.4
6.0	0.25	28.3
6.0	0.50	56.1

The results of the sapphire DSC tests are shown in Figure 20, plotted against temperature with DSC units of mW/mg. Normalizing the DSC heat flow signals with mass allows for the effect of varying mass to be removed, thereby showing only signal variations resulting from geometry in the plot. The two 6.0 mm thick pieces of sapphire gave almost identical results, and the two 5.2 mm pieces of sapphire were about 7% different once the signals became steady. It is also worth noting that the 0.75 mm thick 5.2 mm piece gave a signal identical to the 6.0 mm pieces, however this is may be coincidental, and is not sufficient evidence to suggest that diameter does not matter once thickness is over a certain value. The results show that the mass of the piece of sapphire that is used does not effect the DSC results when normalized on mass provided that the sample covers as much of the sample pan as possible (the 6.0 mm sample covered 90% of the surface area of the 6.35 mm pan, while the 5.2 mm sample covered just 67%). As a result of these tests, the 6.0 mm diameter sapphire standards were used for all specific heat tests, with the thickness of the sapphire selected to match the standard's mass as closely as possible to the predicted average (based on previous data) mass of the sample during the TGA run.

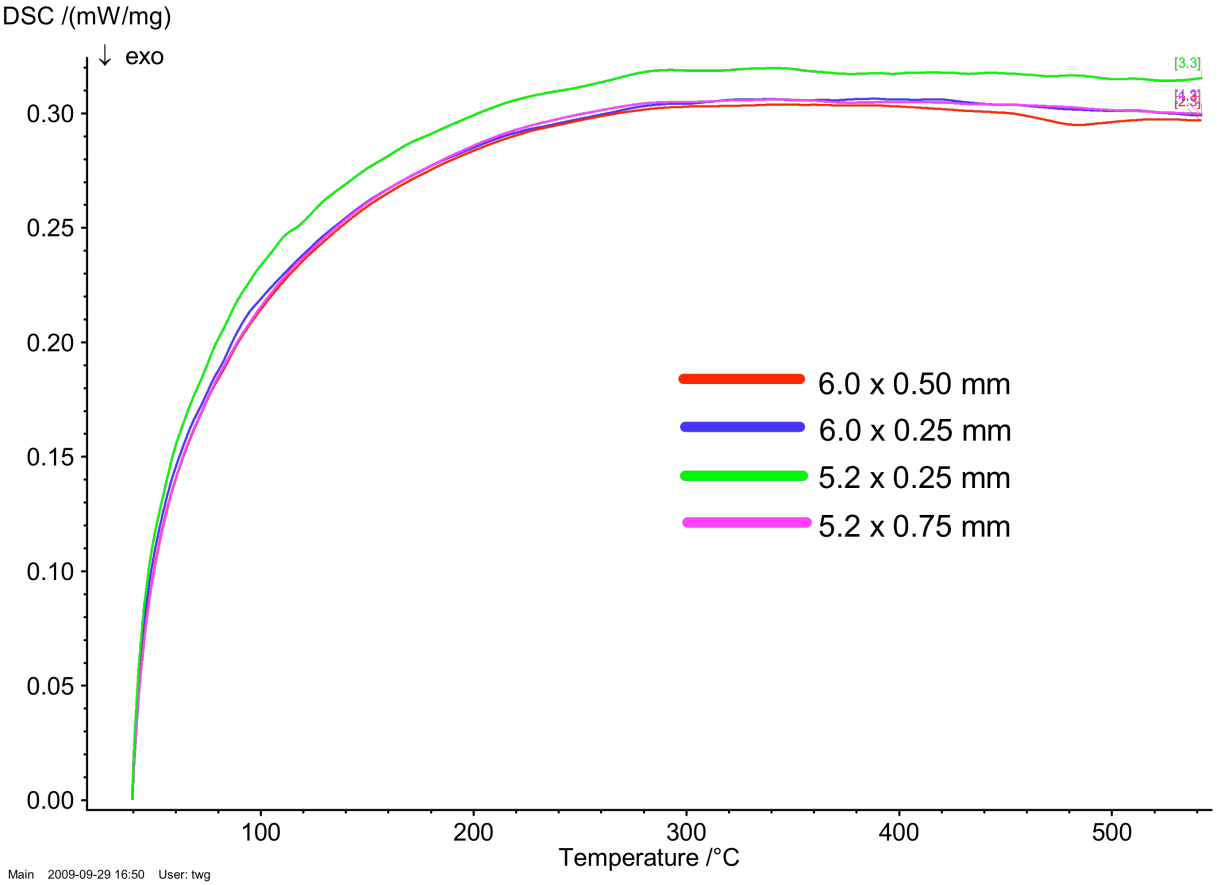

Figure 20. Comparison of sapphire DSC signals

The heating regimen was another item in the standard that was not clearly specified. The standard states that a heating rate of 20°C/min should be used during all heating phases of the DSC experiments used to calculate the specific heat of a given sample, and that isothermal segments at least four minutes in length be used at the beginning and end of the main temperature ramping segment. The standard does not, however, say what temperatures should be used for those isotherms, possibly because the minimum time required may vary between instruments. In order to allow for the instrument, sample, and reference to equilibrate properly before undergoing the temperature ramp, an initial isothermal temperature of 40°C was selected. In addition, a lower heating rate of 5°C/min was used to reach the 40°C initial isothermal temperature in lieu of the suggested rate of 20°C/min in order to prevent any temperature overshoot in the instrument. The final isothermal temperature was typically set somewhere from 20-50°C higher than the desired final sample temperature due to the use of furnace temperature control, which causes the final sample temperature to lag the selected temperature as described previously. Isotherms were typically run for fifteen minutes, as it was observed that it could take up to ten minutes for the differential temperature between the sample and reference thermocouples (i.e., the DSC signal) to go to zero.

All of the experimental techniques developed to get better specific heat results were also applied to all other experiments conducted on the STA. TGA experiments included an initial isotherm, but not a final isotherm.

E-glass Vinyl Ester Composite

The specific heat of E-glass/vinyl-ester as a function of temperature is shown in Figure 21 with the thermogravimetric result overplotted for reference. E-glass/vinyl ester undergoes three major thermal reactions over the temperature range that was examined, 0-900°C. The first is a very slow and small decrease in mass from 100-350°C. The second is resin decomposition, which begins just before 400°C, and the third is possibly due to fiber softening which occurs around 700°C. There is a large mass loss associated with the first major thermal reaction (resin decomposition at 400°C), and no mass loss at all associated with the second. The residual sample mass fraction is fairly large, typically on the range of 0.70-0.76 due to the presence of fibers. After the resin decomposes at 400°C, the sample is reduced to fibers and char in an inert atmosphere.

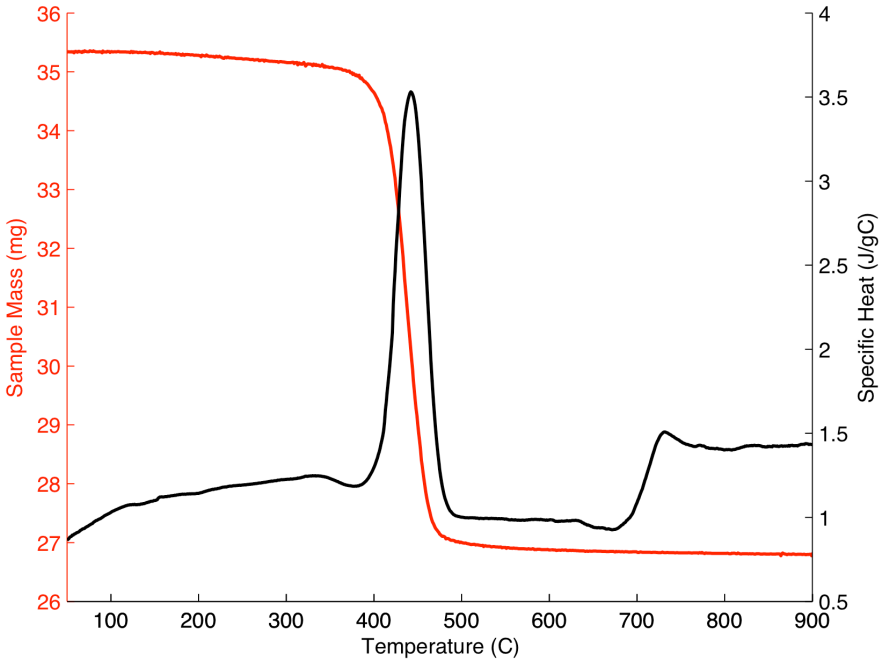

Figure 21. Specific heat for E-glass/vinyl-ester with TGA result (20°C/min)

Additional thermogravimetric tests were conducted on E-glass/vinyl-ester at heating rates of 5, 10, 20, and 40°C/min. Figure 22 shows the raw E-glass/vinyl-ester TGA results, and Figure 23 shows the data reformulated in terms of the normalized mass fraction (Equation 5). While the initial mass of samples was very carefully controlled by sanding the thickness of the disc-shaped pieces, the residual mass varied from 22.5-24.5 mg. The variation in residual mass was attributed to the scale of the samples (6.35 mm diameter, ~0.6 mm thick), which was small enough that the volume fraction of the fabric, which was woven in 4.8 mm widths (see Figure 11), could vary between samples depending on the position at which samples were taken from the panel. The reformulated data demonstrates that the rate of mass loss is dependant on the rate at which the

sample is heated, with a temperature shift of about 15°C each time the heating rate is doubled. The temperature shift results from changes in the chemical reaction processes taking place during decomposition.

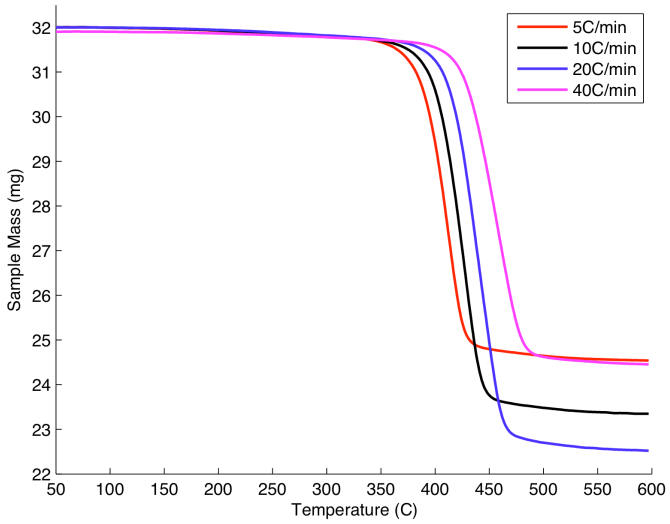

Figure 22. E-glass/vinyl-ester TGA results

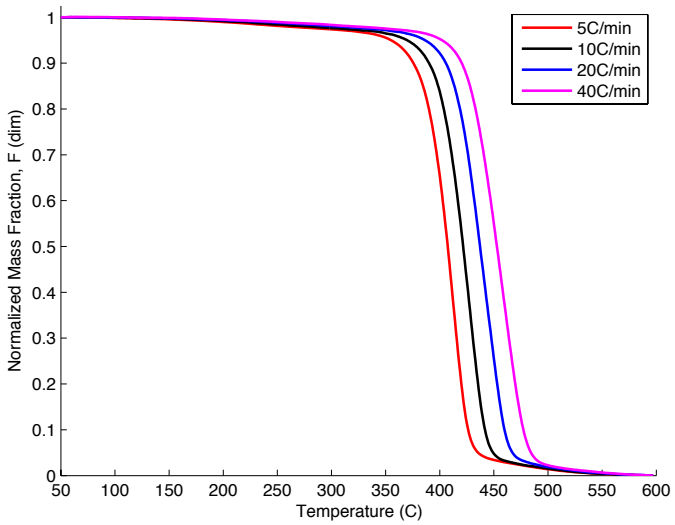

Figure 23. E-glass/vinyl-ester results in terms of normalized mass fraction

In order to further show that most of the mass loss in E-glass/vinyl ester is due to resin loss, further TGA tests were conducted on pure resin and pure fiber samples, and the results were plotted as mass fraction remaining along with a curve generated at the same heating rate (20°C/min) for a composite sample. Figure 24 shows that the mass loss is indeed due almost entirely to the loss of resin from the sample, and also that a very small mass loss takes place from the fibers. Mass loss from the fibers is attributed to the loss of sizing. TGA tests on fibers alone show a mass loss of about 0.6% by 600°C, the result of the sizing, a thin polymer coating applied to help the fibers bond to the resin during composite fabrication, decomposing off of the fibers. All three materials begin to decompose gradually at 140°C. The rate of decomposition increases

dramatically at about 380°C, before tapering off at 480°C. This figure demonstrates that the mass loss from E-glass/vinyl ester samples during heating is due almost entirely to the loss of the resin matrix.

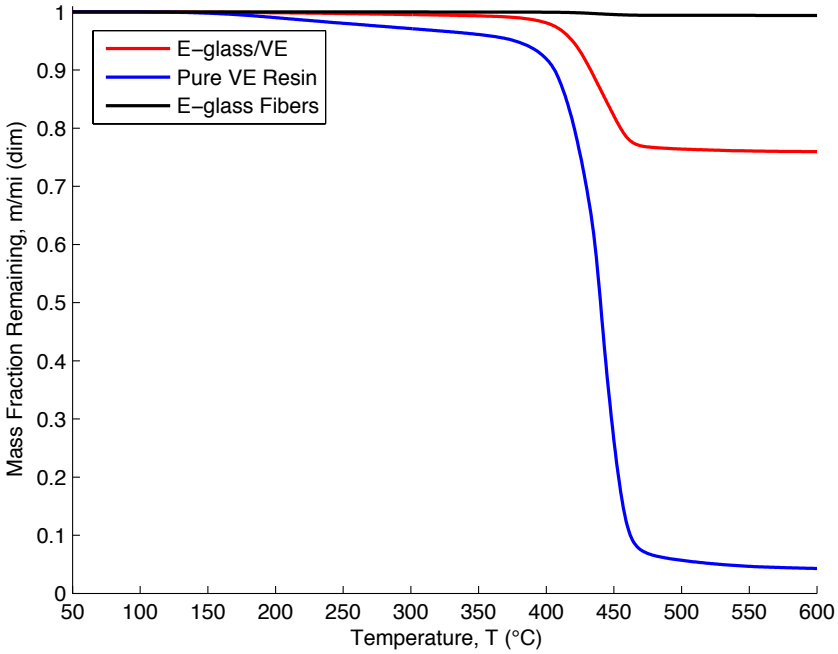

Figure 24. TGA data for fibers, resin, and composite

When the E-glass/VE is heated in an oxidizing atmosphere, the char oxidizes. The char oxidation results in an additional mass loss over samples degraded in the inert environment, the two samples that were fully decomposed in the ISTGA showed final mass fractions of 0.75 for the sample run in nitrogen, and 0.72 for the sample run in atmospheric air.

Balsa Wood

Balsa is a very inconsistent material due to its biological nature. As discussed in Chapter 2, the density can vary by an entire order of magnitude. Balsa wood exhibits as much complexity thermally as it does physically, with the full degradation of balsa involving many stages and exhibiting both endothermic and exothermic thermal reactions that are beyond the scope of this research. Figure 25 shows the specific heat of balsa wood plotted with TGA data. Di Blasi [33] discussed the endothermic and exothermic reactions that take place in wood at some length in the context of modeling wood pyrolysis kinetics as either a single or multi-stage reaction. Figure 25 makes it clear that a multi-stage reaction model is certainly required to capture not only the kinetics, but also the energetics. In addition, balsa will absorb water from the ambient atmosphere due to its porous nature, resulting in an additional energy spike and corresponding loss of mass. This portion of the energetics was removed from the picture by first drying samples by ramping them to 110°C at 10°C/min in the STA, and holding them isothermally for 15 minutes before cooling to 50°C and conducting the TGA test. Water evaporation reactions were

studied separately. Conducting the experiments in this fashion allowed each reaction to be studied independently, as at some heating rates, they could tend to overlap.

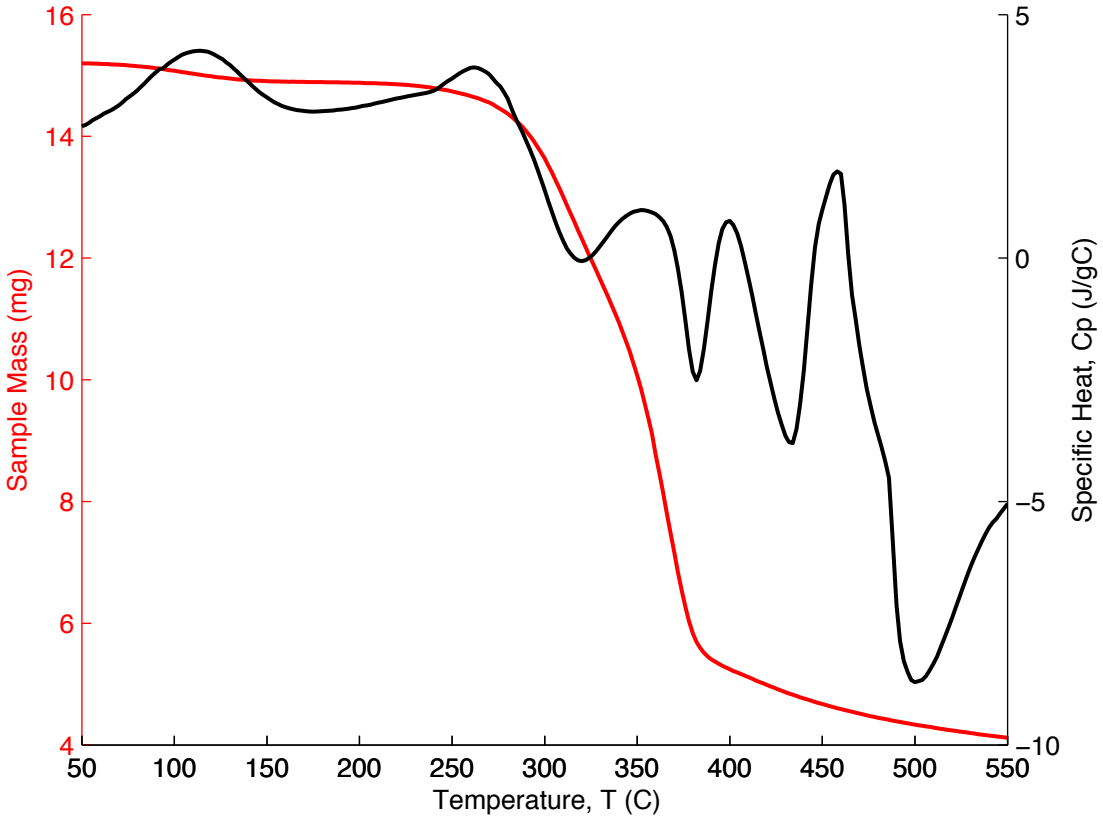

Figure 25. Specific heat and TGA data for balsa wood (20°C/min)

Samples used in these experiments had a density of 320 kg/m^3 with a tolerance of ±10%. The sample density was held at this relatively high value in order to maximize the amount of mass that could be placed in the sample cups, thereby improving the accuracy of the measurement. The very small masses that are obtained by preparing samples at lower densities (as low as 1-3 mg) can be too small to give smooth TGA results, and raise the sensitivity of the results to ambient vibration. The sample thickness was controlled in order to keep the sample masses consistent. Virgin (pre-dehydration) sample mass was held at 16.3 mg for all tests. Due to water content in the samples, masses were on the range of 15.7-16.1 mg after the water was removed in the TGA. Samples were dehydrated by ramping them to 110°C at 10°C/min in the STA and holding them isothermally for 15 minutes before cooling to 50°C and conducting the TGA test. Figure 26 shows the results of TGA tests that were conducted at 5, 10, 20, and 40°C/min. The final masses of the samples were variable due to the biological nature of the material, which makes it impossible to obtain perfectly consistent samples.

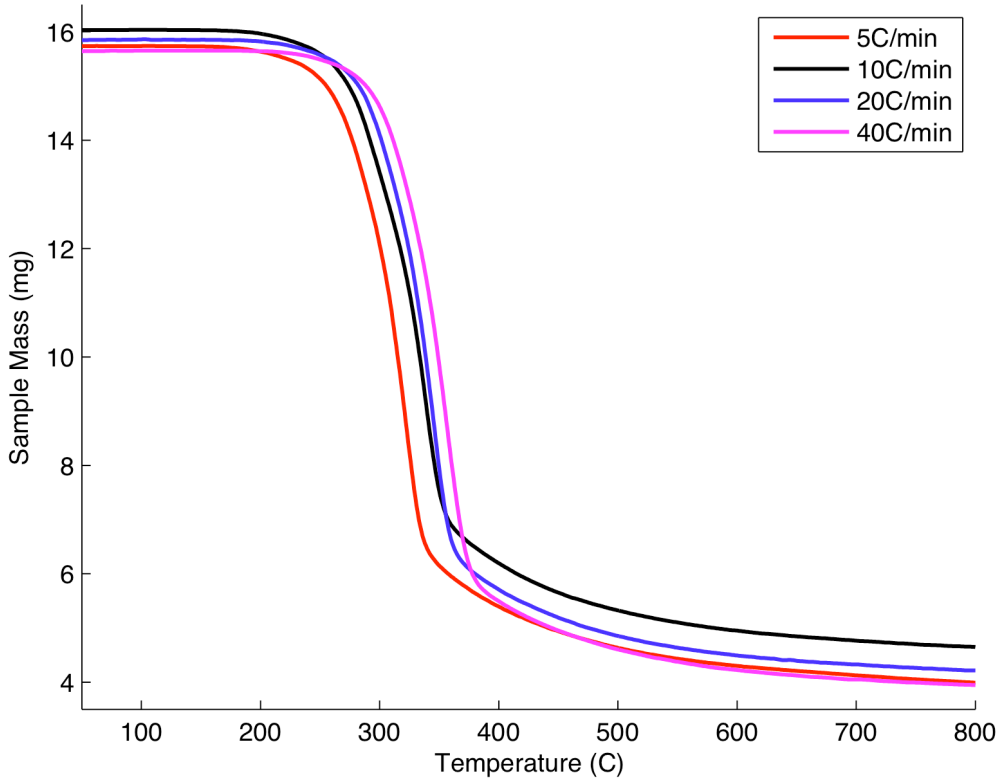

Figure 26. Balsa wood TGA results

As both the initial (due to water content) and final masses of samples were variable, the data was reformulated in terms of the normalized mass fraction, *F*, (Equation 5) as shown in Figure 27. Decomposition begins at 200°C, and exhibits a small rate increase when *F* is about 0.5. After the primary decomposition ends at around 350-400°C, a gradual decomposition continues. Decomposition rate appears to be independent of heating rate at this stage. Mass loss continues to at least 1100°C, the highest temperature at which balsa wood was tested. Balsa decomposition has been classified using both single and multi-step kinetic models [33]. The effect of the heating rate can also be observed in the first part of the decomposition, with higher heating rates resulting in the curve shifting to the right (material loss at higher temperatures). Shifts were on the order of 10°C, but were not totally consistent due to variability between samples.

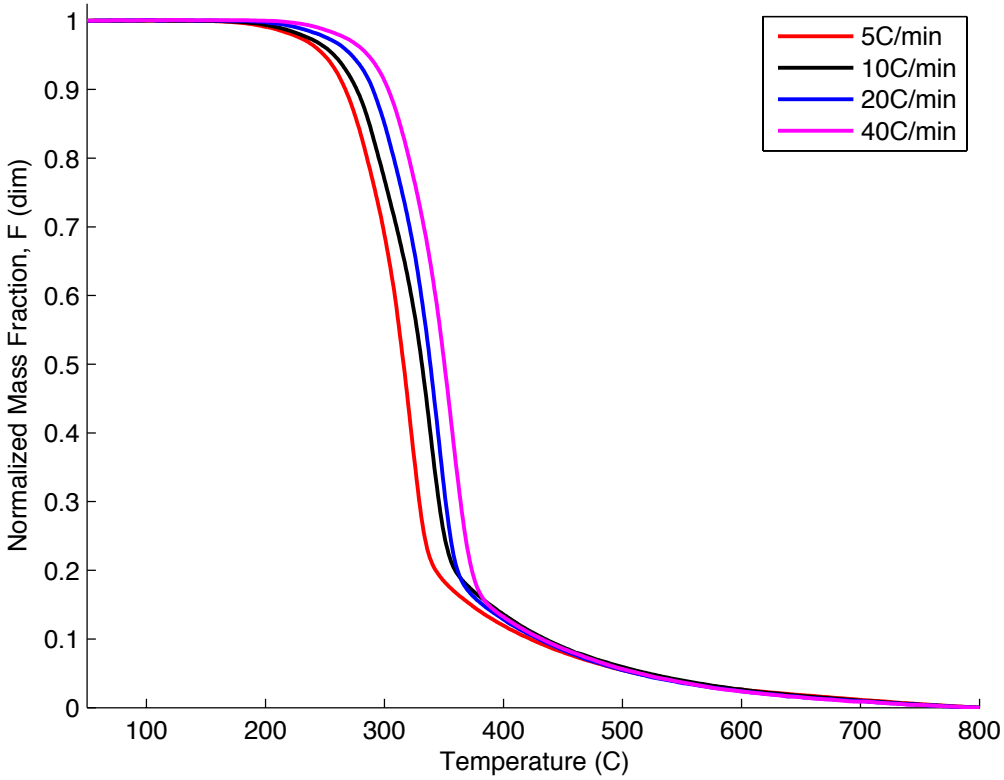

Figure 27. Balsa wood results in terms of normalized mass fraction

Water evaporation reactions were also studied. Over the ten tests that were conducted on the STA, water content was found to vary from 1-4%, with an average at 2.9%. Feih et al. [32] found the water content to average 8%. The difference in water content values is attributed to variations in ambient conditions (humidity, temperature). Relative humidity in the lab was typically 15%, and the temperature was kept at 22°C. Samples were conditioned in the laboratory environment for at least 24 hours after preparation prior to being tested. Figure 28 shows the results of water dehydration tests run at heating rates of 10, 20, and 40°C/min on samples with masses ranging from 15.2-16.4 mg prior to the experiment. Tests were also run at 5°C/min, but the data was not used because the water evaporation overlaps with early decomposition reactions at low heating rates. Figure 28 demonstrates how variable water content can be in the balsa wood. As a result, the data was once again reformulated in terms of the normalized mass fraction, which is provided in Figure 29. Similar to the material decomposition, the dehydration process is dependent on heating rate, with temperature shifts on the order of about 15°C.

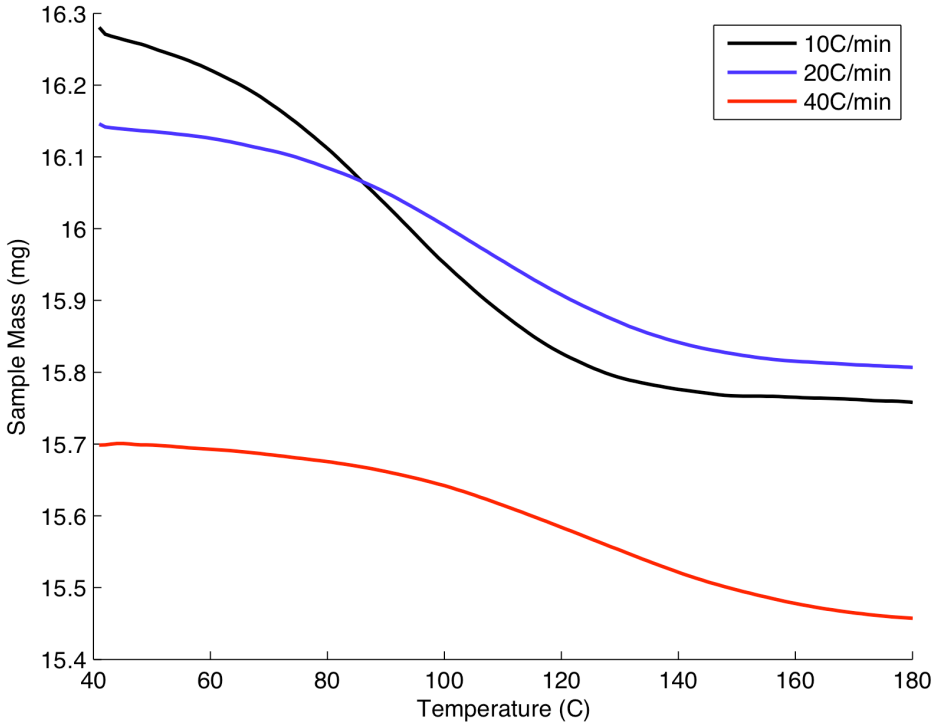

Figure 28. Balsa wood dehydration results

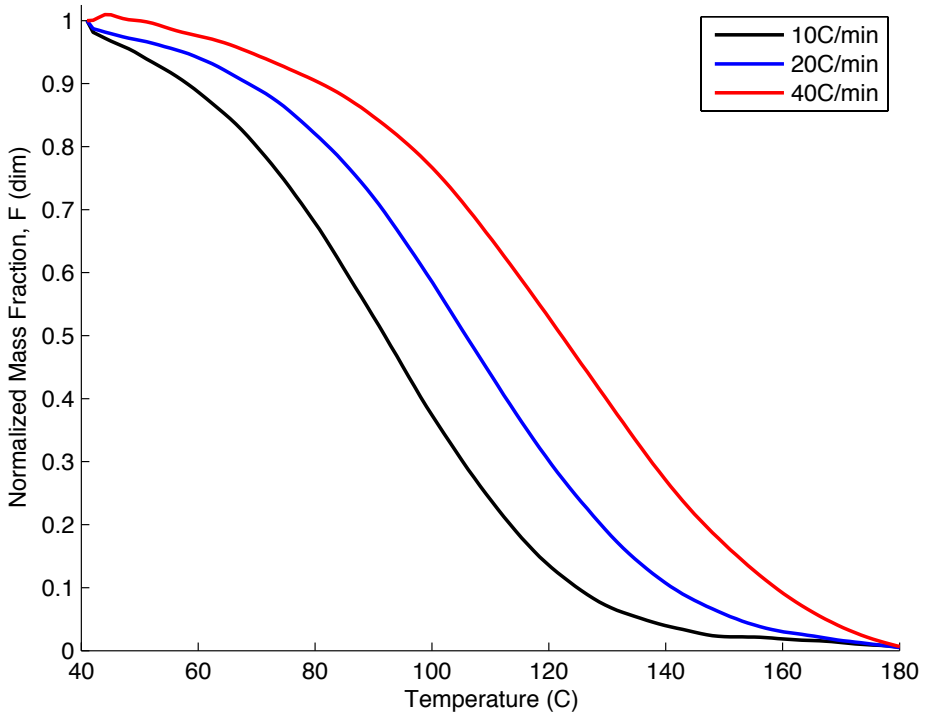

Figure 29. Balsa wood dehydration results in terms of normalized mass fraction

Chapter 4 – Microstructure, Porosity, and Permeability of Balsa Wood

Microstructure

Balsa wood is composed of a series of complex microscopic compartments and vessels. A thorough understanding of the changes during heating in this elaborate microstructure is instrumental in directing modeling efforts, particularly in determining the appropriate types of models to use. In order understand the response of the balsa wood microstructure as it decomposes, two samples were examined on the ESEM heating platform over the temperature range from room temperature to 550°C at heating and cooling rates of 20°C/min. Each sample represented a unique view – the first with the grain running along the width of the image, and the other of the grain cross section. Images are presented and discussed at a series of temperatures that characterize the microstructure changes in the material during heating.

An analysis was conducted on seven images of the grain cross section that characterize decomposition. The analysis quantifies average grain diameter, number of grains, and void fraction as a function of temperature. Images were selected based on both inspection of the videos that were produced from the ESEM sessions, and TGA curves that were generated before the experiments were done. Figure 30 shows a TGA curve for balsa wood heated at 20°C/min that may be referenced while reviewing the images.

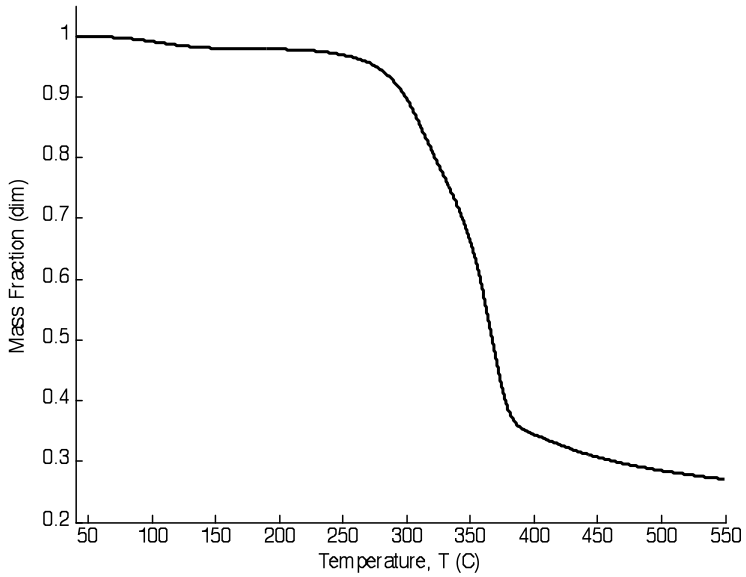

Figure 30. Balsa wood TGA curve from 50-550°C at 20°C/min, including dehydration

Parallel to the Grain

Initial inspection of the balsa wood parallel to the grain under the ESEM shows that rather than continuous solid strands, the grain appears to be comprised of rows of hollow cells with lengths varying from 30-400 μm. Figure 31a shows the balsa wood parallel to the grain

immediately after the heater is activated. The grain appears to be comprised of rows of hollow cells with lengths varying from 30-400 µm.

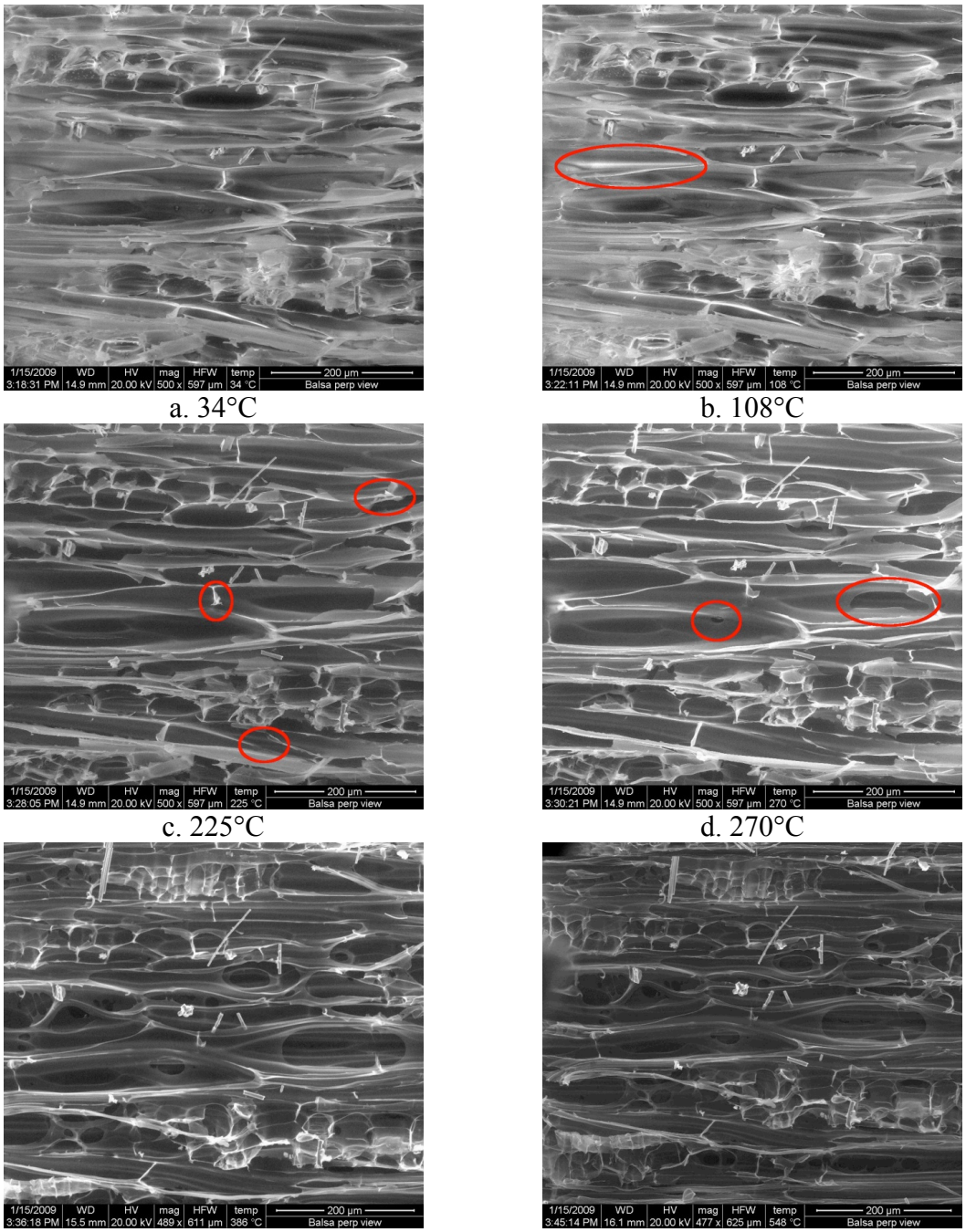

a. 34°C b. 108°C

c. 225°C d. 270°C

e. 386°C f. 548°C

Figure 31. Micrographs of balsa parallel to the grain during heating

The first changes occur immediately following 100°C. One such change is circled in Figure 31b. These are likely due to water evaporation or the beginning of lignin mass loss as per

Table 3. No structural changes appear to occur before this temperature, a fact further confirmed by the flatness of the TGA curve at 100°C.

The next material change does not take place until the sample reaches 200°C. At this point, the grain cell walls begin to pull apart and shrink. The TGA curves confirm that this is the point at which decomposition onsets in the material. Figure 31c shows the material shortly after passing 200°C, and several early decomposition sites are circled in red. At temperatures of about 270°C, holes begin to open up in the grain cell walls as decomposition accelerates. These are shown in Figure 31d, circled in red.

Decomposition completes around 380°C, leaving the grain cell walls eroded and full of voids. All that is left at this point is char. Again, this stage of decomposition corresponds well to the end of decomposition on the TGA curve. The decomposed material is shown in Figure 31e. After 380°C, no further changes are immediately obvious. However, there is one more subtle change that takes place. In order to keep the image in focus, the working distance (WD) of the microscope had to be increased, which indicates that the surface of the material is shrinking away from the electron emitter. An image of the final temperature of 548°C is shown in Figure 31f. As shown in Figure 32, the sample exhibited no changes during cooling.

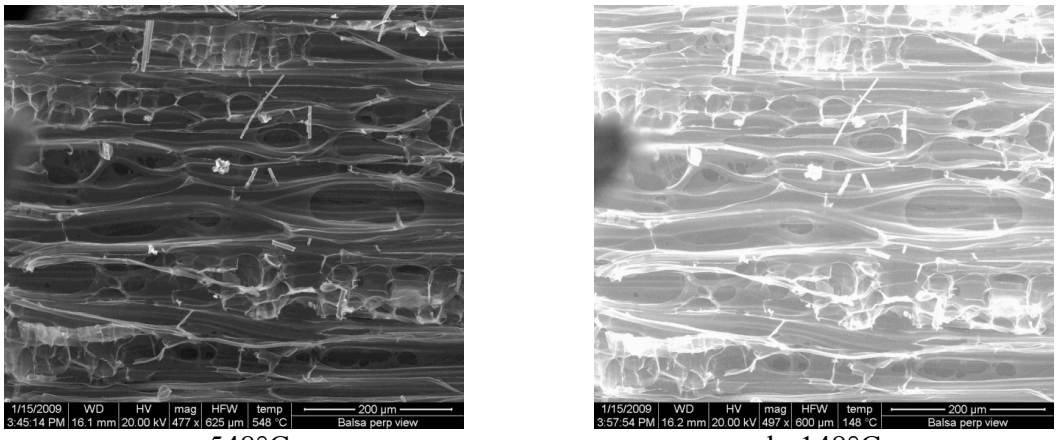

a. 548°C b. 148°C

Figure 32. Micrographs of balsa parallel to the grain (a) before and (b) after cooling.

Grain Cross-section

Images of the grain-cross section at various temperatures are provided in Figure 33. A detailed analysis was conducted on the images to characterize the grain size, void fraction, and sample size as a function of temperature using MATLAB. The cross-sectional view provides better information on both grain cell density (the number of grains per unit area), as well as grain cell size. Figure 33a shows the grain cross-section immediately after the heater was activated. The image indicates that cell size can vary by a great deal, and that there are two types of cells present in this view. The first type is round, and makes up about 80% of the surface in the view shown. These cells are known as trachieds. The latter is formed by rows of rectangular cells, known as rays, which may be used for water transport in the radial direction.

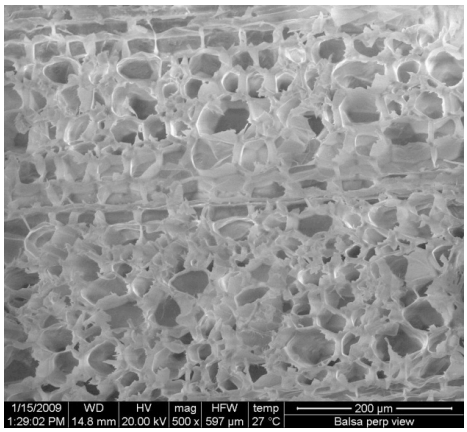

a. 27°C

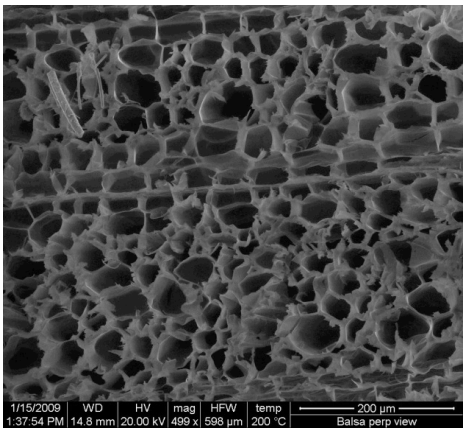

b. 200°C

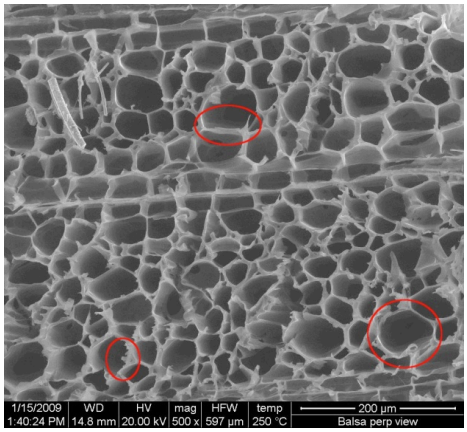

c. 250°C

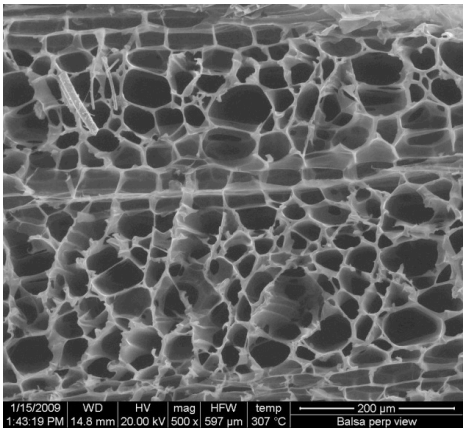

d. 307°C

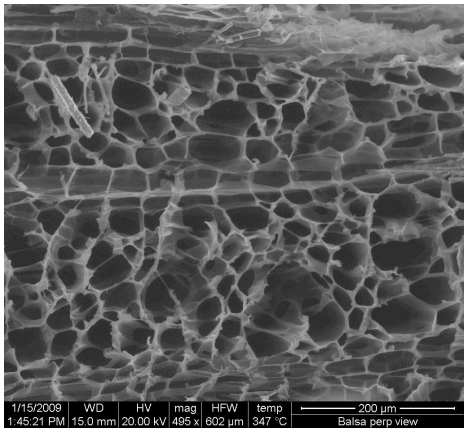

e. 347°C

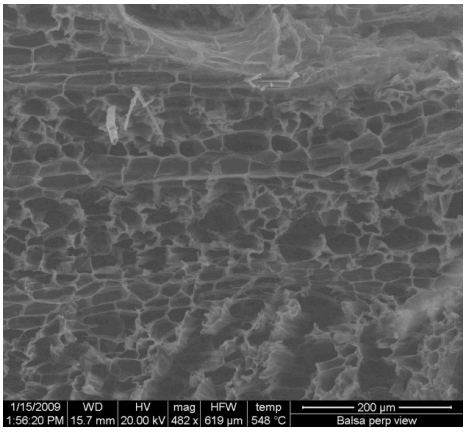

f. 548°C

Figure 33. Micrographs of balsa grain cross section during heating at 20°C/min.

No changes are apparent as the sample passes 100°C, as in the parallel view. However, the image does darken substantially from 120-200°C. Figure 33b shows the surface at 200°C. Although the image has become substantially darker, no significant changes in the sample are evident.

Decomposition becomes apparent as the material passes 200°C, with minor changes taking place along the grain cell walls. Figure 33c shows the material at 250°C as decomposition

is taking place. Several sites where cell walls have begun to erode are circled in red. Note that the contrast and brightness have been adjusted to make the image more visible.

The material continues to decompose after 250°C, and the grain cells begin to grow larger. Figure 33d shows the surface at 307°C with the grain cells slightly enlarged. Grain cell expansion continues slowly until about 320°C, at which point the material begins the final stage of decomposition, which is much less evident in the parallel view. At this point, the wood begins to undergo a global material collapse. This phenomenon is made most obvious by examining the rows of rectangular cells that run horizontally across each image. These can be seen moving closer to each other. The edge of the sample also comes into the image as the sample collapses in the top right corner of the image. Grain cell wall erosion continues and some cells collapse together to form larger voids in the material. Figure 33e shows the material at 347°C, as global collapse is taking place.

Decomposition continues rapidly until 380°C, at which point it quickly ends, and the material's surface undergoes no further changes. Once again, the surface appears to be contracting vertically away from the microscope's electron emitter, which is proven by the increased working distance and less focused image at the final temperature, shown in Figure 33f. Figure 34 shows the material before and after cooling. Again, no further changes took place as the material cooled.

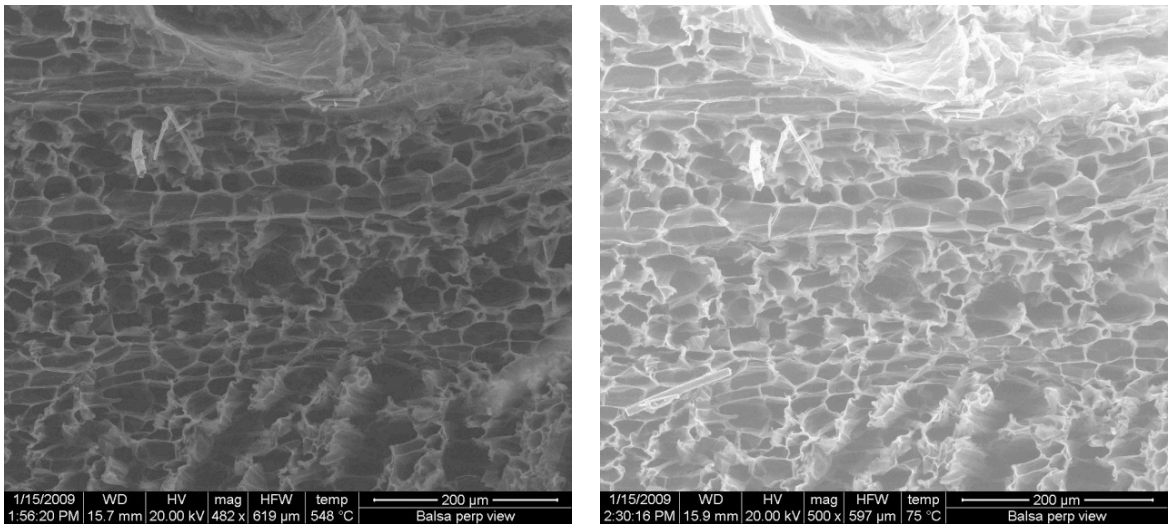

a. 548°C b. 75°C

Figure 34. Micrographs of balsa grain before and after cooling

Grain Cross-Section Analysis

The images shown above of the balsa wood grain cross section were loaded into MATLAB and analyzed using the *regionprops* function. Images were made negative with very high contrast and very low brightness in an image manipulation program, and then cropped to focus on one specific region of the decomposing material in order to keep the grain estimate consistent. Figure 35a-f shows the analysis area at each temperature that was examined. Note the significant decrease in the analysis area as the temperature rises that results from grain cell collapse.

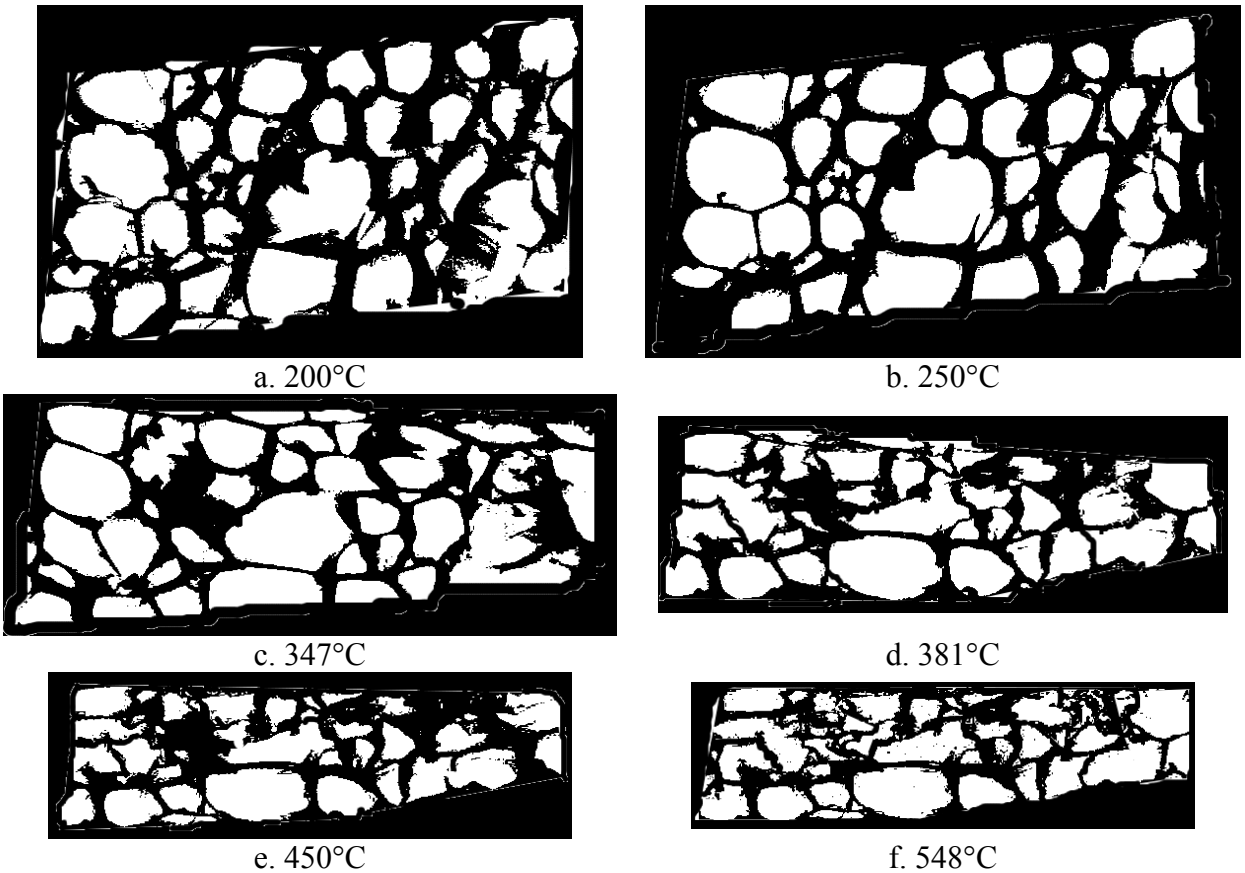

a. 200°C b. 250°C

c. 347°C d. 381°C

e. 450°C f. 548°C

Figure 35. Grain cross-section I mages used in the surface analysis

The grain cell areas that MATLAB recorded were assumed to be circular, and effective grain cell diameters were calculated. Diameters under 10 microns were ignored in order to remove errors from the analysis. MATLAB would count any sectioned white area as a grain, which resulted in a large number of very small grains being detected when in fact none were present. Figure 36 shows a series of histograms of grain diameters in the analysis area at six temperatures ranging from 200-548°C.

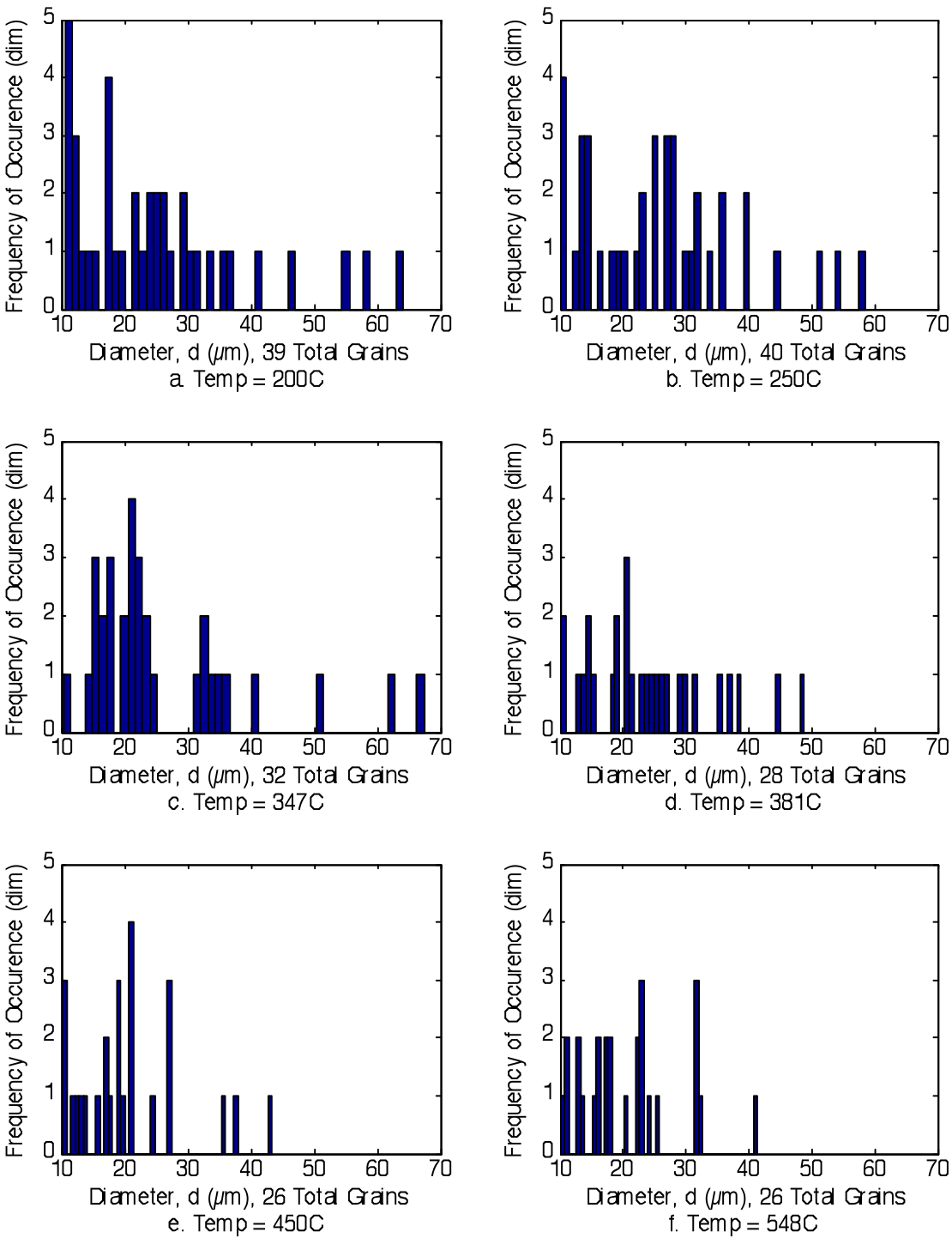

Figure 36. Grain diameter and void fraction of grain cross-section at several temperatures

The areas were then used to calculate several material properties. Average grain cell diameter, void fraction, and the size of the analysis area are shown in Figure 37 plotted as a function of temperature. As stated previously, the material does not appear to change until 200°C. As a result, it was assumed that void fraction and grain diameter are constant below that temperature. Above this temperature, the void fraction was found to increase during the main

decomposition phase and then drop slightly before leveling off. Average grain diameter follows a similar trend, except undergoes a net drop rather than a net gain as void fraction did. The drop that is observed in grain diameter can be attributed to the change in analysis area, which dropped by a factor of just over 3. These observations tie back to what was observed in the ESEM images, where first the cell walls are observed to thin out slightly, resulting in overall grain cell growth before the wall-thinning phenomenon is overwhelmed by analysis area collapse around 300°C.

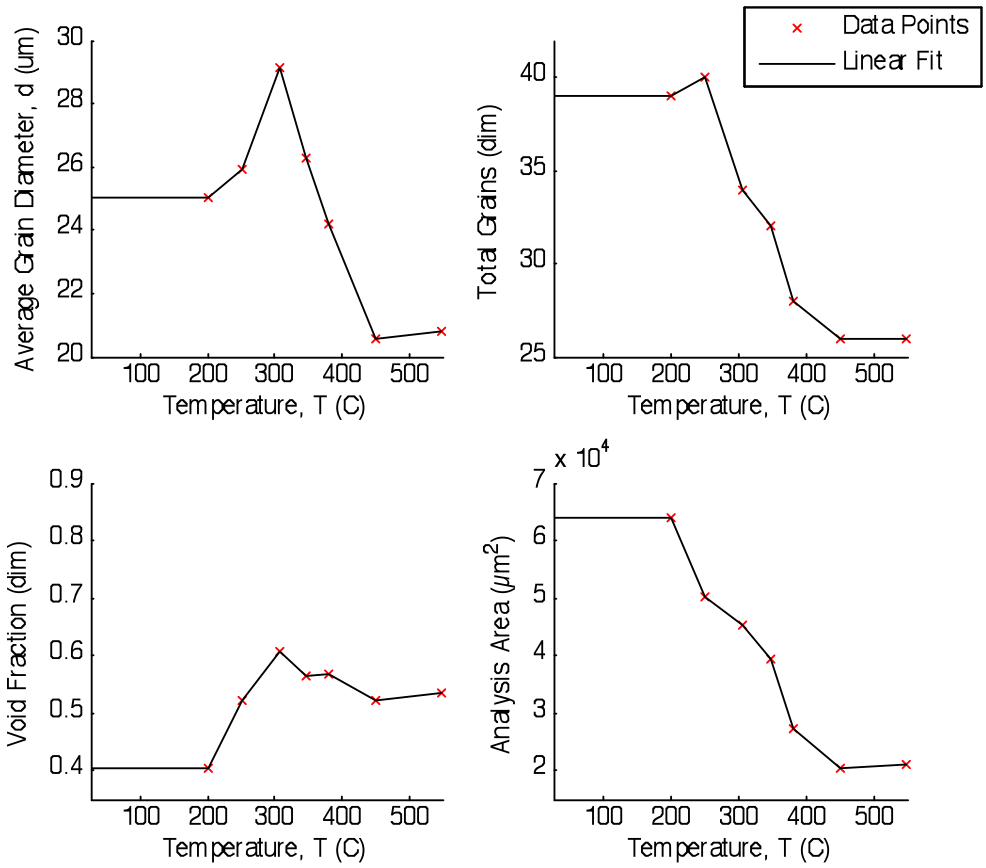

Figure 37. Average grain diameter, grain count, void fraction, and analysis area as functions of temperature.

Water Transport Vessel Analysis

Separate experiments were conducted to classify the water transport vessels in balsa wood. These vessels transport water vertically along the tree, as opposed to rays, which transport water radially within the tree. In terms of permeability, these channels form direct open paths for gas flow through the material. These roughly circular vessels run parallel to the grain, and are visible to the naked eye on a properly cut sample. A sample was prepared by hand cutting with a razor blade, and examined in the ESEM. Figure 38 shows a large view of the balsa water transport pores.

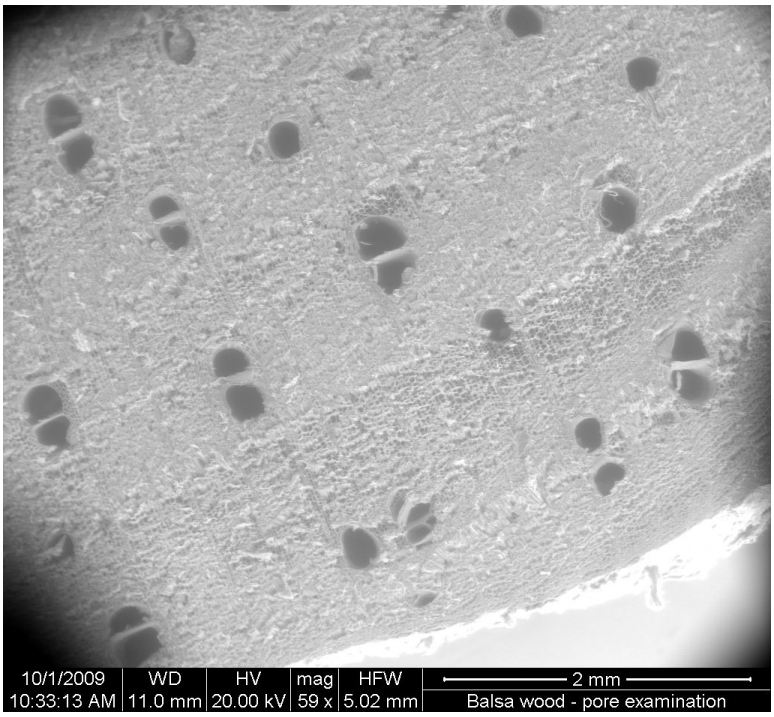

Figure 38. Balsa wood water transport channels

Interesting geometry exists on several scales in the sample. Figure 39 shows a close-up view of one channel on the same sample. Another detail worth noting in this figure is the small pores used for water transport between cells, circled in red in the image. Figure 40 shows a close up of these pores, which are only a few microns in diameter.

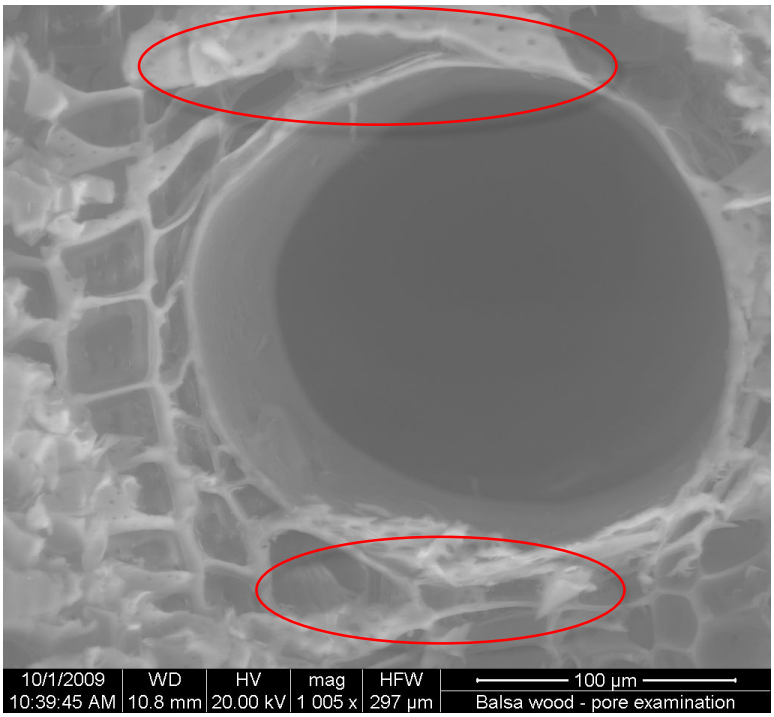

Figure 39. Close of up a water transport channel

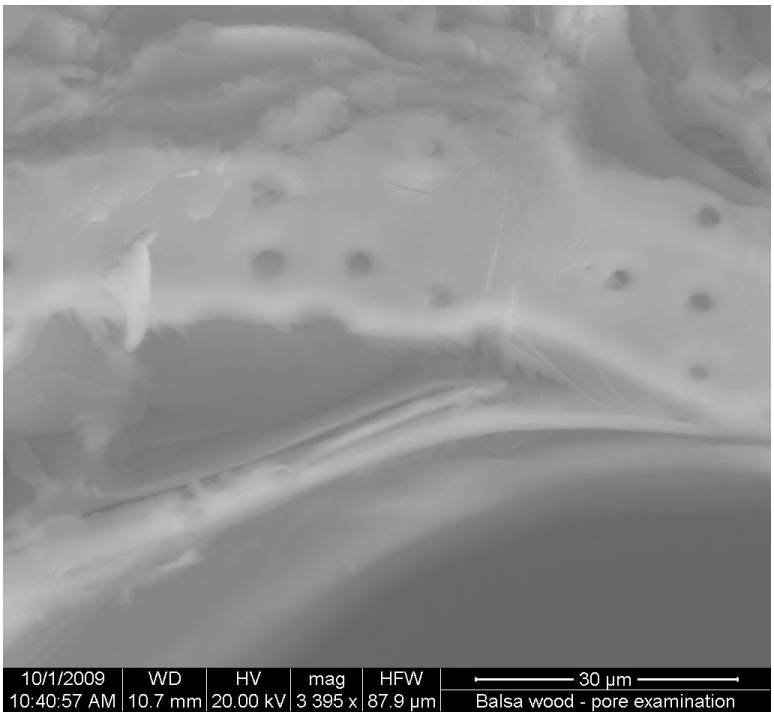

Figure 40. Inter-cell water transport vessels

Three images similar to the one shown in Figure 38 were examined in MATLAB with the same code that was used on the heated ESEM images to determine the diameter and frequency of occurrence of the water transport vessels. The results are shown in Table 5. On average, there were 1.48 vessels/mm^2, and the average vessel size was 184 µm. These water transport vessels are much larger than the grains themselves (as shown in Figure 39), which average around 25 µm in diameter.

Table 5. Balsa wood water transport vessel data

Image	Size (mm^2)	Number of Vessels (dim)	Vessels/mm^2	Average Vessel Diameter (µm)
1	25.2	26	1.03	204
2	22.6	34	1.51	182
3	19.0	36	1.89	167
Average	22.3	32	1.48	184

Porosity & Permeability

Porosity and permeability are very important parameters when modeling degrading balsa wood. These parameters are instrumental in determining the flow rates of gases evolved during decomposition of the material and are also useful in determining internal pressures.

A series of coupon-size samples were cut from a Baltek SB.100 balsa wood panel using the diamond core drill as discussed in Chapter 2. Again, care was taken to avoid glue lines when cutting samples. The full thickness of the panel (typically 0.483") was used to maximize the mass and volume of samples. In order to minimize variability between the sample mass, and therefore the density, several dozen samples were cut and only those that fell near the desired

density were used. In order to maximize the correlation of experimental results to the typical material, the density was kept close to the SB.100 panel's nominal density of 147 kg/m^3. The seven samples that were used had a density of 165 kg/m^3 with bounds of ±4%. Each sample was tested at a different level of decomposition. Samples decomposed beyond a dried normalized mass fraction of 0.56 were too fragile to test for permeability, and fell apart while the silicone potting was being applied. One sample was fully decomposed to a dry mass fraction of 0.27, but broke apart inside of the porosity test section before data could be taken. The decomposition curves from the ISTGA are available in Appendix C.

In order to account for the substantial variability that will inevitably occur in any measurement on balsa wood samples, the porosity was measured both before and after decomposing the samples in the ISTGA. Table 6 contains the results of porosity tests. Complete data is available in Appendix B.

Table 6. Porosity results for balsa wood

Normalized Mass Fraction (dry)	Maximum Temp (C)	Density	Virgin Porosity (dim)	Decomposed Porosity (dim)
1	Not heated	164.6	0.28±0.09	-
1	155	160.9	0.28±0.09	0.28±0.09
0.70	286	160.1	0.25±0.10	0.38±0.10
0.56	303	161.4	0.18±0.09	0.36±0.10
0.43	310	171.0	0.24±0.10	0.87±0.11
0.30	332	158.6	0.34±0.10	0.83±0.11

Table 6 shows that the porosity increases from a virgin value of 0.18-0.34 as it decomposes. Porosity levels tended to level off as the normalized mass fraction dropped below 0.4, as the samples at normalized mass fractions of 0.43 and 0.30 both had decomposed porosities around 0.85. Figure 41 shows the porosity of balsa wood plotted against normalized mass fraction.

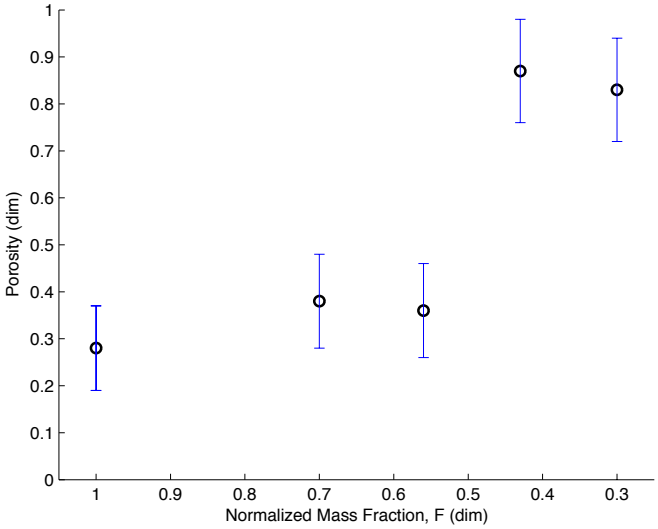

Figure 41. Porosity of balsa wood vs. mass fraction

While porosity defines the amount of empty space in the material, it only describes part of the gas flow problem during decomposition. Permeability is the other part, describing the pressure required to force evolved gases out of the material through its pore structure. Figure 42 shows the data that was used to calculate permeability. Note the linearity of each data set, which in addition to the Reynolds numbers (which have maximum values of 6E-4, still several orders of magnitude below 1), indicates that Darcy's law is valid. Table 7 presents the permeability results. Complete data is available in Appendix B. Error was again fairly small.

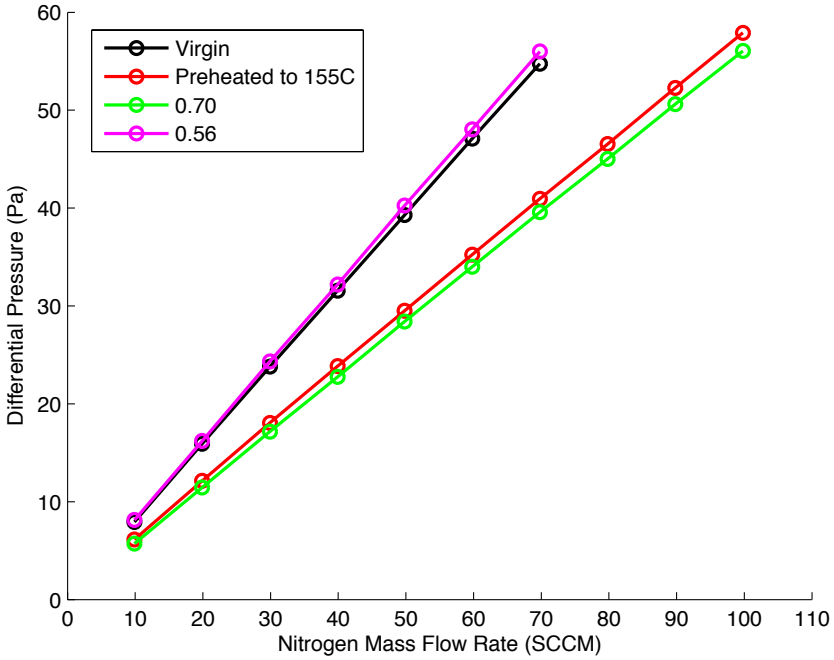

Figure 42. Permeability test data for balsa wood

Table 7. Permeability results for balsa wood

Normalized Mass Fraction (dry)	Maximum Temp (°C)	Permeability (m^2)	Permeability Error (%)
1	Not heated	9.0E-12	3.36
1	155	1.2E-11	3.21
0.70	286	1.3E-11	3.30
0.56	303	8.7E-12	3.38

Figure 43 shows plots of permeability against porosity and mass fraction. Permeability does not appear to be a function of either property, at least as far as tests could be conducted. The permeability is close to 1E-11 m^2 for all four samples. The fact that the permeability does not change is attributed to the water transport vessels, which create (relatively) large, direct paths for gas flow along the grain. Flow through any additional paths that may be formed due to grain degradation during heating is negligible relative to the flow that travels through the water transport vessels.

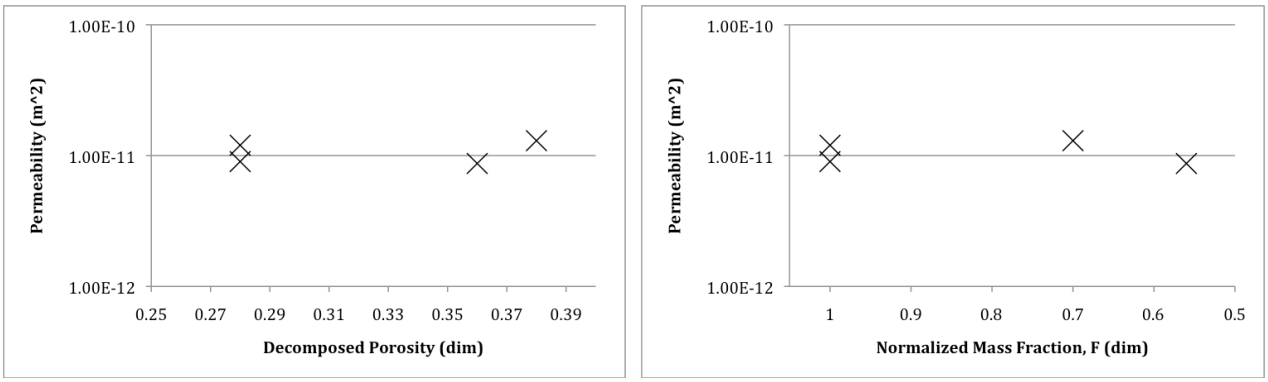

(a) Porosity (b) Normalized Mass Fraction, F

Figure 43. Balsa wood permeability plots

CT Scans

X-ray CT scans were conducted on the virgin (unheated) balsa wood sample after completing porosity and permeability testing. These tests were conducted to attempt to gain information on the three-dimensional microstructure of the material. Figure 44 shows an external view of the sample with the silicone potting in place. Due to the fairly large size of the samples (1.4" diameter and 0.5" thick), image resolution was very limited compared to the ESEM images. The silicone potting that was applied to seal samples was shown in addition to the sample because the CT scans were conducted after permeability testing. No attempt was made to remove the potting due to the potential of damaging the sample in the process.

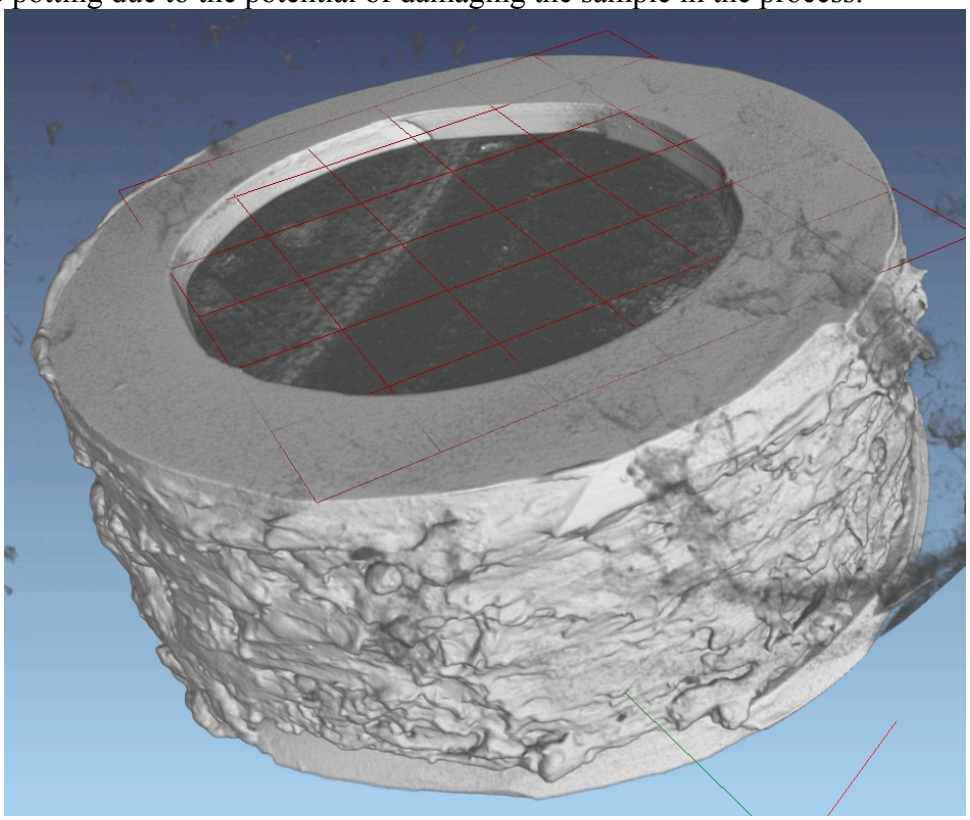

Figure 44. Virgin balsa wood sample external view

Additional cross-sections were generated to investigate microstructure of the material using the X-ray CT technique. Figure 45 shows a cross-sectional view with the grain running vertically along the page. Note the solid barrier formed by the silicone potting around the edges. The bottom center of the sample appears translucent in this image, due to the very low density in that portion of the sample. Figure 46 shows an image of the virgin sample with the grain running into the page. The holes dotting the surface shown in this image are internal vessels that the balsa tree uses for water transport. They are most likely the primary source of gas transfer in virgin samples.

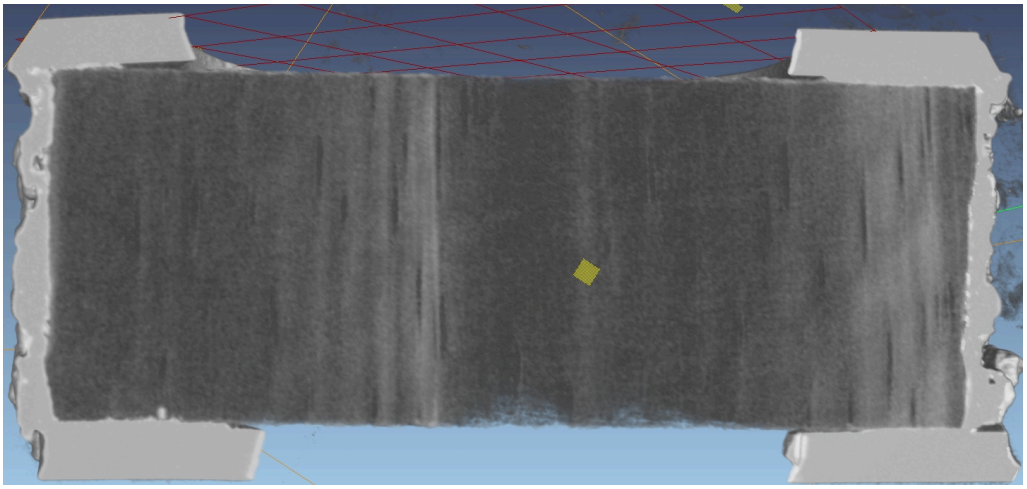

Figure 45. Virgin balsa wood cutaway view (grain vertical)

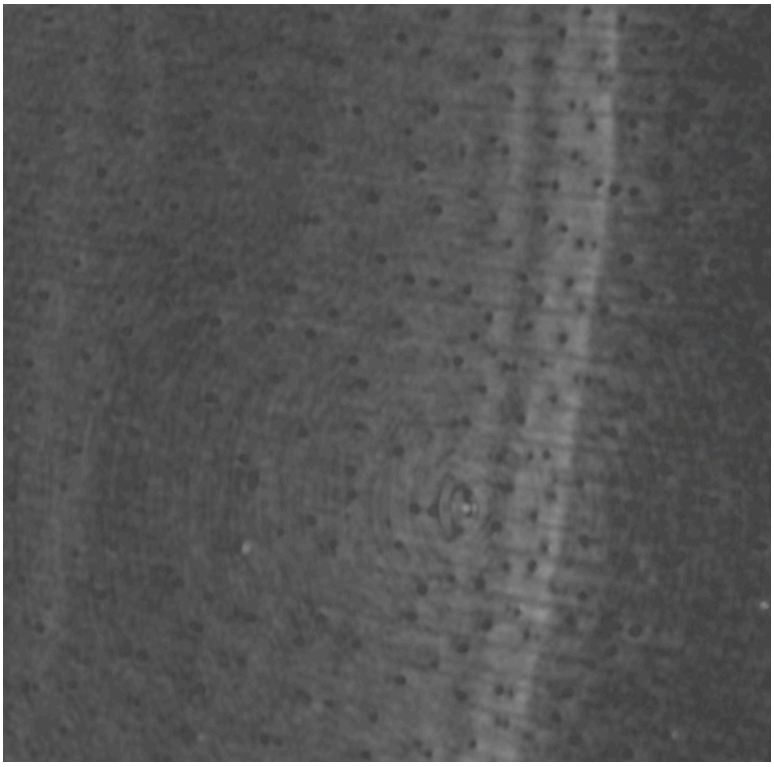

Figure 46. Virgin balsa wood cross-sectional view showing water transport vessels

Chapter 5 – Microstructure, Porosity, and Permeability of E-glass/Vinyl-ester

The thermal aspects of E-glass/vinyl ester studied in Chapter 3 are only one piece of the puzzle. While it is fairly easy to get data for the energetics and kinetics of the material during heating, a greater understanding of microstructural behavior was needed to aid in development of computer models. A series of heated ESEM experiments were conducted on both pure vinyl-ester resin, and also on an E-glass/vinyl ester composite sample to gain an understanding of these physical changes, and also to determine what decomposition phenomena occurred in the resin alone.

In addition to direct physical observational information, data on the gas flow properties (porosity and permeability) was needed to model pyrolysis and analytically determine internal pressures developed in the material during decomposition.

Microstructure

Derakane 411-350 Vinyl-Ester Resin

Initial microstructural evaluations in the ESEM were performed using a pure resin sample to investigate resin decomposition without fibers present. A test was performed on a fully cured Derakane 411-350 resin sample from room temperature to 400°C at 20°C/min in the heated sample holder within the ESEM. Image field width was varied from 100-200 μm in order to examine details of the sample as it was decomposed. Figure 47a-f shows images at a series of temperatures that characterize the decomposition. Magnification and position were changed a few times during the experimental run in order to examine morphological events. As a result, position and magnification of the image are not constant in the images below. Once the sample exceeded 400°C and the rate of decomposition increased, the image became very unstable due to bulk motion of the sample as it degraded. As a result, no additional video was collected above this temperature.

The initial phase of decomposition in resin was observed in the microstructure to begin at about 200°C. The surface of the resin appears to become rougher as this phase begins; indicating small amounts of material are being lost from the surface as well as pore initiation. Figure 47b shows the resin at 251°C, with a roughened surface as described. Pore formation is observed in Figure 47c at 318°C, and pores are observed to grow (Figure 47d-f) until the experiment is terminated at 400°C. As the temperature continues to rise above 350°C, pores begin to enlarge on the surface. Pores were observed to grow to widths of 20-30 μm before the experiment was terminated (typical fiber diameter is 20 μm for the composite sample).

Figure 47f shows one of the last images taken, at which point the ESEM had been set to field width of about 300 μm to show that pore formation was taking place over the whole surface, rather than just the area in which it had been focused for most of the experiment.

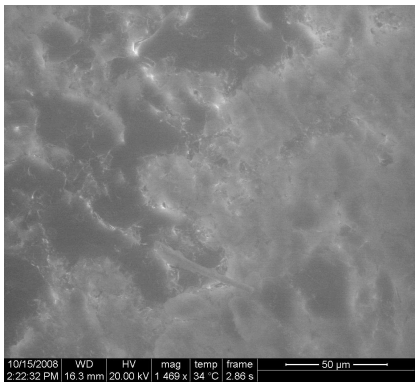

(a) 34°C

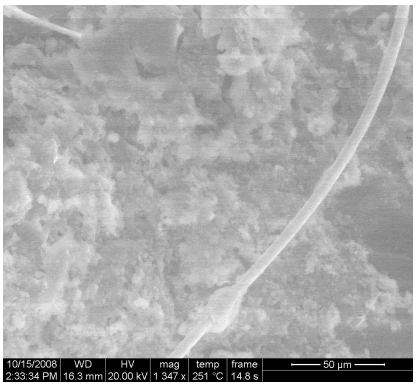

(b) 251°C

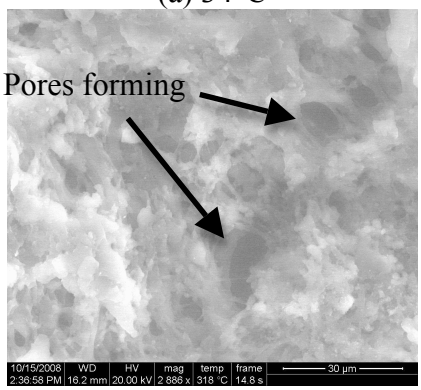

(c) 318°C (field width decreased)

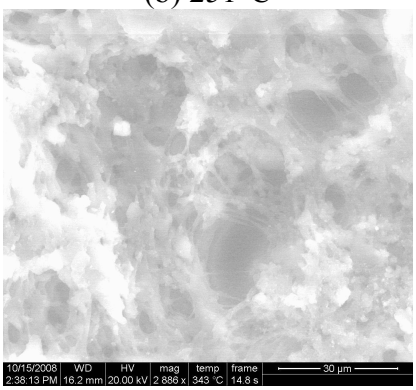

(d) 343°C

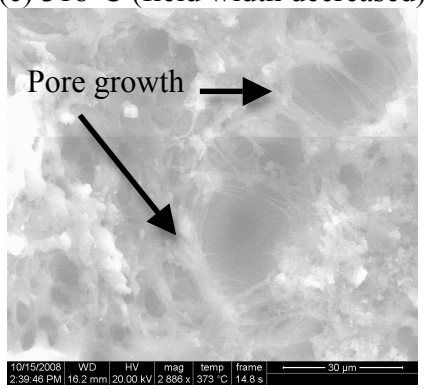

(e) 373°C

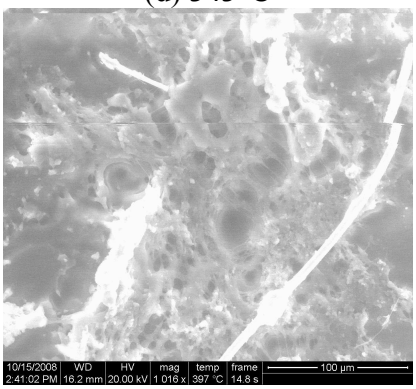

(f) 397°C (field width increased)

Figure 47. Micrographs of Derakane 411-350 vinyl-ester resin

Some interesting parallels can be drawn between the TGA data (Figure 24) and the micrographs (Figure 47a-f) of the pure resin sample. Both sets of data confirm that there is no decomposition below 150°C as observed in TGA data (Figure 24). The initial decomposition is not optically apparent until about 200-250°C. During this initial decomposition stage, pores were observed to form. Above 350°C, pore formation was seen to accelerate, up until the point at which the image was lost at 400°C. This correlates well to the TGA data, which shows that decomposition greatly hastens at 380°C. The ESEM data confirms that pores form and continue to grow up 400°C, at which point the image was lost. No cracks were observed at any point during the experiment.

E-glass/Vinyl-Ester Composite

An E-glass/vinyl-ester sample was placed in the ESEM to observe the changes in the composite material as it was heated and cooled. In order to observe changes in the resin and glass fibers during heating, a sample was prepared that focused in on the region between fiber bundles. A sample was cut such that the fiber cross-section from the woven fabric was on the surface, allowing the resin in the small gaps between the warp and weft fiber directions to be visible. In order to capture a characteristic view of the fibers, the field width was set at 370 μm, somewhat higher than in the resin experiments. The virgin sample is shown in Figure 48. The sample was then ramped to 548°C at 20°C/min, Figure 49a-f shows a progression of images of the decomposition that took place as the sample was heated. Note that these images were taken with a larger field of view than those done with pure resin (Figure 47a-f).

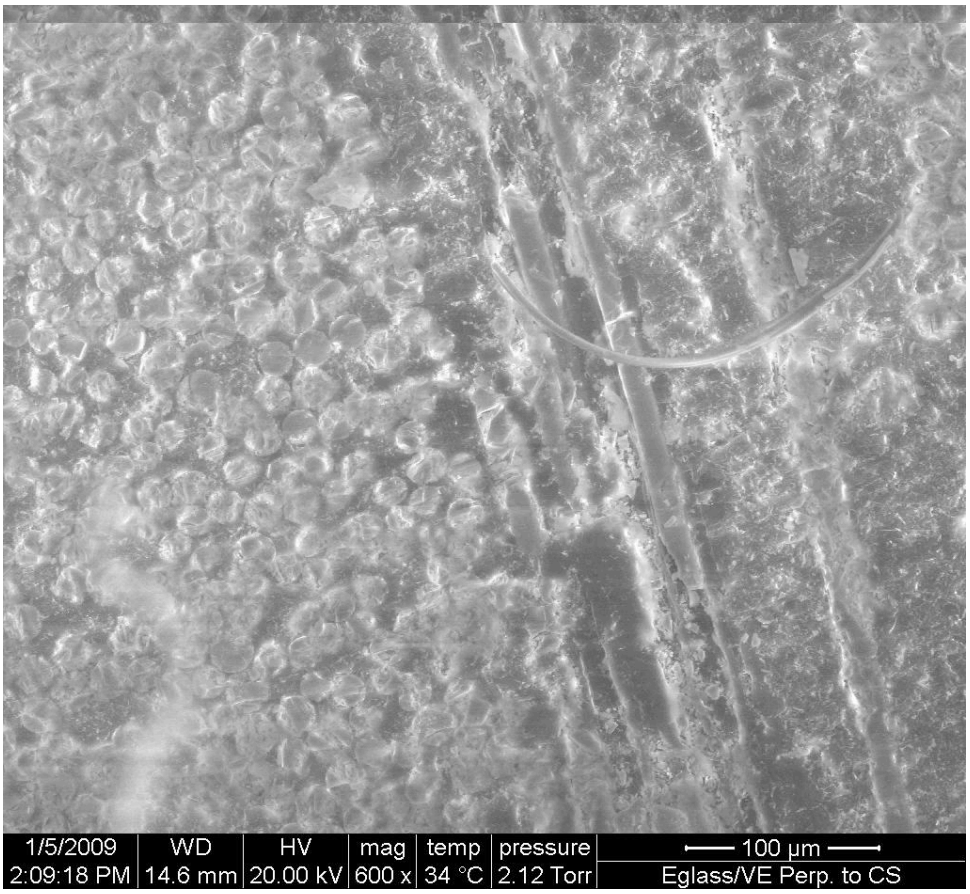

Figure 48. E-glass/vinyl ester before heating

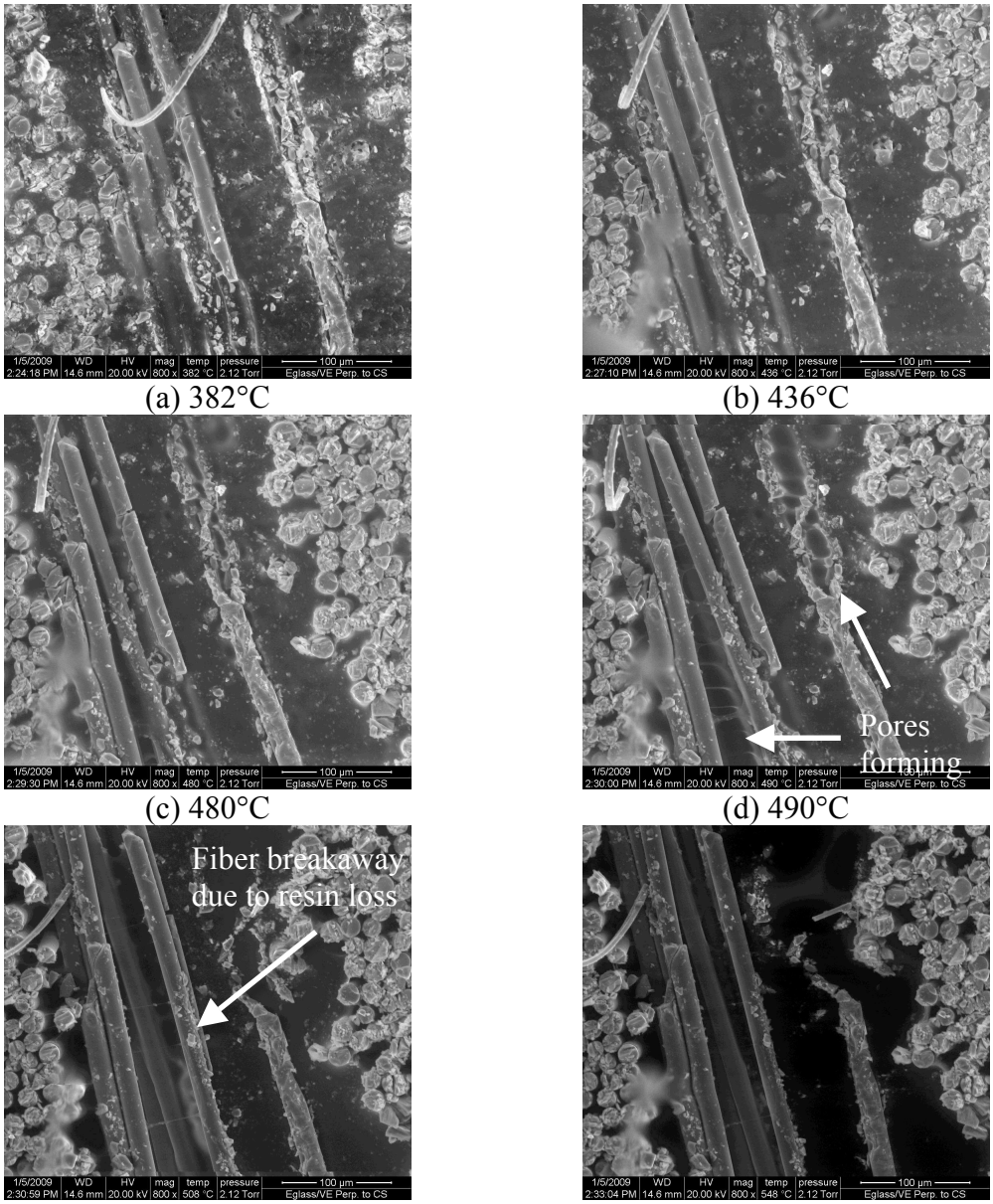

(a) 382°C (b) 436°C

(c) 480°C (d) 490°C

(e) 508°C (f) 548°C

Figure 49. Micrographs of E-glass/VE during heating

In contrast to the pure resin sample, which decomposed at significantly lower temperatures, no pore formation was observed below about 400°C. Unlike the resin samples, pore formation is much less obvious in the temperature range of 300-400°C, even in the resin rich region that was focused on for the ESEM experiment. The lack of observed pore formation may be due to the presence of fibers, which may affect the contrast of the image. The resin decomposition appears to allow for some fiber motion over the temperature range 380-460°C, possibly due to stresses placed on the fibers before resin infusion during manufacture. Figure 49a-c show the change in surface smoothness from 382°C to 480°C, as well as fibers becoming more apparent on the surface. As the sample continued to heat up, pores began to form on the surface in two locations as shown in Figure 49d; in one place along the length of a fiber that had

been partially sanded off, and in another where a fiber began to drift or pull away from adjacent fibers, leaving small strings of resin in its wake. The TGA curves show that at this temperature, only 7% of the resin is still in the material. The single fiber continues to move as the temperature rises from 490°C, finally coming to rest at approximately 520°C. At this very same temperature, the surface in between fibers changes very suddenly, transitioning from the fairly smooth resin surface into a final char pore structure. Figure 50 shows a 1 mm field width view of the sample at 548°C, in which two resin-rich regions are captured. Both of these regions exhibit this large pore structure. The size and geometry of the pores depends most on the arrangement of the adjacent fibers, as they tend to conform to adjacent shapes. A typical range of pore sizes for the sample examined in this paper is 20-200 µm.

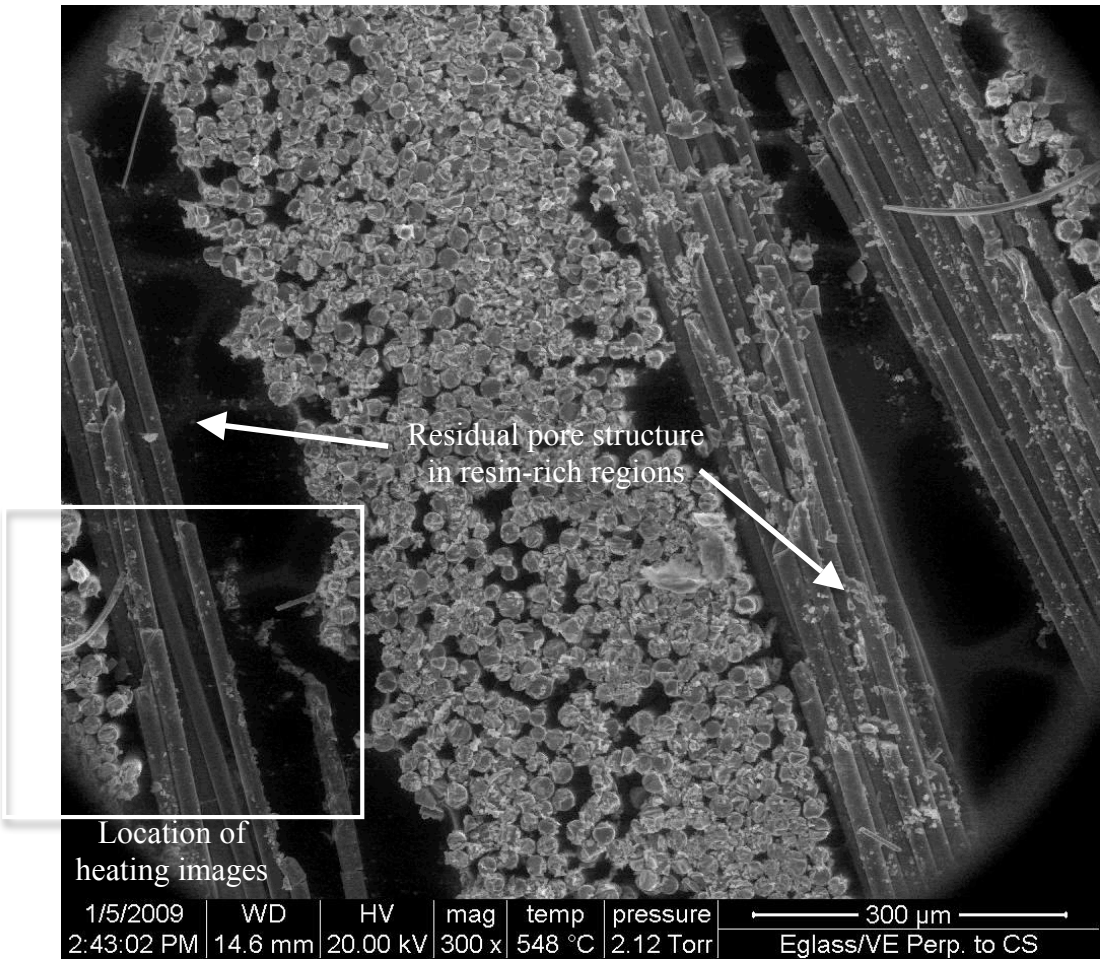

Figure 50. Large view of E-glass/VE at 548°C. Rectangle shows location of higher magnification images from heating, shown in Figures 6a-f.

The sample was then cooled at 20°C/min, back to room temperature. Figure 51a-b shows the sample at high and low temperature. While the surface appears to brighten significantly (most likely due to charging), no further structural changes are apparent.

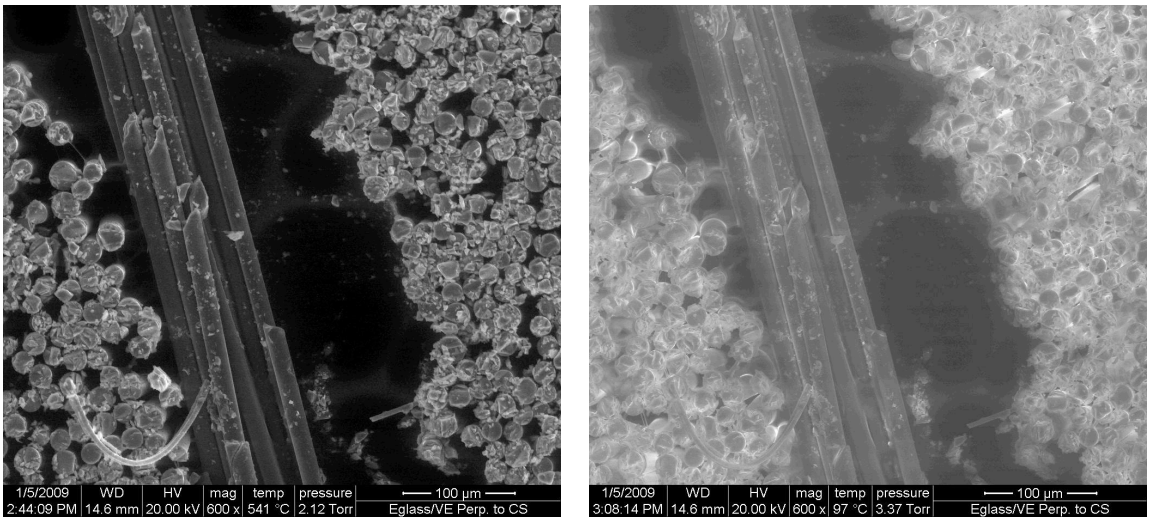

(a) 541°C (b) 97°C

Figure 51. E-glass/VE sample at high and low temperature after cooling

In contrast to the resin sample, only minor surface changes were observed in the E-glass/VE sample up to 400°C, most likely due to thermal expansion. Above this temperature, decomposition became apparent, with pores forming in the gaps between fibers and some fiber motion. The TGA curve for E-glass/VE (Figure 23) confirms that the fastest phase of decomposition is taking place from 380-460°C, which is also the temperature range where pore formation begins to become apparent in the composite. Interestingly, the composite sample clearly continued to degrade beyond 460°C, finally appearing to largely stop around 520°C. Fiber motion was observed at 490°C, possibly due to residual stresses from the VARTM process relaxing out of the decomposing material. In contrast to the result of Mouritz and Mathys [11] in which post-fire SEM micrographs were taken of cone calorimeter samples, no cracking was observed in either sample. The lack of cracking may be attributed to the temperature uniformity and smaller scale of the samples as tested in the ESEM relative to the cone calorimeter. Another difference in the degradation methods was the absence of atmospheric pressure in the ESEM samples, which may be a factor in crack development.

After decomposing the sample entirely, a residual pore char structure remains in the formerly resin-rich regions that lie in gaps between the warp and weft fiber directions of the woven fiber system. This pore structure remains as the sample is cooled. While the surface appears to undergo no further changes during cooling, and DSC tests confirm that no further thermal reactions take place during cooling, the surface becomes a great deal brighter. It becomes so much brighter, in fact, that in a few instances fibers can be seen extending down into the residual pore structure. This increase in brightness may be due to electron charging in the char formed after the resin has decomposed.

Porosity & Permeability

In order to classify the gas flow properties through virgin and decomposed E-glass/vinyl ester samples, porosity and permeability tests were carried out. These parameters are instrumental in implementing computerized decomposition models and are also useful in calculating internal pressures in partially decomposed material

A series of coupon-size samples were cut from an E-glass/vinyl-ester composite panel with the diamond core drill as discussed in Chapter 2, and decomposed in the ISTGA. The panel had a nominal thickness of 0.24", with some slight waviness on one side as a result of the VARTM process by which it was manufactured. A total of nine samples were tested: a virgin sample, seven at different levels of decomposition in a nitrogen (inert) atmosphere, and one that was decomposed in air. The decomposition curves from the ISTGA are available in Appendix C. While the porosity of virgin E-glass/VE is known to be zero, a small porosity (0.09) was measured due to instrument error and an inability to perfectly measure the thickness of the composite discs due to the waviness on one side.

The results of the porosity tests on E-glass/VE are presented in Table 8. Complete data is available in Appendix B. The error was higher in the porosity tests for E-glass/VE than for balsa due to the smaller sample size relative to the size of the test chamber (E-glass/VE samples were half the thickness of the balsa samples).

Table 8. Porosity results for E-glass/VE

Normalized mass fraction (dim)	Maximum Temperature (°C)	Thickness (mm)	Porosity (dim)
1	-	6.1	0.09±0.20
0.97	325	6.1	0.09±0.20
0.64	400	6.6	0.18±0.19
0.39	408	6.9	0.31±0.18
0.26	432	8.4	0.53±0.15
0.18	437	9.1	0.61±0.13
0.12	435	9.1	0.62±0.13
0	555	8.9	0.68±0.14
Oxidation, 1 hr @ 600C	600	7.6	0.64±0.16

Permeability is another property of interest as E-glass/VE degrades. E-glass/VE has no permeability in the virgin state, which leaves gases evolved during pore formation and decomposition to collect inside of the material until the pore structure forms flow channels to the surface. The sealed nature of the pores in E-glass/VE can lead to high internal pressures, accelerating failure. Table 9 presents the permeability results for E-glass/VE. Two sample data sets are plotted in Figure 52. Complete data is available in Appendix B. Permeability error was considerable for some tests due to the very low pressures at which permeability tests were conducted, in some cases only about 10% of the range of the ±62 Pa pressure transducer was used. All tests were well below the Reynolds number limit (Re < 1), with the highest value being 7.3E-3 for the tests conducted at F = 0.

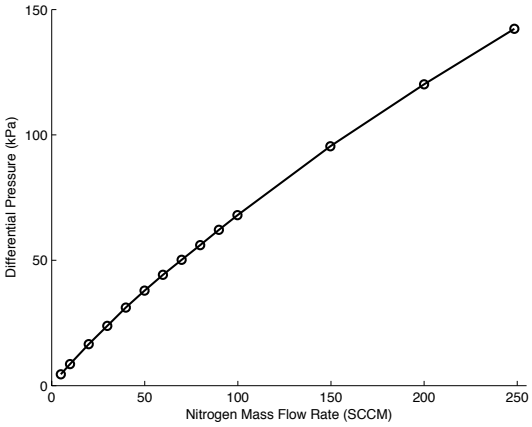

(a) F = 0.39

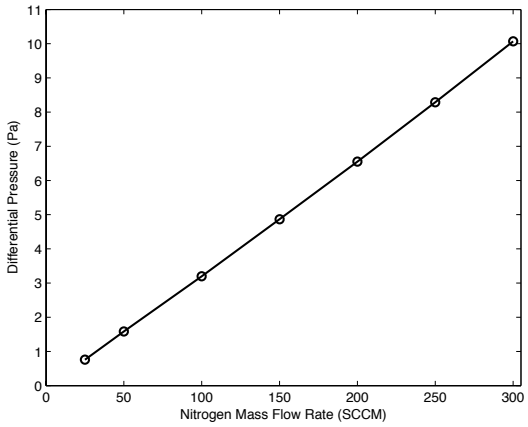

(b) F = 0

Figure 52. Selected E-glass/VE permeability sample data sets

Table 9. Permeability results for E-glass/VE

Normalized mass fraction (dim)	Maximum Temperature (°C)	Thickness (mm)	Permeability (m^2)	Permeability Error (%)
1	-	6.1	0	0
0.97	325	6.1	0	0
0.64	400	6.6	8.29E-16	3.88
0.39	408	6.9	5.72E-15	3.64
0.26	432	8.4	6.36E-11	17.26
0.18	437	9.1	7.79E-11	17.73
0.12	435	9.1	1.31E-10	28.11
0	555	8.9	1.56E-10	28.86
Oxidation, 1 hr @ 600C	600	7.6	8.55E-12	7.18

The porosity data is plotted in Figure 53. Porosity increases slowly at first, and the rate of increase then rises as the material decomposes before reaching a final value of 0.68 in the fully decomposed sample. The slow initial rise in the porosity (an increase of just 0.09 from normalized mass fractions of 1 to 0.64) may be explained by the fact that only pores that are accessible to the test gas are included in the measurement (open-pore porosity). Greater pore structure may exist internally in the material, but it does not factor into the porosity measurement until it becomes accessible from the outside. This behavior is demonstrated in the porosity data beyond a normalized mass fraction of 0.64, after which the rate at which porosity is rising increases substantially before leveling off at the final value.

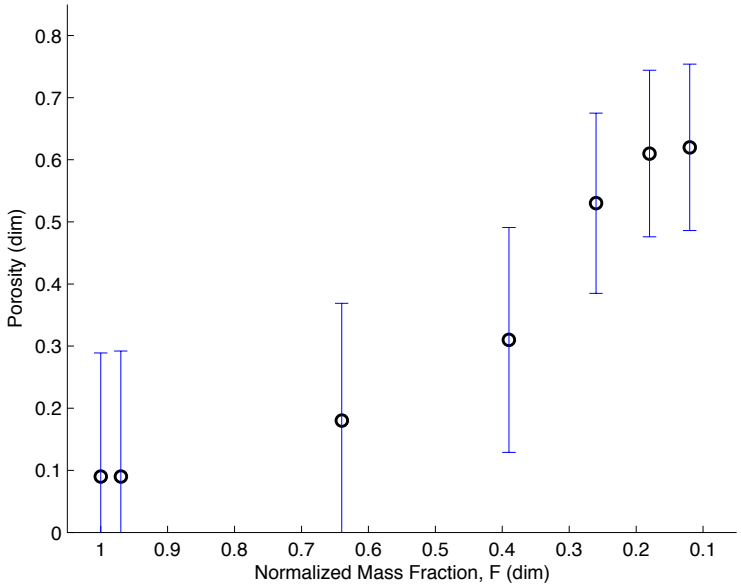

Figure 53. E-glass/VE porosity

The permeability data is plotted in Figure 54. In addition to the test data, the lowest measurable permeability is plotted as a black circle at a normalized mass fraction of 1.0 in order to provide a frame of reference for the "zero" value in the context of the permeability data. In a similar manner to the porosity data, the permeability does not increase substantially until the normalized mass fraction is fairly low (0.4-0.3 in this case). This behavior can be explained by the pore structure, which initially does not form paths through the material. From a normalized mass fraction of 0.4 to 0.3 the permeability undergoes a four order-of-magnitude increase. In this range there is a corresponding spike in the porosity that was measured on the same samples.

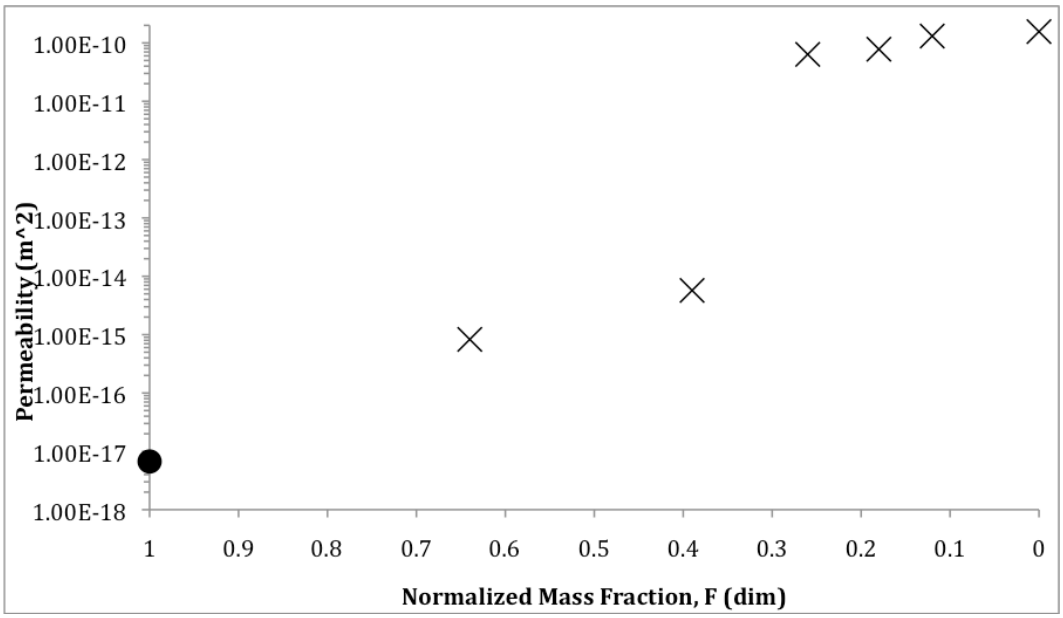

Figure 54. E-glass/VE permeability data and fit. Black circle represents measureable zero value.

The porosity and permeability were both observed to increase monotonically with the normalized mass fraction. The sample did not become permeable at all until a normalized mass fraction of 0.64 was reached, and did not become highly permeable until it was below a normalized mass fraction of 0.39. Beginning at a normalized mass fraction of 0.39, the permeability jumps by four orders of magnitude over a normalized mass fraction change of 0.13. Both permeability and porosity results on fully degraded samples were in line with previous tests on plain woven mats [30], which showed typical permeability for woven FRP mats to be from 6E-11 m^2 at a porosity of 0.51 to 2.1E-10 m^2 at a porosity of 0.59. Permeability is plotted against porosity in Figure 55, with the "zero" permeability value shown at a porosity of zero.

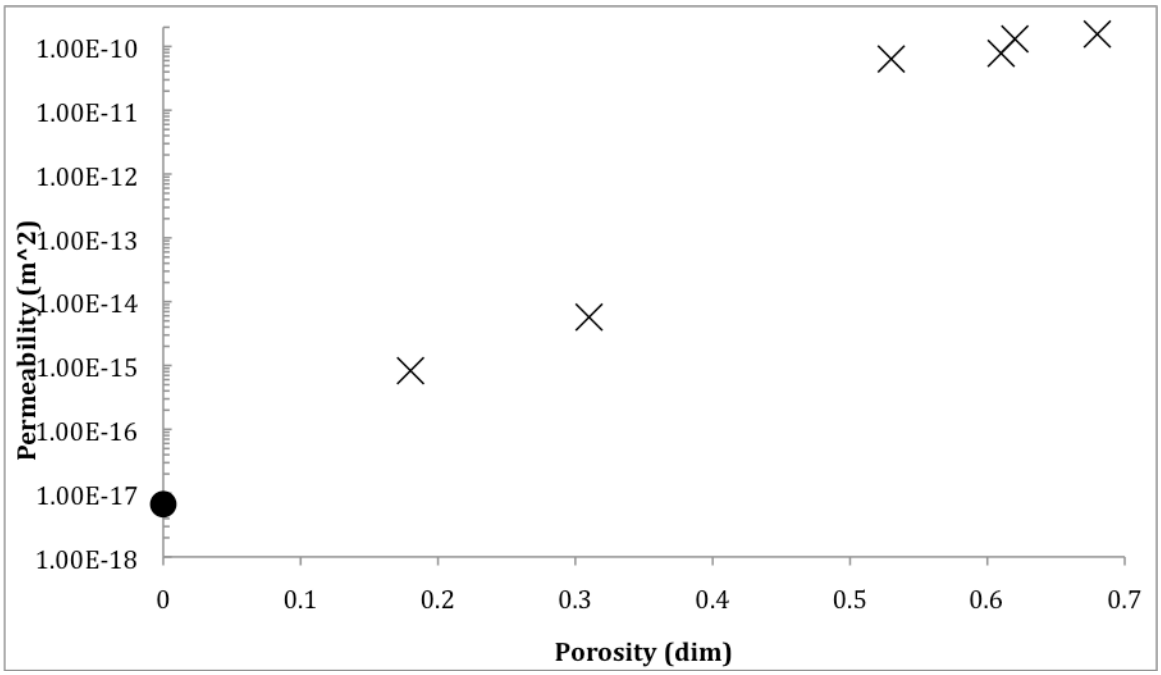

Figure 55. E-glass/VE permeability vs. porosity

The behavior of the porosity and permeability data of E-glass/VE as the samples degrade can be explained by the manner in which the sample is degrading. Pores are formed both internally and on the surface, but initially do not form paths through which gas may flow. As a result, the open-pore porosity test measures fairly low values for porosity until a normalized mass fraction of 0.4 is reached, at which point the porosity begins to increase rapidly. The same behavior is observed in the permeability, in which a four order-of-magnitude spike is observed when the sample decomposes past a normalized mass fraction of 0.4. The large increases in porosity and permeability at this normalized mass fraction range are attributed to the interlinking of internal pores.

While the porosity of the oxidized sample was in line with the numbers obtained for samples decomposed in an inert atmosphere, the permeability of 8.55E-12 m^2 was significantly lower that recorded for the sample that was fully decomposed in the inert atmosphere, as was the final thickness. The two samples had fundamentally different structures, with one that was decomposed in nitrogen basically falling apart, and the one that was burned in air holding its shape as a cohesive disc. The two samples are shown in Figure 56.

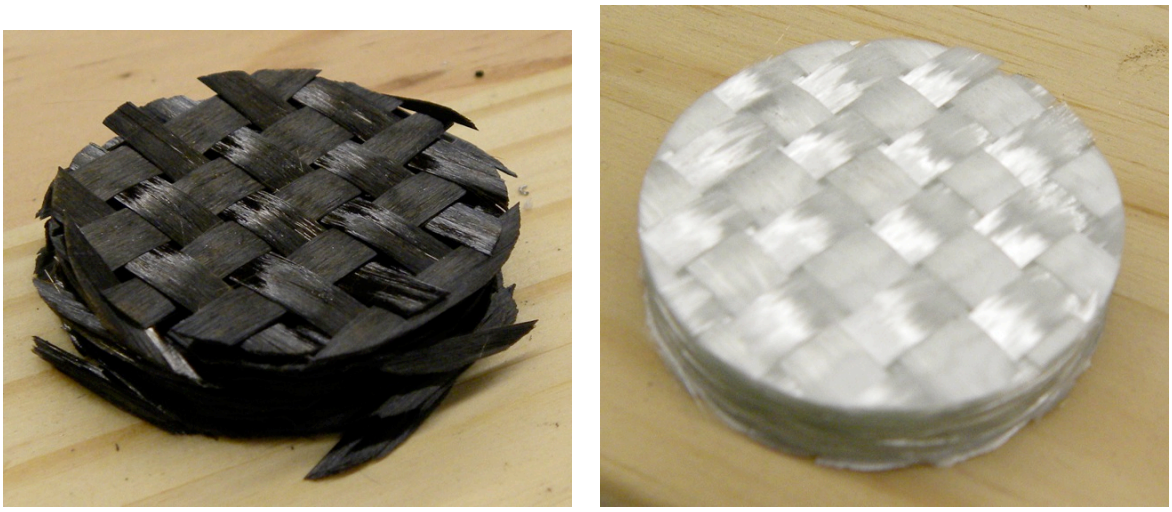

(a) Nitrogen (b) Air

Figure 56. E-glass/VE samples fully decomposed in (a) nitrogen and (b) air

After permeability and porosity testing, the intermediate scale samples were examined at room temperature in the ESEM. Some cracking was observed on the sample that was degraded to a normalized mass fraction of 0.39, shown in Figure 57, which gives rise to the question of whether cracking is caused by partially degrading the sample and then cooling it, or whether it is simply a matter of scale.

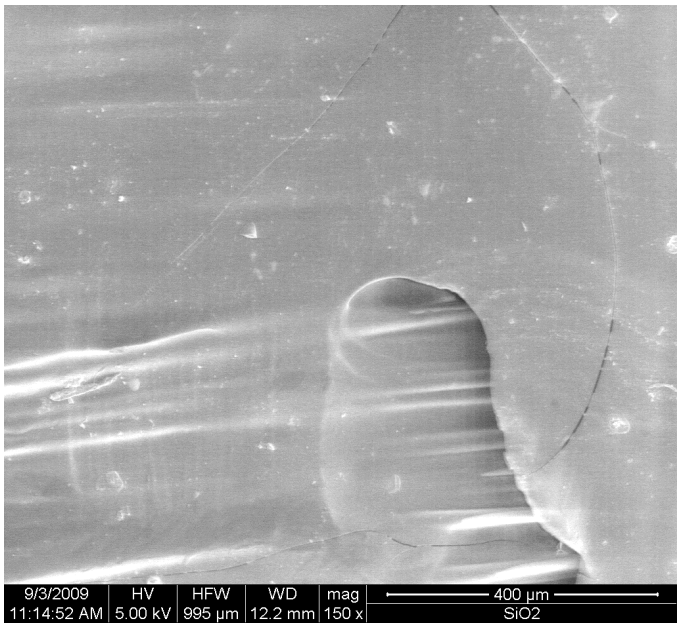

Figure 57. Cracked intermediate-scale sample, F = 0.39

CT Scans

X-ray CT scans were performed to obtain three-dimensional images of the physical changes in the material after decomposition. CT scans were conducted on the virgin and fully decomposed E-glass/vinyl-ester specimens. Figure 58 shows an internal-cross sectional view of both samples. Note the good sealing provided along the jagged edges of the sample by the

silicone sealant. Many resin rich regions are evident in the virgin sample, and the layers have pulled apart to create large internal voids in the decomposed sample. Figure 59 shows internal layer views of each sample. The virgin sample appears very flat due to the presence of the resin matrix, while the decomposed sample appears very three-dimensional. In both views, the individual fiber tows that make up each layer have shifted in the decomposed specimen resulting in jagged, misaligned edges.

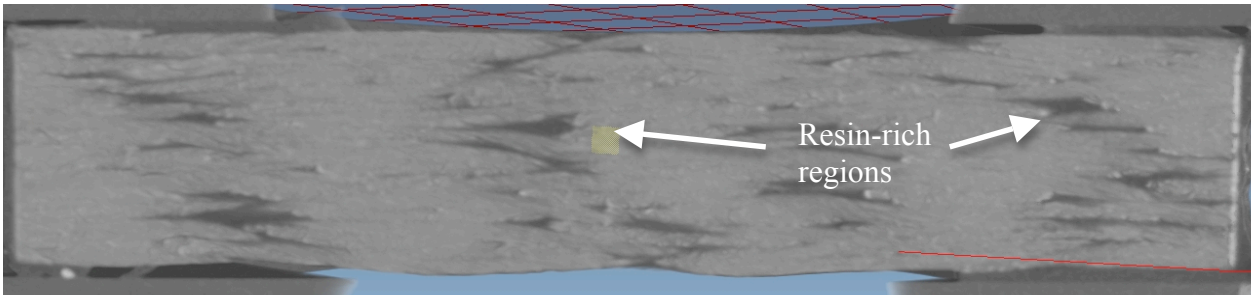

(a) Virgin

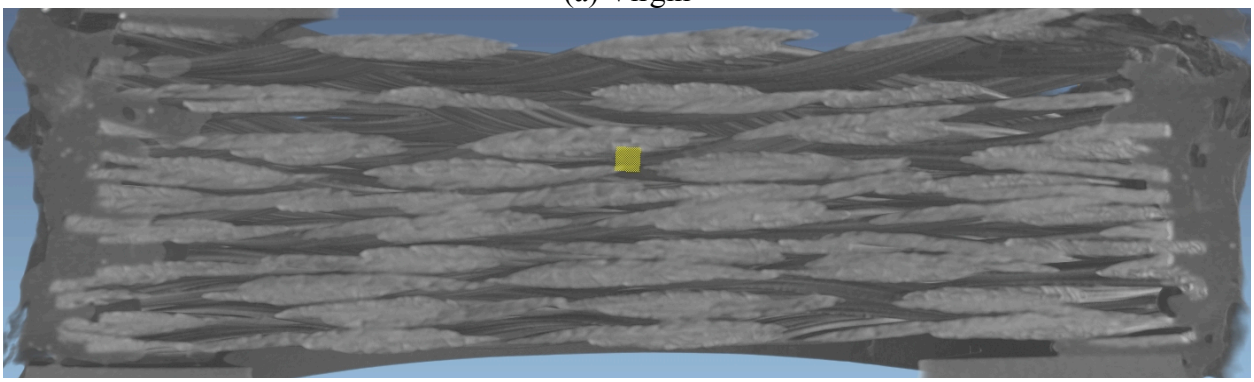

(b) Decomposed

Figure 58. Internal cross-sectional views of virgin (top) and decomposed (bottom) E-glass/VE

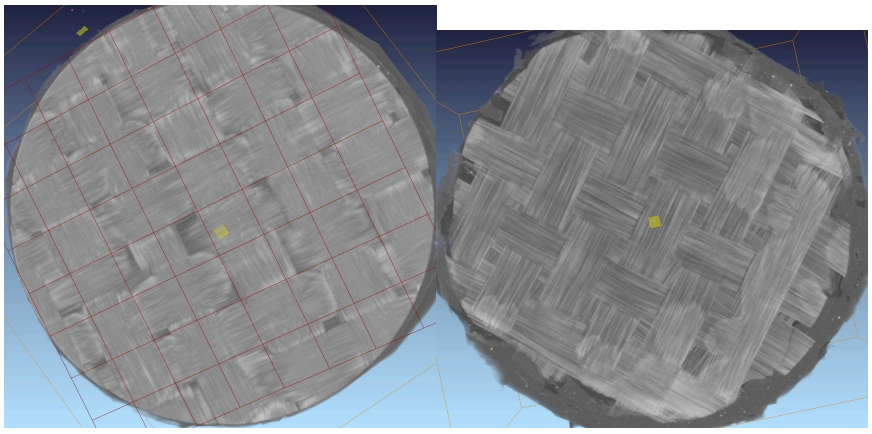

Figure 59. Internal layer views of virgin (left) and decomposed (right) E-glass/VE

Chapter 6 – Summary & Conclusions

Summary

A series of experiments was conducted that investigated the behavior of E-glass/vinyl-ester composite and balsa wood during heating. DSC and TGA were used to examine the energy transfers and mass losses occurring during in decomposition. Samples of each material were then examined in the ESEM in addition to a pure vinyl-ester sample, and the changes that were observed were then correlated back to observations made of the DSC/TGA results. Permeability and porosity tests on degraded samples were conducted at room temperature to further classify physical changes in the material, which affect the pyrolysis of the material by determining the flow rates of evolved gases from the material.

Decomposition occurs in three phases for E-glass/VE at 20°C/min: a slow loss of material from 150-400°C, a rapid mass loss spike from 400-460°C, and a second slow loss of mass from 460-600°C. The primary decomposition phenomenon for E-glass/VE was the charring of resin, which began at 350-400°C, resulted in a mass loss of approximately 25%, and caused the apparent specific heat to spike from 1.2 to 3.5 J/g°C. The decomposition of balsa wood was somewhat more complex, with a pre-decomposition mass loss associated with the evacuation of water from the sample, followed by a multi-stage decomposition reaction resulting in loss of about 75% of the virgin mass (depending on the final temperature). The rate mass loss of balsa was not observed to go to zero up to the maximum test temperature of 1100°C.

E-glass/viny-ester and pure vinyl-ester samples were examined in the ESEM to observe micro-structural changes in the material during decomposition. Pore formation was observed as early as 200°C in the resin samples, and pore growth was seen from 300-400°C prior to the loss of the image at 400°C. Pore formation was also observed in the composite samples, although it did not become obvious until 400°C. In the composite samples, the resin decomposition was observed to allow fibers to come loose from the composite entirely. Once heated to the final temperature, the composite sample exhibited a residual pore structure, primarily in the resin-rich regions between warp and weft fiber directions. The size of the pores in this structure depended most largely on the adjacent arrangement of the fibers, and a range of sizes for the sample used in this paper was found to be 20-200 μm. During cooling, the surface of the composite sample appeared to become highlighted. No cracking was observed in either sample.

Balsa wood samples were also observed in the ESEM. The virgin structure of the wood was made up of rows of hollow cylindrical cells aligned end-to-end in one direction, forming the grain. During heating, the grain cell walls began to erode at 200°C, resulting in the growth and coalescing of grain cells. Grain cell wall erosion continues in this manner until about 325°C, at which point the entire structure of the sample collapses on itself, resulting in massive shrinkage of the grain cells.

Permeability and porosity experiments gave insight into the gas transport properties of virgin, partially degraded, and fully degraded samples of each material. The permeability of E-glass/VE was initially zero, with no gas flow possible, and increased to a final value of 1.56E-10 m^2, in line with previous tests [30]. The porosity increased from approximately 0 to a final value

of 0.68, also in line with previous tests [30]. Balsa wood behaved very differently, with the permeability remaining near the virgin value of 1E-11 m^2 over the range of mass fractions that were tested. The porosity increased from a virgin value ranging from 0.18-0.34 to a final value of about 0.85.

Conclusions

Many conclusions were made based on this research. Some are general in nature, and others offer specific information on each material that was studied. The lists below give the conclusions that were made.

General

- The STA, a combination DSC/TGA, can be used to obtain quantitative specific heat capacity and gravimetric response data for describing decomposition of materials.
- Solid samples for DSC measurement should ideally be formed into thin discs that fully cover the base of the sample pan.
- Highly conductive metallic pans provide superior temperature sensitivity over alumina during DSC measurement.
- When finding specific heat by the sapphire ratio method, sapphire mass should be matched to that of the sample, and should cover as much of the sample pan base as possible.
- Porosity and permeability do not scale with just mass fraction decomposed for either material.
- X-ray CT was not able to capture microstructure of 36 mm diameter samples.

E-glass/Vinyl Ester

- E-glass/VE decomposition occurs in three stages as the sample temperature increases.
- The decomposition process of E-glass vinyl ester was measured using the DSC to be endothermic.
- The primary microscopic physical response during decomposition was pore formation. No cracks were observed in ESEM experiments, which were performed by uniformly heating samples in an inert atmosphere.
- Once heated to the final temperature, the composite sample exhibited a residual pore structure, primarily in the resin-rich regions between warp and weft fiber directions. The size of the pores in this structure depended most largely on the adjacent arrangement of the fibers. Char pore sizes ranged from 20-200 μm.
- During cooling, the surface of the composite sample appeared to become highlighted. This is attributed to charging, and no further microstructural changes were observed on cooling. No further changes were observed in the char structure on cooling.
- Cracking was observed in post-experimental microscopic inspection of a partially decomposed (F = 0.39) 36 mm diameter sample. This was potentially due to the sample being cooled from a partially decomposed state, or the larger scale relative to the ESEM samples.
- Open-cell porosity and permeability follow similar trends with normalized mass fraction. E-glass/VE becomes permeable when pores formed become interconnected. Porosity begins to rise rapidly at this point.
- Char structure appears to be established at a normalized mass fraction (F) of approximately 0.3. At this level, the change in permeability levels off, however porosity continues to increase.

Balsa Wood

- The decomposition of balsa wood is complex. It was measured to include a pre-decomposition mass loss associated with the evacuation of water (averaging about 2.9% of initial mass) from the sample followed by a multi-stage decomposition reaction resulting in loss of about 75% of the virgin mass (depending on the final temperature). Mass loss continued at a low rate up to the maximum test temperature of 1100°C.
- The decomposition of balsa wood was measured to include both endothermic and exothermic segments.
- Primary microscopic physical response during decomposition in uniformly heated samples in an inert atmosphere was degradation of grain cell walls.
- The primary gas transport mechanism through balsa wood along the grain at room temperature is through water transport vessels that extend through the thickness of the wood. Water transport vessels were measured to average 184 μm in diameter and at a frequency of 1.48 vessels/mm^2. Permeability did not vary over the mass fractions tested, indicating that the primary gas flow path is through water transport vessels. Gas flow through paths formed by grain cells becoming interconnected during decomposition appears to be negligible.
- Porosity rises significantly with mass fraction due to erosion of grain cell walls during decomposition.

Chapter 7 – Recommendations

While this research has made substantial progress over what was known before it was undertaken, there is still a great deal of work to be done. The following list outlines some of those points.

- STA methods should be developed to obtain separate values for sensible and latent heat of decomposing materials
- Further work should be conducted to examine the effects of sample cup material on DSC results
- A series of intermediate-scale E-glass/vinyl ester samples should be oxidized in the ISTGA and the TGA to obtain a distribution for the final mass fraction obtained with each instrument.
- Effects of density on porosity and permeability of balsa wood should be studied, at least over the range at which Baltek supplies panels (90-250 kg/m^3).
- Further analysis should be done on the ESEM images that were generated perpendicular to the balsa wood grain
- X-ray CT scans should be conducted on smaller samples of both materials in order to obtain three-dimensional models of the microstructure of each material.
- Further attempts should be made to obtain data on the permeability and porosity of decomposed balsa wood past a normalized mass fraction of 0.56.
- ESEM work remains to examine the small (~3 μm diameter) pores in the cell walls of balsa wood. Nothing is known on the behavior of these pores during heating. It would be most beneficial to attempt to cut a section of cell wall and heat it.
- More ESEM work should be done on balsa wood to study the behavior of the water transport vessels during heating. None were visible in the section examined on the heated sample, and so their behavior during heating remains unknown.
- ESEM experiments should be conducted in which samples are partially decomposed and cooled to see if cracks occur.
- A DSC sample holder could be constructed to go inside of the ISTGA, thereby allowing for intermediate-scale DSC experiments to be conducted. However, better heat transfer from the furnace heating elements into the sample would be required to make this practical. Heating rates higher than 10°C/min would likely be impossible, as the balance reading is affected by heating rates above that. Higher heating rates also shorten the life of the furnace. It is also noteworthy that the ISTGA is designed for samples a great deal larger than the maximum size of sapphire stipulated in ASTM E-1269 (100 mg).
- Permeability should be tested perpendicular to the grain in balsa wood.
- Permeability and porosity tests could be attempted at high temperature on both materials, but better sealing methods (higher temperature o-rings) will be required to accomplish this.
- Additional ESEM tests should be conducted on materials that have been heated non-uniformly, to check the effect of the heating type against the decomposition mechanisms.
- Additional permeability tests could be conducted on E-glass/vinyl ester to obtain additional data between F values of 0.97 and 0.64, which in this work are essentially considered impermeable and permeable, respectively.

- The porosity and permeability data should be used to develop models for gas flow through charred material.
- Models for porosity should be developed based on porosity results and ESEM observations.
- Porosity experiments should be run with multiple gases in order to verify that there are no gas adsorption effects on charred samples.

References

1. ASTM Standard E1269, 2005, "Standard Test Method for Determining Specific Heat Capacity by Differential Scanning Calorimetry," ASTM International, West Conshohocken, PA, 2007, DOI: 10.1520/E1269-05, www.astm.org
2. ASTM Standard E1641, 2007, "Standard Test Method for Decomposition Kinetics by Thermogravimetry," ASTM International, West Conshohocken, PA, 2007, DOI: 10.1520/E1641-07, www.astm.org
3. He, Fang, Weiming Yi, and Xueyuan Bai. "Investigation on caloric requirement of biomass pyrolysis using TG–DSC analyzer." *Energy Conversion and Management* 47 (2006): 2461-469.
4. Birol, Yucil. "The effect of sample preparation on the DSC analysis of 6061 alloy." *Journal of Materials Science* 40 (2005): 6357-361. La
5. Birol, Yucil. "DSC Analysis of the Precipitation Reactions in the Alloy AA6082 Effect of sample preparation." *Journal of Thermal Analysis and Calorimetry* 83.1 (2006): 219-22.
6. Garcia Cordovilla, C., and E. Louis. "Preparation of Samples of Heat Treatable Aluminum Alloys for Differential Scanning Calorimetry: Punching versus Spark Cutting." *Scripta Metallurgica* 18 (1984): 291-94. Print.
7. Starink, M.J., A.J. Hobson, and P.J. Gregson. "DSC Sample Preparation for Al-Based Alloys." *Scripta Meterialia* 34.11 (1996): 1711-716.
8. Stoliarov, Stanislav I., and Richard N. Walters. "Determination of the heats of gasification of polymers using differential scanning calorimetry." *Polymer Degradation and Stability* 93 (2008): 422-27.
9. Wolfinger MG, Rath J, Krammer G, et al. “Influence of the emissivity of the sample on the differential scanning calorimetry measurements” *Thermchimica* 2001;372:11–8.
10. Henderson, J.B., M.R. Tant, G.R. Moore, and J.A. Wiebelt. "Method for the Determination of the Specific Heat and Heat of Decomposition of Composite Materials." *Thermochimica Acta* 57 (1982): 161-71.
11. Mouritz, A.P. and Mathys, Z., 2001, *Composite Science and Technology,* Vol. 61, pp.475-490.
12. Chang, C.I., 1986, *Theoretical and Applied Fracture Mechanics 6*, pp.113-120.
13. Shanmuganathan, Kadhiravan, Sarang Deodhar, Nicholas Dembsey, Qinguo Fan, Paul D. Calvert, Steven B. Warner, and Prabir K. Patra. "Flame Retardancy and Char Microstructure of Nylon-6/Layered Silicate Nanocomposites." *Wiley Interscience* (2006). *Wiley Interscience*. 13 Aug. 2006.
14. Hanu, L.G., G.P. Simon, J. Mansouri, R.P. Burford, and Y.B. Cheng. "Development of polymer-ceramic composites for improved fire resistance." *Journal of Materials Processing Technology* 153-154 (2004): 401-07.

15. Boscoletto, A.B., M. Checchin, M. Tavan, G. Camino, L. Costa, and M.P. Luda. "Combustion and fire retardance of poly(2,6-dimethyl-1,4-phenylene ether)-high-impact polystyrene blends. I. Morphological aspects." *Journal of applied polymer science* 53.1 (1994): 121.

16. Hossenlopp, J., 2009, *Layered Double Hydroxide Polymer Nanocomposites Flammability*, NIST Annual Fire Conference.

17. Grunlan, J., 2009, *Layer-by-Layer Preparation of Nanocomposite Coatings*, NIST Annual Fire Conference.

18. Darvennes, Corinne, Lance Lowe, and Christopher Wilson. "Porosity determination in thin graphite-epoxy composite laminates using histograms of ultrasonic c-scans." *Proceedings of SPIE, the international society for optical engineering* 5393.1 (2004): 194.

19. Prokop, Josef. "E: Porosity measurement method by X-ray computed tomography." *Key engineering materials* 409 (2009): 402.

20. Birt, E.A., and R.A. Smith. "A review of NDE methods for porosity measurement in fiber-reinforced polymer composites." *Insight (Northampton)* 46.11 (2004): 681.

21. Connolly "The Measurement of Porosity in Composite Materials Using Infrared Thermography" *Journal of Reinforced Plastics and Composites.*1992; 11: 1367-1375

22. S. Gray, S. Ganchev, N. Qaddoumi, G. Beauregard, D. Radford, and R. Zoughi, 'Porosity level estimation in polymer composites using microwaves,' *Mat. Eval. 51,* No 3, pp 404-408. 1995.

23. Dehl, R.E. "On the characterization of porosity in PTFE-carbon composite implant materials by mercury porosimetry." *Journal of biomedical materials research* 18.5 (1982): 715.

24. Leclaire, P., O. Umnova, K.V. Horoshenkov, and L. Maillet. "Porosity measurement by comparison of air volumes." *Review of Scientific Instruments* 74.3 (2003): 1366-1370.

25. Beranek, Leo L. "Acoustic impedance of porous materials." *The Journal of the Acoustical Society of America* 13 (1942): 248.

26. H. Darcy. *Les Fontaines Publiques de la Ville de Dijon*, Delmont, Paris (1856).

27. Morse, Bolt, and Brown, Paper No. 31, Twenty-Fourth Meeting of the A.S.A., Chicago, Illinois, November, 1940

28. Hino, T., E. Hayashishita, A. Kohyama, Y. Yamauchi, and Y. Hirohata. "Helium gas permeability of SiC/SiC composite after heat cycles." *Journal of Nuclear Materials* 367-370 (2007): 736-41.

29. Wiecek, Thomas E. *A Study of the High Temperature Thermal Response of Decomposing and Expanding Polymer Composites*. Thesis. University of Rhode Island, 1986.

30. Golestanian, Hossain. "Preform permeability variation with porosity of FRP and carbon mats." *Journal of Materials Science* 43.20 (2008): 6676-681.

31. Zeng, Zhengwen, and Reid Grigg. "A Criterion for Non-Darcy Flow in Porous Media." *Transport in Porous Media* 63 (2006): 57-69.

32. S. Feih, A.P. Mouritz and Z. Mathys, “Milestone 10 report, *Develop and validate a thermal-mechanical model for predicting the change in compressive mechanical response of composite sandwich materials during fire exposure*, Cooperative Research Centre for Advanced Composite Structures, Melbourne, TM06084, September 2006.

33. Di Blasi, Columba. "Modeling chemical and physical processes of wood and biomass pyrolysis." *Science Direct* (2007). 23 Apr. 2007.

34. Schaffer, E. L., “Effect of pyrolytic temperatures on the longitudinal strength of dry Douglas-Fir”, *Journal of Testing and Evaluation*, JTEVA, Vol. 1, No. 4, 1973, pp. 319-322.

35. "MatWeb - The Online Materials Information Resource." *Aluminum 5083-H116; 5083-H321*. Web. 18 Oct. 2009. <http://www.matweb.com/search/DataSheet.aspx?MatGUID=1efe7441a72f4a22a53c0dc1bd9c87ec&ckck=1>

36. "MatWeb - The Online Materials Information Resource." *MatWeb - Corning Macor® Machinable Glass Ceramic*. Web. 18 Oct. 2009. http://www.matweb.com/search/DataSheet.aspx?MatGUID=848bdecf89b74ef986925162e6a6255e

37. "MACOR." *Wikipedia, the free encyclopedia*. Web. 18 Oct. 2009. http://en.wikipedia.org/wiki/MACOR

38. Lattimer, B.Y. and Ouellette, J., "Properties of Composite Materials for Thermal Analysis involving Fires," *Composites Part A*, 37 (7), pp. 1068-1081, 2006.

Appendices

Appendix A: Relevant Calculations

Porosity Error

The error for porosity is calculated in multiple steps. First, the error from pressure measurement is calculated based on Equation 8:

$$E_{\Delta P} = \sqrt{\left(P_2 E_P\right)^2 + \left(P_{vac} E_P\right)^2} \qquad \text{Equation 12}$$

Then, the error from the gas volume is determined by combining the pressure, temperature, and mass measurement errors along with the appropriate derivatives of ideal gas law:

$$E_{V_{gas}} = \sqrt{\left(\frac{RT}{M\Delta P} E_m\right)^2 + \left(\frac{mR}{M\Delta P} E_T\right)^2 + \left(-\frac{mRT}{M\Delta P^2} E_{\Delta P}\right)^2} \qquad \text{Equation 13}$$

Next, the error in the volume measurement using calipers is determined:

$$E_{V_{sample}^{calipers}} = \sqrt{\left(\frac{\pi D^2}{4} E_{caliper}\right)^2 + \left(\pi D t E_{caliper}\right)^2} \qquad \text{Equation 14}$$

Next, the total gas sample measurement error (sample + baseline runs) is combined:

$$E_{V_{sample}^{gas}} = \sqrt{\left(V_{empty} E_{V_{gas}}\right)^2 + \left(V_{sample} E_{V_{gas}}\right)^2} \qquad \text{Equation 15}$$

Lastly, the porosity error is determined by combining the caliper error with the total gas sample measurement error:

$$E_{\phi} = \sqrt{\left(-\frac{1}{V_{calipers}} E_{V_{gv}}\right)^2 + \left(\frac{V_{gv}}{V_{calipers}^2} E_{V_{cv}}\right)^2} \qquad \text{Equation 16}$$

Appendix B: Porosity & Permeability Test Data

E-Glass/Vinyl Ester

Normalized Mass Fraction (F) = 1 (Virgin)

VIRGIN				
POROSITY				
	Baseline Gas Mass Flow:		Sample Gas Mass Flow:	
Sample	Empty	Empty	Eglass	Eglass
Temp (C)	19	19	19	19
Initial Pressure (psia)	1.24	1.25	1.24	1.245
Final Pressure (psia)	54.11	54.11	54.11	54.11
Initial pressure (Pa)	8549	8618	8549	8584
Final Pressure (Pa)	373100	373100	373100	373100
SCC	133.2	132.1	112.3	112.4
SL	0.1332	0.1321	0.1123	0.1124
Gas Density (g/L)	1.1453	1.1453	1.1453	1.1453
Gas Mass (g)	0.1526	0.1513	0.1286	0.1287
Volume (m^3)	3.63E-05	3.60E-05	3.06E-05	3.06E-05
Volume (cm^3)	36.28	35.99	30.59	30.62
Volume Change (cm^3)	0	0.2928	5.693	5.662
Pressure Error (Pa)	7801	7801	7801	7801
Mass Error (g)	0.001908	0.001898	0.001716	0.001717
Temp Error (C)	1.5	1.5	1.5	1.5
Volume Error (m^3)	9.18E-07	9.12E-07	7.87E-07	7.88E-07
Percent	0.025	0.025	0.026	0.026
Sample Calcs				
Mass	11.139			
Initial Mass	11.139			
Mass Fraction	1			
Diameter (in)	1.398			
Thickness(in)	0.241			
Volume (in^3)	0.37	Volume Error (in^3):	0.0021	
Volume (cm^3)	6.06	Volume Error (cm^3):	0.03	
Gas Volume (cm^3)	5.53	Gas Volume Error: (cm^3):	1.21	
Porosity	0.09	Total Error (dim):	0.199	

Normalized Mass Fraction (F) = 1 (Virgin)

Permeability				
Pressure (Psi)	MFC (SCCM)	MFM (SCCM)	Permeability (m^2)	
2.74	0	0	0	
5.82	0	0	0	
9.89	0	0	0	
15.89	0	0	0	
21.85	0	0	0	
30.5	0	0	0	
40.76	0	0	0	
49.89	0	0	0	

Normalized Mass Fraction (F) = 0.97

VIRGIN				
POROSITY				
	Baseline Gas Mass Flow:		Sample Gas Mass Flow:	
Sample	Empty	Empty	Eglass	Eglass
Temp (C)	19	19	19	19
Initial Pressure (psia)	1.24	1.25	1.245	1.23
Final Pressure (psia)	54.11	54.11	54.11	54.11
Initial pressure (Pa)	8549	8618	8584	8481
Final Pressure (Pa)	373100	373100	373100	373100
SCC	133.2	132.1	112.8	112.4
SL	0.1332	0.1321	0.1128	0.1124
Gas Density (g/L)	1.1453	1.1453	1.1453	1.1453
Gas Mass (g)	0.1526	0.1513	0.1292	0.1287
Volume (m^3)	3.63E-05	3.60E-05	3.07E-05	3.06E-05
Volume (cm^3)	36.28	35.99	30.73	30.61
Volume Change (cm^3)	0	0.2928	5.553	5.671
Pressure Error (Pa)	7801	7801	7801	7801
Mass Error (g)	0.001908	0.001898	0.001721	0.001717
Temp Error (C)	1.5	1.5	1.5	1.5
Volume Error (m^3)	9.18E-07	9.12E-07	7.90E-07	7.88E-07
Percent	0.025	0.025	0.026	0.026
Sample Calcs				
Mass	11.008			
Initial Mass	11.008			
Mass Fraction	1			
Diameter (in)	1.4			
Thickness(in)	0.24			
Volume (in^3)	0.37	Volume Error (in^3):	0.0021	
Volume (cm^3)	6.05	Volume Error (cm^3):	0.03	
Gas Volume (cm^3)	5.47	Gas Volume Error: (cm^3):	1.21	
Porosity	0.1	Porosity Error (dim)	0.2	

Normalized Mass Fraction (F) = 0.97

DECOMPOSED				
POROSITY				
	Baseline Gas Mass Flow:		Sample Gas Mass Flow:	
Sample	Empty	Empty	Eglass	Eglass
Temp ©	19	19	19	19
Initial Pressure (psia)	1.25	1.25	1.24	1.24
Final Pressure (psia)	54.11	54.11	54.11	54.11
Initial pressure (Pa)	8618	8618	8549	8549
Final Pressure (Pa)	373100	373100	373100	373100
SCC	133.5	134.8	113.5	114.2
SL	0.1335	0.1348	0.1135	0.1142
Gas Density (g/L)	1.1453	1.1453	1.1453	1.1453
Gas Mass (g)	0.1529	0.1544	0.13	0.1308
Volume (m^3)	3.64E-05	3.67E-05	3.09E-05	3.11E-05
Volume (cm^3)	36.37	36.72	30.91	31.1
Volume Change (cm^3)	0	-36.72	-30.91	-31.1
Pressure Error (Pa)	7801	7801	7801	7801
Mass Error (g)	0.00191	0.001922	0.001727	0.001734
Temp Error (C)	1.5	1.5	1.5	1.5
Volume Error (m^3)	9.20E-07	9.29E-07	7.95E-07	7.99E-07
Percent	0.025	0.025	0.026	0.026
Sample Calcs				
Mass	10.923			
Initial Mass	11.008			
Heated Temp ©	325			
Mass Fraction	0.99			
Est. MFD	0.97			
Diameter (in)	1.4			
Thickness(in)	0.24			
Volume (in^3)	0.37	Volume Error (in^3):	0.0021	
Volume (cm^3)	6.05	Volume Error (cm^3):	0.03	
Gas Volume (cm^3)	5.54	Gas Volume Error: (cm^3):	1.22	
Porosity	0.09	Total Error (dim)	0.202	

Normalized Mass Fraction (F) = 0.97

PERMEABILITY				
Pressure (Psi)	MFC (SCCM)	MFM (SCCM)	Permeability (m^2)	
2.09	0	0	0	
5.05	0	0	0	
9.93	0	0	0	
16.74	0	0	0	
20.76	0	0	0	
30.14	0	0	0	
40.08	0	0	0	
49.97	0	0	0	

Normalized Mass Fraction (F) = 0.64

VIRGIN				
POROSITY				
		Baseline Gas Mass Flow:		Sample Gas Mass Flow:
Sample	Empty	Empty	Eglass	Eglass
Temp (C)	19	19	19	19
Initial Pressure (psia)	1.25	1.25	1.24	1.23
Final Pressure (psia)	54.11	54.11	54.13	54.11
Initial pressure (Pa)	8618	8618	8549	8481
Final Pressure (Pa)	373100	373100	373200	373100
SCC	133.5	134.8	113.2	113.8
SL	0.1335	0.1348	0.1132	0.1138
Gas Density (g/L)	1.1453	1.1453	1.1453	1.1453
Gas Mass (g)	0.1529	0.1544	0.1296	0.1303
Volume (m^3)	3.64E-05	3.67E-05	3.08E-05	3.10E-05
Volume (cm^3)	36.37	36.72	30.82	30.99
Volume Change (cm^3)	0	-0.3542	5.548	5.378
Pressure Error (Pa)	7801	7801	7801	7801
Mass Error (g)	0.00191	0.001922	0.001724	0.00173
Temp Error (C)	1.5	1.5	1.5	1.5
Volume Error (m^3)	9.20E-07	9.29E-07	7.92E-07	7.96E-07
Percent	0.025	0.025	0.026	0.026
Sample Calcs				
Mass	11.072			
Initial Mass	11.072			
Mass Fraction	1			
Diameter (in)	1.4			
Thickness(in)	0.24			
Volume (in^3)	0.37	Volume Error (in^3):	0.0021	
Volume (cm^3)	6.05	Volume Error (cm^3):	0.03	
Gas Volume (cm^3)	5.64	Gas Volume Error: (cm^3):	1.22	
Porosity	0.07	Porosity Error (dim)	0.201	

Normalized Mass Fraction (F) = 0.64

DECOMPOSED				
POROSITY				
	Baseline Gas Mass Flow:		Sample Gas Mass Flow:	
Sample	Empty	Empty	Eglass	Eglass
Temp ©	16	16	16	16
Initial Pressure (psia)	1.25	1.25	1.26	1.26
Final Pressure (psia)	54.12	54.12	54.11	54.12
Initial pressure (Pa)	8618	8618	8687	8687
Final Pressure (Pa)	373100	373100	373100	373100
SCC	134.5	135.1	115	115.2
SL	0.1345	0.1351	0.115	0.1152
Gas Density (g/L)	1.1453	1.1453	1.1453	1.1453
Gas Mass (g)	0.154	0.1547	0.1317	0.1319
Volume (m^3)	3.63E-05	3.64E-05	3.10E-05	3.11E-05
Volume (cm^3)	36.26	36.42	31.01	31.06
Volume Change (cm^3)	0	-36.42	-31.01	-31.06
Pressure Error (Pa)	7801	7801	7801	7801
Mass Error (g)	0.00192	0.001925	0.001741	0.001743
Temp Error (C)	1.5	1.5	1.5	1.5
Volume Error (m^3)	9.17E-07	9.21E-07	7.97E-07	7.98E-07
Percent	0.025	0.025	0.026	0.026
Sample Calcs				
Mass	10.077			
Initial Mass	11.072			
Heated Temp ©	400			
Mass Fraction	0.91			
Est. MFD	0.64			
Diameter (in)	1.4			
Thickness(in)	0.255			
Volume (in^3)	0.39	Volume Error (in^3):	0.0021	
Volume (cm^3)	6.43	Volume Error (cm^3):	0.03	
Gas Volume (cm^3)	5.3	Gas Volume Error: (cm^3):	1.22	
Porosity	0.18	Total Error (dim)	0.189	

Normalized Mass Fraction (F) = 0.64

PERMEABILITY				
Mass Flow (SCCM)	Pressure (Psi)	Permeability (m^2)	Total Error (m^2)	Total Error Percent
9.8	9.79	5.44E-16	5.21E-17	9.57
19.8	17	6.33E-16	3.50E-17	5.52
29.8	22.27	7.28E-16	3.06E-17	4.2
39.8	27.57	7.85E-16	2.75E-17	3.5
49.8	31.8	8.52E-16	2.63E-17	3.09
59.6	36	9.00E-16	2.53E-17	2.81
69.7	39.69	9.55E-16	2.49E-17	2.61
79.7	43.26	1.00E-15	2.46E-17	2.46
89.7	46.57	1.05E-15	2.45E-17	2.33

Normalized Mass Fraction (F) = 0.39

VIRGIN				
POROSITY				
	Baseline Gas Mass Flow:		Sample Gas Mass Flow:	
Sample	Empty	Empty	Eglass	Eglass
Temp (C)	16	16	16	16
Initial Pressure (psia)	1.25	1.25	1.25	1.255
Final Pressure (psia)	54.12	54.12	54.11	54.12
Initial pressure (Pa)	8618	8618	8618	8653
Final Pressure (Pa)	373100	373100	373100	373100
SCC	134.5	135.1	113.2	114.2
SL	0.1345	0.1351	0.1132	0.1142
Gas Density (g/L)	1.1453	1.1453	1.1453	1.1453
Gas Mass (g)	0.154	0.1547	0.1296	0.1308
Volume (m^3)	3.63E-05	3.64E-05	3.05E-05	3.08E-05
Volume (cm^3)	36.26	36.42	30.52	30.79
Volume Change (cm^3)	0	-0.1617	5.736	5.469
Pressure Error (Pa)	7801	7801	7801	7801
Mass Error (g)	0.00192	0.001925	0.001724	0.001734
Temp Error (C)	1.5	1.5	1.5	1.5
Volume Error (m^3)	9.17E-07	9.21E-07	7.85E-07	7.91E-07
Percent	0.025	0.025	0.026	0.026
Sample Calcs				
Mass	10.983			
Initial Mass	10.983			
Mass Fraction	1			
Diameter (in)	1.4			
Thickness(in)	0.233			
Volume (in^3)	0.36	Volume Error (in^3):	0.0021	
Volume (cm^3)	5.88	Volume Error (cm^3):	0.03	
Gas Volume (cm^3)	5.68	Gas Volume Error: (cm^3):	1.21	
Porosity	0.03	Porosity Error (dim)	0.206	

Normalized Mass Fraction (F) = 0.39

DECOMPOSED				
POROSITY				
	Baseline Gas Mass Flow:		Sample Gas Mass Flow:	
Sample	Empty	Empty	Eglass	Eglass
Temp ©	19	19	19	19
Initial Pressure (psia)	1.19	1.18	1.19	1.19
Final Pressure (psia)	54.12	54.12	54.12	54.11
Initial pressure (Pa)	8205	8136	8205	8205
Final Pressure (Pa)	373100	373100	373100	373100
SCC	133.6	133.4	116.2	116.3
SL	0.1336	0.1334	0.1162	0.1163
Gas Density (g/L)	1.1453	1.1453	1.1453	1.1453
Gas Mass (g)	0.153	0.1528	0.1331	0.1332
Volume (m^3)	3.63E-05	3.63E-05	3.16E-05	3.16E-05
Volume (cm^3)	36.35	36.29	31.61	31.65
Volume Change (cm^3)	0	-36.29	-31.61	-31.65
Pressure Error (Pa)	7801	7801	7801	7801
Mass Error (g)	0.001911	0.001909	0.001752	0.001753
Temp Error (C)	1.5	1.5	1.5	1.5
Volume Error (m^3)	9.19E-07	9.17E-07	8.10E-07	8.11E-07
Percent	0.025	0.025	0.026	0.026
Sample Calcs				
Mass	9.321			
Initial Mass	10.983			
Heated Temp ©	408			
Mass Fraction	0.85			
Est. MFD	0.39			
Diameter (in)	1.4			
Thickness(in)	0.269			
Volume (in^3)	0.41	Volume Error (in^3):	0.0021	
Volume (cm^3)	6.79	Volume Error (cm^3):	0.03	
Gas Volume (cm^3)	4.69	Gas Volume Error: (cm^3):	1.22	
Porosity	0.31	Total Error (dim)	0.181	

Normalized Mass Fraction (F) = 0.39

PERMEABILITY				
Mass Flow (SCCM)	Pressure (Psi)	Permeability (m^2)	Total Error (m^2)	Total Error Percent
4.9	0.66	4.26E-15	2.05E-15	48.16
9.8	1.24	4.53E-15	1.17E-15	25.79
19.9	2.4	4.76E-15	6.53E-16	13.73
29.9	3.46	4.96E-15	4.85E-16	9.78
39.8	4.52	5.05E-15	3.90E-16	7.72
49.9	5.5	5.21E-15	3.39E-16	6.51
59.8	6.41	5.35E-15	3.06E-16	5.72
69.8	7.28	5.50E-15	2.83E-16	5.15
79.8	8.13	5.63E-15	2.65E-16	4.71
89.8	9.01	5.72E-15	2.49E-16	4.35
99.8	9.86	5.81E-15	2.36E-16	4.06
149.7	13.85	6.20E-15	1.98E-16	3.19
200	17.43	6.58E-15	1.81E-16	2.74
248.5	20.64	6.91E-15	1.71E-16	2.48

Normalized Mass Fraction (F) = 0.26

VIRGIN				
POROSITY				
	Baseline Gas Mass Flow:		Sample Gas Mass Flow:	
Sample	Empty	Empty	Eglass	Eglass
Temp (C)	19	19	19	19
Initial Pressure (psia)	1.21	1.205	1.2	1.21
Final Pressure (psia)	54.61	54.6	54.62	54.61
Initial pressure (Pa)	8343	8308	8274	8343
Final Pressure (Pa)	376500	376500	376600	376500
SCC	134.4	133.2	114.3	114.3
SL	0.1344	0.1332	0.1143	0.1143
Gas Density (g/L)	1.1453	1.1453	1.1453	1.1453
Gas Mass (g)	0.1539	0.1526	0.1309	0.1309
Volume (m^3)	3.62E-05	3.59E-05	3.08E-05	3.08E-05
Volume (cm^3)	36.24	35.92	30.81	30.82
Volume Change (cm^3)	0	0.3202	5.432	5.42
Pressure Error (Pa)	7801	7801	7801	7801
Mass Error (g)	0.001919	0.001908	0.001734	0.001734
Temp Error (C)	1.5	1.5	1.5	1.5
Volume Error (m^3)	9.10E-07	9.03E-07	7.86E-07	7.86E-07
Percent	0.025	0.025	0.026	0.026
Sample Calcs				
Mass	11.062			
Initial Mass	11.062			
Mass Fraction	1			
Diameter (in)	1.4			
Thickness(in)	0.233			
Volume (in^3)	0.36	Volume Error (in^3):	0.0021	
Volume (cm^3)	5.88	Volume Error (cm^3):	0.03	
Gas Volume (cm^3)	5.27	Gas Volume Error: (cm^3):	1.2	
Porosity	0.1	Porosity Error (dim)	0.204	

Normalized Mass Fraction (F) = 0.26

DECOMPOSED				
POROSITY				
	Baseline Gas Mass Flow:		Sample Gas Mass Flow:	
Sample	Empty	Empty	Eglass	Eglass
Temp ©	19	19	19	19
Initial Pressure (psia)	1.21	1.22	1.21	1.21
Final Pressure (psia)	54.6	54.61	54.62	54.6
Initial pressure (Pa)	8343	8412	8343	8343
Final Pressure (Pa)	376500	376500	376600	376500
SCC	134.3	134.5	119.2	120.2
SL	0.1343	0.1345	0.1192	0.1202
Gas Density (g/L)	1.1453	1.1453	1.1453	1.1453
Gas Mass (g)	0.1538	0.154	0.1365	0.1377
Volume (m^3)	3.62E-05	3.63E-05	3.21E-05	3.24E-05
Volume (cm^3)	36.22	36.28	32.14	32.42
Volume Change (cm^3)	0	-36.28	-32.14	-32.42
Pressure Error (Pa)	7801	7801	7801	7801
Mass Error (g)	0.001918	0.00192	0.001779	0.001789
Temp Error (C)	1.5	1.5	1.5	1.5
Volume Error (m^3)	9.10E-07	9.11E-07	8.16E-07	8.23E-07
Percent	0.025	0.025	0.025	0.025
Sample Calcs				
Mass	9.026			
Initial Mass	11.062			
Heated Temp ©	432			
Mass Fraction	0.82			
Est. MFD	0.26			
Diameter (in)	1.4			
Thickness(in)	0.335			
Volume (in^3)	0.52	Volume Error (in^3):	0.0023	
Volume (cm^3)	8.45	Volume Error (cm^3):	0.04	
Gas Volume (cm^3)	3.97	Gas Volume Error: (cm^3):	1.22	
Porosity	0.53	Total Error (dim)	0.145	

Normalized Mass Fraction (F) = 0.26

PERMEABILITY				
Mass Flow (SCCM)	Pressure (Psi)	Permeability (m^2)	Total Error (m^2)	Total Error Percent
9.9	0.00011	6.43E-11	1.84E-10	286.59
19.9	0.00022	6.46E-11	9.29E-11	143.73
29.9	0.00033	6.47E-11	6.22E-11	96.12
39.9	0.00044	6.48E-11	4.69E-11	72.31
49.8	0.00055	6.47E-11	3.75E-11	58.03
59.8	0.00066	6.47E-11	3.14E-11	48.51
69.8	0.000765	6.52E-11	2.74E-11	41.97
79.8	0.00087	6.55E-11	2.43E-11	37.01
89.8	0.000985	6.51E-11	2.14E-11	32.79
99.8	0.001095	6.51E-11	1.93E-11	29.59
149.8	0.00166	6.45E-11	1.28E-11	19.83
199.8	0.00224	6.37E-11	9.51E-12	14.93
249.8	0.00284	6.28E-11	7.52E-12	11.97
299.5	0.00345	6.20E-11	6.21E-12	10.01

Normalized Mass Fraction (F) = 0.18

VIRGIN				
POROSITY				
	Baseline Gas Mass Flow:		Sample Gas Mass Flow:	
Sample	Empty	Empty	Eglass	Eglass
Temp (C)	19	19	19	19
Initial Pressure (psia)	1.22	1.23	1.23	1.22
Final Pressure (psia)	54.59	54.61	54.61	54.61
Initial pressure (Pa)	8412	8481	8481	8412
Final Pressure (Pa)	376400	376500	376500	376500
SCC	128.2	128.9	109.6	109.3
SL	0.1282	0.1289	0.1096	0.1093
Gas Density (g/L)	1.1453	1.1453	1.1453	1.1453
Gas Mass (g)	0.1468	0.1476	0.1255	0.1252
Volume (m^3)	3.46E-05	3.48E-05	2.96E-05	2.95E-05
Volume (cm^3)	34.59	34.77	29.57	29.48
Volume Change (cm^3)	0	-0.1824	5.024	5.111
Pressure Error (Pa)	7801	7801	7801	7801
Mass Error (g)	0.001862	0.001868	0.001691	0.001689
Temp Error (C)	1.5	1.5	1.5	1.5
Volume Error (m^3)	8.73E-07	8.77E-07	7.58E-07	7.56E-07
Percent	0.025	0.025	0.026	0.026
Sample Calcs				
Mass	10.987			
Initial Mass	10.987			
Mass Fraction	1			
Diameter (in)	1.4			
Thickness(in)	0.233			
Volume (in^3)	0.36	Volume Error (in^3):	0.0021	
Volume (cm^3)	5.88	Volume Error (cm^3):	0.03	
Gas Volume (cm^3)	5.16	Gas Volume Error: (cm^3):	1.16	
Porosity	0.12	Porosity Error (dim)	0.197	

Normalized Mass Fraction (F) = 0.18

DECOMPOSED				
POROSITY				
	Baseline Gas Mass Flow:		Sample Gas Mass Flow:	
Sample	Empty	Empty	Eglass	Eglass
Temp ©	19	19	19	19
Initial Pressure (psia)	1.21	1.22	1.21	1.23
Final Pressure (psia)	54.6	54.61	54.61	54.62
Initial pressure (Pa)	8343	8412	8343	8481
Final Pressure (Pa)	376500	376500	376500	376600
SCC	134.3	134.5	122	120.5
SL	0.1343	0.1345	0.122	0.1205
Gas Density (g/L)	1.1453	1.1453	1.1453	1.1453
Gas Mass (g)	0.1538	0.154	0.1397	0.138
Volume (m^3)	3.62E-05	3.63E-05	3.29E-05	3.25E-05
Volume (cm^3)	36.22	36.28	32.9	32.5
Volume Change (cm^3)	0	-36.28	-32.9	-32.5
Pressure Error (Pa)	7801	7801	7801	7801
Mass Error (g)	0.001918	0.00192	0.001805	0.001791
Temp Error (C)	1.5	1.5	1.5	1.5
Volume Error (m^3)	9.10E-07	9.11E-07	8.34E-07	8.25E-07
Percent	0.025	0.025	0.025	0.025
Sample Calcs				
Mass	8.736			
Initial Mass	10.987			
Heated Temp ©	437			
Mass Fraction	0.8			
Est. MFD	0.18			
Diameter (in)	1.4			
Thickness(in)	0.364			
Volume (in^3)	0.56	Volume Error (in^3):	0.0023	
Volume (cm^3)	9.18	Volume Error (cm^3):	0.04	
Gas Volume (cm^3)	3.55	Gas Volume Error: (cm^3):	1.23	
Porosity	0.61	Total Error (dim)	0.134	

Normalized Mass Fraction (F) = 0.18

PERMEABILITY				
Mass Flow (SCCM)	Pressure (Psi)	Permeability (m^2)	Total Error (m^2)	Total Error Percent
9.9	0.00009	8.54E-11	2.74E-10	321.26
19.9	0.00019	8.13E-11	1.24E-10	152.71
29.9	0.00029	8.00E-11	8.03E-11	100.36
39.9	0.00039	7.94E-11	5.94E-11	74.84
49.8	0.000495	7.81E-11	4.62E-11	59.16
59.8	0.000585	7.94E-11	3.98E-11	50.17
69.8	0.000685	7.91E-11	3.40E-11	42.97
79.8	0.00078	7.94E-11	3.01E-11	37.83
89.8	0.00088	7.92E-11	2.66E-11	33.63
99.8	0.00098	7.91E-11	2.39E-11	30.28
149.8	0.00148	7.86E-11	1.60E-11	20.33
199.8	0.00199	7.79E-11	1.20E-11	15.33
249.8	0.00251	7.73E-11	9.53E-12	12.33
299.5	0.00303	7.67E-11	7.95E-12	10.36

Normalized Mass Fraction (F) = 0.10

VIRGIN				
POROSITY				
	Baseline Gas Mass Flow:		Sample Gas Mass Flow:	
Sample	Empty	Empty	Eglass	Eglass
Temp (C)	19	19	19	19
Initial Pressure (psia)	1.23	1.23	1.23	1.23
Final Pressure (psia)	54.63	54.64	54.63	54.64
Initial pressure (Pa)	8481	8481	8481	8481
Final Pressure (Pa)	376700	376700	376700	376700
SCC	136	134.9	114.3	113.8
SL	0.136	0.1349	0.1143	0.1138
Gas Density (g/L)	1.1453	1.1453	1.1453	1.1453
Gas Mass (g)	0.1558	0.1545	0.1309	0.1303
Volume (m^3)	3.67E-05	3.64E-05	3.08E-05	3.07E-05
Volume (cm^3)	36.68	36.37	30.82	30.68
Volume Change (cm^3)	0	0.3034	5.852	5.992
Pressure Error (Pa)	7801	7801	7801	7801
Mass Error (g)	0.001933	0.001923	0.001734	0.00173
Temp Error (C)	1.5	1.5	1.5	1.5
Volume Error (m^3)	5.16E-07	5.17E-07	4.23E-07	4.25E-07
Percent	0.014	0.014	0.014	0.014
Sample Calcs				
Mass	11.171			
Initial Mass	11.171			
Mass Fraction	1			
Diameter (in)	1.4			
Thickness(in)	0.24			
Volume (in^3)	0.37	Volume Error (in^3):	0.0021	
Volume (cm^3)	6.05	Volume Error (cm^3):	0.03	
Gas Volume (cm^3)	5.77	Gas Volume Error: (cm^3):	0.669	
Porosity	0.05	Porosity Error (dim)	0.111	

Normalized Mass Fraction (F) = 0.10

DECOMPOSED				
POROSITY				
	Baseline Gas Mass Flow:		Sample Gas Mass Flow:	
Sample	Empty	Empty	Eglass	Eglass
Temp ©	19	19	19	19
Initial Pressure (psia)	1.21	1.22	1.21	1.21
Final Pressure (psia)	54.6	54.61	54.61	54.63
Initial pressure (Pa)	8343	8412	8343	8343
Final Pressure (Pa)	376500	376500	376500	376700
SCC	134.3	134.5	120.8	122.4
SL	0.1343	0.1345	0.1208	0.1224
Gas Density (g/L)	1.1453	1.1453	1.1453	1.1453
Gas Mass (g)	0.1538	0.154	0.1384	0.1402
Volume (m^3)	3.62E-05	3.63E-05	3.26E-05	3.30E-05
Volume (cm^3)	36.22	36.28	32.58	33
Volume Change (cm^3)	0	-36.28	-32.58	-33
Pressure Error (Pa)	7801	7801	7801	7801
Mass Error (g)	0.001918	0.00192	0.001794	0.001809
Temp Error (C)	1.5	1.5	1.5	1.5
Volume Error (m^3)	9.10E-07	9.11E-07	8.26E-07	8.36E-07
Percent	0.025	0.025	0.025	0.025
Sample Calcs				
Mass	8.711			
Initial Mass	11.171			
Heated Temp ©	435			
Mass Fraction	0.78			
Est. MFD	0.12			
Diameter (in)	1.4			
Thickness(in)	0.36			
Volume (in^3)	0.55	Volume Error (in^3):	0.0023	
Volume (cm^3)	9.08	Volume Error (cm^3):	0.04	
Gas Volume (cm^3)	3.46	Gas Volume Error: (cm^3):	1.23	
Porosity	0.62	Total Error (dim)	0.136	

Normalized Mass Fraction (F) = 0.10

PERMEABILITY				
Mass Flow (SCCM)	Pressure (Psi)	Permeability (m^2)	Total Error (m^2)	Total Error Percent
9.9	0.000041	1.85E-10	1.24E-09	666.67
19.9	0.0001	1.53E-10	4.19E-10	274.19
29.9	0.00016	1.43E-10	2.46E-10	171.77
39.9	0.00022	1.39E-10	1.74E-10	125.18
49.8	0.00028	1.37E-10	1.35E-10	98.55
59.8	0.00034	1.35E-10	1.10E-10	81.31
69.8	0.00039	1.37E-10	9.75E-11	70.99
79.8	0.00045	1.36E-10	8.39E-11	61.64
89.8	0.00051	1.35E-10	7.37E-11	54.49
99.8	0.00057	1.34E-10	6.57E-11	48.84
149.8	0.00087	1.32E-10	4.27E-11	32.29
199.8	0.00117	1.31E-10	3.18E-11	24.23
249.8	0.00149	1.29E-10	2.47E-11	19.21
299.5	0.00181	1.27E-10	2.03E-11	15.96

Normalized Mass Fraction (F) = 0 (fully decomposed)

VIRGIN				
POROSITY				
	Baseline Gas Mass Flow:		Sample Gas Mass Flow:	
Sample	Empty	Empty	Eglass	Eglass
Temp (C)	19	19	19	19
Initial Pressure (psia)	1.2	1.2	1.19	1.205
Final Pressure (psia)	54.16	54.13	54.11	54.13
Initial pressure (Pa)	8274	8274	8205	8308
Final Pressure (Pa)	373400	373200	373100	373200
SCC	133.1	132.2	113.3	113.5
SL	0.1331	0.1322	0.1133	0.1135
Gas Density (g/L)	1.1453	1.1453	1.1453	1.1453
Gas Mass (g)	0.1524	0.1514	0.1298	0.13
Volume (m^3)	3.62E-05	3.60E-05	3.08E-05	3.09E-05
Volume (cm^3)	36.19	35.97	30.83	30.88
Volume Change (cm^3)	0	0.2243	5.361	5.309
Pressure Error (Pa)	7801	7801	7801	7801
Mass Error (g)	0.001907	0.001898	0.001725	0.001727
Temp Error (C)	1.5	1.5	1.5	1.5
Volume Error (m^3)	5.16E-07	5.17E-07	4.23E-07	4.25E-07
Percent	0.014	0.014	0.014	0.014
Sample Calcs				
Mass	11.006			
Initial Mass	11.006			
Mass Fraction	0.247			
Diameter (in)	1.398			
Thickness(in)	0.24			
Volume (in^3)	0.37	Volume Error (in^3):	0.0021	
Volume (cm^3)	6.04	Volume Error (cm^3):	0.03	
Gas Volume (cm^3)	5.22	Gas Volume Error: (cm^3):	0.669	
Porosity	0.13	Porosity Error (dim)	0.111	

Normalized Mass Fraction (F) = 0 (fully decomposed)

DECOMPOSED				
POROSITY				
	Baseline Gas Mass Flow:		Sample Gas Mass Flow:	
Sample	Empty	Empty	Eglass	Eglass
Temp ©	19	19	19	19
Initial Pressure (psia)	1.24	1.23	1.23	1.24
Final Pressure (psia)	54.11	54.12	54.12	54.11
Initial pressure (Pa)	8549	8481	8481	8549
Final Pressure (Pa)	373100	373100	373100	373100
SCC	132.8	132.8	121.9	123.2
SL	0.1328	0.1328	0.1219	0.1232
Gas Density (g/L)	1.1453	1.1453	1.1453	1.1453
Gas Mass (g)	0.1521	0.1521	0.1396	0.1411
Volume (m^3)	3.62E-05	3.62E-05	3.32E-05	3.36E-05
Volume (cm^3)	36.17	36.16	33.19	33.56
Volume Change (cm^3)	0	-36.16	-33.19	-33.56
Pressure Error (Pa)	7801	7801	7801	7801
Mass Error (g)	0.001904	0.001904	0.001804	0.001816
Temp Error (C)	1.5	1.5	1.5	1.5
Volume Error (m^3)	9.16E-07	9.15E-07	8.47E-07	8.55E-07
Percent	0.025	0.025	0.026	0.025
Sample Calcs				
Mass	8.23			
Initial Mass	11.006			
Heated Temp ©	555			
Mass Fraction	0.75			
Est. MFD	-0.01			
Diameter (in)	1.4			
Thickness(in)	0.35			
Volume (in^3)	0.54	Volume Error (in^3):	0.0023	
Volume (cm^3)	8.83	Volume Error (cm^3):	0.04	
Gas Volume (cm^3)	2.79	Gas Volume Error: (cm^3):	1.25	
Porosity	0.68	Total Error (dim)	0.142	

Normalized Mass Fraction (F) = 0 (fully decomposed)

PERMEABILITY				
Mass Flow (SCCM)	Pressure (Psi)	Permeability (m^2)	Total Error (m^2)	Total Error Percent
25	0.00011	1.70E-10	4.35E-10	256.22
50	0.00023	1.62E-10	2.00E-10	123.03
100	0.000464	1.61E-10	9.88E-11	61.42
150	0.000706	1.59E-10	6.45E-11	40.66
200	0.00095	1.57E-10	4.78E-11	30.44
250	0.001202	1.55E-10	3.76E-11	24.24
300	0.00146	1.53E-10	3.08E-11	20.11

Char Oxidation (burned in air at 600°C for one hour)

VIRGIN				
POROSITY				
	Baseline Gas Mass Flow:		Sample Gas Mass Flow:	
Sample	Empty	Empty	Eglass	Eglass
Temp (C)	19	19	19	19
Initial Pressure (psia)	1.26	1.26	1.26	1.26
Final Pressure (psia)	54.91	54.915	54.93	54.91
Initial pressure (Pa)	8687	8687	8687	8687
Final Pressure (Pa)	378600	378600	378700	378600
SCC	135.3	134.8	114.5	115
SL	0.1353	0.1348	0.1145	0.115
Gas Density (g/L)	1.1453	1.1453	1.1453	1.1453
Gas Mass (g)	0.155	0.1544	0.1311	0.1317
Volume (m^3)	3.63E-05	3.62E-05	3.07E-05	3.09E-05
Volume (cm^3)	36.32	36.18	30.72	30.87
Volume Change (cm^3)	0	0.1376	5.594	5.449
Pressure Error (Pa)	7801	7801	7801	7801
Mass Error (g)	0.001927	0.001922	0.001736	0.001741
Temp Error (C)	1.5	1.5	1.5	1.5
Volume Error (m^3)	9.08E-07	9.05E-07	7.81E-07	7.84E-07
Percent	0.025	0.025	0.025	0.025
Sample Calcs				
Mass	11.094			
Initial Mass	11.094			
Mass Fraction	0.247			
Diameter (in)	1.4			
Thickness(in)	0.24			
Volume (in^3)	0.37	Volume Error (in^3):	0.0021	
Volume (cm^3)	6.05	Volume Error (cm^3):	0.03	
Gas Volume (cm^3)	5.45	Gas Volume Error: (cm^3):	1.2	
Porosity	0.1	Porosity Error (dim)	0.198	

Char Oxidation (burned in air at 600°C for one hour)

DECOMPOSED				
POROSITY				
	Baseline Gas Mass Flow:		Sample Gas Mass Flow:	
Sample	Empty	Empty	Eglass	Eglass
Temp ©	19	19	19	19
Initial Pressure (psia)	1.22	1.23	1.23	1.23
Final Pressure (psia)	54.59	54.61	54.6	54.6
Initial pressure (Pa)	8412	8481	8481	8481
Final Pressure (Pa)	376400	376500	376500	376500
SCC	128.2	128.9	118.5	118.5
SL	0.1282	0.1289	0.1185	0.1185
Gas Density (g/L)	1.1453	1.1453	1.1453	1.1453
Gas Mass (g)	0.1468	0.1476	0.1357	0.1357
Volume (m^3)	3.46E-05	3.48E-05	3.20E-05	3.20E-05
Volume (cm^3)	34.59	34.77	31.97	31.97
Volume Change (cm^3)	0	-34.77	-31.97	-31.97
Pressure Error (Pa)	7801	7801	7801	7801
Mass Error (g)	0.001862	0.001868	0.001773	0.001773
Temp Error (C)	1.5	1.5	1.5	1.5
Volume Error (m^3)	8.73E-07	8.77E-07	8.13E-07	8.13E-07
Percent	0.025	0.025	0.025	0.025
Sample Calcs				
Mass	7.968			
Initial Mass	11.094			
Heated Temp ©	600			
Mass Fraction	0.72			
Est. MFD	-0.13			
Diameter (in)	1.4			
Thickness(in)	0.295			
Volume (in^3)	0.45	Volume Error (in^3):	0.0022	
Volume (cm^3)	7.44	Volume Error (cm^3):	0.04	
Gas Volume (cm^3)	2.71	Gas Volume Error: (cm^3):	1.19	
Porosity	0.64	Total Error (dim)	0.16	

Char Oxidation (burned in air at 600°C for one hour)

PERMEABILITY				
Mass Flow (SCCM)	Pressure (Psi)	Permeability (m^2)	Total Error (m^2)	Total Error Percent
9.9	0.00074	8.42E-12	4.28E-12	50.89
19.9	0.00148	8.46E-12	2.19E-12	25.94
29.9	0.00222	8.47E-12	1.49E-12	17.63
39.9	0.00294	8.54E-12	1.16E-12	13.55
49.8	0.00367	8.54E-12	9.44E-13	11.06
59.8	0.0044	8.55E-12	8.03E-13	9.39
69.8	0.00512	8.58E-12	7.04E-13	8.21
79.8	0.00587	8.55E-12	6.24E-13	7.29
89.8	0.00661	8.55E-12	5.63E-13	6.59
99.8	0.00736	8.53E-12	5.14E-13	6.02
109.8	0.00811	8.52E-12	4.74E-13	5.56

Balsa Wood

Normalized Mass Fraction (F) = 1 (Virgin)

VIRGIN				
POROSITY				
	Baseline Gas Mass Flow:		Sample Gas Mass Flow:	
Sample	Empty	Empty	Eglass	Eglass
Temp (C)	18	18	18	18
Initial Pressure (psia)	1.23	1.225	1.22	1.23
Final Pressure (psia)	54.11	54.11	54.1	54.11
Initial pressure (Pa)	8481	8446	8412	8481
Final Pressure (Pa)	373100	373100	373000	373100
SCC	132.7	133.2	99.59	100.4
SL	0.1327	0.1332	0.09959	0.1004
Gas Density (g/L)	1.1453	1.1453	1.1453	1.1453
Gas Mass (g)	0.152	0.1526	0.1141	0.115
Volume (m^3)	3.60E-05	3.61E-05	2.70E-05	2.72E-05
Volume (cm^3)	36.01	36.15	27.03	27.25
Volume Change (cm^3)	0	-0.1323	8.986	8.766
Pressure Error (Pa)	7801	7801	7801	7801
Mass Error (g)	0.001903	0.001908	0.0016	0.001607
Temp Error (C)	1.5	1.5	1.5	1.5
Volume Error (m^3)	9.12E-07	9.15E-07	7.05E-07	7.10E-07
Percent	0.025	0.025	0.026	0.026
Sample Calcs				
Mass	2.048			
Initial Mass	2.048			
Mass Fraction	1			
Diameter (in)	1.412			
Thickness(in)	0.485			
Volume (in^3)	0.76	Volume Error (in^3):	0.0026	
Volume (cm^3)	12.45	Volume Error (cm^3):	0.04	
Gas Volume (cm^3)	8.94	Gas Volume Error: (cm^3):	1.16	
Porosity	0.28	Total Error (dim):	0.0929	

Normalized Mass Fraction (F) = 1 (Virgin)

PERMEABILITY				
Mass Flow (SCCM)	Pressure (Psi)	Permeability (m^2)	Total Error (m^2)	Total Error Percent
9.9	0.00115	8.91E-12	7.15E-13	8.03
19.9	0.00231	8.91E-12	3.84E-13	4.31
29.9	0.00345	8.96E-12	2.76E-13	3.08
39.9	0.00458	9.01E-12	2.23E-13	2.47
49.8	0.00570	9.04E-12	1.90E-13	2.10
59.8	0.00683	9.06E-12	1.68E-13	1.86
69.8	0.00794	9.09E-12	1.53E-13	1.68

Normalized Mass Fraction (F) = 1 (Preheated)

VIRGIN				
POROSITY				
	Baseline Gas Mass Flow:		Sample Gas Mass Flow:	
Sample	Empty	Empty	Eglass	Eglass
Temp (C)	19	19	19	19
Initial Pressure (psia)	1.23	1.23	1.23	1.23
Final Pressure (psia)	54.11	54.1	54.11	54.11
Initial pressure (Pa)	8481	8481	8481	8481
Final Pressure (Pa)	373100	373000	373100	373100
SCC	131.1	131.7	98.97	98.85
SL	0.1311	0.1317	0.09897	0.09885
Gas Density (g/L)	1.1453	1.1453	1.1453	1.1453
Gas Mass (g)	0.1501	0.1508	0.1134	0.1132
Volume (m^3)	3.57E-05	3.59E-05	2.70E-05	2.69E-05
Volume (cm^3)	35.7	35.87	26.95	26.92
Volume Change (cm^3)	0	-0.1702	8.75	8.782
Pressure Error (Pa)	7801	7801	7801	7801
Mass Error (g)	0.001888	0.001894	0.001594	0.001593
Temp Error (C)	1.5	1.5	1.5	1.5
Volume Error (m^3)	9.05E-07	9.09E-07	7.04E-07	7.03E-07
Percent	0.025	0.025	0.026	0.026
Sample Calcs				
Mass	1.975			
Initial Mass	1.975			
Mass Fraction	1			
Diameter (in)	1.405			
Thickness(in)	0.483			
Volume (in^3)	0.75	Volume Error (in^3):	0.0026	
Volume (cm^3)	12.27	Volume Error (cm^3):	0.04	
Gas Volume (cm^3)	8.85	Gas Volume Error: (cm^3):	1.15	
Porosity	0.28	Porosity Error (dim)	0.0936	

Normalized Mass Fraction (F) = 1 (Preheated)

DECOMPOSED				
POROSITY				
	Baseline Gas Mass Flow:		Sample Gas Mass Flow:	
Sample	Empty	Empty	Eglass	Eglass
Temp ©	19	19	19	19
Initial Pressure (psia)	1.225	1.23	1.24	1.24
Final Pressure (psia)	54.11	54.11	54.11	54.11
Initial pressure (Pa)	8446	8481	8549	8549
Final Pressure (Pa)	373100	373100	373100	373100
SCC	133.1	132.6	100.6	100.4
SL	0.1331	0.1326	0.1006	0.1004
Gas Density (g/L)	1.1453	1.1453	1.1453	1.1453
Gas Mass (g)	0.1524	0.1519	0.1152	0.115
Volume (m^3)	3.62E-05	3.61E-05	2.74E-05	2.73E-05
Volume (cm^3)	36.24	36.11	27.4	27.35
Volume Change (cm^3)	0	-36.11	-27.4	-27.35
Pressure Error (Pa)	7801	7801	7801	7801
Mass Error (g)	0.001907	0.001902	0.001609	0.001607
Temp Error (C)	1.5	1.5	1.5	1.5
Volume Error (m^3)	9.17E-07	9.14E-07	7.14E-07	7.13E-07
Percent	0.025	0.025	0.026	0.026
Sample Calcs				
Mass	1.902			
Initial Mass	1.975			
Heated Temp ©	155			
Mass Fraction	0.96			
Diameter (in)	1.4			
Thickness(in)	0.483			
Volume (in^3)	0.741397906	Volume Error (in^3):	0.0026	
Volume (cm^3)	12.15	Volume Error (cm^3):	0.043	
Gas Volume (cm^3)	8.8	Gas Volume Error: (cm^3):	1.08	
Porosity	0.28	Total Error (dim)	0.0891	

Normalized Mass Fraction (F) = 1 (Preheated)

PERMEABILITY				
Mass Flow (SCCM)	Pressure (Psi)	Permeability (m^2)	Total Error (m^2)	Total Error Percent
9.9	0.000891	1.14E-11	1.07E-12	9.36
19.9	0.00176	1.16E-11	5.84E-13	5.02
29.9	0.00262	1.18E-11	4.19E-13	3.57
39.9	0.00346	1.19E-11	3.38E-13	2.84
49.8	0.00428	1.20E-11	2.89E-13	2.41
59.8	0.00511	1.21E-11	2.55E-13	2.12
69.8	0.00594	1.21E-11	2.31E-13	1.91
79.8	0.00675	1.22E-11	2.13E-13	1.75
89.8	0.00758	1.22E-11	1.98E-13	1.63
99.8	0.0084	1.22E-11	1.87E-13	1.53

Normalized Mass Fraction (F) = 0.70

VIRGIN				
POROSITY				
	Baseline Gas Mass Flow:		Sample Gas Mass Flow:	
Sample	Empty	Empty	Eglass	Eglass
Temp (C)	19	19	19	19
Initial Pressure (psia)	1.23	1.23	1.245	1.245
Final Pressure (psia)	54.13	54.11	54.11	54.11
Initial pressure (Pa)	8481	8481	8584	8584
Final Pressure (Pa)	373200	373100	373100	373100
SCC	132.6	133.5	99.25	100.2
SL	0.1326	0.1335	0.09925	0.1002
Gas Density (g/L)	1.1453	1.1453	1.1453	1.1453
Gas Mass (g)	0.1519	0.1529	0.1137	0.1148
Volume (m^3)	3.61E-05	3.64E-05	2.70E-05	2.73E-05
Volume (cm^3)	36.1	36.35	27.04	27.29
Volume Change (cm^3)	0	-0.2587	9.061	8.802
Pressure Error (Pa)	7801	7801	7801	7801
Mass Error (g)	0.001902	0.00191	0.001597	0.001605
Temp Error (C)	1.5	1.5	1.5	1.5
Volume Error (m^3)	9.14E-07	9.20E-07	7.06E-07	7.12E-07
Percent	0.025	0.025	0.026	0.026
Sample Calcs				
Mass	1.941			
Initial Mass	1.941			
Mass Fraction	1			
Diameter (in)	1.395			
Thickness(in)	0.484			
Volume (in^3)	0.74	Volume Error (in^3):	0.0026	
Volume (cm^3)	12.12	Volume Error (cm^3):	0.04	
Gas Volume (cm^3)	9.06	Gas Volume Error: (cm^3):	1.16	
Porosity	0.25	Porosity Error (dim)	0.0956	

Normalized Mass Fraction (F) = 0.70

DECOMPOSED				
POROSITY				
	Baseline Gas Mass Flow:		Sample Gas Mass Flow:	
Sample	Empty	Empty	Eglass	Eglass
Temp ©	19	19	19	19
Initial Pressure (psia)	1.195	1.205	1.235	1.28
Final Pressure (psia)	54.11	54.1	53.85	53.85
Initial pressure (Pa)	8239	8308	8515	8825
Final Pressure (Pa)	373100	373000	371300	371300
SCC	132	133	104.5	104.9
SL	0.132	0.133	0.1045	0.1049
Gas Density (g/L)	1.1453	1.1453	1.1453	1.1453
Gas Mass (g)	0.1512	0.1523	0.1197	0.1201
Volume (m^3)	3.59E-05	3.62E-05	2.86E-05	2.87E-05
Volume (cm^3)	35.92	36.21	28.6	28.73
Volume Change (cm^3)	0	-36.21	-28.6	-28.73
Pressure Error (Pa)	7801	7801	7801	7801
Mass Error (g)	0.001897	0.001906	0.001645	0.001648
Temp Error (C)	1.5	1.5	1.5	1.5
Volume Error (m^3)	9.09E-07	9.16E-07	7.44E-07	7.48E-07
Percent	0.025	0.025	0.026	0.026
Sample Calcs				
Mass	1.515			
Initial Mass	1.941			
Heated Temp ©	286			
Mass Fraction	0.78			
L1 (in)	1.4			
L2 (in)	1.378			
Thickness(in)	0.483			
Volume (in^3)	0.73	Volume Error (in^3):	0.0026	
Volume (cm^3)	11.98	Volume Error (cm^3):	0.04	
Gas Volume (cm^3)	7.4	Gas Volume Error: (cm^3):	1.18	
Porosity	0.38	Total Error (dim)	0.0985	

Normalized Mass Fraction (F) = 0.70

PERMEABILITY				
Mass Flow (SCCM)	Pressure (Psi)	Permeability (m^2)	Total Error (m^2)	Total Error Percent
9.9	0.00083	1.23E-11	1.20E-12	9.75
19.9	0.00166	1.23E-11	6.39E-13	5.18
29.9	0.00249	1.24E-11	4.52E-13	3.66
39.9	0.0033	1.25E-11	3.62E-13	2.91
49.8	0.00412	1.25E-11	3.05E-13	2.45
59.8	0.00493	1.25E-11	2.69E-13	2.15
69.8	0.00574	1.25E-11	2.42E-13	1.93
79.8	0.00653	1.26E-11	2.23E-13	1.77
89.8	0.00734	1.26E-11	2.07E-13	1.64
99.8	0.00813	1.26E-11	1.95E-13	1.54

Normalized Mass Fraction (F) = 0.56

VIRGIN				
POROSITY				
	Baseline Gas Mass Flow:		Sample Gas Mass Flow:	
Sample	Empty	Empty	Eglass	Eglass
Temp (C)	19	19	19	19
Initial Pressure (psia)	1.21	1.2	1.22	1.21
Final Pressure (psia)	54.11	54.11	54.11	54.1
Initial pressure (Pa)	8343	8274	8412	8343
Final Pressure (Pa)	373100	373100	373100	373000
SCC	134.4	134.1	97.28	97.43
SL	0.1344	0.1341	0.09728	0.09743
Gas Density (g/L)	1.1453	1.1453	1.1453	1.1453
Gas Mass (g)	0.1539	0.1536	0.1114	0.1116
Volume (m^3)	3.66E-05	3.65E-05	2.65E-05	2.65E-05
Volume (cm^3)	36.59	36.5	26.49	26.53
Volume Change (cm^3)	0	0.08856	10.1	10.06
Pressure Error (Pa)	7801	7801	7801	7801
Mass Error (g)	0.001919	0.001916	0.001578	0.00158
Temp Error (C)	1.5	1.5	1.5	1.5
Volume Error (m^3)	9.25E-07	9.23E-07	6.93E-07	6.94E-07
Percent	0.025	0.025	0.026	0.026
Sample Calcs				
Mass	1.972			
Initial Mass	1.972			
Mass Fraction	1			
Diameter (in)	1.402			
Thickness(in)	0.483			
Volume (in^3)	0.75	Volume Error (in^3):	0.0026	
Volume (cm^3)	12.22	Volume Error (cm^3):	0.04	
Gas Volume (cm^3)	10.04	Gas Volume Error: (cm^3):	1.16	
Porosity	0.18	Porosity Error (dim)	0.0946	

Normalized Mass Fraction (F) = 0.56

DECOMPOSED				
POROSITY				
	Baseline Gas Mass Flow:		Sample Gas Mass Flow:	
Sample	Empty	Empty	Eglass	Eglass
Temp ©	19	19	19	19
Initial Pressure (psia)	1.22	1.21	1.26	1.21
Final Pressure (psia)	54.12	54.13	54.11	54
Initial pressure (Pa)	8412	8343	8687	8343
Final Pressure (Pa)	373100	373200	373100	372300
SCC	134.8	135.4	106.7	107.3
SL	0.1348	0.1354	0.1067	0.1073
Gas Density (g/L)	1.1453	1.1453	1.1453	1.1453
Gas Mass (g)	0.1544	0.1551	0.1222	0.1229
Volume (m^3)	3.67E-05	3.68E-05	2.91E-05	2.93E-05
Volume (cm^3)	36.7	36.84	29.07	29.27
Volume Change (cm^3)	0	-36.84	-29.07	-29.27
Pressure Error (Pa)	7801	7801	7801	7801
Mass Error (g)	0.001922	0.001928	0.001665	0.00167
Temp Error (C)	1.5	1.5	1.5	1.5
Volume Error (m^3)	9.27E-07	9.31E-07	7.53E-07	7.58E-07
Percent	0.025	0.025	0.026	0.026
Sample Calcs				
Mass	1.305			
Initial Mass	1.972			
Heated Temp ©	303			
Mass Fraction	0.66			
L1 (in)	1.40			
L2 (in)	1.369			
Thickness(in)	0.479			
Volume (in^3)	0.72	Volume Error (in^3):	0.0026	
Volume (cm^3)	11.84	Volume Error (cm^3):	0.04	
Gas Volume (cm^3)	7.60	Gas Volume Error: (cm^3):	1.2	
Porosity	0.36	Total Error (dim)	0.101	

Normalized Mass Fraction (F) = 0.56

PERMEABILITY				
Mass Flow (SCCM)	Pressure (Psi)	Permeability (m^2)	Total Error (m^2)	Total Error Percent
9.9	0.00118	8.57E-12	6.90E-13	8.06
19.9	0.00235	8.65E-12	3.76E-13	4.34
29.9	0.00353	8.65E-12	2.68E-13	3.1
39.9	0.00467	8.73E-12	2.17E-13	2.49
49.8	0.00584	8.71E-12	1.84E-13	2.12
59.8	0.00697	8.77E-12	1.64E-13	1.87
69.8	0.00812	8.78E-12	1.49E-13	1.69

Normalized Mass Fraction (F) = 0.43

VIRGIN				
POROSITY				
	Baseline Gas Mass Flow:		Sample Gas Mass Flow:	
Sample	Empty	Empty	Eglass	Eglass
Temp (C)	19	19	19	19
Initial Pressure (psia)	1.19	1.18	1.21	1.21
Final Pressure (psia)	54.61	54.62	54.45	54.56
Initial pressure (Pa)	8205	8136	8343	8343
Final Pressure (Pa)	376500	376600	375400	376200
SCC	134.5	135.9	100.5	100.7
SL	0.1345	0.1359	0.1005	0.1007
Gas Density (g/L)	1.1453	1.1453	1.1453	1.1453
Gas Mass (g)	0.154	0.1556	0.1151	0.1153
Volume (m^3)	3.63E-05	3.66E-05	2.72E-05	2.72E-05
Volume (cm^3)	36.26	36.62	27.18	27.18
Volume Change (cm^3)	0	-0.3637	9.074	9.076
Pressure Error (Pa)	7801	7801	7801	7801
Mass Error (g)	0.00192	0.001932	0.001608	0.00161
Temp Error (C)	1.5	1.5	1.5	1.5
Volume Error (m^3)	9.10E-07	9.18E-07	7.05E-07	7.04E-07
Percent	0.025	0.025	0.026	0.026
Sample Calcs				
Mass	2.085			
Initial Mass	2.085			
Mass Fraction	1			
Diameter (in)	1.405			
Thickness(in)	0.48			
Volume (in^3)	0.74	Volume Error (in^3):	0.0026	
Volume (cm^3)	12.2	Volume Error (cm^3):	0.04	
Gas Volume (cm^3)	9.26	Gas Volume Error: (cm^3):	1.15	
Porosity	0.24	Porosity Error (dim)	0.0947	

Normalized Mass Fraction (F) = 0.43

DECOMPOSED				
POROSITY				
	Baseline Gas Mass Flow:		Sample Gas Mass Flow:	
Sample	Empty	Empty	Eglass	Eglass
Temp ©	19	19	19	19
Initial Pressure (psia)	1.21	1.21	1.3	1.29
Final Pressure (psia)	54.69	54.63	54.27	54.2
Initial pressure (Pa)	8343	8343	8963	8894
Final Pressure (Pa)	377100	376700	374200	373700
SCC	134.2	133.6	127.8	126.3
SL	0.1342	0.1336	0.1278	0.1263
Gas Density (g/L)	1.1453	1.1453	1.1453	1.1453
Gas Mass (g)	0.1537	0.153	0.1464	0.1447
Volume (m^3)	3.61E-05	3.60E-05	3.47E-05	3.44E-05
Volume (cm^3)	36.14	36.01	34.74	34.37
Volume Change (cm^3)	0	-36.01	-34.74	-34.37
Pressure Error (Pa)	7801	7801	7801	7801
Mass Error (g)	0.001917	0.001911	0.001858	0.001844
Temp Error (C)	1.5	1.5	1.5	1.5
Volume Error (m^3)	9.07E-07	9.05E-07	8.81E-07	8.74E-07
Percent	0.025	0.025	0.025	0.025
Sample Calcs				
Mass	1.151			
Initial Mass	2.085			
Heated Temp ©	310			
Mass Fraction	0.55			
L1 (in)	1.38			
L2 (in)	1.352			
Thickness(in)	0.48			
Volume (in^3)	0.70	Volume Error (in^3):	0.0025	
Volume (cm^3)	11.53	Volume Error (cm^3):	0.04	
Gas Volume (cm^3)	1.52	Gas Volume Error: (cm^3):	1.26	
Porosity	0.87	Total Error (dim)	0.109	

Normalized Mass Fraction (F) = 0.30

VIRGIN				
POROSITY				
	Baseline Gas Mass Flow:		Sample Gas Mass Flow:	
Sample	Empty	Empty	Eglass	Eglass
Temp (C)	16	16	16	16
Initial Pressure (psia)	1.25	1.25	1.26	1.31
Final Pressure (psia)	54.11	54.11	53.7	53.9
Initial pressure (Pa)	8618	8618	8687	9032
Final Pressure (Pa)	373100	373100	370200	371600
SCC	133.3	134.3	102.7	103.8
SL	0.1333	0.1343	0.1027	0.1038
Gas Density (g/L)	1.1453	1.1453	1.1453	1.1453
Gas Mass (g)	0.1527	0.1538	0.1176	0.1189
Volume (m^3)	3.59E-05	3.62E-05	2.79E-05	2.81E-05
Volume (cm^3)	35.94	36.21	27.91	28.13
Volume Change (cm^3)	0	-0.2696	8.029	7.81
Pressure Error (Pa)	7801	7801	7801	7801
Mass Error (g)	0.001909	0.001918	0.001628	0.001638
Temp Error (C)	1.5	1.5	1.5	1.5
Volume Error (m^3)	9.10E-07	9.16E-07	7.30E-07	7.33E-07
Percent	0.025	0.025	0.026	0.026
Sample Calcs				
Mass	1.932			
Initial Mass	1.932			
Mass Fraction	1			
Diameter (in)	1.4			
Thickness(in)	0.483			
Volume (in^3)	0.74	Volume Error (in^3):	0.0026	
Volume (cm^3)	12.18	Volume Error (cm^3):	0.04	
Gas Volume (cm^3)	8.05	Gas Volume Error: (cm^3):	1.17	
Porosity	0.34	Porosity Error (dim)	0.0961	

Normalized Mass Fraction (F) = 0.30

DECOMPOSED				
POROSITY				
	Baseline Gas Mass Flow:		Sample Gas Mass Flow:	
Sample	Empty	Empty	Eglass	Eglass
Temp ©	16	16	16	16
Initial Pressure (psia)	1.24	1.26	1.27	1.26
Final Pressure (psia)	54.11	54.11	54	54.04
Initial pressure (Pa)	8549	8687	8756	8687
Final Pressure (Pa)	373100	373100	372300	372600
SCC	134.1	133.1	126.1	126.3
SL	0.1341	0.1331	0.1261	0.1263
Gas Density (g/L)	1.1453	1.1453	1.1453	1.1453
Gas Mass (g)	0.1536	0.1524	0.1444	0.1447
Volume (m^3)	3.62E-05	3.59E-05	3.41E-05	3.41E-05
Volume (cm^3)	36.15	35.89	34.08	34.11
Volume Change (cm^3)	0	-35.89	-34.08	-34.11
Pressure Error (Pa)	7801	7801	7801	7801
Mass Error (g)	0.001916	0.001907	0.001843	0.001844
Temp Error (C)	1.5	1.5	1.5	1.5
Volume Error (m^3)	9.15E-07	9.09E-07	8.69E-07	8.69E-07
Percent	0.025	0.025	0.025	0.025
Sample Calcs				
Mass	0.927			
Initial Mass	1.932			
Heated Temp ©	332			
Mass Fraction	0.48			
L1 (in)	1.40			
L2 (in)	1.32			
Thickness(in)	0.48			
Volume (in^3)	0.70	Volume Error (in^3):	0.0025	
Volume (cm^3)	11.42	Volume Error (cm^3):	0.04	
Gas Volume (cm^3)	1.93	Gas Volume Error: (cm^3):	1.26	
Porosity	0.83	Total Error (dim)	0.11	

Normalized Mass Fraction (F) = 0 (Fully Decomposed)

VIRGIN				
POROSITY				
		Baseline Gas Mass Flow:	Sample Gas Mass Flow:	
Sample	Empty	Empty	Eglass	Eglass
Temp (C)	16	16	16	16
Initial Pressure (psia)	1.25	1.25	1.28	1.29
Final Pressure (psia)	54.11	54.19	54	54
Initial pressure (Pa)	8618	8618	8825	8894
Final Pressure (Pa)	373100	373600	372300	372300
SCC	132.7	132.7	100.4	100.8
SL	0.1327	0.1327	0.1004	0.1008
Gas Density (g/L)	1.1453	1.1453	1.1453	1.1453
Gas Mass (g)	0.152	0.152	0.115	0.1154
Volume (m^3)	3.58E-05	3.57E-05	2.71E-05	2.73E-05
Volume (cm^3)	35.78	35.73	27.14	27.26
Volume Change (cm^3)	0	0.05407	8.637	8.524
Pressure Error (Pa)	7801	7801	7801	7801
Mass Error (g)	0.001903	0.001903	0.001607	0.001611
Temp Error (C)	1.5	1.5	1.5	1.5
Volume Error (m^3)	9.06E-07	9.04E-07	7.09E-07	7.12E-07
Percent	0.025	0.025	0.026	0.026
Sample Calcs				
Mass	1.985			
Initial Mass	1.985			
Mass Fraction	1			
Diameter (in)	1.405			
Thickness(in)	0.482			
Volume (in^3)	0.75	Volume Error (in^3):	0.0026	
Volume (cm^3)	12.25	Volume Error (cm^3):	0.04	
Gas Volume (cm^3)	8.55	Gas Volume Error: (cm^3):	1.15	
Porosity	0.3	Porosity Error (dim)	0.094	

Normalized Mass Fraction (F) = 0 (Fully Decomposed)

DECOMPOSED				
POROSITY				
		Baseline Gas Mass Flow:		Sample Gas Mass Flow:
Sample	Empty	Empty	Eglass	Eglass
Temp ©	16	16	16	16
Initial Pressure (psia)	1.21	1.215	1.28	1.23
Final Pressure (psia)	54.12	54.13	54.08	54.1
Initial pressure (Pa)	8343	8377	8825	8481
Final Pressure (Pa)	373100	373200	372900	373000
SCC	132.6	132.8	138.1	137.1
SL	0.1326	0.1328	0.1381	0.1371
Gas Density (g/L)	1.1453	1.1453	1.1453	1.1453
Gas Mass (g)	0.1519	0.1521	0.1582	0.157
Volume (m^3)	3.57E-05	3.58E-05	3.73E-05	3.70E-05
Volume (cm^3)	35.72	35.77	37.28	36.96
Volume Change (cm^3)	0	-35.77	-37.28	-36.96
Pressure Error (Pa)	7801	7801	7801	7801
Mass Error (g)	0.001902	0.001904	0.001953	0.001943
Temp Error (C)	1.5	1.5	1.5	1.5
Volume Error (m^3)	9.04E-07	9.05E-07	9.42E-07	9.34E-07
Percent	0.025	0.025	0.025	0.025
Sample Calcs				
Mass	0.531			
Initial Mass	1.985			
Heated Temp ©	651			
Mass Fraction	0.27			
L1 (in)	1.40			
L2 (in)	1.155			
Thickness(in)	0.397			
Volume (in^3)	0.50	Volume Error (in^3):	0.0021	
Volume (cm^3)	8.24	Volume Error (cm^3):	0.03	
Gas Volume (cm^3)	-1.37	Gas Volume Error: (cm^3):	1.3	
Porosity	1.17	Total Error (dim)	0.158	

Appendix C: ISTGA Curves and ESEM Images of Intermediate-scale Samples

E-glass/Vinyl Ester

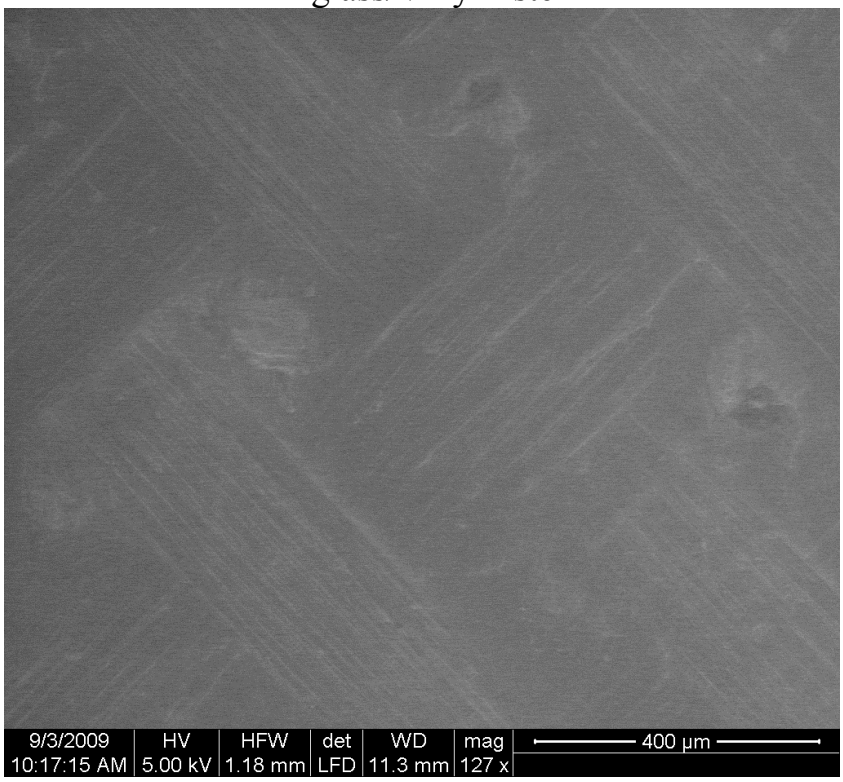

Normalized Mass Fraction (F) = 1 (virgin)

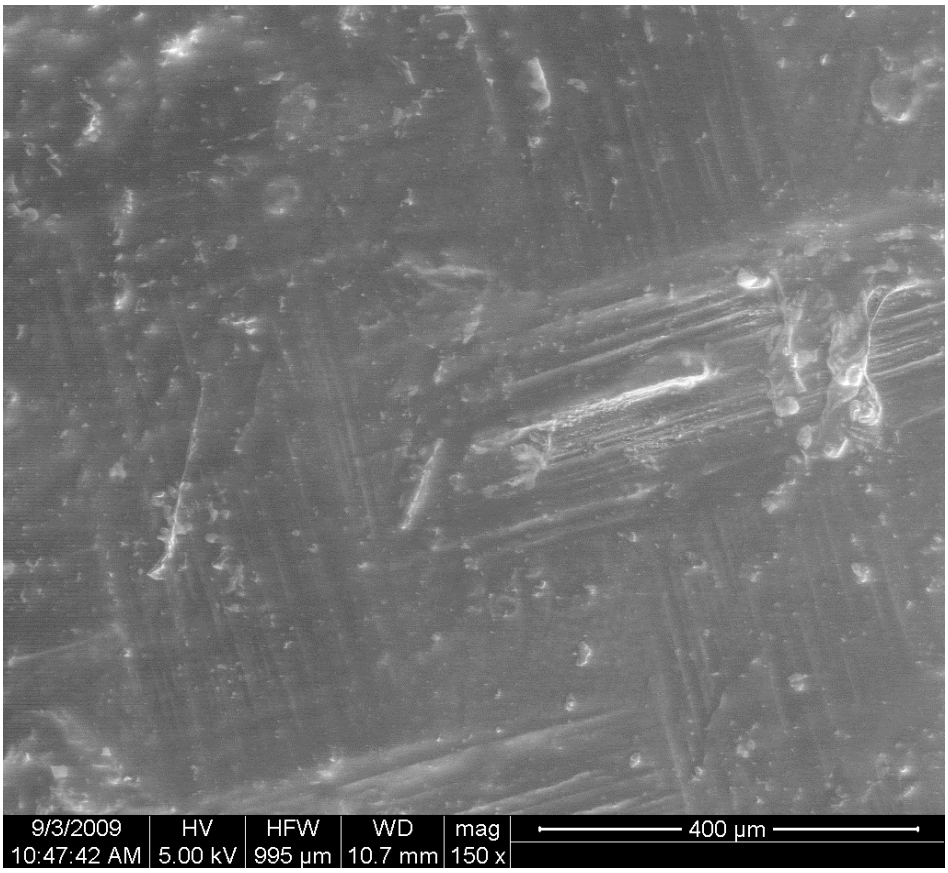

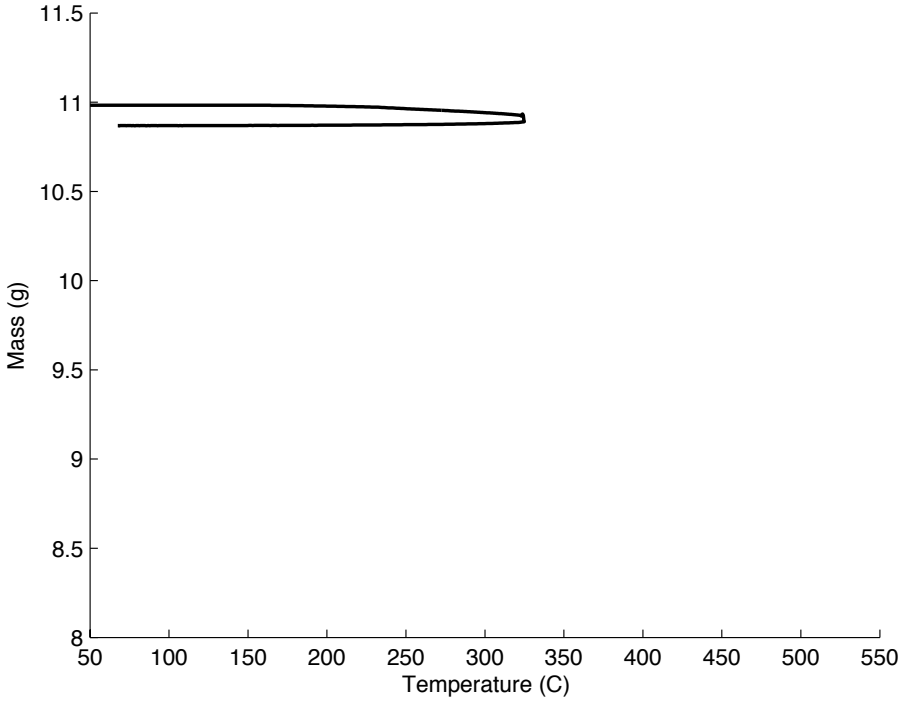

Normalized Mass Fraction (F) = 0.97

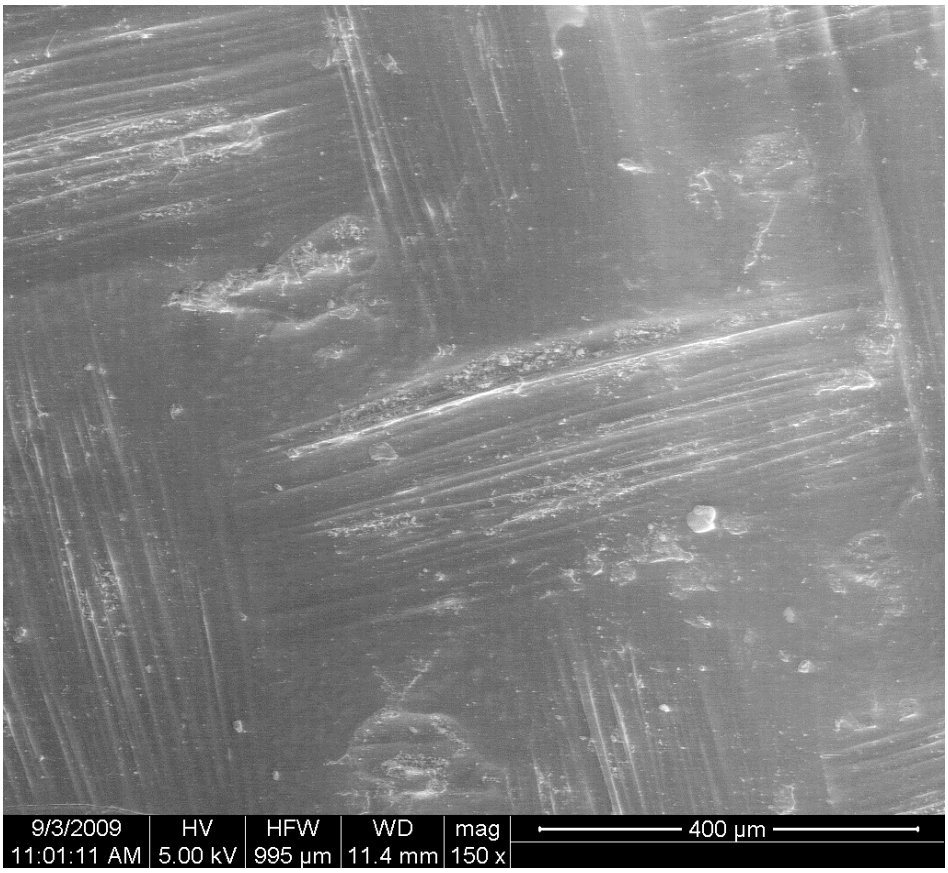

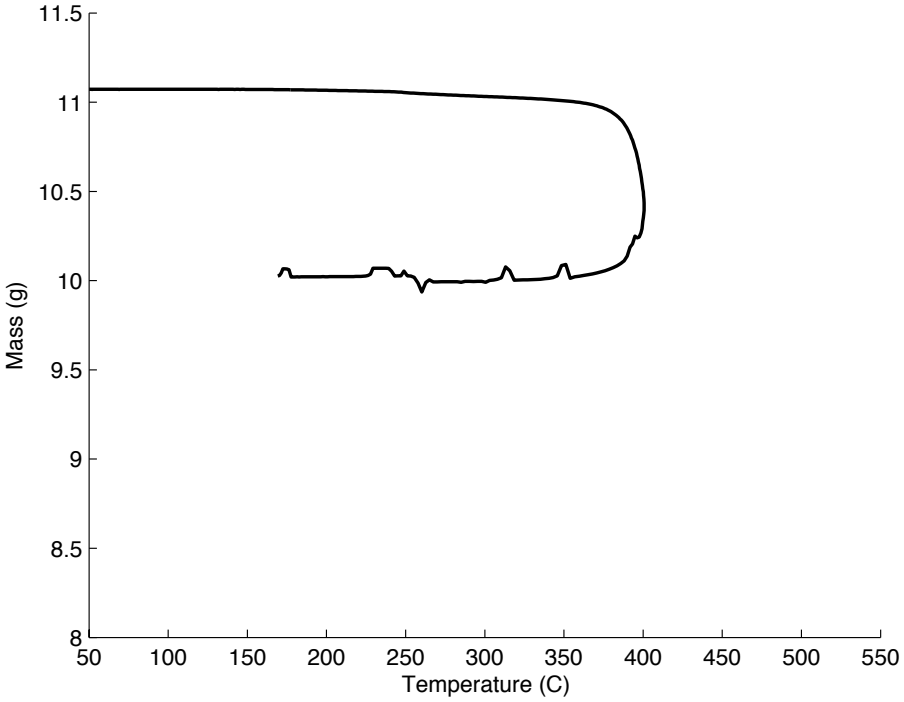

Normalized Mass Fraction (F) = 0.64

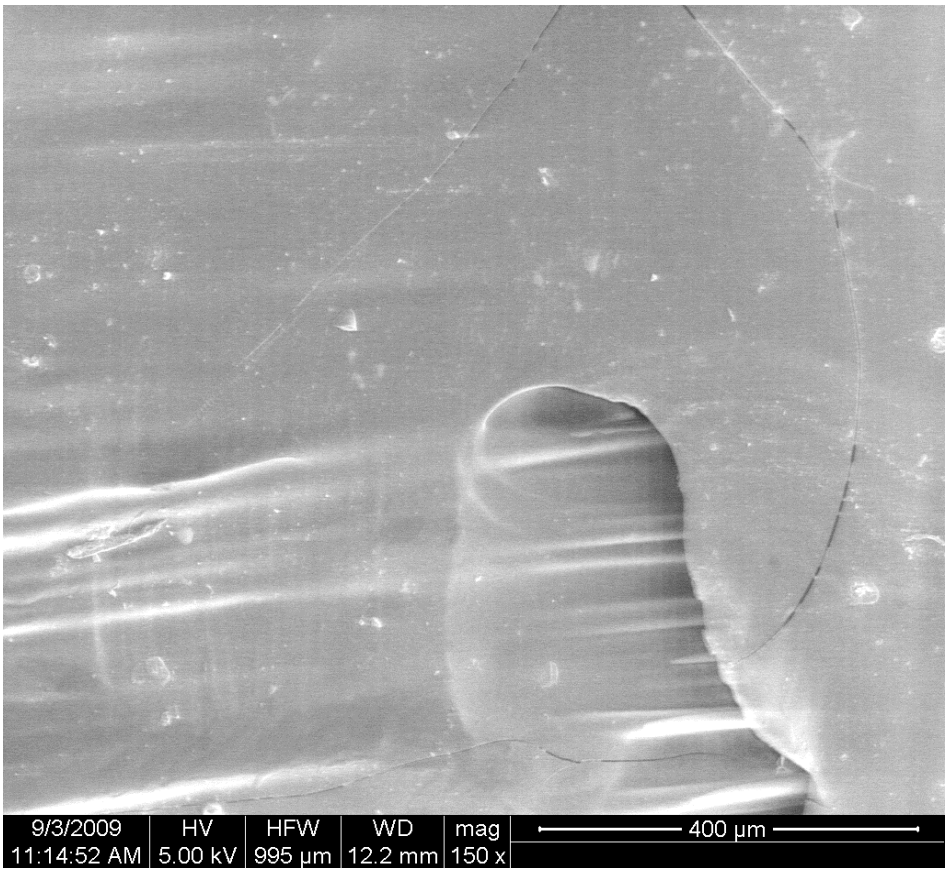

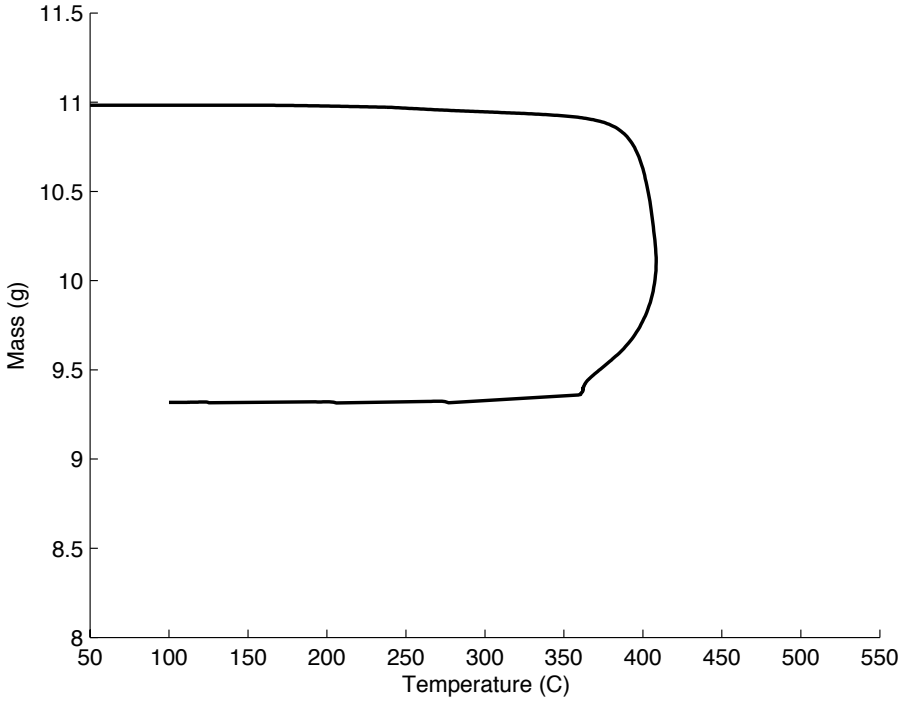

Normalized Mass Fraction (F) = 0.39

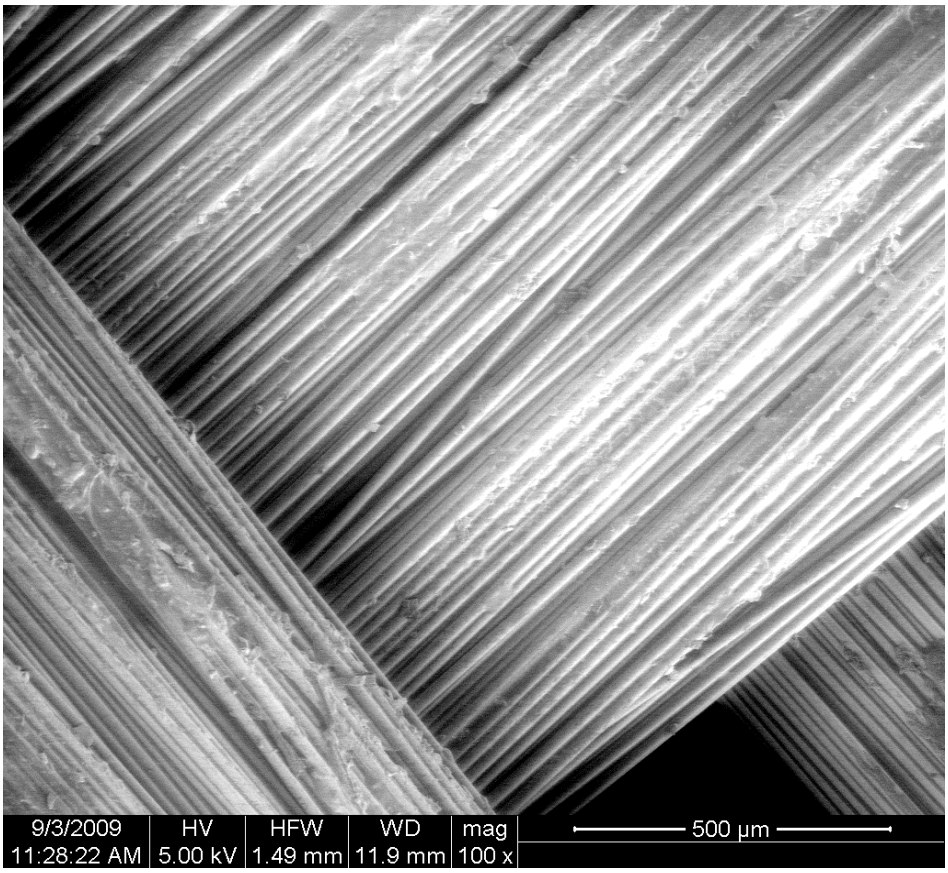

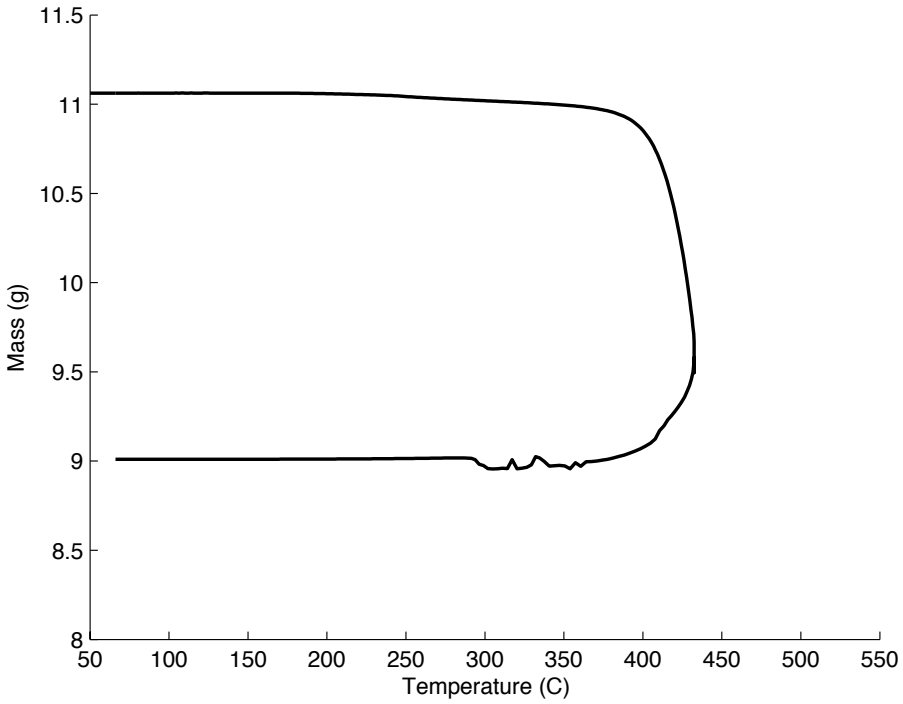

Normalized Mass Fraction (F) = 0.26

ESEM image not shown due to silicone sealant contamination on surface.

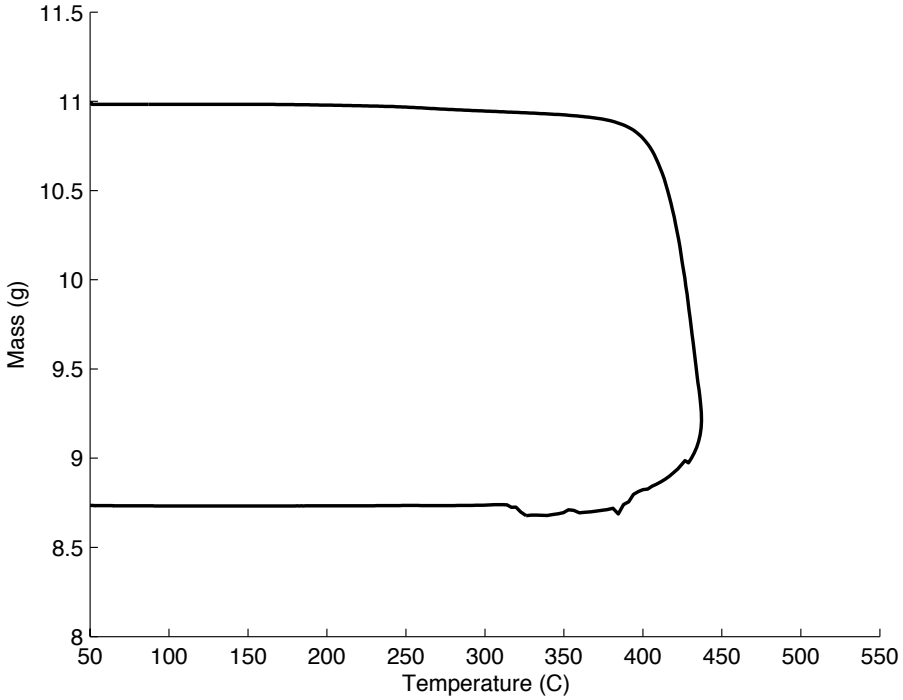

Normalized Mass Fraction (F) = 0.18

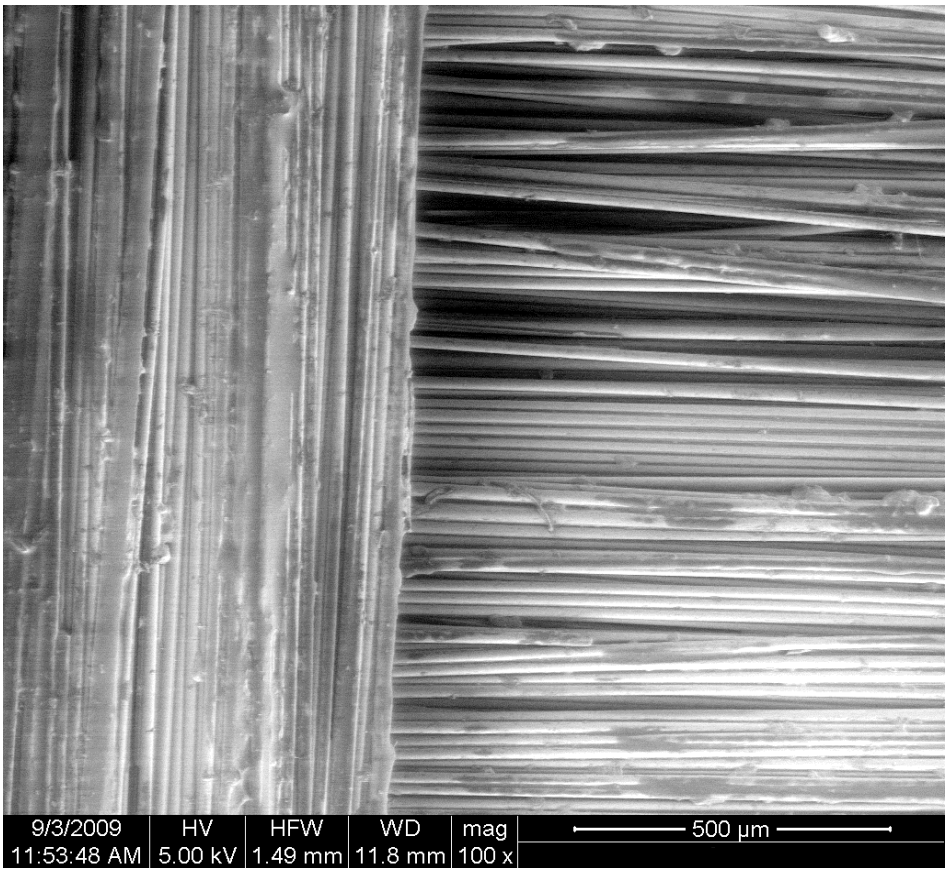

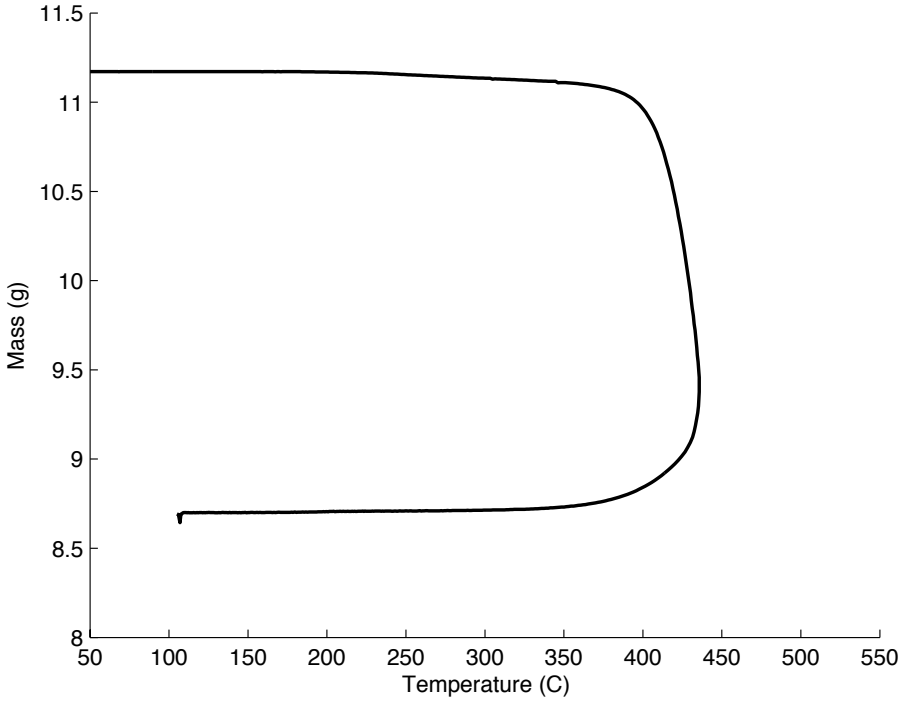

Normalized Mass Fraction (F) = 0.10

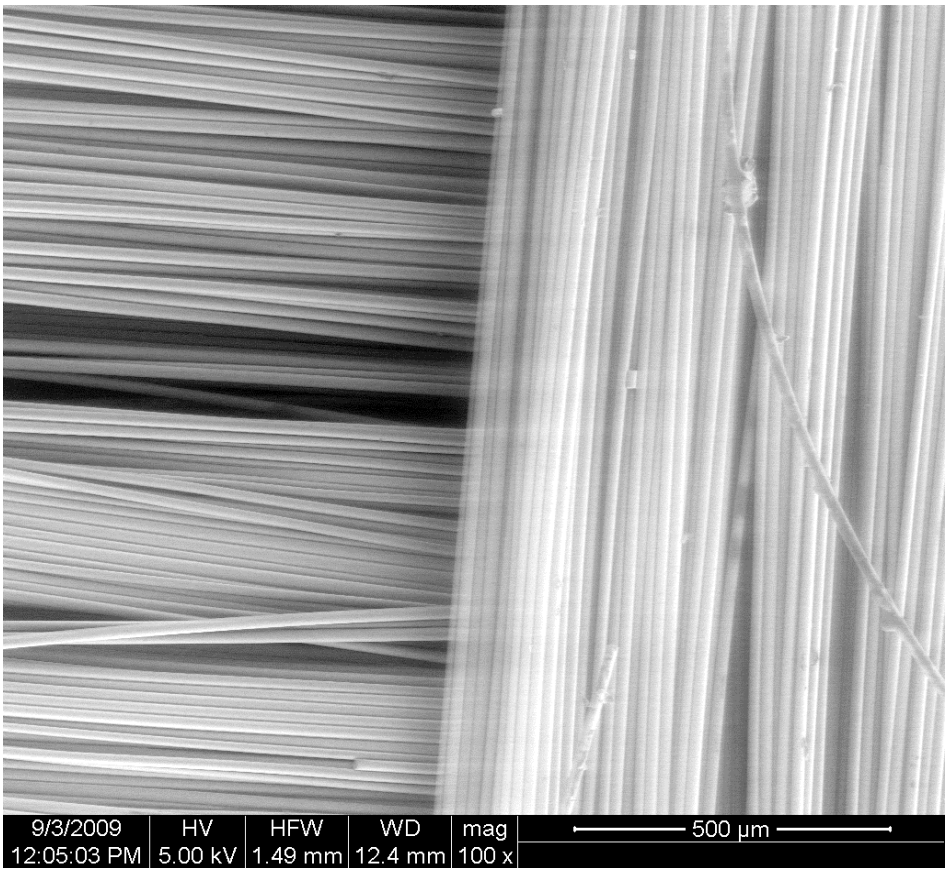

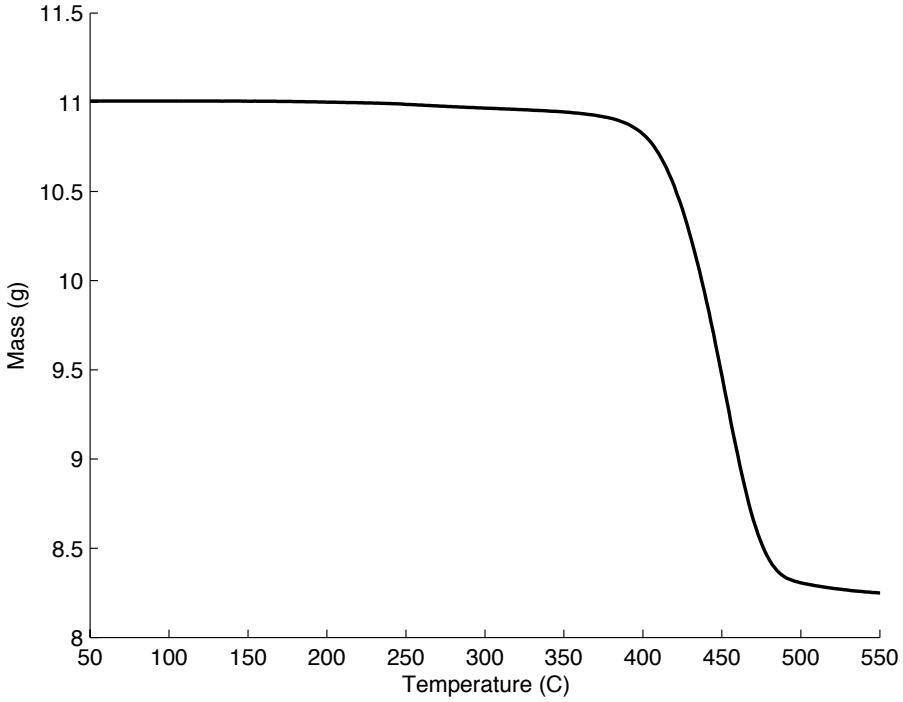

Normalized Mass Fraction (F) = 0

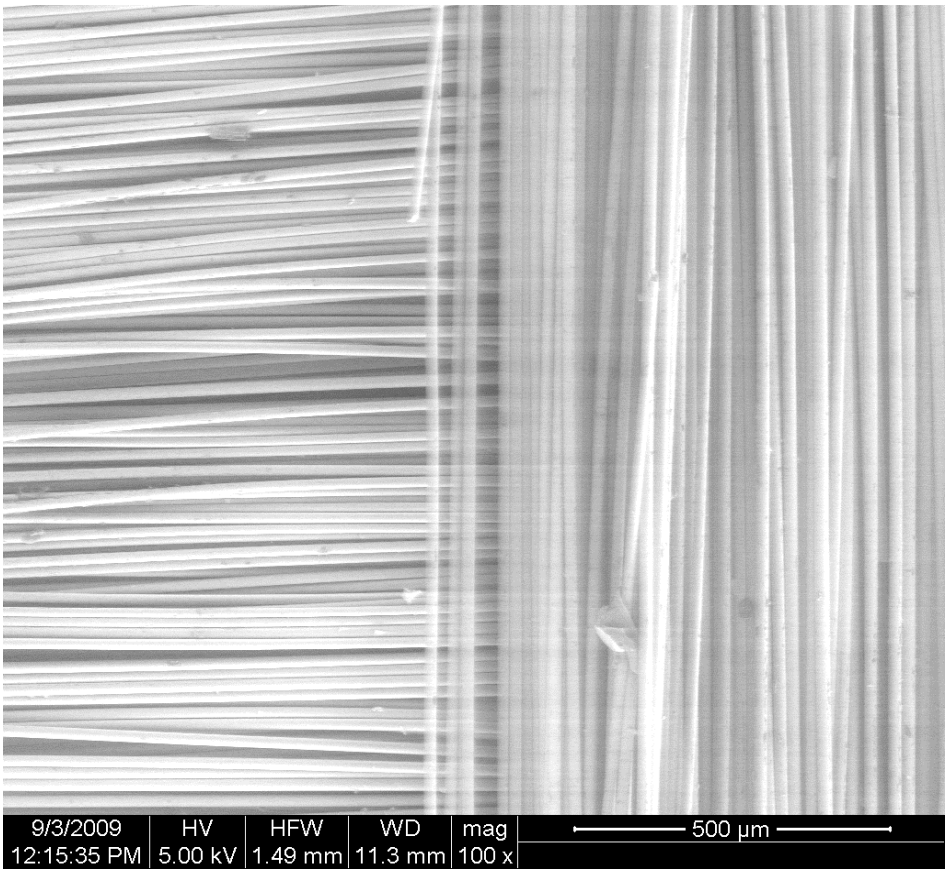

Normalized Mass Fraction (F) = 0 (char oxidation)

Balsa Wood

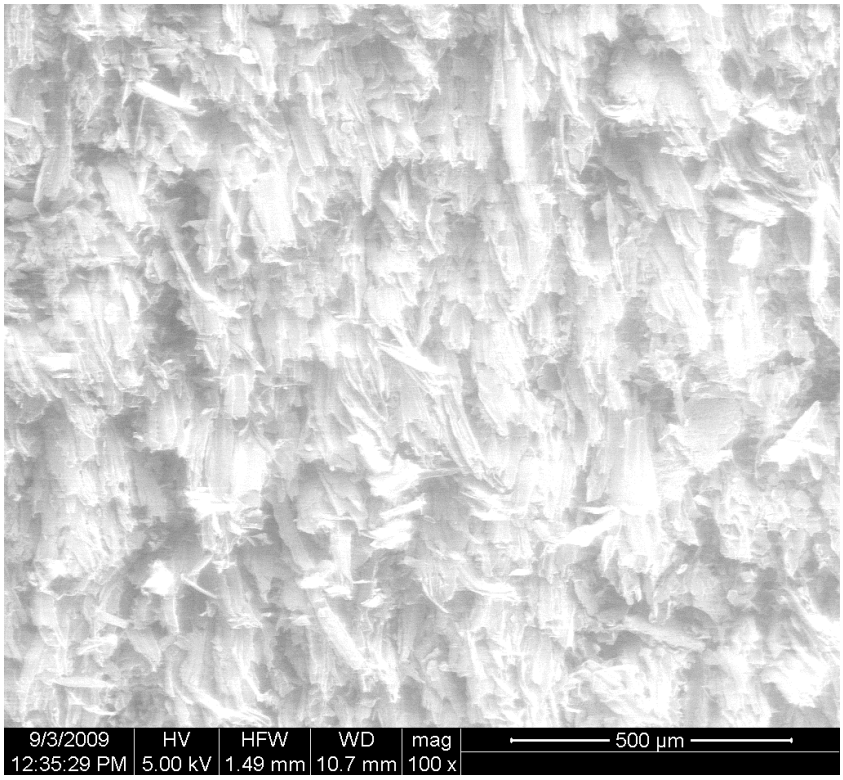

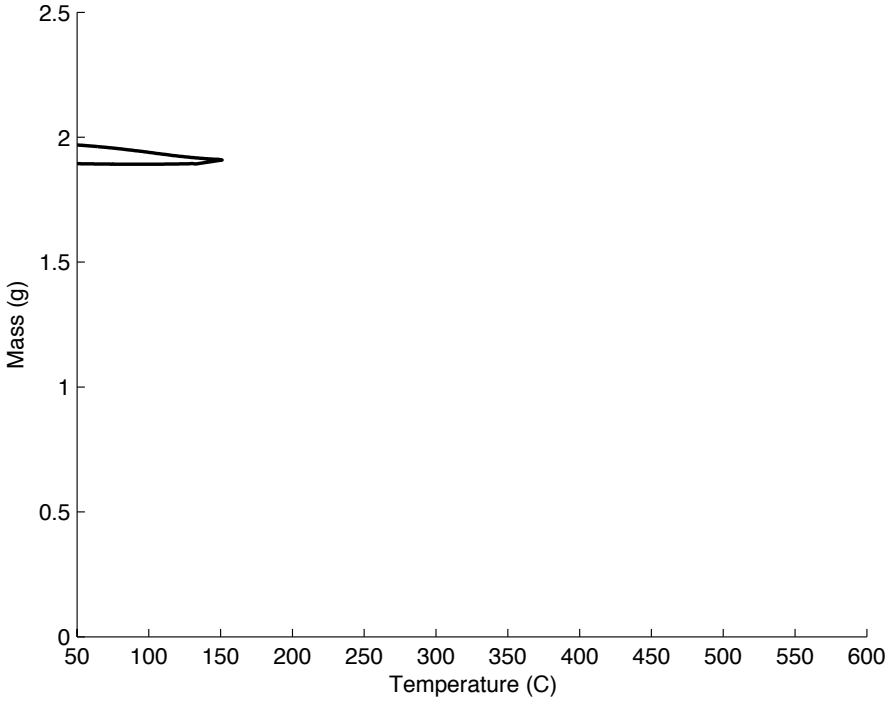

Normalized Mass Fraction (F) = 1 (Preheated)

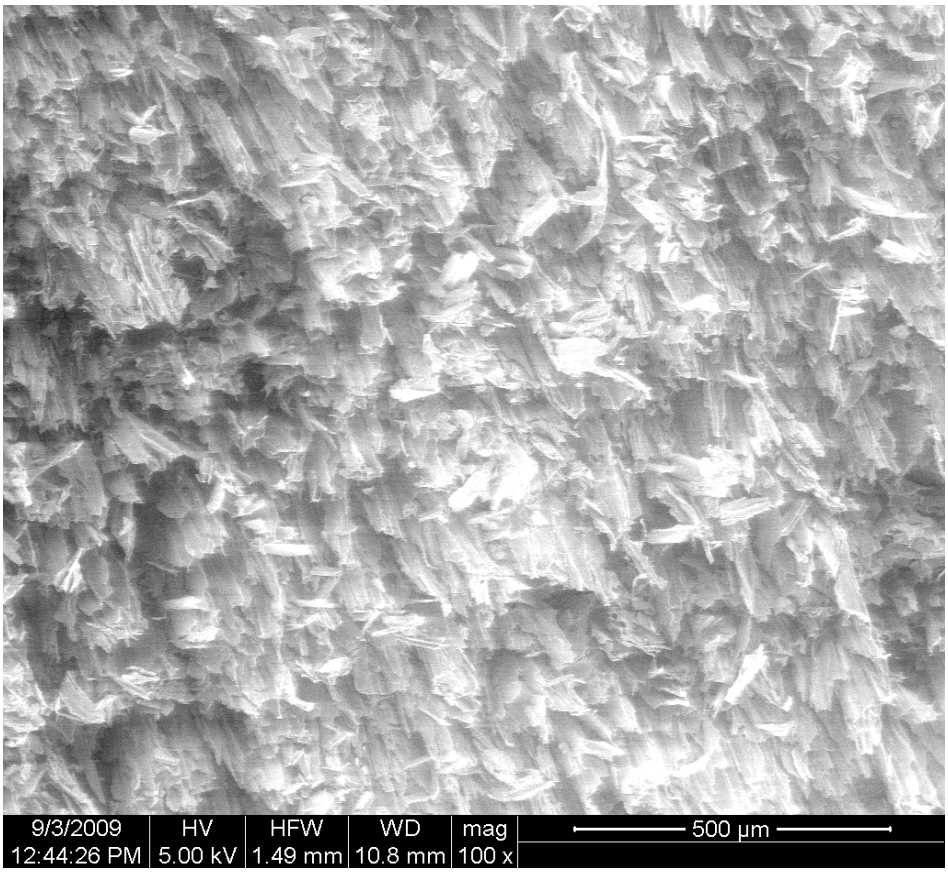

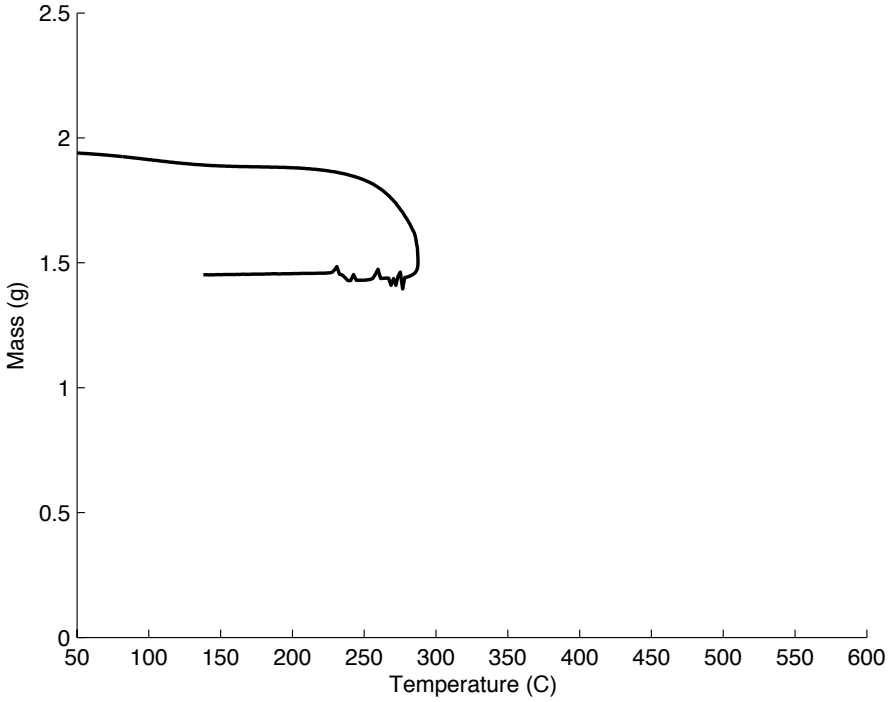

Normalized Mass Fraction (F) = 0.70

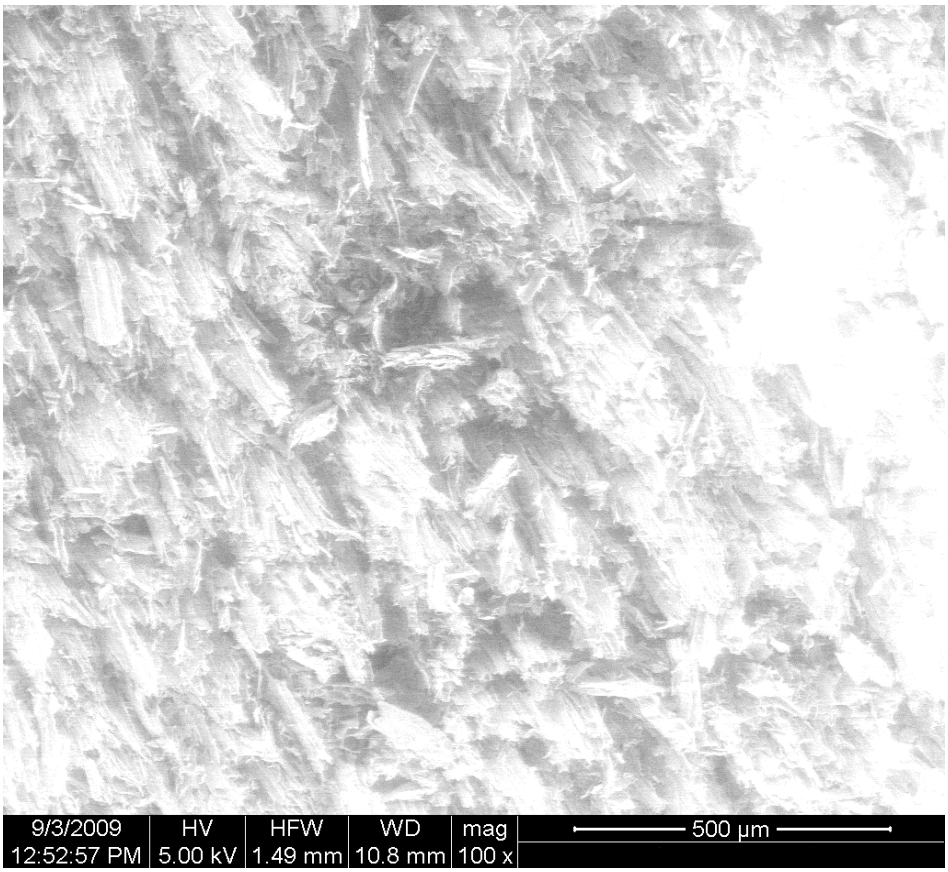

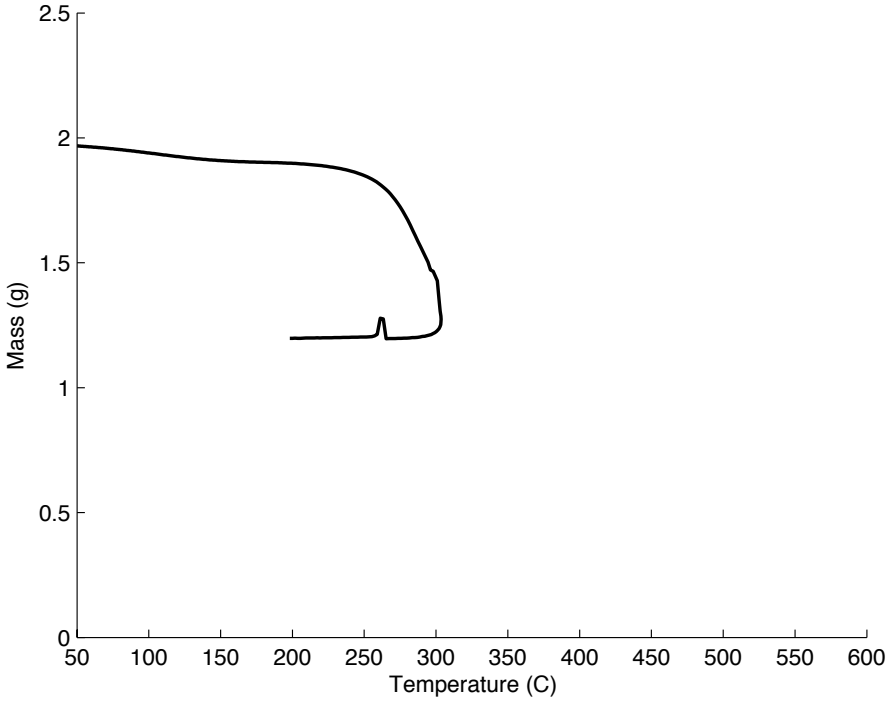

Normalized Mass Fraction (F) = 0.56

Balsa samples beyond a normalized mass fraction of 0.56 were not examined in the ESEM.

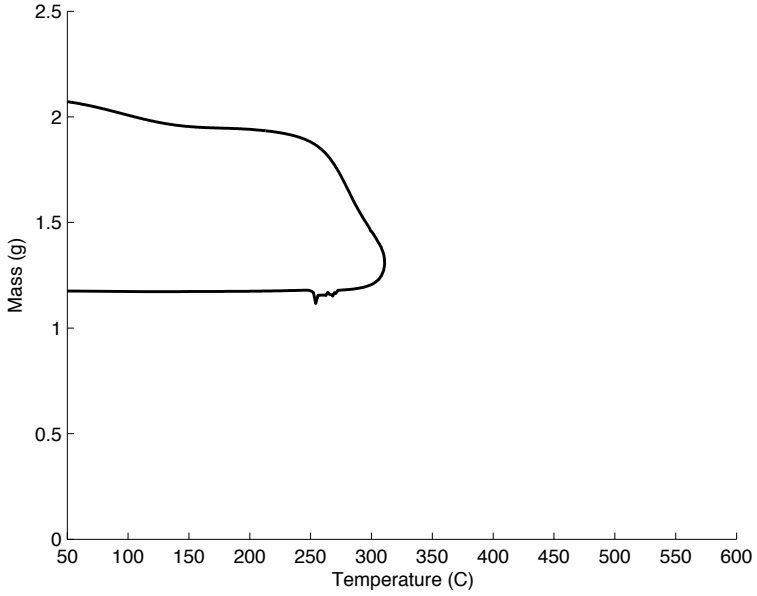

Normalized Mass Fraction (F) = 0.43

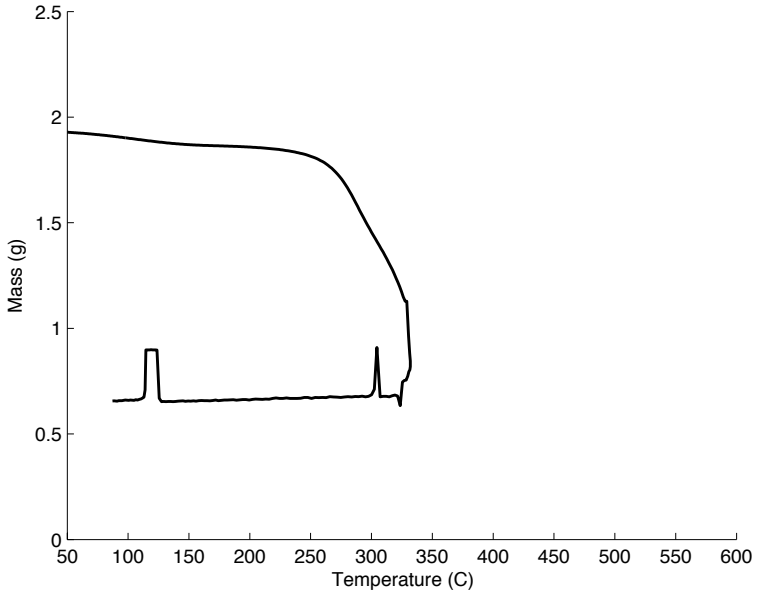

Normalized Mass Fraction (F) = 0.30

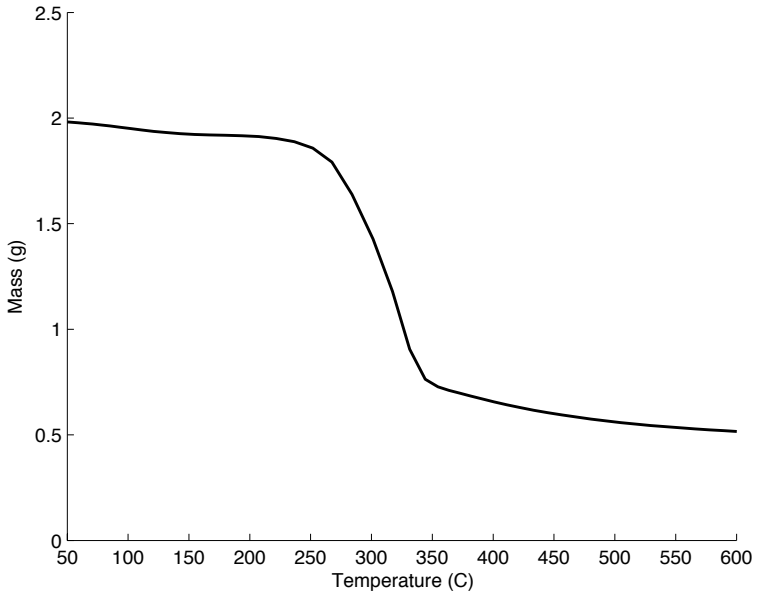

Normalized Mass Fraction (F) = 0 (Fully Decomposed)

Appendix D: Technical Drawings

Porosity Test Section

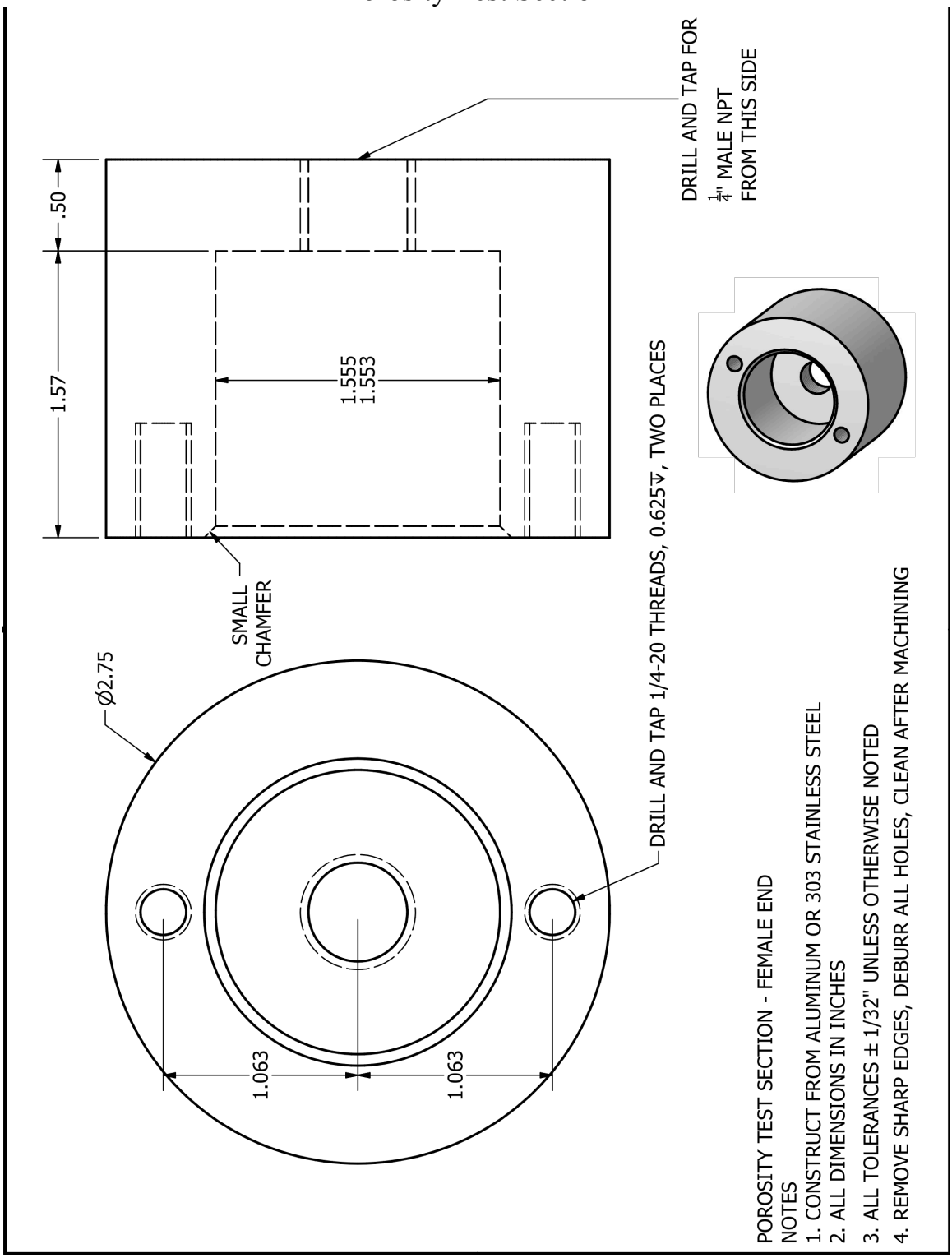

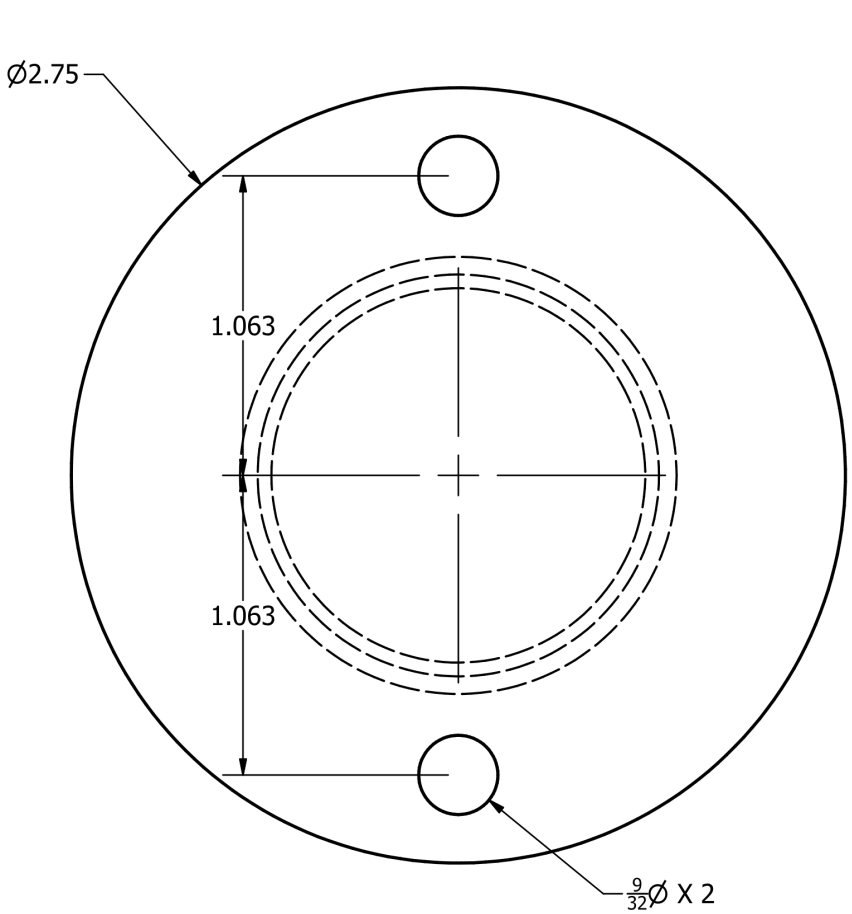

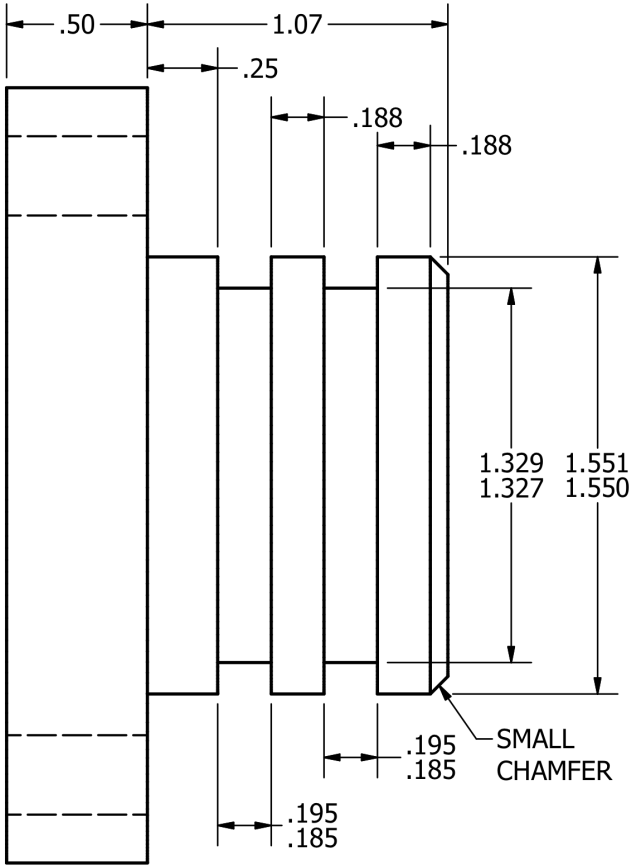

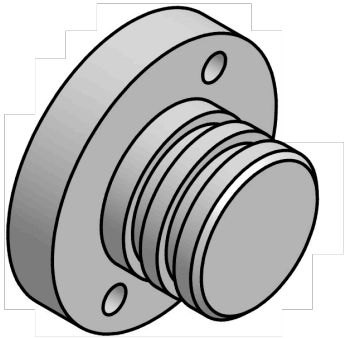

POROSITY TEST SECTION - MALE END

NOTES

1. CONSTRUCT FROM ALUMINUM OR 303 STAINLESS STEEL
2. ALL DIMENSIONS IN INCHES
3. ALL TOLERANCES ± 1/32" UNLESS OTHERWISE NOTED
4. REMOVE SHARP EDGES, DEBURR ALL HOLES, CLEAN AFTER MACHINING

Permeability Test Section

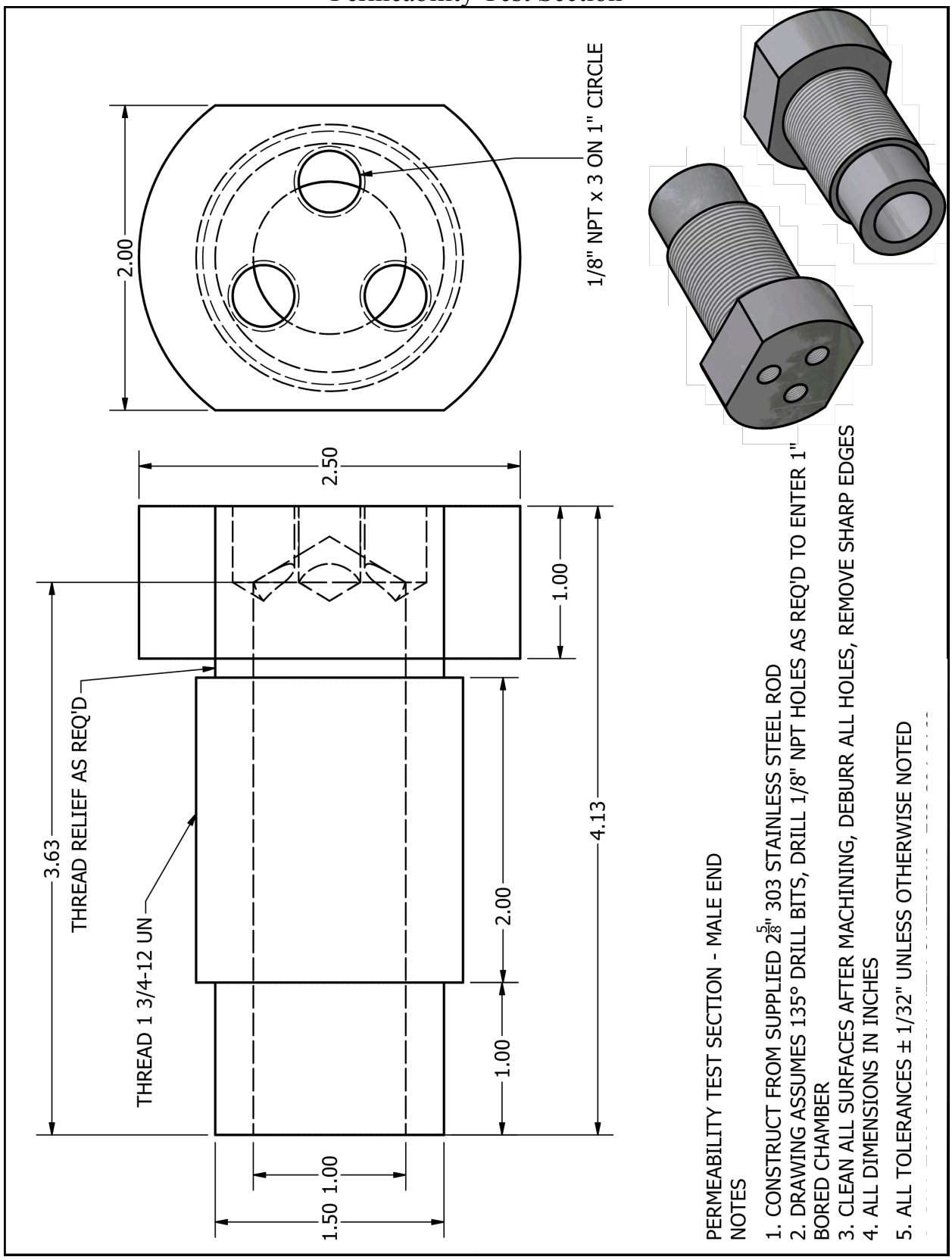

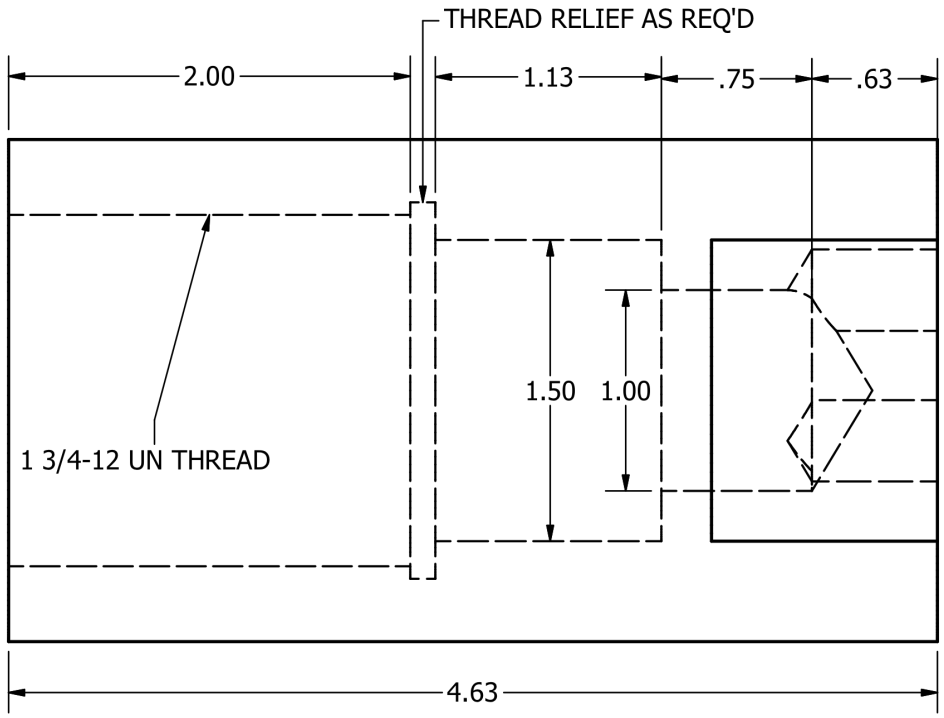

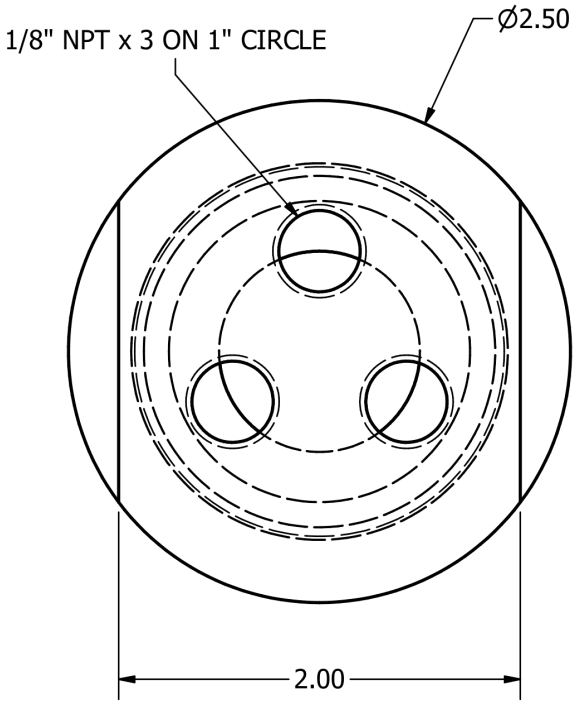

PERMEABILITY TEST SECTION - FEMALE END

NOTES

1. CONSTRUCT FROM SUPPLIED $2\frac{5}{8}$" 303 STAINLESS STEEL ROD
2. DRAWING ASSUMES 135° DRILL BITS, DRILL 1/8" NPT HOLES AS REQ'D TO ENTER 1" BORED CHAMBER
3. EXPAND 1.50 HOLE AS REQ'D TO FIT MALE END WITHOUT SIGNIFICANT INTERFERENCE
4. CLEAN ALL SURFACES AFTER MACHINING, DEBURR ALL HOLES, REMOVE SHARP EDGES
5. ALL DIMENSIONS IN INCHES
6. ALL TOLERANCES ± 1/32" UNLESS OTHERWISE NOTED

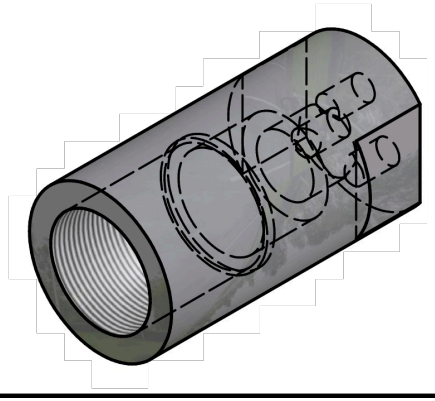

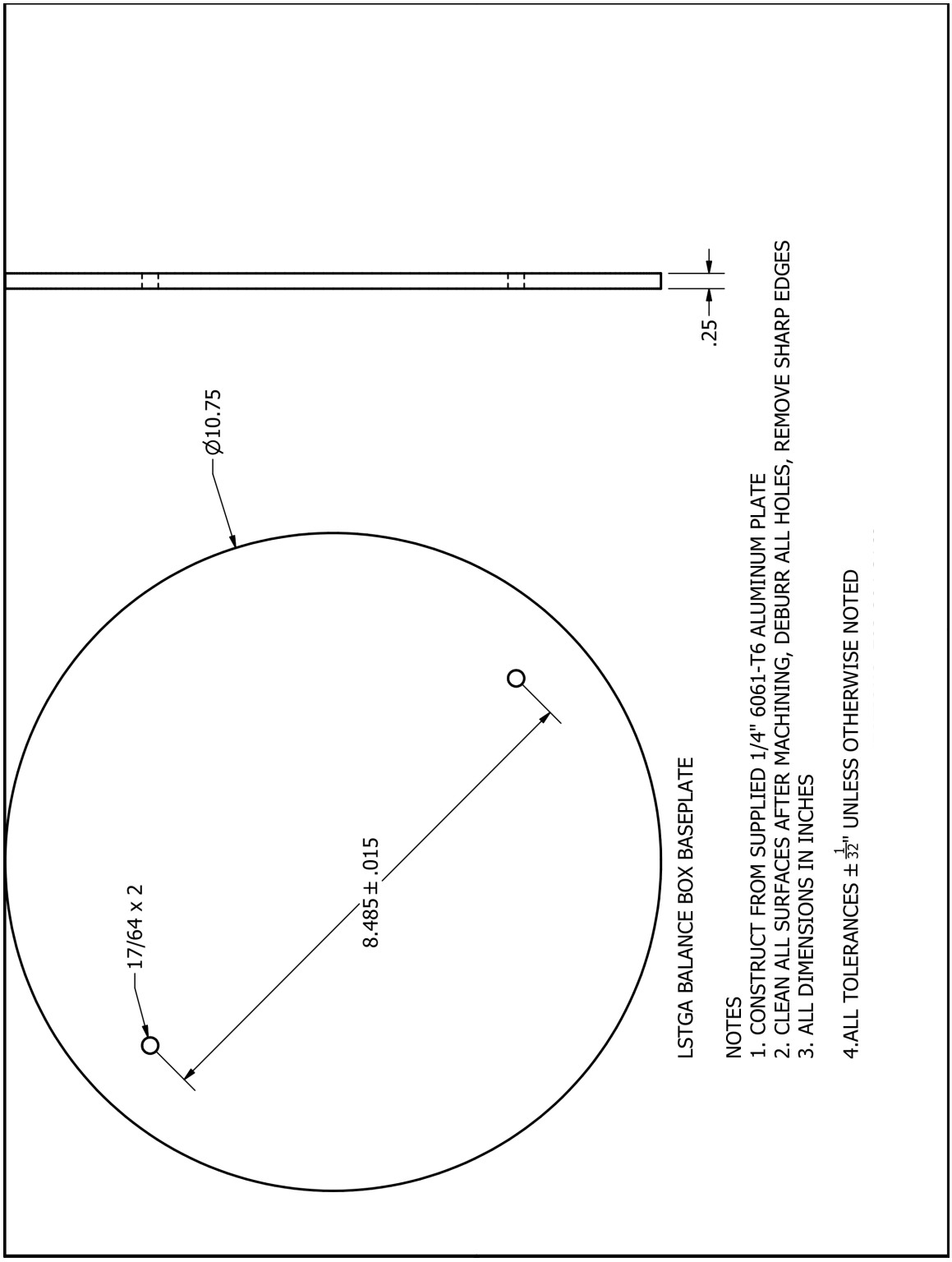
.25
Ø10.75
17/64 x 2
8.485 ± .015
LSTGA BALANCE BOX BASEPLATE
NOTES
1. CONSTRUCT FROM SUPPLIED 1/4" 6061-T6 ALUMINUM PLATE
2. CLEAN ALL SURFACES AFTER MACHINING, DEBURR ALL HOLES, REMOVE SHARP EDGES
3. ALL DIMENSIONS IN INCHES
4.ALL TOLERANCES ± 1/32" UNLESS OTHERWISE NOTED

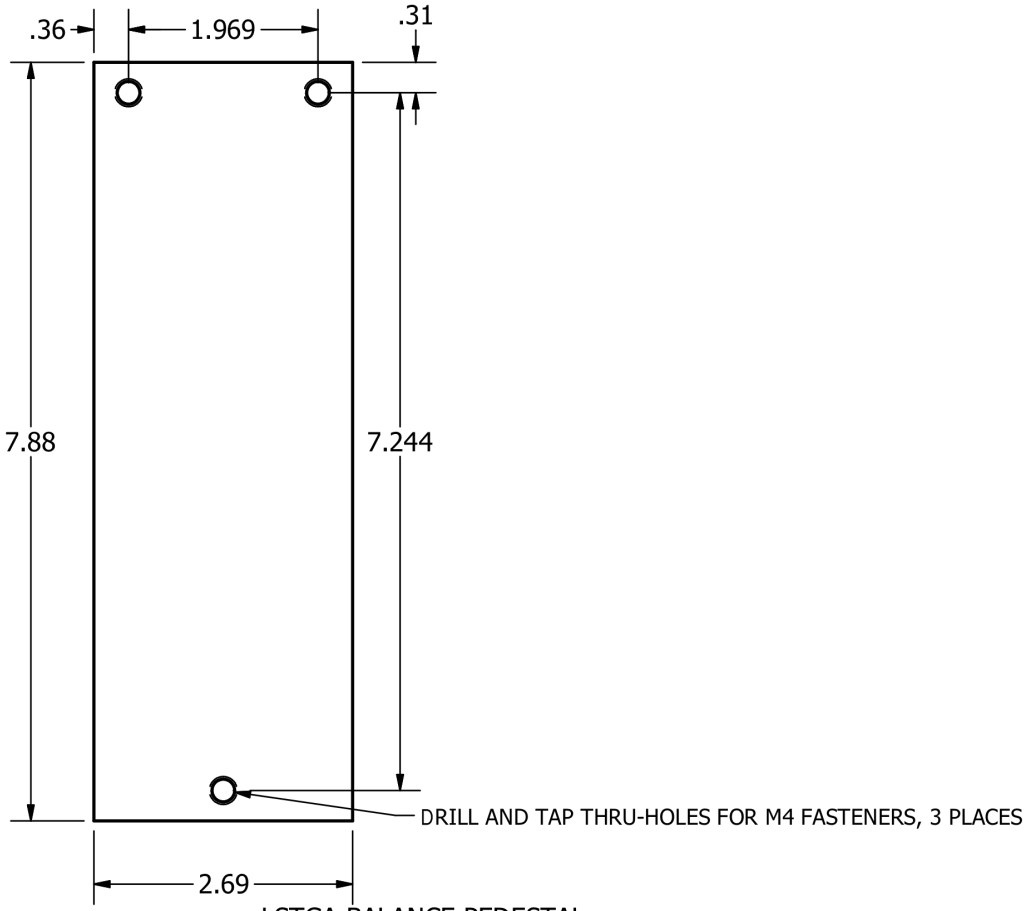

LSTGA BALANCE PEDESTAL

NOTES
1. USE SUPPLIED 6061-T6 ALUMINUM BLOCK
2. CLEAN ALL SURFACES AFTER MACHINING, DEBURR ALL HOLES, REMOVE SHARP EDGES
3. ALL DIMENSIONS IN INCHES

4.ALL TOLERANCES $\pm \frac{1}{32}$" UNLESS OTHERWISE NOTED, HOLE POSITION $\pm \frac{1}{64}$"

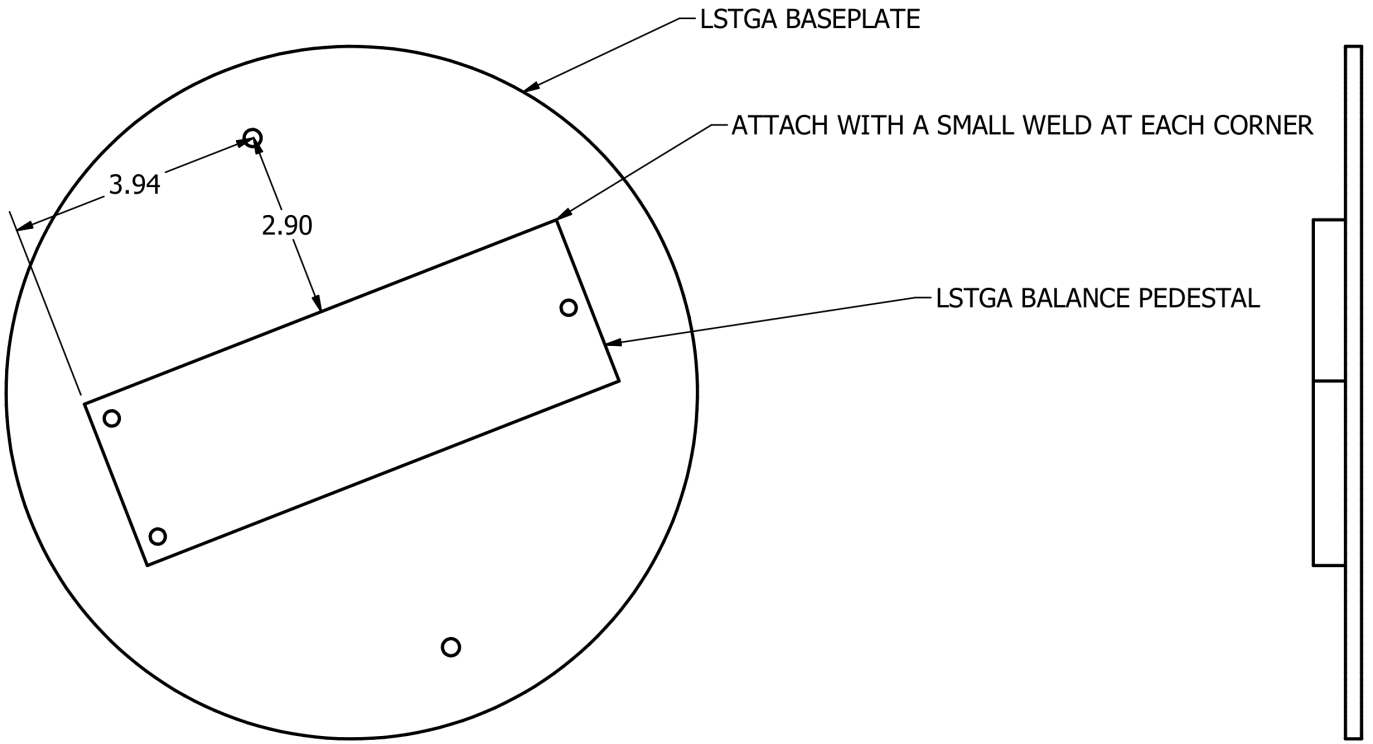

LSTGA BALANCE BOX LOWER ASSEMBLY

NOTES
1. CLEAN ALL SURFACES AFTER WELDING, REMOVE ALL WELD SPLATTER
2. ALL DIMENSIONS IN INCHES

3.ALL TOLERANCES $\pm \frac{1}{32}$" UNLESS OTHERWISE NOTED

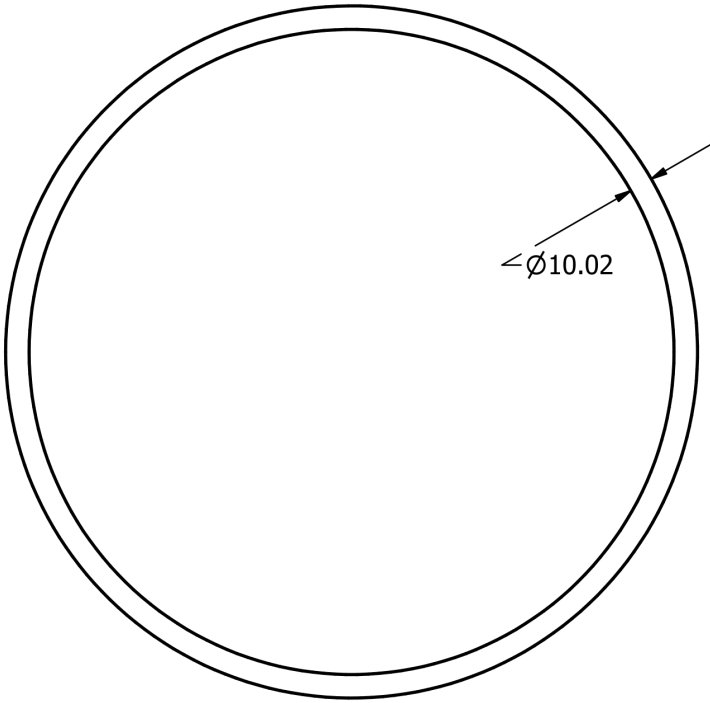

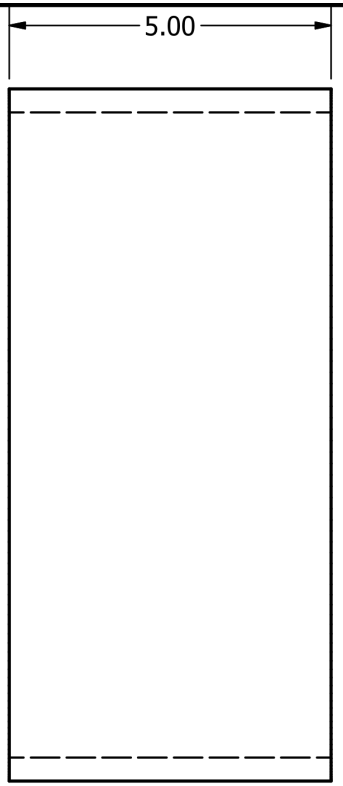

LSTGA BALANCE CHAMBER TUBE

NOTES
1. SUPPLIED CUT TO SIZE IN 6061-T6 ALUMINUM
2. MACHINE SURFACES TO BE WELDED AS REQUIRED
3. CLEAN ALL SURFACES AFTER MACHINING
4. ALL DIMENSIONS IN INCHES

5.ALL TOLERANCES $\pm \frac{1}{32}$" UNLESS OTHERWISE NOTED

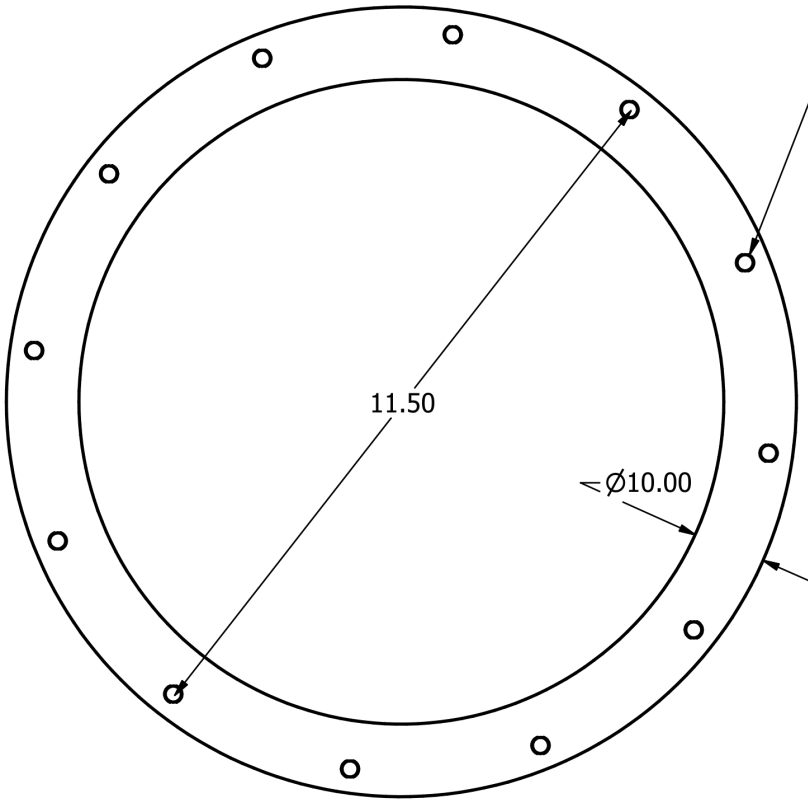

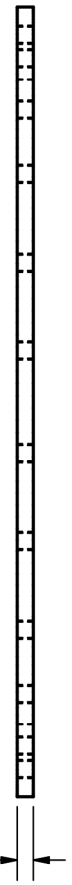

LSTGA BALANCE BOX UPPER FLANGE

NOTES
1. CONSTRUCT FROM SUPPLIED 1/4" 6061-T6 ALUMINUM PLATE
2. CLEAN ALL SURFACES AFTER MACHINING, REMOVE ALL BURRS AND SHARP EDGES
3. ALL DIMENSIONS IN INCHES

4.ALL TOLERANCES $\pm \frac{1}{32}$" UNLESS OTHERWISE NOTED

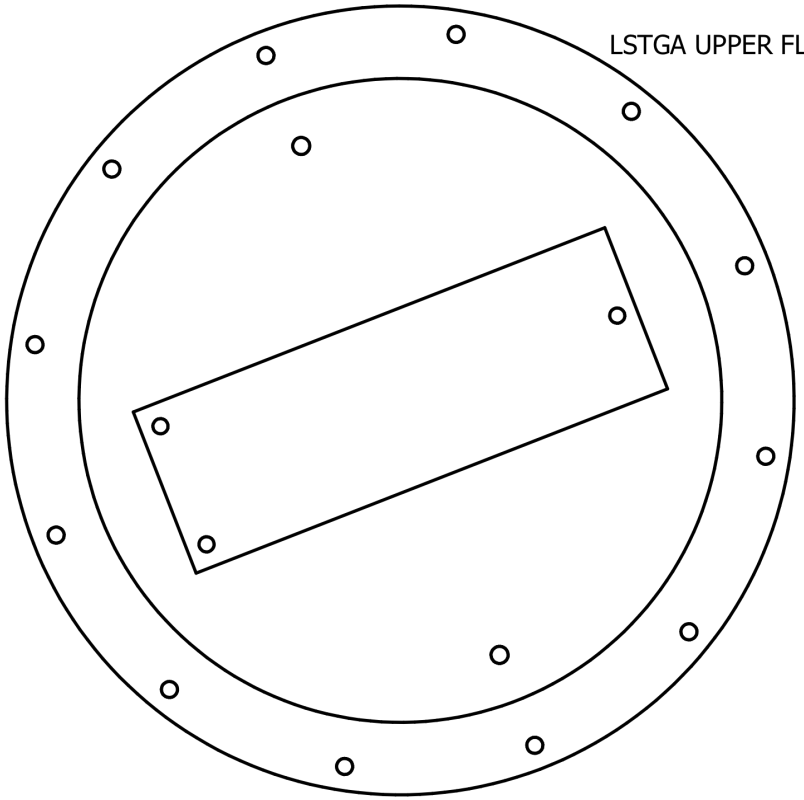

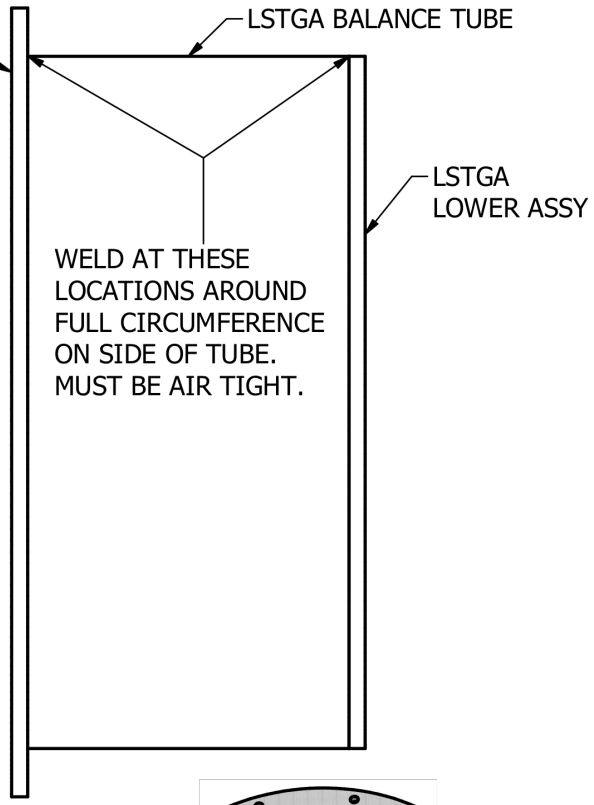

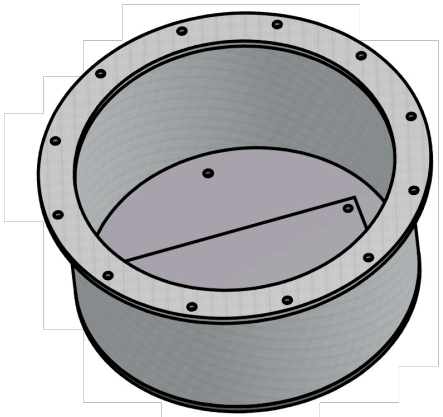

LSTGA BALANCE BOX MAIN ASSEMBLY

NOTES

1. ENSURE PARTS ARE IN CORRECT ORIENTATION BASED ON HOLES
2. USE WELD BEAD SIZE APPROPRIATE FOR MATERIAL THICKNESS
3. WELDS MUST BE AIR TIGHT
4. CLEAN ALL SURFACES AFTER WELDING, REMOVE ALL WELD SPLATTER, MILL TOP FLANGE SMOOTH AGAIN AFTER WELDING IF REQUIRED
5. ALL DIMENSIONS IN INCHES

6.ALL TOLERANCES $\pm \frac{1}{32}$" UNLESS OTHERWISE NOTED

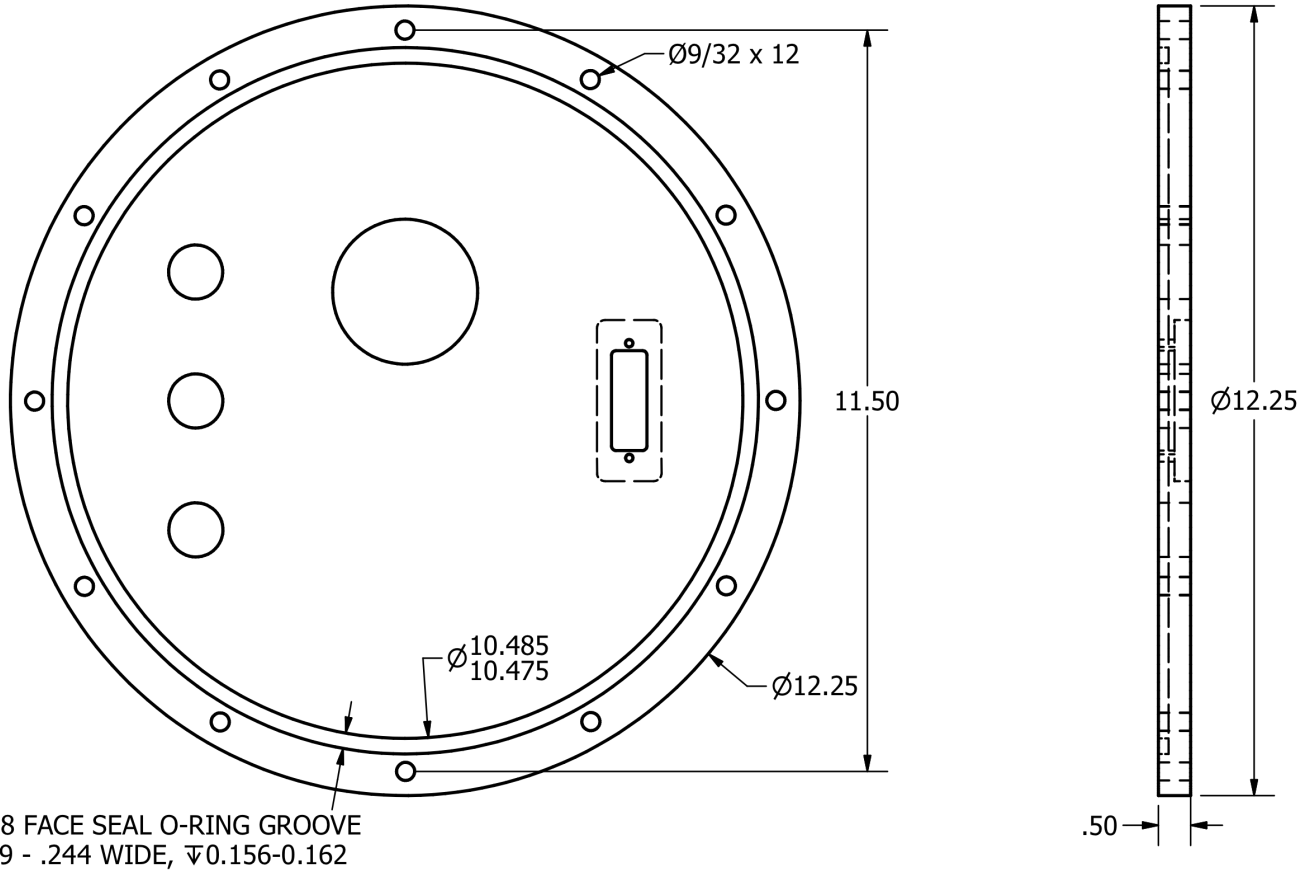

LSTGA JOINT ASSEMBLY BASE FLANGE DRAWING 1/2

NOTES

1. CONSTRUCT FROM SUPPLIED 1/2" ALUMINUM PLATE
2. CLEAN ALL SURFACES AFTER MACHINING, DEBURR ALL HOLES, REMOVE SHARP EDGES
3. MILL SURFACE FLAT/SMOOTH ON O-RING SIDE FROM Ø9.5 OUTWARDS (OR WHOLE SURFACE)
4. ALL DIMENSIONS IN INCHES
5. ALL TOLERANCES ± 1/64" UNLESS OTHERWISE NOTED

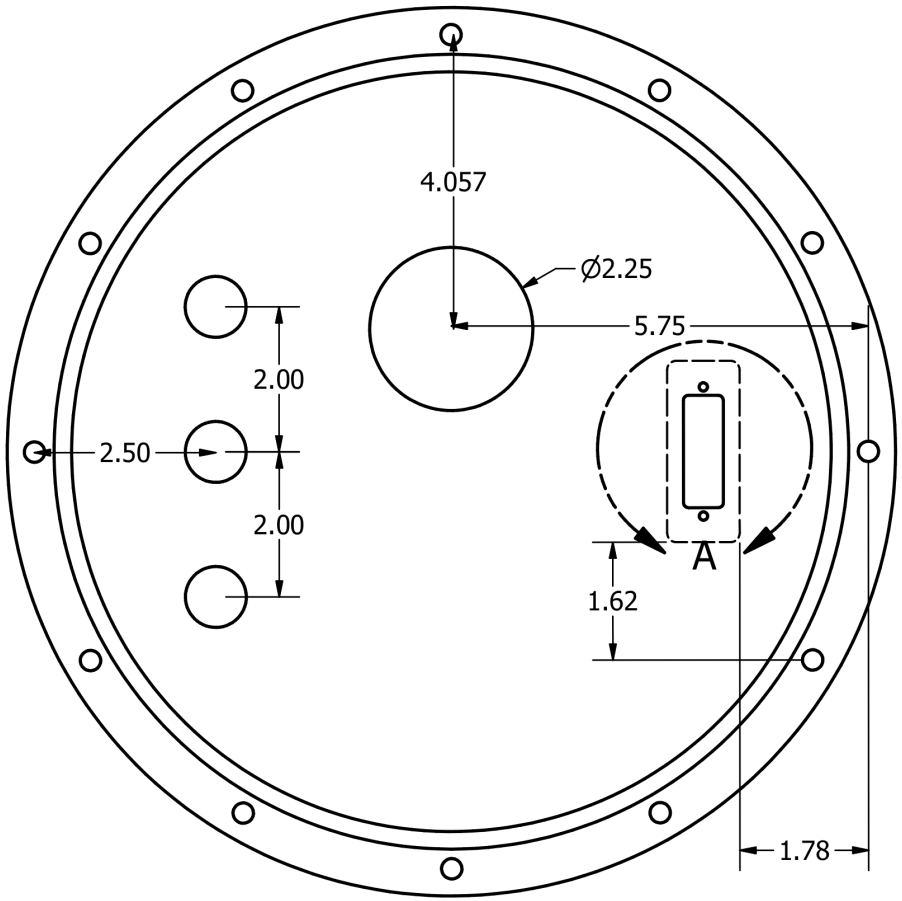

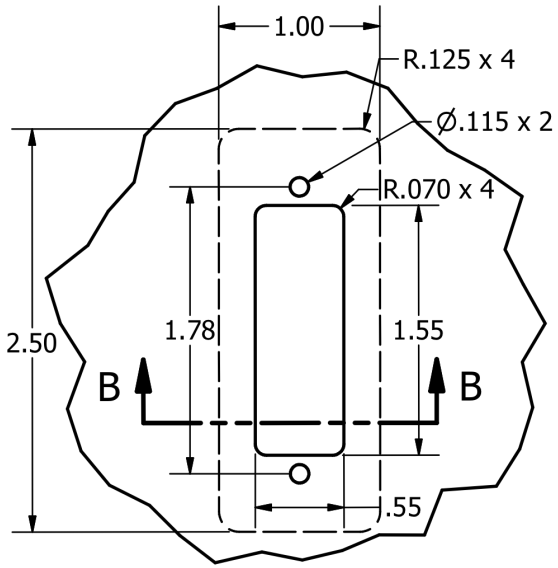

DETAIL A
SCALE 1 : 1

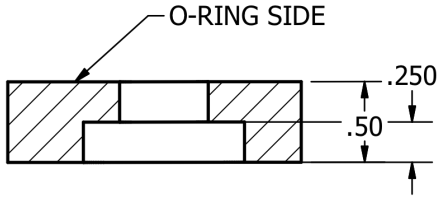

SECTION B-B
SCALE 1 : 1

LSTGA JOINT ASSEMBLY BASE FLANGE DRAWING 2/2

NOTES

1. CONSTRUCT FROM SUPPLIED 1/2" ALUMINUM PLATE
2. CLEAN ALL SURFACES AFTER MACHINING, DEBURR ALL HOLES, REMOVE SHARP EDGES
3. MILL SURFACE FLAT ON O-RING SIDE OUTSIDE OF O-RING GROOVE
4. ALL DIMENSIONS IN INCHES
5. ALL TOLERANCES ± 1/64" UNLESS OTHERWISE NOTED
6. ADVISE IF HOLE/CORNER SIZES IN DETAIL A ARE NOT POSSIBLE, SPECS FROM FEEDTHROUGH MANUFACTURER

LSTGA JOINT ASSEMBLY BASE FLANGE ISOMETRIC VIEWS

NOTES

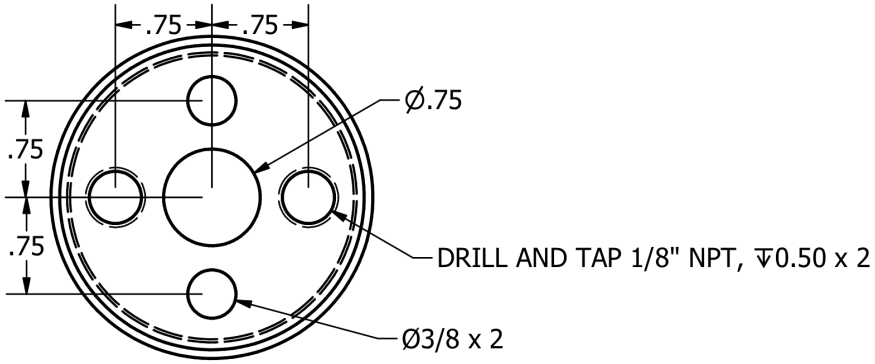

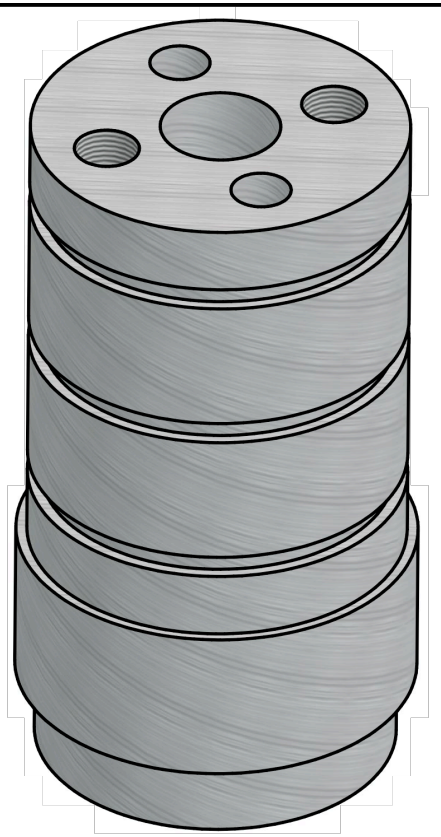

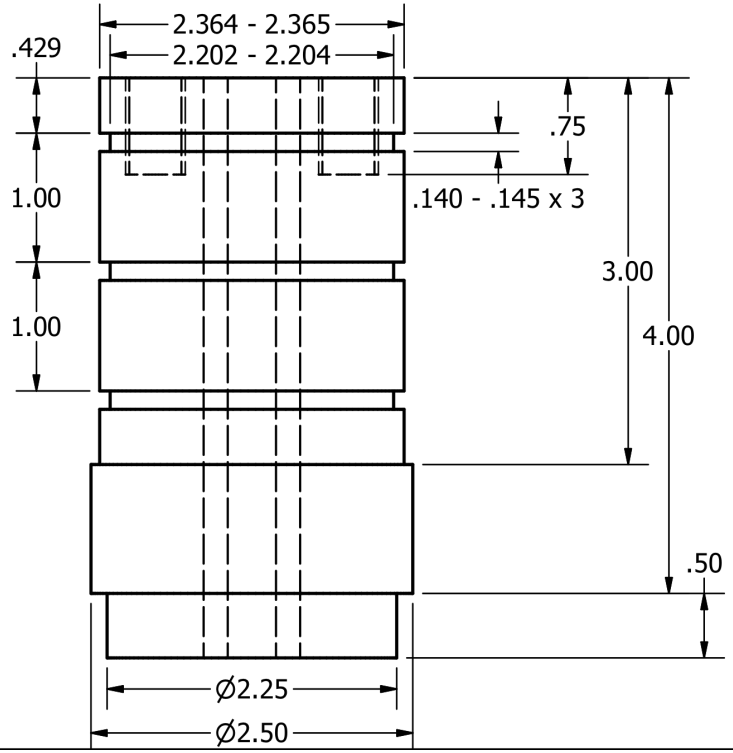

LSTGA JOINT ASSEMBLY PEDESTAL

NOTES
1. CONSTRUCT FROM SUPPLIED 2.5" X 8" 304 STAINLESS STEEL ROD
1a. REST OF ROD TO BE USED FOR LATER PARTS
2. CLEAN ALL SURFACES AFTER MACHINING, DEBURR ALL HOLES, REMOVE SHARP EDGES
3. ALL DIMENSIONS IN INCHES
4.ALL TOLERANCES ± 1/64" UNLESS OTHERWISE NOTED

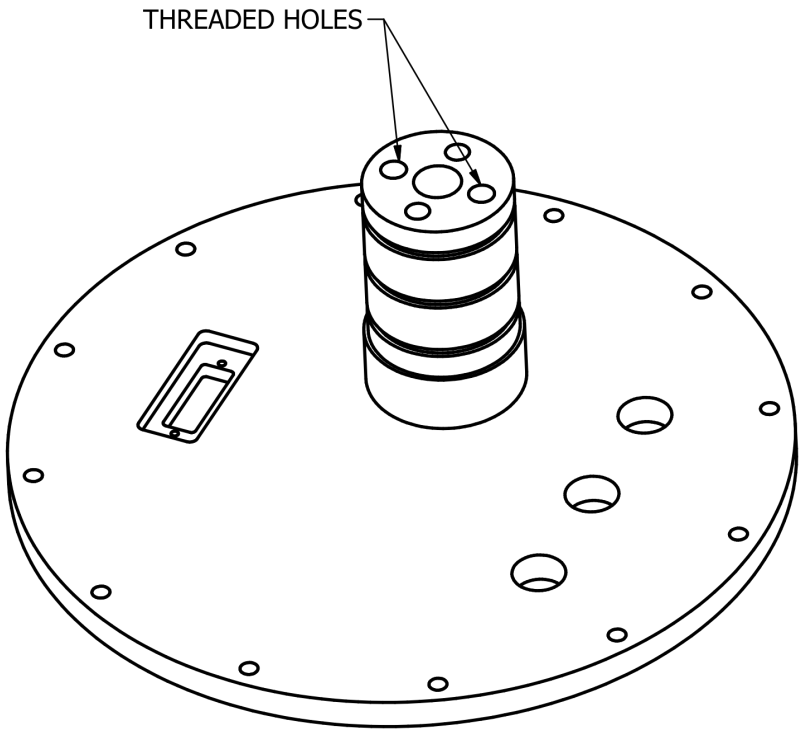

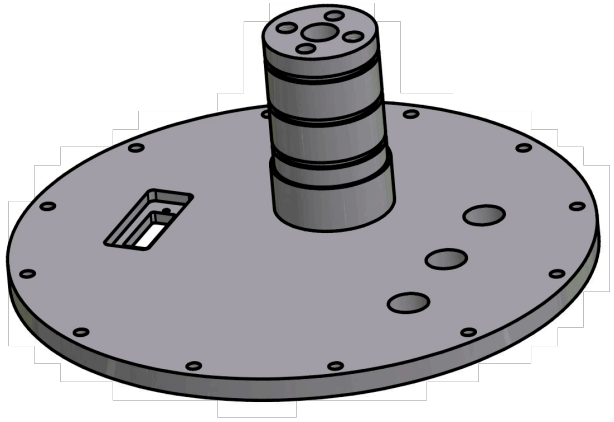

LSTGA JOINT ASSEMBLY

NOTES

1. COVER ALL O-RING GROOVES PRIOR TO WELDING - WELD SPLATTER CANNOT BE ALLOWED TO ENTER THEM
2. ENSURE PIECES ARE CENETERED OVER HOLES BEFORE WELDING - PROPER CENTERING IS FUNCTION CRITICAL
3. CLEAN ALL SURFACES AFTER WELDING, REMOVE ALL WELD SPLATTER
4. MILL SURFACE FLAT ON O-RING SIDE OUTSIDE OF O-RING GROOVE
5. ALL DIMENSIONS IN INCHES
6. ALL TOLERANCES ± 1/32" UNLESS OTHERWISE NOTED

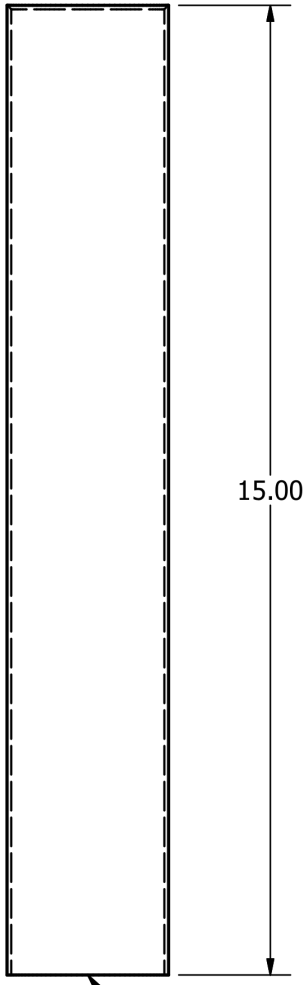

LSTGA WORKTUBE ASSEMBLY - MAIN TUBE

NOTES

1. CONSTRUCT FROM SUPPLIED 316L STAINLESS STEEL TUBING
2. TUBING SUPPLIED AT CORRECT INNER/OUTER DIAMETERS
3. TUBE ENDS MUST BE SQUARE
4. CLEAN ALL SURFACES AFTER MACHINING, REMOVE SHARP EDGES
5. ALL DIMENSIONS IN INCHES
6. ALL TOLERANCES ± 1/32" UNLESS OTHERWISE NOTED

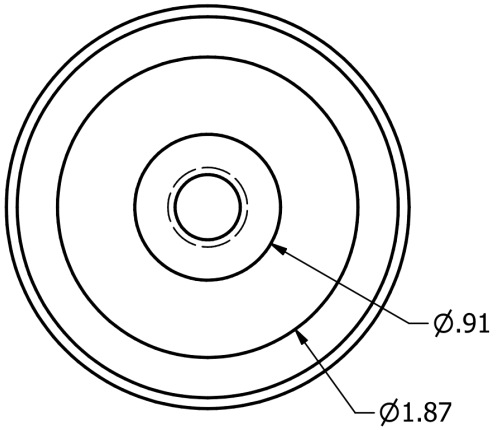

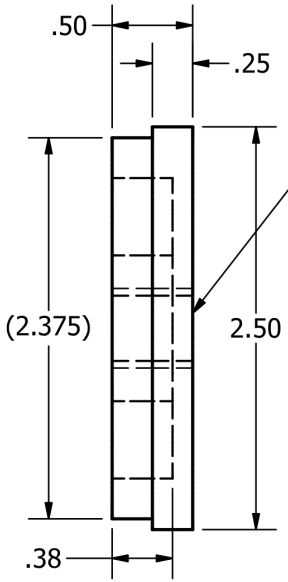

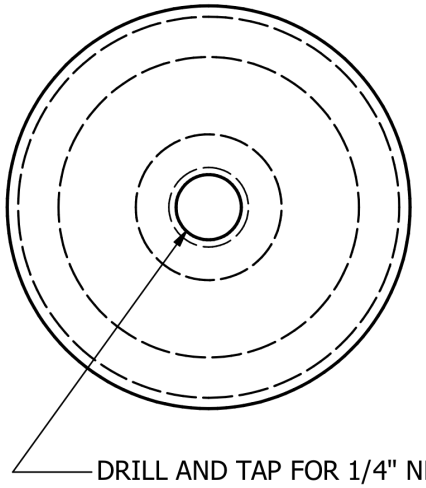

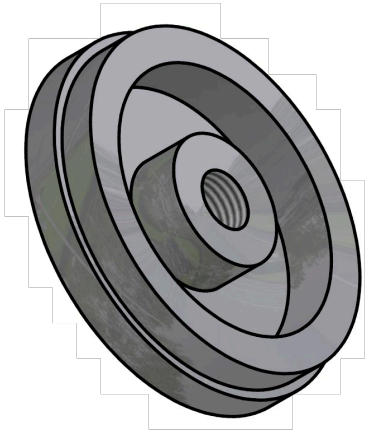

LSTGA WORKTUBE ASSEMBLY - TUBE CAP

NOTES

1. CONSTRUCT FROM SUPPLIED 303 STAINLESS STEEL DISC
2. 2.375" DIMENSION FOR REFERENCE ONLY - MACHINE FOR SHRINK FIT IN TUBE
3. CLEAN ALL SURFACES AFTER MACHINING, REMOVE SHARP EDGES
4. ALL DIMENSIONS IN INCHES
5. ALL TOLERANCES ± 1/32" UNLESS OTHERWISE NOTED

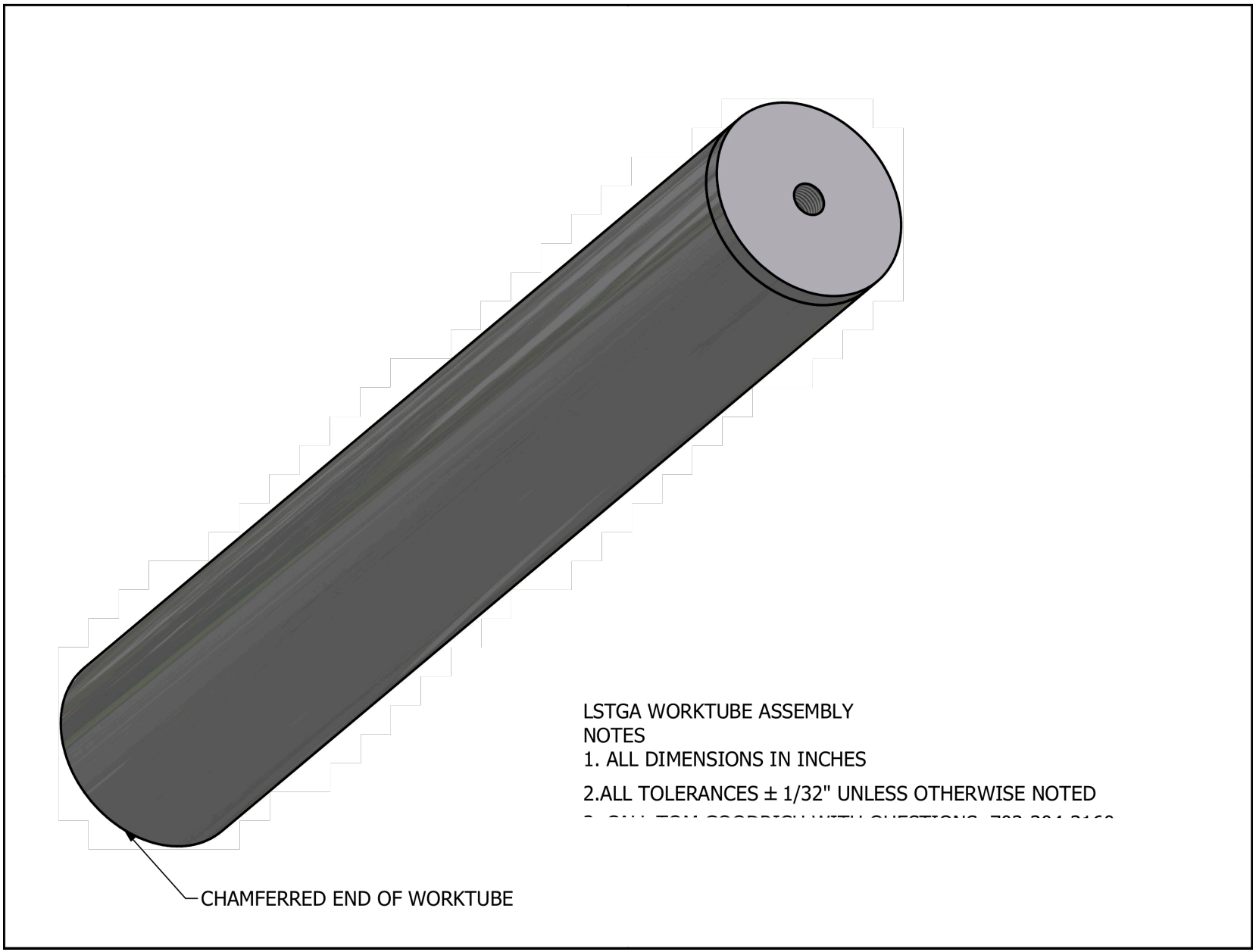
CHAMFERRED END OF WORKTUBE
LSTGA WORKTUBE ASSEMBLY
NOTES
1. ALL DIMENSIONS IN INCHES
2.ALL TOLERANCES ± 1/32" UNLESS OTHERWISE NOTED

Appendix E: Additional Specific Heat Data

Aluminum 5083-H116

Aluminum 5083-H116 is a common alloy used in marine construction as a lighter alternative to steel. Similar to composites, there is some concern with the fire performance of aluminum. The HMS Sheffield was destroyed in the Falklands war as the result of an aluminum bulkhead melting and potentially even burning. The melting point of aluminum alloys is typically around 600°C, hugely lower than the melting point of steel, typically around 1500°C. Due to the difficulty of cutting samples with moderate surface hardness using the core drill (Figure 18) without a drill press, a chunk was cut from a larger panel with a hacksaw, and then finished into a 0.25" disc by hand filing. The sample had a mass of 55.8 mg. The only major thermal reaction involved is melting, which began at 580°C and caused the specific heat to spike from 1.2 to 11 J/(g°C). Figure 60 shows the specific heat curve that was generated on two different scales. No mass changes were observed during the experiment. The value at 50°C of 0.94 J/(g°C) is in very good agreement with the room temperature value published by Matweb of 0.90 J/(g°C) [35].

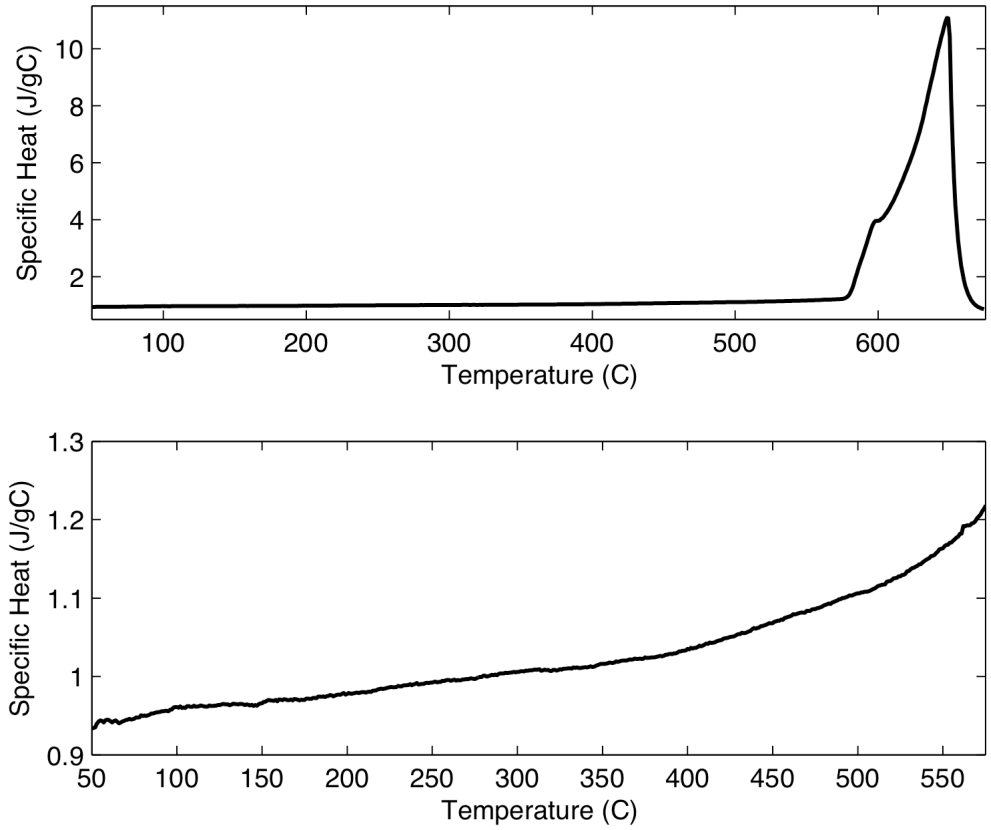

Figure 60. Specific heat of aluminum 5083-H116 on two scales

MACOR™

MACOR™ is a machinable glass-ceramic manufactured by Corning Incorporated. . Its composition is roughly 46% silicon, 17% magnesium, 16% aluminum, 10% potassium, 7% boron, and 4% fluorine [37]. The sample was prepared by mounting a rod 6.73 mm in diameter in the chuck of a drill, and then turning the rod against a piece of coarse-grit sandpaper to reduce the diameter to 0.250". A 2.5 mm thick section was then cut from the end of the rod with a hacksaw, and sanded to the final thickness of 0.76 mm. The sample mass was 56.12 mg, and a mass loss of 0.025 mg, or 0.03% was recorded. Figure 61 shows the specific heat curve that was generated. Aside from a small pike around 500°C, the specific heat is fairly stable until 850°C, at which point it begins to ramp very rapidly until the end of the test at 1000°C. The manufacturer rates the material for use at temperatures of up to 1000°C, which is why it was selected as the final temperature. The value at 50°C of 0.85 J/(g°C) is in very good agreement with the to room temperature the value published by Matweb of 0.79 J/(g°C) [36].

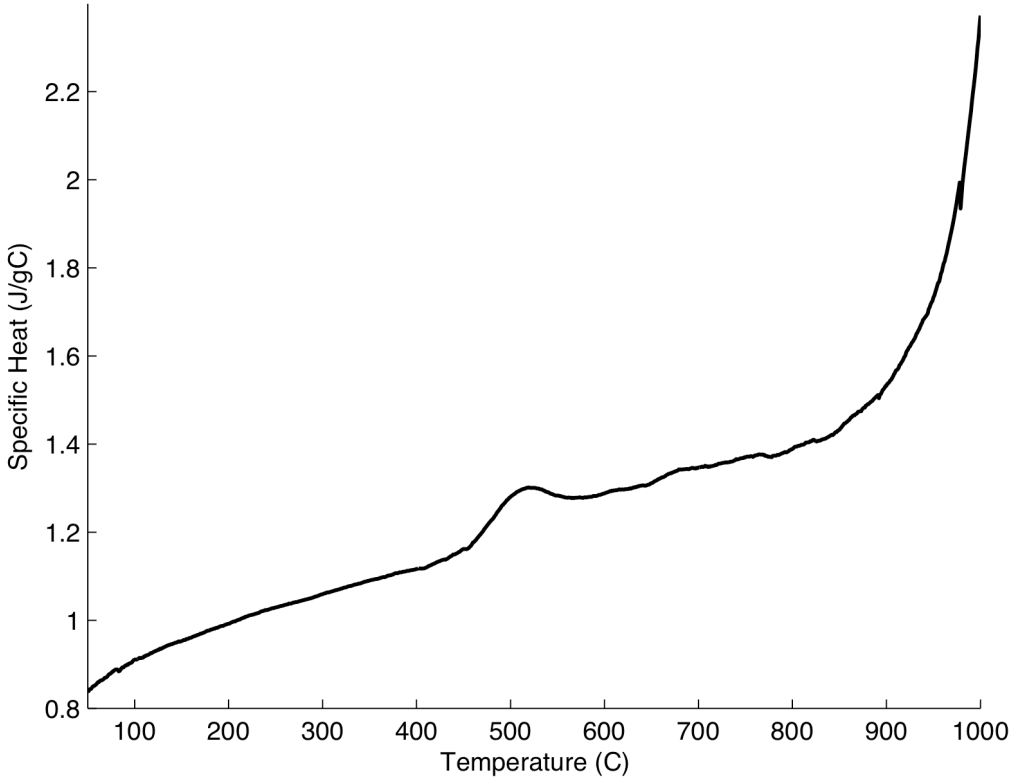

Figure 61. Specific heat of MACOR™

NAD-11

NAD-11 is a structural insulating board made of high-density cement reinforced with inorganic fibers. It is rated for a continuous service temperature of 500°C, which was selected as the final temperature for the specific heat experiment – conveniently allowing for the use of aluminum sample cups, which give the best possible temperature sensitivity. Mass loss began immediately on heating, and totaled 2.05 mg, or 7.5%. Relative to aluminum, MACOR™, and sapphire, NAD-11 has a fairly high apparent specific heat that averages around 2.8 J/g°C. Due to the changes in mass, the specific heat that was measured likely represents the latent and sensible portions of the specific heat capacity combined.

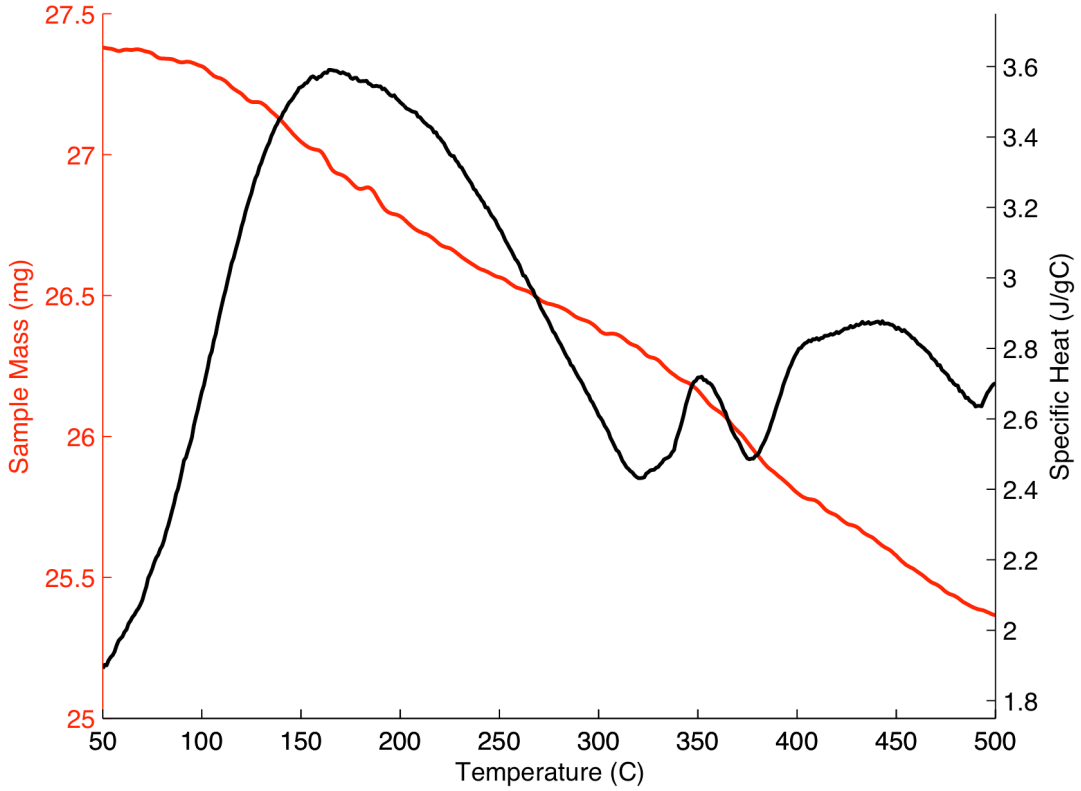

Figure 62. Specific heat of NAD-11